



**British  
Geological Survey**

NATURAL ENVIRONMENT RESEARCH COUNCIL

# New methodologies for volcanic-hosted copper sulphide mineralization on Cyprus: A GIS–prospectivity analysis-based approach

Economic Minerals Programme

Internal Report CR/06/129





BRITISH GEOLOGICAL SURVEY

ECONOMIC MINERALS PROGRAMME

INTERNAL REPORT CR/06/129

# New methodologies for volcanic-hosted copper sulphide mineralization on Cyprus: A GIS–prospectivity analysis-based approach

## *Keywords*

GIS, Cyprus, Volcanic massive sulphide.

J Naden, RJ Herrington, SM Jowitt, FM McEvoy, JP Williamson, AJ Monhemius

## *Front cover*

Photograph looking east at the Alestos open cast pit that was mined at the end of the 1930s. Alestos hill rises to the north

## *With contributions from*

AG Gunn, L Bateson, KE Rollin, R Thomas, C White, R Osborn

## *Bibliographical reference*

J NADEN, RJ HERRINGTON, SM JOWITT, FM MCEVOY, JP WILLIAMSON, AJ MONHEMIUS. 2006. New methodologies for volcanic-hosted copper sulphide mineralization on Cyprus: A GIS–prospectivity analysis-based approach. *British Geological Survey Internal Report*, CR/06/129. 242pp.

Copyright in materials derived from the British Geological Survey's work is owned by the Natural Environment Research Council (NERC) and/or the authority that commissioned the work. Contact the BGS Intellectual Property Rights Section, British Geological Survey, Keyworth, e-mail [ipr@bgs.ac.uk](mailto:ipr@bgs.ac.uk). You may quote extracts of a reasonable length without prior permission, provided a full acknowledgement is given of the source of the extract.

Keyworth, Nottingham British Geological Survey 2006

## BRITISH GEOLOGICAL SURVEY

The full range of Survey publications is available from the BGS Sales Desks at Nottingham, Edinburgh and London; see contact details below or shop online at [www.geologyshop.com](http://www.geologyshop.com)

The London Information Office also maintains a reference collection of BGS publications including maps for consultation.

The Survey publishes an annual catalogue of its maps and other publications; this catalogue is available from any of the BGS Sales Desks.

*The British Geological Survey carries out the geological survey of Great Britain and Northern Ireland (the latter as an agency service for the government of Northern Ireland), and of the surrounding continental shelf, as well as its basic research projects. It also undertakes programmes of British technical aid in geology in developing countries as arranged by the Department for International Development and other agencies.*

*The British Geological Survey is a component body of the Natural Environment Research Council.*

*British Geological Survey offices*

### **Keyworth, Nottingham NG12 5GG**

☎ 0115-936 3241 Fax 0115-936 3488  
e-mail: [sales@bgs.ac.uk](mailto:sales@bgs.ac.uk)  
[www.bgs.ac.uk](http://www.bgs.ac.uk)  
Shop online at: [www.geologyshop.com](http://www.geologyshop.com)

### **Murchison House, West Mains Road, Edinburgh EH9 3LA**

☎ 0131-667 1000 Fax 0131-668 2683  
e-mail: [scotsales@bgs.ac.uk](mailto:scotsales@bgs.ac.uk)

### **London Information Office at the Natural History Museum (Earth Galleries), Exhibition Road, South Kensington, London SW7 2DE**

☎ 020-7589 4090 Fax 020-7584 8270  
☎ 020-7942 5344/45 email: [bgs london@bgs.ac.uk](mailto:bgs london@bgs.ac.uk)

### **Forde House, Park Five Business Centre, Harrier Way, Sowton, Exeter, Devon EX2 7HU**

☎ 01392-445271 Fax 01392-445371

### **Geological Survey of Northern Ireland, Colby House, Stranmillis Court, Belfast BT9 5BF**

☎ 028-9038 8462 Fax 028-9038 8461

### **Maclean Building, Crowmarsh Gifford, Wallingford, Oxfordshire OX10 8BB**

☎ 01491-838800 Fax 01491-692345

### **Columbus House, Greenmeadow Springs, Tongwynlais, Cardiff, CF15 7NE**

☎ 029-2052 1962 Fax 029-2052 1963

*Parent Body*

### **Natural Environment Research Council, Polaris House, North Star Avenue, Swindon, Wiltshire SN2 1EU**

☎ 01793-411500 Fax 01793-411501  
[www.nerc.ac.uk](http://www.nerc.ac.uk)

# Foreword

In 2002, the Republic of Cyprus commissioned a research and development programme to upgrade its role in the sector of the Metallic Mineral Wealth of Cyprus. The programme concerned the development of new methodologies for the exploration and exploitation of cupriferous sulphide ores. This report documents the results of the programme and is product of a collaborative study between the British Geological Survey (BGS), the Natural History Museum, London (NHM) Geological Survey Department (GSD), Ministry Agriculture, Environment and Natural Resources Cyprus.

# Acknowledgements

In addition to the BGS, NHM and GSD staff acknowledged above, staff at Hellenic Copper Mines, Eastern Mediterranean Minerals and Eastern Mediterranean Resources made significant intellectual and material contributions to this report. In particular, Nicos Adamides and George Maliotis are recognised for their invaluable input to the project

# Contents

<b>Foreword</b> .....	<b>5</b>
<b>Acknowledgements</b> .....	<b>5</b>
<b>Contents</b> .....	<b>5</b>
<b>Executive summary</b> .....	<b>15</b>
<b>1 Introduction</b> .....	<b>17</b>
<b>2 Mineralization on Cyprus</b> .....	<b>20</b>
2.1 General geology.....	20
2.2 Mineralization.....	27
2.3 Limassol Forest Ni-Cu-Co mineralizAtion .....	31
<b>3 Mineral deposit models and prospectivity analysis</b> .....	<b>36</b>
3.1 VHMS mineralization.....	37
3.2 Ophiolite-hosted VHMS deposits.....	40
3.3 Mineral deposit model—Cyprus-type VHMS deposits.....	42
3.4 Exploration model .....	47
<b>4 Assessment of previous work and data used in the study</b> .....	<b>49</b>
4.1 Exploration concepts used in United Nations work .....	49
4.2 Geological data .....	50
4.3 Geophysical data.....	50
4.4 Remote sensing data .....	52

4.5	Geochemical data.....	52
<b>5</b>	<b>Alteration mineralogy and putative epithermal-style mineralization.....</b>	<b>54</b>
5.1	Background information and introduction.....	54
5.2	Background alteration of the Troodos ophiolite.....	55
5.3	Alteration associated with VHMS deposits.....	55
5.4	Epithermal ore deposits.....	58
5.5	Geology of the studied prospects.....	59
5.6	Portable infrared mineral analyser (PIMA).....	67
5.7	Results of the PIMA investigation.....	69
5.8	X-Ray diffraction analysis of alteration minerals.....	88
5.9	Petrological Analysis.....	92
5.10	Discussion.....	100
<b>6</b>	<b>Whole rock geochemistry.....</b>	<b>105</b>
6.1	Discriminant plots.....	105
6.2	Hydrothermal alteration.....	107
6.3	Hydrothermal alteration indices.....	108
<b>7</b>	<b>Mineralogical research.....</b>	<b>114</b>
7.1	Processes of supergene upgrade in VHMS Systems.....	114
7.2	Discussion of supergene mineralization.....	132
<b>8</b>	<b>Considerations on the application of recent advances in copper hydrometallurgy at the Hellenic Copper Mines Skouriotissa copper production plant.....</b>	<b>135</b>
8.1	Description of the Skouriotissa plant.....	135
8.2	Overview of heap leaching-SX-EW.....	137
8.3	Heap leaching of sulphide ores.....	138
8.4	Production of copper concentrate using Froth flotation technology.....	142
8.5	Discussion.....	145
8.6	Conclusions from metallurgical studies.....	147
<b>9</b>	<b>Geophysical modelling.....</b>	<b>149</b>
9.1	Gravity data.....	149
9.2	Magnetic data.....	149
<b>10</b>	<b>Remote sensing.....</b>	<b>157</b>
10.1	PIMA.....	157
10.2	Satellite imagery.....	159
<b>11</b>	<b>Prospectivity mapping.....</b>	<b>170</b>
11.1	Information for spatial data modelling.....	176
11.2	Results—regional prospectivity.....	178
11.3	Discussion—regional prospectivity.....	199
<b>12</b>	<b>Pilot study.....</b>	<b>203</b>
12.1	Introduction.....	203
12.2	Detailed prospectivity analysis and location of boreholes.....	203

12.3	Results of drilling .....	207
12.4	Borehole MR2-06 .....	212
<b>13</b>	<b>Results, conclusions and future work.....</b>	<b>217</b>
13.1	Project Results and conclusions.....	217
13.2	Future work.....	219
<b>References</b>	<b>.....</b>	<b>224</b>
<b>Appendix 1</b>	<b>Copper mineralization associated mineral occurrences in Cyprus .....</b>	<b>230</b>
<b>Appendix 2</b>	<b>Gossan occurrence data .....</b>	<b>234</b>
<b>Appendix 3</b>	<b>Publications and presentations at international conferences .....</b>	<b>239</b>
<b>Appendix 4</b>	<b>Outline prospectivity guide.....</b>	<b>240</b>

## FIGURES

Figure 1	The position of Cyprus within the Eastern Mediterranean area .....	20
Figure 2	Map showing the three major geological terranes of Cyprus.....	23
Figure 3	A generalised stratigraphic column showing the relative positions of copper mineralization and other deposits in the Troodo .....	27
Figure 4	Former asbestos workings at Amiandos.....	28
Figure 5	Copper cathode production at the Phoenix–Skouriotissa–Three Hills mine site .....	30
Figure 6	Extract of geological map of the Limassol Forest showing the location of the two main Ni–Cu–Co showings.....	31
Figure 7	TiO <sub>2</sub> vs. Al <sub>2</sub> O <sub>3</sub> plot showing chromite compositions of Limassol Forest mineralization.....	32
Figure 8	Photographs of the Lakxia tou Mavrou set of showings. ....	33
Figure 9	Pevkos showing: A—View from gossanous outcrop southwest towards coast. Showing comprises rubbly gossanous outcrops next to field pack with small reclaimed dumps; B—Closeup of altered serpentinite with gossanous material after pyrrhotite? .....	35
Figure 10	Conceptual diagram of an exploration model .....	36
Figure 11	Major VHMS deposits and provinces around the world.....	37
Figure 12	Examples of tectonic settings for the formation of Cyprus/ophiolite-hosted, Besshi and Kuroko/Noranda-type VHMS deposits .....	38
Figure 13	Some well-known ophiolite related VHMS deposits.....	40
Figure 14	Cross section through the East Lefka VHMS deposit.....	45
Figure 15	A map of south-west Cyprus showing the locations of the five deposits in relation to lithologies.....	54
Figure 16	A photograph looking south at the bleached mill breccia that was mined during the 1930s .....	60

Figure 17	Photograph looking east at the open cast pit that was mined at the end of the 1930s .....	61
Figure 18	A photograph of the quartz-breccia showing the sub-angular to rounded clasts supported by an Fe-rich silicic matrix .....	62
Figure 19	A close up photograph of the quartz-breccia as it grades into the hematite–quartz–jasper breccia.....	62
Figure 20	A photograph of a boulder of the silica volcanics breccia .....	64
Figure 21	Geological map of Tourounjia with the locations of samples shown as black crosses with numbers. ....	65
Figure 22	View of Tourounjia looking west. ....	66
Figure 23	A plot showing the major spectral absorption bands in SWIR from which the minerals producing the spectra can be identified .....	68
Figure 24	Downhole log for borehole CY2A (140 to 226m) from the Agrokipia Mine comparing PIMA, geological, geochemical and geophysical data. ....	71
Figure 25	Downhole log for borehole CY2A (226 to 306 m) from the Agrokipia Mine comparing PIMA, geological, geochemical and geophysical data. ....	72
Figure 26	Downhole log of the data from ERD-1a borehole. ....	73
Figure 27	Downhole log of the data from the EPS-2 borehole .....	74
Figure 28	Downhole log of the data from EAD-2 borehole (surface to 100 m). ....	75
Figure 29	Downhole log of the data from EAD-2 borehole (100 to 200 m). ....	76
Figure 30	Downhole log of the data from the ETS-2 borehole .....	77
Figure 31	Downhole log of the data from the ETS-1 borehole (surface to 100 m). ....	78
Figure 32	Graphs showing the variation in the wavelength of the FeOH and MgOH absorption features for chlorites in the CY-2a borehole. ....	79
Figure 33	A photograph of the ERD-1a drill core at a depth of 57.5m showing the late stage white clay filled veins that host most of the palygorskite. Montmorillonite is also commonly identified from spectra taken from these veins. ....	80
Figure 34	Graphs showing the variation in the wavelength of FeOH and MgOH absorption features for the chlorites in the ERD-1a borehole.....	81
Figure 35	Graphs showing the variation in wavelength of the FeOH and MgOH absorption features for chlorites in the EPS-2 borehole. ....	82
Figure 36	A photograph of the pebble breccia zone from a depth of 18.5m in the EAD-2 borehole. ....	83
Figure 37	Graphs showing the variation in the wavelength of the FeOH and MgOH absorption feature for the chlorites of the EAD-2 borehole. ....	84
Figure 38	A plot showing the variation of the K1/K2 ratio in the ETS-1 borehole of samples containing kaolinite with depth. ....	86
Figure 39	A plot showing the variation of the ratio of absorption intensities between the K1 absorption feature (at 2206nm) and the K2 absorption feature (at 2162nm) from sample containing kaolinite with depth. ....	87
Figure 40	XRD patterns for EAD-2 (Alestos) at a depth of 18 m. ....	89
Figure 41	XRD patterns for ETS-2 (Tourounjia) at a depth of 1 m. ....	90

Figure 42	Transmitted light photographs of T09 from the silicified propylitically altered volcanics. ....	93
Figure 43	Reflected light photographs of mineralization. ....	93
Figure 44	Back scattered electron micrograph, showing blades of pyrite and non sulphide in sample T06. ....	94
Figure 45	Spectrum detected over a 10 second period showing the phases detected which are compatible with the elements found in gypsum. ....	95
Figure 46	Back scattered electron micrograph, showing arsenopyrite in T03 with pyrite, sphalerite and copper sulphide. ....	95
Figure 47	Fluid inclusion wafer from sample T06 with the two areas that contained the fluid inclusions analysed marked. ....	96
Figure 48	Histogram showing the distributions of last ice melting temperatures .....	98
Figure 49	Histogram showing the distributions of homogenization temperatures .....	99
Figure 50	Graph showing fluid inclusion data for Tourounjia, including salinities of seawater and the range of those found at the TAG hydrothermal mound. ....	99
Figure 51	A P–T diagram for a NaCl–H <sub>2</sub> O solution of seawater salinity .....	102
Figure 52	Zirconium versus yttrium values for CY and Adamides datasets. ....	106
Figure 53	Plot of zirconium versus titanium for the dataset. ....	106
Figure 54	Aluminium versus titanium data plotted for the dataset. ....	107
Figure 55	Down-hole graphical log of CY2a showing selected oxide variation .....	108
Figure 56	Down-hole plot of CY2a showing calculated Ishikawa alteration index and total iron as a graphical log (II=60 marked as a horizontal line). ....	109
Figure 57	Yttrium versus zirconium for the Adamides data set. ....	110
Figure 58.	Titanium oxide versus zirconium for the Adamides data set .....	110
Figure 59	Comparison of chlorite alteration index against digital 1:250,000 geology and mineral prospectivity. ....	111
Figure 60	Comparison of Ishihara alteration index against digital 1:250,000 geology and mineral prospectivity. ....	111
Figure 61	Yttrium versus zirconium for the EMM regional data set. ....	112
Figure 62	Titanium oxide versus zirconium for the EMM regional data set. ....	112
Figure 63	Schematic diagram for the formation of supergene mineralization by meteoric water .....	114
Figure 64	Geological Map of the Skouriotissa region, note Phoenix, Phoukassa and Three Hills orebodies. Scale 1:50 000, Phoenix Phoukassa Three Hills. ....	116
Figure 65	Simplified Geology of the Skouriotissa–Phoenix open pit—note as this a view of the pit that works the supergene sulphides the main stockwork zone is hidden from view .....	117
Figure 66	Detail of the massive sulphide–umber interface, Skouriotissa. ....	118
Figure 67	Hand specimen of massive pyrite from the Phoukassa deposit. ....	118
Figure 68	Hand specimen of supergene sulphate mineralization from the Phoukassa deposit. ....	119

Figure 69	Sugary pyrite showing oxidation to hydrated iron oxides. ....	119
Figure 70	Hand specimen from Phoukassa showing stockwork vein cutting through the chlorite, smectite host rock. ....	120
Figure 71	Hand specimen from the Phoukassa deposit showing disseminated mineralization. ....	120
Figure 72	Mineralization paragenesis for the Phoukassa deposit. ....	121
Figure 73	Position in Phoenix pit showing supergene malachite veins, photo viewing north, December 2003. ....	121
Figure 74	Reflected light microscopy photograph of malachite vein. ....	122
Figure 75	Hand specimen showing veins of supergene malachite, with later chalcocite veins. ....	122
Figure 76	Face in Phoenix Pit showing fracture network.....	123
Figure 77	Hand specimen from Phoenix stockwork. ....	123
Figure 78	Intermediate vein. Note variation in pyrite crystal size and shape. 124	
Figure 79	Heavily fractured pyrite crystals. Note chalcocite on, but not altering the pyrite.....	124
Figure 80	Small anhedral pyrite crystals .....	125
Figure 81	Hand specimen of vein showing anhedral pyrite and supergene sulphates. ....	125
Figure 82	Mineralization paragenesis for the Phoenix deposit. ....	126
Figure 83	Stockwork mineralization from the Three Hills deposit. ....	126
Figure 84	Chalcocite blanket in stockwork. Note pyrite, but little visible chalcopyrite. ....	127
Figure 85	Supergene chalcocite grading into bornite. ....	128
Figure 86	Hand specimen of Three Hills stockwork showing hypogene sulphide minerals and later gypsum. ....	128
Figure 87	Reflected light section of Three Hills stockwork, photo .....	129
Figure 88	Mineralization paragenesis for the Three Hills Pit. ....	130
Figure 89	Digenite alteration exploiting fracture in chalcopyrite. ....	131
Figure 90	Digenite alteration exploiting chalcopyrite cleavage. ....	131
Figure 91	Chalcopyrite crystals fully pseudomorphed by chalcocite. ....	132
Figure 92	Mineralization paragenesis for the West Apliki deposit. ....	132
Figure 93	Topographic map of the pre-mining surface at the Skouriotissa deposit showing the relative elevations of the remnant massive sulphide and the Phoenix secondary orebody .....	133
Figure 94	High-grade leach heaps. ....	135
Figure 95	Stripping mixer-settler. ....	136
Figure 96	Finished cathodes being removed from cell. ....	136
Figure 97	The effect of pH on flotation .....	143
Figure 98	Illustration of the principles of a mechanically-agitated flotation cell .....	144
Figure 99	Illustration of a typical simple froth floatation circuit. ....	144

Figure 100	Gravity survey points used in mineralization potential modelling (data from Gass and Masson-Smith, 1963). .....	149
Figure 101	Locations of the three generations of survey that were available. ....	154
Figure 102	The combined aeromagnetic anomalies after merging the three generations of data as described in the text (NE illumination). ....	155
Figure 103	The preliminary geophysical interpretation of linear and polygonal features. ....	156
Figure 104	Hull quotient spectrum for a jarosite sample from Phoenix mine, showing diagnostic absorption troughs. ....	157
Figure 105	False-colour SWIR mosaic image of Cyprus, showing Phoenix and Skouriotissa mines for reference, and separate satellite overhead passages .....	160
Figure 106	PIMA spectra for sample taken from Phoenix working pit, sample Cyr_010b, showing mid-ranges for ASTER SWIR spectral bands 1-6. ....	161
Figure 107	Greyscale band ratio image for ASTER SWIR Bands 1 / 3.....	162
Figure 108	Greyscale band ratio image for ASTER SWIR bands 1 / 5. ....	163
Figure 109	Greyscale band ratio image for ASTER SWIR bands 2 / 3. ....	163
Figure 110	Greyscale band ratio image for ASTER SWIR bands 2 / 5. ....	164
Figure 111	Greyscale band ratio image for ASTER SWIR bands 4 / 5. ....	164
Figure 112	Greyscale band ratio image for ASTER SWIR bands 1 / 5. ....	165
Figure 113	DEM of part of northern Cyprus, lit from an azimuth of 225° to show NW–SE trending lineations. ....	166
Figure 114	DEM of part of northern Cyprus, showing NE-SW trending lineations.....	166
Figure 115	Graphical comparison between ASTER and Landsat-5 sensor imagery .....	167
Figure 116	Stacked red-green-blue image formed from three LandSat TM band ratio images. ....	168
Figure 117	Greyscale combination image of three LandSat TM band ratio images, showing the distribution of areas of high concentrations of ferrous minerals, iron oxides and clay minerals associated with mineralization related alteration. ....	169
Figure 118	Binary map of the geology of Cyprus. Prospective geology is brown, unprospective geology is yellow, and missing data is Blue. ....	171
Figure 119	Map of part of Cyprus, showing faults digitised from 1:250 000 geological map of Cyprus, GSD. ....	172
Figure 120	Buffered 1:250 000 faults, buffered at 250 m intervals from 0–1500 m. ....	172
Figure 121	Binary map of 1:250,000 faults, showing prospective and non-prospective areas. ....	173
Figure 122	Digitised geology coverage at 1:31 680. ....	176
Figure 123	Comparison between 1:31 680 and 1:250 000 scale geological maps. ....	177
Figure 124.	1:250 000 geological map of Cyprus, digitised by the GSD .....	177
Figure 125.	Binary prospectivity map of 1:250 000 geology of Cyprus. ....	180
Figure 126	Binary mineralization prospectivity map for the contact between the Upper and Lower Pillow Lavas, based on 1:250 000 geology.....	180

Figure 127	Binary mineralization prospectivity map for the contact between Lower Pillow Lavas and the underlying Basal Group, based on 1:250 000 geology. ....	181
Figure 128	Binary mineralization prospectivity map for the contact between the Basal Group and the underlying Sheeted Dyke Complex, based on 1:250 000 geology. ....	181
Figure 129	Binary mineralization prospectivity map based on 1:250 000 fault data. ....	182
Figure 130	Binary mineralization prospectivity map based on 1:31 680 fault data.....	182
Figure 131	Binary mineralization potential map based on gossan occurrence data taken from 1:31 680 memoir based geological maps.....	184
Figure 132	Binary mineralization potential map based on Bouguer gravity anomaly contour values. Red indicates prospective areas, green unprospective. ....	184
Figure 133	Binary mineralization potential map created from an ASTER band ratio image, SWIR bands 1/3 .....	185
Figure 134	Binary mineralization potential map created from an ASTER band ratio image, SWIR bands 1/5.....	186
Figure 135	Binary mineralization potential map created from an ASTER band ratio image, SWIR bands 2/3.....	186
Figure 136	Binary mineralization potential map created from an ASTER band ratio image, SWIR bands 2/.....	186
Figure 137	Binary mineralization potential map created from an ASTER band ratio image, SWIR bands 4/5. ....	187
Figure 138	Binary mineralization potential map created from an ASTER band ratio image, SWIR bands 6/1. ....	187
Figure 139	Binary mineralization potential map created from 3 Landsat TM greyscale band ratio images. ....	188
Figure 140	Binary mineralization potential map, created from East-West aligned satellite lineations; obtained from ASTER satellite DEM. ....	188
Figure 141	Binary mineralization potential map, created from Northeast-Southwest aligned satellite lineations, obtained from ASTER satellite DEM. ....	189
Figure 142	Copper-bearing massive sulphide and stockwork mineralization related mineral occurrences on Cyprus. ....	189
Figure 143	Mineralization potential map for copper mineralization on Cyprus. ....	190
Figure 144	Areas of high mineralization potential (>93% and >98%) for copper-bearing massive sulphide and stockwork mineralization. ....	190
Figure 145	Area A, high prospectivity zone around Ampelikou, Apliki and Agios Epiphanos Soleas,.....	192
Figure 146.	Area B high prospectivity zone around Agios Georgios Kafkallou.....	193
Figure 147	Area C high prospectivity zone around Klirou and Malounta .....	194
Figure 148	Area D, high prospectivity zone around Ampelikou, Apliki and Agios Epiphanos Soleas.....	195
Figure 149	Area E, high prospectivity zone around Lythrodontas.....	196

Figure 150	Area F, high prospectivity zone around Arakapas, Dierouna and Eptagoneia.....	197
Figure 151.	Area G, high prospectivity zone around Asgata .....	198
Figure 152.	Area H, high prospectivity zone around Mandria Lemesou, .....	199
Figure 153	Results of the geophysical prospectivity analysis. ....	204
Figure 154	Prospective areas hosted by the Upper Pillow Lavas in the Alestos–Memi zone. ....	205
Figure 155	EMR Geophysical data and local geological mapping with prospective areas overlaid .....	206
Figure 156	Location of pilot project boreholes. ....	207
Figure 157	Sequence collage of core boxes from borehole MR1-2006 .....	209
Figure 158	Sequence collage of core boxes from borehole MR2-2006 .....	213
Figure 159	Selected areas of interest for futher investigation .....	220
Figure 160	Location of prospectivity anomaly close to village of Strongyli with indicated site for a possible borehole .....	221

## TABLES

Table 1	Generalised schematic stratigraphy and associated nomenclature of the Troodos ophiolite, Cyprus. ....	24
Table 2	In-Situ sedimentary cover of the Troodos ophiolite, Cyprus .....	26
Table 3	Timeline of recent mining activity on Cyprus .....	29
Table 4	Total and average grades and tonnages for worldwide (excluding former USSR and Chinese deposits) VHMS deposits. ....	39
Table 5	Resources and grades for selected orebodies on Cyprus.....	42
Table 6	Alteration facies associated with mineralization in the Troodos ophiolite .....	43
Table 7	Common mineralized stockwork alteration facies observed in the Troodos ophiolite.....	44
Table 8	A table summarising the alteration assemblages of the alteration facies associated with P, K and M-type pipes. ....	57
Table 9	Summary of investigated boreholes .....	69
Table 10	Key to headings in borehole logs .....	70
Table 11.	A table showing the main high-temperature alteration minerals identified by the PIMA according to prospect and borehole. ....	88
Table 12	The main peaks used to identify between the polytypes of the kaolin group minerals. ....	90
Table 13	Phases identified in the EAD-2 borehole at Alestos through XRD compared with those identified by a PIMA. ....	91
Table 14	Phases identified in the ETS-1 and ETS-2 boreholes at Tourounjia through XRD compared with those identified by a PIMA. ....	92
Table 15	Table showing the results of the fluid inclusion analysis. The temperatures have been corrected according to stage calibration. ....	97
Table 16	Relative solubilities of copper sulphide minerals. ....	138
Table 17	New sulphate processes for chalcopyrite concentrate leaching .....	139
Table 18	Estimated heap leaching direct production costs as a function of ore grade .....	148
Table 19	System of classification used for linear features. ....	152
Table 20	PIMA sampling localities.....	158
Table 21	Characteristics of the three ASTER sensor systems .....	159
Table 22	Calculation of pixel values in band ratio images .....	161
Table 23	Characteristics of the TM and MSS sensors on the Landsat-5 platform .....	168
Table 24.	Data used in prospectivity mapping, showing buffer distances and threshold distances as well $W^+$ , $W^-$ and contrast for each input theme. ....	179
Table 25.	Data used in prospectivity mapping, showing buffer distances and threshold distances as well $W^+$ , $W^-$ and contrast for each input theme. ....	183
Table 26.	Summary of areas with high copper mineralization potential (>98%) .....	191
Table 27	Contrast table for the geophysics prospectivity analysis .....	203
Table 28	Summary borehole log for MR-1 2006 .....	208
Table 29	Summary borehole log for MR-2 2006 .....	213

# Executive summary

This report documents the results of a three-year collaborative research project between the British Geological Survey (BGS), The Natural History Museum, London (NHM) and the Geological Survey Department, Cyprus (GSD). It was funded by the Ministry of Agriculture, Natural Resources and Environment, Cyprus. The objectives of the programme were to develop new methodologies for the exploration and exploitation of cupriferous sulphide ore and re-establish metalliferous mineral exploration research on Cyprus and within the GSD. Initially the project only involved the BGS, the NHM and the GSD. However, early on, it became apparent that mining and mineral exploration companies held key datasets, needed to develop the new methodologies. Therefore, negotiations were conducted with the Hellenic Mining Company, Eastern Mediterranean Minerals and Hellenic Copper Mines<sup>1</sup>. These established a framework for collaboration and all parties signed a confidentiality agreement. This allowed the BGS–NHM–GSD team to use proprietary data in their combined metallogenic–prospectivity analysis and the companies to have exclusive access to project results for six months after project completion.

The project comprised five distinct components:

- Technology transfer and institutional strengthening.
- Development of new metallogenic models for ophiolite–hosted mineralization, including an examination of gold-rich epithermal-style mineralization associated with submarine basalts.
- Mineralogical and metallurgical analysis of low-grade copper mineralization, with a review of solvent extraction electro-winning (SX-EW) technologies.
- The use of legacy and new data at the regional to district scales for GIS-based prospectivity modelling. This included a reinterpretation of geophysical data.
- A pilot study, using the prospectivity analysis, to define and test the mineralization potential of prospectivity anomalies.

To facilitate technology transfer and institutional strengthening the project delivered a number of office and field-based seminars and workshops. These included training in the use of GIS for prospectivity analysis, examination of potential epithermal style mineralization, lectures on: (i) epithermal mineralization in the Aegean, (ii) VHMS mineralization in the Urals and (iii) SX-EW hydrometallurgical techniques—these were given to the Cyprus Society of Geologists and Engineers to ensure the widest dissemination. In addition, to give the project an international dimension, the prospectivity analyses were presented at two international conferences in Thessaloniki and Beijing.

The project produced, using ArcSDM and a variety of geological, geophysical and remote sensing datasets, two prospectivity investigations: (i) a regional prospectivity map covering all of the Troodos Massif. This identified eight separate areas of high mineralization potential. The areas are generally located within 10 km of the boundary between the Troodos ophiolite and the autochthonous sedimentary cover sequences draping the ophiolite. (ii) A more detailed map focussed on an area of the northern Troodos. This identified drilling targets in the Memi–Aleostos area. Key components to the prospectivity analysis undertaken by the project team

---

<sup>1</sup> Since commencement of the project, Hellenic Copper Mines' operations at Skouriotissa have ceased. However, at the time of writing it is believed that these will recommence in the near future. In addition, exploration activities previously undertaken by Eastern Mediterranean Minerals have been taken over by Eastern Mediterranean Resources (EMED—[www.emed-resources.com](http://www.emed-resources.com))

included: (i) The digitisation of mineral occurrences and gossan distribution. (ii) The analysis of remote sensing data using band ratio image processing techniques to highlight regional alteration trends. (iii) The modelling and interpretation of airborne magnetic geophysics comprised the amalgamation of three generations of data into a single data set and the identification of lineaments and regions with positive and negative magnetic anomalies.

In addition to the development of an ophiolite-hosted prospectivity GIS for the Troodos, the project addressed two new metallogenetic concepts for Cyprus—namely (i) The investigation of potential epithermal style VHMS mineralization using infrared spectroscopic and X-ray diffraction techniques. This study identified high temperature advanced argillic alteration phases and concluded that sub-seafloor boiling was responsible for some of the gold enrichment recorded in Cyprus-type VHMS mineralization (ii) The development of low-grade supergene Cu mineralization associated with massive sulphide mineralization. This showed that the favourable interplay between the mineralization and topography played an important role in the development of the large secondary low-grade orebodies. A strategy for exploring for such a supergene copper target would be to assess all surface gossans developed in topographic highs and seek potential downslope areas of mineralization—the use of high resolution digital elevation models provided by techniques such as LiDAR could be a way forward in this respect

Professor John Monhemius, Imperial College London, undertook a review of the use of SX-EW hydrometallurgical techniques as applied to Cyprus. This study concluded that the decline in copper recoveries in the heap leach process used at Skouriotissa is due to increasing amounts of primary chalcopyrite, a refractory mineral that is very resistant to dissolution by oxidation, in the run-of-mine ore as mining gets deeper. Recent processes developed for the hydrometallurgical treatment of chalcopyrite all involve the use of extreme conditions, such as high temperature pressure leaching, ultra-fine grinding, or intensified bacterial leaching—these may not be appropriate for Skouriotissa and the best option for extending the life of the plant may be the discovery and exploitation of further reserves of supergene altered copper ores containing leachable copper oxide and secondary sulphide minerals This will allow production to continue using the heap leaching technology currently in use. If necessary, the effectiveness of this leaching method towards secondary copper sulphide minerals could be improved by introducing tanks for bacterially pre-oxidising the leach solutions under optimum conditions, prior to being sprayed on to the ore heaps.

One key component of the project was to formulate and implement a pilot project based on the results of the regional GIS. The goal of the pilot project was to site a borehole to test if prospectivity analysis had the capability to predict the location of unknown mineralization. The application of a detailed prospectivity GIS using public domain and proprietary geophysical data focussed on the northern Troodos identified a high prospectivity zone in the Memi–Aleostos region. Two boreholes were sited to test for the presence of mineralization beneath Upper Pillow Lava cover and one of these encountered over 20 m of argillically and propylitically altered lavas containing minor amounts of pyrite and chalcopyrite. This shows that prospectivity analysis approach used in this project could be a useful tool for locating buried VHMS mineralization on Cyprus. This is especially so when high-resolution geophysical data are available.

In terms of future work, the project identified development in the following areas:

- The need for national high-resolution geochemical and geophysical datasets to provide pre-competitive information for mineral exploration and environmental assessment
- The development of fuzzy logic techniques for prospectivity mapping
- Processing and interpretation of high-resolution airborne remote sensing data

# 1 Introduction

This report documents the results of a three-year collaborative research project between the British Geological Survey (BGS), The Natural History Museum, London (NHM) and the Geological Survey Department, Cyprus (GSD). It was funded by the Ministry of Agriculture, Natural Resources and Environment, Cyprus. The objectives of the programme were to develop new methodologies for the exploration and exploitation of cupriferous sulphide ore and re-establish metalliferous mineral exploration research on Cyprus and within the GSD. Initially the project only involved the BGS, the NHM and the GSD. However, early on, it became apparent that mining and mineral exploration companies held key datasets, needed to develop the new methodologies. Therefore, negotiations were conducted with the Hellenic Mining Company, Eastern Mediterranean Minerals and Hellenic Copper Mines<sup>2</sup>. These established a framework for collaboration and all parties signed a confidentiality agreement. This allowed the BGS–NHM–GSD team to use proprietary data in their combined metallogenic–prospectivity analysis and the companies to have exclusive access to project results for six months after project completion.

The project comprised five distinct components:

- Technology transfer and institutional strengthening.
- Development of new metallogenic models for ophiolite–hosted mineralization, including an examination of gold-rich epithermal-style mineralization associated with submarine basalts.
- Mineralogical and metallurgical analysis of low-grade copper mineralization, with a review of solvent extraction electro-winning (SX-EW) technologies.
- The use of legacy and new data at the regional to district scales for GIS-based prospectivity modelling. This included a reinterpretation of geophysical data.
- A pilot study, using the prospectivity analysis, to define and test the mineralization potential of prospectivity anomalies.

These relate to the following Tasks as originally outlined in the tender documents:

1. Collection of all available data (geological, geochemical, geophysical, mining and metallogenetic).
2. Evaluation of all available geological, geochemical, geophysical, mining and metallogenetic data relating to exploration for sulphide orebodies.
3. Reinterpretation of existing data resulting from previous exploration/research works with the application of new modern methods and techniques.
4. The review of current new metallurgical methods for recovery of low-grade cupriferous orebodies.

---

<sup>2</sup> Since commencement of the project, Hellenic Copper Mines' operations at Skouriotissa have ceased. However, at the time of writing it is believed that these will recommence in the near future. In addition, exploration activities previously undertaken by Eastern Mediterranean Minerals have been taken over by Eastern Mediterranean Resources (EMED—[www.emed-resources.com](http://www.emed-resources.com))

5. Re-evaluation of theories and models of metallogenesis on the basis of modern concepts, theories and practices.
6. Developing a suitable methodology for the research which will fulfill the objectives of the project
7. The Consultant must propose a methodology of exploration and a model of genesis based on the conclusions and outcomes of the project.
8. Application on a pilot scale of the methodology proposed by the end of the second year, will be designed and executed on a known mining area.
9. The training/specialization of the personnel of the Geological Survey Department who will participate during and after the pilot testing if needed.

The development and description of metallogenic models is given in Chapters 2 and 2.3. They deal first with volcanic-hosted massive sulphide (VHMS) mineralization in general and then Cyprus-type VHMS deposits in particular. In addition, to classical VHMS deposits a new potential epithermal style of mineralization was recently recognised (Nillos and Elipane, 1998; Nillos et al., 1998a; Nillos et al., 1998b; Nillos et al., 1998c; Maliotis and Herzig, 2000). The occurrence of epithermal style mineralization in VHMS terranes is unusual, so this metallogenic concept was tested on drill-core material using a portable infrared mineral analyser (PIMA). The results of this self-contained study are described in Chapter 5. These three Chapters specifically address Task 5—re-evaluation of theories and models of metallogenesis on the basis of modern conceptions, theories and practices.

One key task in the project was the examination and assessment of existing data for suitability for prospectivity analysis—the approach and results of this exercise are described in Chapter 4 and relate to Tasks 2 and 3 in the work programme. In addition, proprietary company geophysical and geochemical data were also provided and the evaluations of these data are given in Chapters 6 and 9

In addition to the geological project tasks there was a requirement to undertake a review of current and new metallurgical methods for recovery of low-grade cupriferous orebodies (Task 4 above). This was undertaken by Professor John Monhemius of Imperial College, an internationally recognised scientist in the field of solvent extraction electro-winning technologies. Coupled with this review the NHM team undertook a mineralogical study of low-grade copper mineralization to identify the processes that formed them and to evaluate the mineralogy in terms of its suitability for solvent extraction electro-winning technologies. These activities are reported on in Chapters 7 and 8

The core objective of the project was to undertake a statistically-based prospectivity analysis and develop a metallogenic GIS that could be used for prospect targeting. This aspect of the work is covered in Chapter 10 and these Chapters relate to Tasks 3 and 7 above. The results of this identified several areas worthy of further investigation by drilling and/or ground-based geophysical surveys and formed the basis of the pilot project (Task 8 above). The rationale behind selecting the areas for the pilot project and the results of the drilling programme are given in Chapter 12.

In addition, it is important to recognise that significant contributions were made to the project by a series of Masters degree students, who, under the close supervision of the project leaders, undertook key elements of the project. The individual theses are

Jowitt, SM (2003) *The Potential for Copper Mineralization on Cyprus: A GIS based Methodology*. Unpublished MSc Thesis, Cambourne School of Mines, Exeter University, 209 p.

White, C (2003) *New Copper Deposits in the Troodos Cyprus: The results of Interplay Between Hydrothermal and Supergene Processes*. Unpublished MSci Dissertation, Imperial College of Science and Technology–London, 60 p.

Osborn RGM (2004) *The application of short wavelength infrared spectroscopy to characterise typical and atypical alteration in Cyprus-type VHMS deposits*. Unpublished MSc Thesis, Cambourne School of Mines, Exeter University, 122 p.

Thomas, RDH (2005) *Evidence for low sulphidation epithermal mineralization in the Troodos ophiolite, Cyprus*. Unpublished MSci Dissertation, Imperial College of Science and Technology–London, 88 p.

These are available in print and electronic format from the Geological Survey Department, Nicosia, Cyprus

## 2 Mineralization on Cyprus

### 2.1 GENERAL GEOLOGY

#### 2.1.1 Introduction

Cyprus is situated in the easternmost part of the Mediterranean, around 130 km from Turkey in the north, around 160 km from the coasts of Syria and Lebanon to the east and, to the south, around 500 km from Egypt and Israel (Figure 1).



Figure 1 The position of Cyprus within the Eastern Mediterranean area (adapted from multimap.com).

The regional geology of the eastern Mediterranean is complex and generally thought to be a relic of the Mesozoic Tethyan Ocean. It is composed of two separate tectonic domains—the northern Alpine orogenic belt and the southern Eastern Mediterranean basin, with the two linked by subduction and plate collision. Cyprus forms part of the eastern Mediterranean basin, although the suture between the two separate domains runs across the island, marked, as it is to the east of Cyprus, by a series of ophiolites and related nappe sequences (Garfunkel, 1998).

Cyprus comprises juxtaposed fragments of oceanic and continental crust generated during the later stages of closure of the Tethyan Ocean, which formed the constituents of the Alpine-Himalayan orogenic belt. Oceanic crustal fragments are preserved as ophiolite sequences and are seen in various localities in and around the eastern Mediterranean (Dilek and Moores, 1990)—typical examples include the ophiolites in Bosnia, Croatia, Greece (e.g. Othris, Pindos ophiolites), Oman (e.g. Semail ophiolite), Syria (e.g. Hatay, Baer-Bassit ophiolites), Turkey (e.g. Lycian, Armutlu ophiolites,) and Cyprus itself. Continental fragments composed of Palaeozoic and older metamorphic basement and overlying Mesozoic carbonate

sequences separate these Triassic, Jurassic and Cretaceous ophiolitic units (Robertson, 2002).

Ophiolite sequences in the Eastern Mediterranean can be split into two groups. Typically, northern ophiolites, found in Croatia, Bosnia, and Greece are usually highly deformed, dismembered and are commonly associated with metamorphic soles and tectonic melanges. Southern ophiolites are relatively undeformed, and are in many cases thought to be almost complete sequences through the ocean crust. Examples of these are seen in the ophiolites of Cyprus (Troodos), southern Turkey (Kizildag), and the Baer-Bassit ophiolite of Syria (Dilek and Moores, 1990).

The well-preserved nature of the Troodos ophiolite and its surrounding and adjacent units has made it a target for study over a number of years. However, the history of the exploitation of the geology of Cyprus, for copper and other metals and minerals, has been far longer than any study of the processes that formed the geology. The earliest workings for copper, gold and other metals date back to Bronze age times, as long as 5000 years ago or longer, with later Phoenician and Roman smelting shown by the extensive slag heaps that are visible on the island today. Ancient surface and underground workings are also numerous on the island, with shafts, galleries, timbering and other manifestations of small-scale underground workings visible across the island. Exploration, via the excavation of small untimbered shafts, was also widespread in Roman times, with many of the characteristic gossans that mark underlying sulphide bodies having been explored or prospected at one or more times in the past. Indeed, the word 'copper' may have been derived from the Greek for Cyprus, or vice versa (Bear, 1963).

Scientific research of the Troodos occurred in three main phases—(i) in the 1950's and 60's the Troodos massif was first mapped in detail by members of the Cyprus Geological Survey and resulted in the publication of a number of memoirs. (ii) The identification of the massif as an ophiolite sequence by Moores and Vine, 1971 started another phase of investigation and culminated in 1979 with the International Ophiolite Symposium, held on Cyprus. (iii) International Crustal Research Drilling Group (ICRDG) and the Cyprus Geological Survey Department (GSD), in the form of the Cyprus Crustal Project undertook deep drilling through the ophiolite. This work was intended to resolve some of the outstanding issues and problems posed by the previous work. All of this research makes Troodos one of the most studied ophiolite sequence in the world (Robinson and Malpas, 1990).

Cyprus comprises four distinct geological terranes: (i) The Troodos itself comprises an Upper Cretaceous ophiolite complex and *in situ* Cretaceous to mid-Tertiary deep-sea deposits and Neogene shallow-marine to continental sediments. (ii) The Mamonia terrane, situated to the west of the Troodos, is a structurally complex amalgamation of Palaeozoic and Cretaceous igneous, sedimentary and metamorphic rocks. (iii) In the north of the island—the Kyrenia range of hills and mountains running close to the northern coast of the island, consists of a sedimentary succession of Late Palaeozoic to Recent rocks, with minor metamorphic units (Robertson and Xenophontos, 1997). (iv) The Southern Troodos, or Arakapas, Transform Fault Zone, located to the south of the Troodos, is considered to be a fossil oceanic transform fault zone, separating the Troodos from the Anti-Troodos Plate. Accumulation of the Mamonia and the Kyrenia terranes with the already amalgamated Troodos–Anti-Troodos began in the Cretaceous, with final juxtaposition occurring before the Eocene (Robertson, 2000).

### **2.1.2 Kyrenia**

The Kyrenia Range consists of an East–West running series of hills and mountains parallel to the northern coast of Cyprus and contains a series of Permian to early Tertiary rocks. The lower eastern Kyrenia Range contains the oldest rocks on Cyprus—Permian olistostromes, along with the Kantara Limestone formation. Thrust sheets make up the higher western Kyrenia—comprising steeply dipping shallow water carbonates that range from Triassic to mid-Cretaceous in age (Robertson and Xenophontos, 1997). The terrane developed in four main stages: (i) First, there was the development of a Permian to mid-Cretaceous rifted passive margin sedimentary sequence. (ii) This was superseded by Upper Cretaceous–Early Tertiary deformation associated with the development of the Troodos ophiolite microplate. (iii) Eocene compression and thrusting then formed the western Kyrenia range thrust sheets and docked the Kyrenia units with the Troodos to the south. (iv) Finally, Africa–Eurasia plate convergence in the Plio-Quaternary caused the range of hills and mountains seen today to develop (Robertson, 2000).

### **2.1.3 Mamonia Complex**

The Mamonia complex is perhaps the most contentious aspect of Cyprus geology. It consists of two major and one minor lithotectonic components. The first and lowermost comprises Mesozoic sediments and volcanics that predate genesis of the Troodos ophiolite—these are the Dhiarizos Group (Robertson, 1990). The second upper component is made up of Upper Cretaceous Ophiolitic rocks, with minor slivers of metamorphic rocks and serpentinite of unconfirmed origin. Finally, these units are overlain unconformably by several hundred metres of debris flows, known as the Kathikas Melange or Formation (Swarbrick, 1980).

The Mamonia complex is thought to have formed in three distinct periods prior to final submarine compression, thrusting, and erosion that resulted in the formation of the Kathikas Formation. First, the Dhiarizos Group was generated during the opening of the Mesozoic Tethys. Second, the Upper Cretaceous Ophiolitic rocks are interpreted as remnants of oceanic crust and mantle—similar in type to those seen around the Arakapas, or Southern Troodos Transform Fault Zone (STTFZ). Last, minor metamorphic units are interpreted as being similar to metamorphic soles seen in other Tethyan ophiolites—e.g. Oman. These soles are presumed to have formed during plate convergence, with the metamorphic units underplating the overriding hot upper mantle. However, no such sole is exposed beneath the Troodos, possibly due to later disruption due to strike-slip and/or thrust faulting (Robertson and Xenophontos, 1997).

### **2.1.4 Arakapas Transform Fault and Anti–Troodos Fault**

The Arakapas, or Southern Troodos, Transform Fault Zone (STTFZ) marks the southern edge of the Troodos ophiolite. It is interpreted as a fossil oceanic transform fault zone that separates the Troodos ophiolite from the Anti-Troodos Plate—a section of ophiolitic crust around 3-5km thick (Gass et al., 1994). The STTFZ comprises a chaotically juxtaposed and distributed variety of lithologies that bears little similarity to the relatively undeformed ophiolite sequence seen elsewhere in the Troodos. Two main sequences of lithological units associated with the transform fault are recognised: (i) the older axis sequence of lithologies consisting of plutonic and hypabyssal rocks of mafic and ultramafic composition, and (ii) a volcanic sequence of pillow lavas, massive lavas and volcanoclastic sediments.

In the STTFZ, the plutonic and hypabyssal sequence is mainly tectonised harzburgites, with high-level trondhjemitic gabbros and dykes, including wehrlites, with masses of sheared serpentinites and zones of fragmented Sheeted Dykes. Covering this is a succession of alternating volcanics and sediments, including boninitic lavas similar to those exposed in the higher levels of the Troodos (Robertson and Xenophontos, 1997). The Anti-Troodos Plate (ATP), located to the south of the Transform Fault Zone, is a section of ophiolitic crust that formed coevally with the Troodos plate and closely resembles sections of the axis-generated Troodos ophiolite (Gass et al., 1994). The major difference being that the ATP lithological units have suffered disaggregation, block rotation and intrusion by the products of a later magmatic episode within the transform domain (Gass et al., 1994). The main units found in the ATP are Upper and Lower Pillow Lavas, the Sheeted Dyke Complex, Gabbros, wehrlites and leucogabbros containing small lenses of plagiogranite, and a small lens of mantle sequence rocks, consisting of highly tectonised harzburgitic and dunitic rocks, showing no difference from the similar rocks found as a part of the main Troodos ophiolite (Gass et al., 1994; Robertson, 1978).

### 2.1.5 Troodos Ophiolite and sedimentary cover sequences

Figure 2 shows the outcrop of the three major terranes on Cyprus with the highest point of the island, Mount Olympus (1951 m) of the Troodos range, marked for reference.

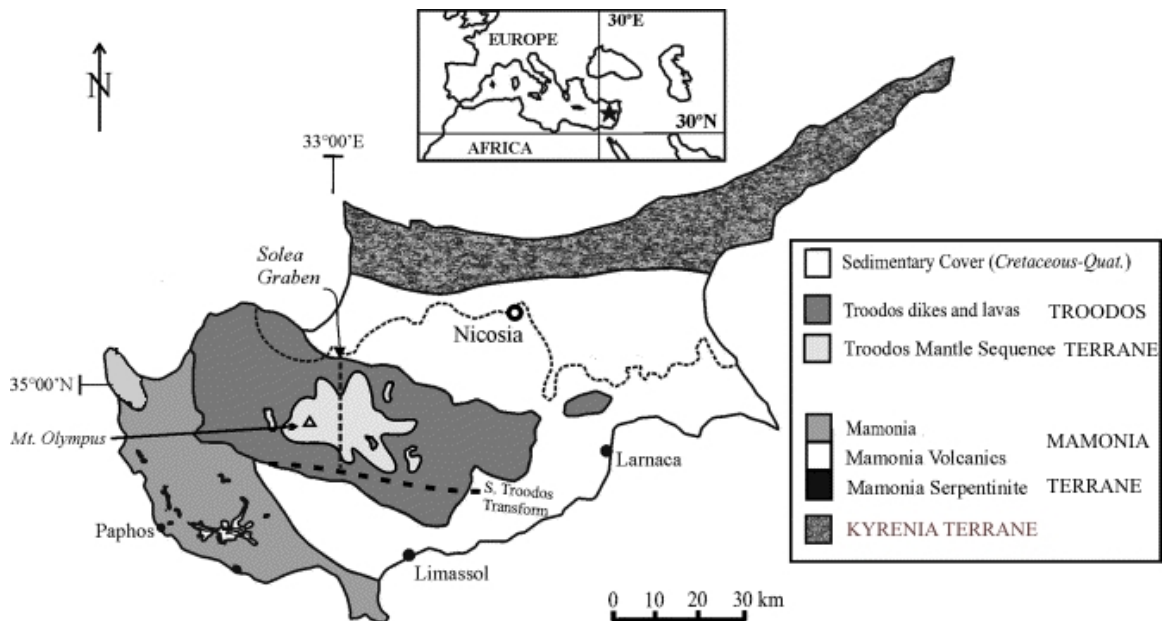


Figure 2 Map showing the three major geological terranes of Cyprus (adapted from Borraidaile and Lucas, 2003).

The Troodos ophiolite is considered to be formed above a subduction zone, similar to the present day Mariana–Bonin arc in the southern Pacific. However, this view is not universally accepted with the formation at a mid-ocean ridge, such as the present day Mid-Atlantic ridge being an alternative view (Robertson and Xenophontos, 1997).

The ophiolite has a threefold division (i) the structurally deepest, but topographically highest, Plutonic Complex is at the centre (ii) this is overlain and surrounded by the Sheeted Dyke Complex. (iii) The stratigraphically highest part of the ophiolite is the

Pillow Lava Series, which forms a discontinuous ring around the main massif. This can be further simplified into bi-fold division, which consist of a lower mantle sequence, and an upper crustal sequence separated by the petrological Mohorovicic discontinuity. This division has been applied to most ophiolites around the world, and is considered the standard way to partition coherent ophiolites, such as the Troodos, to enable comparison between ophiolites (Gass, 1990). Table 1 summarises the stratigraphy of the Troodos ophiolite sequence, along with the relative naming conventions:

<b>In Situ Sedimentary Cover</b>		
<b>Umbers</b>		
<b>Crustal Sequence</b>	<b>Pillow Lavas</b>	Upper Pillow Lavas
		Lower Pillow Lavas
	<b>Sheeted Dyke Complex</b>	Basal Group
<b>Mantle Sequence</b>	<b>Plutonic Complex</b>	Plagiogranites
		Gabbros
		Ultramafics

Table 1 Generalised schematic stratigraphy and associated nomenclature of the Troodos ophiolite, Cyprus.

In detail, depleted mantle rocks are exposed at the highest levels of the Troodos massif, around the Mt. Olympus peak, and form the highest topography on the island. Approximately 1 km of succession is exposed and comprises mainly tectonised harzburgites, dunites, lherzolites, wehrlites, and gabbroic rocks. The majority of this sequence is harzburgitic, forming around 80% of the total outcrop of the mantle sequence, with pods of dunite forming the majority of the remaining 20% (Robertson and Woodcock, 1980). Field relations and the chemical and mineralogical homogeneity of the depleted mantle sequence units suggest formation from residual plagioclase lherzolite mantle, from which basaltic material was extracted. In addition, localised patches of plagioclase lherzolite are also seen and these are thought to represent mantle undepleted by partial melting (Gass, 1980).

The crustal sequence overlies the petrological Moho—the boundary between the crustal and mantle sequences. They are formed or derived from one or more magma chambers that were thought to have originally formed beneath the ophiolite spreading-axis. Moores and Vine, 1971 originally suggested that the plutonic sequence of the Troodos ophiolite was formed from multiple magma chambers, an idea that was borne out by the Cyprus Crustal Study Project’s drilling results from deep (over 2km) boreholes such as CY-4, which drilled through sheeted dykes, and plutonic rocks, penetrating at least two fossil magma chambers (Robinson and Malpas, 1990).

Crustal sequence rocks form several distinct units (Table 1). The lowest unit, the Gabbros, also known as the Layered Sequence, comprises cumulate gabbros, with dunite and wehrlite, formed in a series of spreading axis magma chambers (Gass, 1980). The gabbroic sequence is overlain in places by high-level intrusives, which form a suite of plagiogranite intrusions, derived from the residual melts of the magma chamber. These represent the final stage of the evolution of basic magma in spreading axis magma chambers (Bebien et al., 1997). Above the plutonic complex

and high-level intrusions is the Sheeted Dyke Complex. This forms a 1–1.5 km thick unit consisting entirely of vertical, or near vertical diabase dykes. Near the upper and lower contacts of the complex, these inter-finger with lava and gabbro screens (Gass, 1990). These dykes provide direct evidence for formation in an extensional environment. Furthermore Varga and Moores, 1990 identified three separate domains of fossil spreading, seen as three structural grabens on the northern flank of Troodos (Solea, Ayios Epiphanius and Larnaka grabens), which in turn may also be linked with the formation of the major mining districts in Cyprus.

The Sheeted Dyke Complex represents the conduits for lava transport from the underlying source to the seafloor. This implies that the dykes should record the same range of compositions found in the extrusive sequence. The dykes do span the same range of compositions, but sharp breaks in composition—recorded in the lavas—are not recorded in the dykes. This fact, combined with the fact that no consistent relationships are evident between age and composition, suggests that within each individual spreading axis, dykes were intruded at a number of spreading centres, possibly overlapping (Robinson and Malpas, 1990). The dykes also have been metamorphosed, ranging in grade from zeolite to greenschist facies, with epidote (epidote–quartz–sphene) zones marking the base of hydrothermal recharge systems (Richardson et al., 1987).

Above the Sheeted Dykes complex is the Basal Group. Sandwiched between the dykes and the overlying Pillow Lavas, it consists of both dykes and lavas. Here, lava screens and pillows fill inter-dyke space. This combination of both intrusive and extrusive factors means that this group does not fit neatly into either the Sheeted Dyke Complex, or the Pillow Lavas, having characteristics of both (Robertson and Xenophontos, 1997). However, it covers the gap in the stratigraphy between the Sheeted Dykes and the Pillow Lavas. The mixed unit that emerges is somewhat arbitrarily defined, and should possibly be considered to cover anything with less than 100 % dykes, but not entirely composed of pillow lavas and feeder tubes (Gass, 1980).

The pillow lava sequence is split into Upper and Lower Pillow Lavas (UPL and LPL) according to their place in the stratigraphy. This original division of the Pillow Lava sequence was based on the colour, mineralogy, abundance of dykes and relationship to massive sulphide orebodies—the majority of massive sulphide bodies being mapped as forming between the two Pillow Lava sequences. However, this boundary, in the majority of places, was poorly mapped, or arbitrarily assigned to a local unconformity or intercalated sediment band. Robinson and Malpas, 1990, in their review of the Troodos ophiolite, and its origins and emplacement, describe a threefold geochemical division of the entire Pillow Lava sequence—named A, B and C. Suite A comprises a relatively evolved island-arc tholeiitic suite. This occurs at the base of the lava pile on the northern and southern flanks of the Troodos. Suite B, a depleted arc tholeiite suite, is located at the top of the lava pile on the northern flank of the Troodos, whilst suite C, a highly depleted boninitic suite, is associated with the southern Arakapas fault zone. The relatively enriched lavas of suite A, and the depleted lavas of suites B and C correspond approximately to the Upper and Lower Pillow Lava suites respectively. However, interfingering of the depleted and enriched lava suites occurs in several localities (Robinson and Malpas, 1990).

The presence of suite C, the highly depleted boninite-type lavas, also has significance for the tectonic setting. Such a high MgO, high SiO<sub>2</sub> but generally depleted lava could not be generated at a normal mid-ocean spreading ridge. The

formation of boninitic lava appears to require a combination of melt-depleted thermally anomalous mantle, an extensional tectonic regime, and relatively high  $P_{H_2O}$  conditions. This provides evidence for the formation of Troodos in a supra-subduction zone setting, such as the present-day Bonin arc (Flower et al., 2001). The location of the Suite C lavas, around the Arakapas Transform fault zone, implies that extension within the transform zone is inferred to have induced melt separation and emplacement as products of remelted depleted upper mantle (Robertson et al., 2003b).

Age (Ma)		Formation	Lithology
2.0	Pleistocene	'Fanglomerate' Apalos Kakkaristra Athalassa	Conglomerates and Sandstones, Calcarenite, Sandstones, Conglomerates
5.2	Pliocene		
23.3	Miocene	Nicosia	Marls, Silts, Muds, Sandstones, Conglomerates
		Kalavassos	Evaporites
		Pakhna	Reefal and Bioclastic Limestone
Pelagic Chalks, Marls, Calcarenites, Conglomerates			
Reefal and Bioclastic Limestone			
35.4	Oligocene	Upper Lefkara	Pelagic Chalk and Marls
56.5	Eocene	Middle Lefkara	Massive Pelagic Chalks
65.0	Palaeocene		Pelagic Chalks, Replacement Chert
74.0	Maastrichtian	Lower Lefkara	Pelagic Chalks
83.0	Campanian	Kannaviou	Volcaniclastic Sandstones, Bentonitic Clays
90.4	Turonian	Perapedhi	Umbers, Radiolarites
Ophiolitic Basement			

Table 2 In-Situ sedimentary cover of the Troodos ophiolite, Cyprus (modified from Robertson et al., 2003a).

Directly overlying the ophiolite sequence are iron–manganese sediments (umbers). These metallogenic sediments mark the start of the *in situ* sedimentary sequence that covers a large part of the island of Cyprus and describes much of the development of Cyprus after the formation of the ophiolite sequence. It records a general progression from deep marine Turonian sediments through shallow marine to later alluvial ophiolite-derived clastic sedimentation and documents the uplift and emergence of

the ophiolite from deep marine conditions to the mountainous setting seen today— where the highest parts of the island reach over 1900 m. The uplift of the Troodos can be ascribed to one or a combination of three factors. First, the Troodos ophiolite may have been emplaced onto a continental fragment in the Late Cretaceous. Second, the continental crust below Cyprus is effectively an extension of the Eratosthenes seamount (to the south of the island, and currently undergoing subduction), and was emplaced beneath Cyprus in Neogene–Holocene times. Third is that the uplift was due to a diapiric serpentinisation of the underlying mantle sequence.

## 2.2 MINERALIZATION

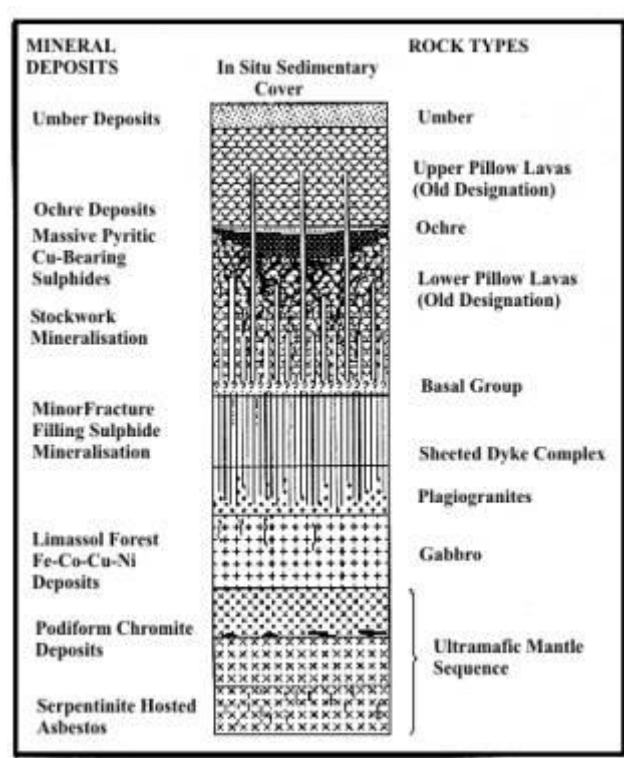


Figure 3 A generalised stratigraphic column showing the relative positions of copper mineralization and other deposits in the Troodos.

Cyprus has been a major exporter of various mineral commodities, from copper exports in ancient times to salt exports in the Middle Ages. More recently large amounts of asbestos were exported in the early to mid 20<sup>th</sup> century (Mobbs, 2000). Copper exports began again in the early part of the last century, and have been active for much of the last 100 or so years. Gypsum, gold, silver, chromite, umber, ochre and terra verte (mineral pigments) and building stone have also been produced. The Troodos ophiolite is the most significant host to mineralization on the island. The major deposits explored for and worked on Cyprus are the copper-bearing massive sulphide bodies that have been worked for many thousands of years. However, other resources have also been won from the Troodos. These include asbestos, chromite, iron-copper-cobalt-nickel sulphide mineralization, and gold-bearing umbers. The stratigraphic column shown in Figure 3 displays the general outline and location of ore deposits within the Troodos Ophiolite.

The asbestos deposits on Cyprus are found in the core of the Troodos plutonic complex, in the form of serpentinised ultramafic material. A total outcrop area of

around 35 km<sup>2</sup> is present and faults at the edges of the serpentinite body define the transition from the serpentinite to unaltered dunite. The deposit area coincides with a negative gravity anomaly, interpreted as the top of a diapiric low-density body extending to around 11 km deep (Constantinou, 1980). The eastern part of the body of serpentinitised rocks was subjected to a more intense serpentinitisation than the rest of the affected ultramafic rocks and is described as the *Bastite Serpentinite Zone* in Cyprus Geological Survey memoirs (Wilson, 1959). On the eastern slopes of this zone, in the area around Amiandos, asbestos was extracted from 1904 to 1988 over a 10 km<sup>2</sup> mining lease area with huge resource potential. However, the site is now considered to form a potential health hazard and steps to restore and remediate the site are being taken. Figure 4 shows the former works at Amiandos, displaying the extensive area covered by the disused mine workings.



Figure 4 Former asbestos workings at Amiandos.

The Troodos ophiolite is moderately rich in chromite when compared to other ophiolite sequences (e.g. the Lizard, Cornwall) and chromite occurs as an accessory mineral in several ultramafic rock types. However formerly economic chromite deposits in the Troodos are rare, only being found in podiform orebodies within dunites and harzburgites. These deposits were worked by small-scale operations, often mining very selectively and the overall production of chromite from the Troodos was low (Constantinou, 1980). Some minor platinum group elements have also been found, associated with a copper-zinc alloy in the Troodos chromitites, but again at sub-economic levels (Constantinides et al., 1980).

Iron–copper–cobalt–nickel sulphide deposits on Cyprus are located in the Limassol Forest complex—a plutonic complex associated with the Arakapas transform fault. A shattered serpentinite body, thought to have originally been an olivine-rich dunite or peridotite but now highly deformed and serpentinitised, hosts the mineralization. The entire mineralized area is around 6 km long and around 200 m wide, with the ore forming pods, lenses, veins and disseminations within this zone. The ore was worked from Roman times onwards, but the irregular nature of the mineralization

Date	Mineral Concerned	Notes
Historical	All	Ancient mining of copper, salt, and asbestos by Bronze Age, Roman and Phoenician peoples. Small scale production, with no major mining until the early 20 <sup>th</sup> century.
1919	Copper, Gold	Cyprus Mines Corporation starts copper production at Mavrovouni Mine, with production starting at Skouriotissa in 1922.
1929	Copper, Gold, Silver	Cyprus Sulphur and Copper Company starts mining at Kynousa underground and Limni opencast Mines.
1931	Chrome	Cyprus Chrome Company buys leases for chromite mines around Mount Olympus from Eastern Minerals Ltd and Deutsche-Orient Graben Gesellschaft with chromite production starting immediately.
1936	Asbestos	Tunnel Portland Cement Company starts large-scale production of asbestos. Deposit worked since 1906, but only on a small-scale production basis, and subsequently transferred to the Cyprus Asbestos Mines Ltd (1948).
1937	Pyrite, Copper, Gold, Silver	Hellenic Company of Chemical Products and Manures (subsequently the Hellenic Mining Company) starts mining for pyrites at Kalavastos, Kambia, Sha, Mitsero, Agrokipia and Xyliatos, both underground and opencast.
1939-1945	All	Mining Hiatus due to Second World War
1963	Copper, Gold, Silver, Pyrite	Berdy Mining Company Ltd starts mining and exploration in the Troulli Inlier.
1974	All	Turkish Invasion of Cyprus – Hiatus in production during and after hostilities. Cyprus Mines Corporation terminated operations due to bisection of mines and facilities by Turkish – Cyprus cease-fire line ('Green Line').
1979	Copper, Gold, Silver, Pyrite	Fall of Copper price causes all copper mining operations to cease working. Pyrite demand and price also slumps during 1960's and 1970's, due to lack of demand for sulphur in chemical industries, etc.
1981	Copper	Hellenic Mining Company starts recovering copper cement from leached mine wastes at former Skouriotissa mine.
1988	Asbestos	Demand for asbestos falls due to concerns about safety and cheaper production from foreign sources. Amiandos asbestos mine shuts in 1988, although reports suggest that small-scale production continued until 1995.
1996	Copper	Hellenic Copper Mines Ltd (a consortium including the Hellenic Mining Company and Oxiana Resources) starts mining for copper at Phoenix opencast site, near Skouriotissa. Production of ~4-5,000t/year of 99.999% Copper Cathode starts, reaching capacity level of 8000t/year in 1998. Feasibility study for increasing production to 20,000t/year also considered.
1998	Copper	Hellenic Mining Company forms joint venture with Oxiana Resources NL of Australia to explore for base and precious metals in Cyprus – known as Eastern Mediterranean Minerals (EMM). Recent drilling (2003) has confirmed the presence of massive sulphide hosted polymetallic mineralization at one prospect at least in Cyprus.

Table 3 Timeline of recent mining activity on Cyprus (adapted from Bear, 1963; Mobbs, 2001; Mobbs, 2000 and Michalski, 1998).

has precluded any modern extraction. The orebody itself is unusual in the high levels of copper it contains, not a usual characteristic of orebodies associated with ultramafic rocks. One suggestion is that the sulphides were segregated as an immiscible liquid during magma differentiation produced by melting of the upper

mantle at depth (Panayiotou, 1980), although later work has suggested a hydrothermal origin for the ores (Thalhammer et al., 1986).



Figure 5 Copper cathode production at the Phoenix–Skouriotissa–Three Hills mine site.

Overlying and interstitial to the Pillow Lava are sedimentary umber and ochre deposits. Ochres are manganese-poor ferruginous sediments generally associated with sulphide ores, whilst umbers are manganese-rich ferruginous mudstones. Umbers have been worked since pre-Roman times on Cyprus, for use as dyes and as a flux for copper smelting (Boyle, 1990). Some umbers, such as those around the Skouriotissa mining district, were also worked for gold, with soft, friable deposits known as ‘devil’s mud’ often containing economic amounts of gold, but in small quantities (Prichard and Maliotis, 1998). Ochres, often mined for pigments and also gold, were also worked at various times in history, and are still worked today for pigments, albeit in small amounts (Robertson and Degnan, 1998).

Mining for copper on Cyprus has been almost continuous for around 6000 years, and the island was famed in ancient times for its copper production. However copper production on Cyprus has suffered in recent times, with periods during the last century when no copper production at all was taking place. The major mining activity on Cyprus over the last 100 years was not to produce copper, but to produce pyrite for use in sulphur production. However, copper, in the form of copper concentrate and copper cement, was still a major mineral export, making up 49 % of the value of all minerals exported from 1958–1962, a period with high levels of mining activity on Cyprus. Cupriferous pyrite made up 8% of the value of mineral exports, with iron pyrites forming 30 %, asbestos 10 %, chrome concentrate 1.5 % and others (gypsum, umber, etc.) 1.5 % (Bear, 1963). Data regarding production during the 20<sup>th</sup> century is sporadic, but certain important dates can be identified, as displayed in Table 3, which shows a brief history of the mining industry of Cyprus.

Recent positive developments since the late 1990’s have meant a resurgence in exploration and mining activity in Cyprus – with recent positive developments in resolving the Turkish / Greek Cypriot crisis increasing the attraction for companies



associated with a linear zone of intensely sheared and brecciated serpentinite (Panayiotou, 1980). Sulphides are dominated by pyrrhotite in both cases accompanied by pyrite, pentlandite, chalcopyrite (+cubanite), löllingite and vallerite (which constitutes a major phase at Pevkos). Chromite and magnetite are common phases in the mineralization whilst traces of gold are recorded. No analyses for PGEs are recorded.

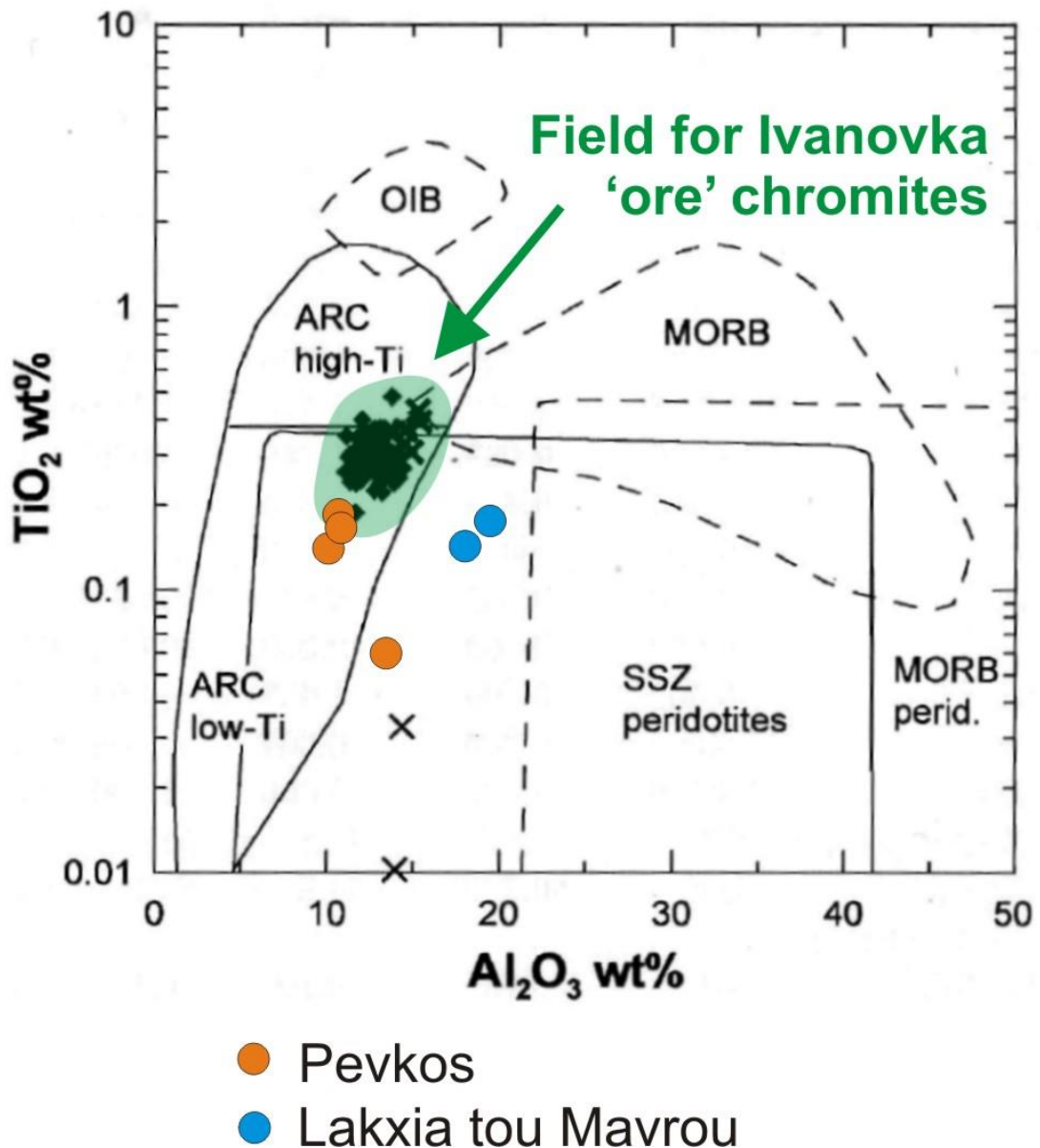


Figure 7  $\text{TiO}_2$  vs.  $\text{Al}_2\text{O}_3$  plot showing chromite compositions of Limassol Forest mineralization. Shaded blue field encloses black diamonds marking compositions of chromite in the Ivanovka VHMS deposit in the south Urals forearc sequence (modified from Tesalina et al., 2003).

Previous work by Thalhammer et al., 1986 presented mineral chemical data for both sulphides and chromite. Chromite chemistry has been successfully used as a geochemical discriminant in the study of tectonic setting for ophiolites (Tesalina et al., 2003). Analyses of chromite grains from both the Pevkos and Lakxia tou Mavrou prospects, shows them to have distinctively low Al, Ti compositions (Thalhammer et al., 1986), similar to chromite associated with the ultramafic-hosted VHMS deposits in the southern Urals (Tesalina et al., 2003) (Figure 7). These

deposits occur in an interpreted supra-subduction, fore-arc setting within serpentinites, a view expressed for the setting for the serpentinites of the Limassol Forest (and Troodos complex in general). Such environments are now recognised as likely sites for ultramafic-hosted seafloor hydrothermal mineralization.

At Lakxia tou Mavrou, large ochreous gossans are testament to the trial mining of massive pyrrhotite lenses (Figure 8A). Mineralization is hosted within sheared and brecciated serpentinites (Figure 8B, C, D), with minor boudins of sulphide seen in outcropping sheared serpentinite, believed to represent the setting of the mineralization as described in the literature. Primary relationships of the sulphides are difficult to ascertain because of the deformation. This deformation appears, at least in part, to post-date mineralization (Thalhammer et al., 1986).



Figure 8 Photographs of the Lakxia tou Mavrou set of showings. A – Main trial adit dump showing extreme gossan after pyrrhotite; B – Trial pit and adit; C – In-situ sheared boudin of massive pyrrhotite mineralization in sheared serpentinite exposed in southern river cut; D – Sulphide-cemented serpentinite breccia from dump material at Lakxia tou Mavrou.

The showings at Pevkos are harder to locate although gossanous outcrops are evidence of sub-cropping mineralization near to the active quarrying. Here the precise field relationships are less clear than at Lakxia tou Mavrou. Gossanous outcrops of serpentinite were located where seemingly altered rocks host disseminated to massive sulphides (Figure 9). Very little massive sulphide was seen in the short visit to the property by the authors although the assemblage has been described in detail previously (Thalhammer et al., 1986). The host serpentinites appear bleached and altered peripheral to mineralization although it is difficult to ascertain in the field whether this is deuteric alteration or the result of hydrothermal activity. Samples have been collected in order to investigate this.

Two contrasting models of formation have been proposed for the deposits; an orthomagmatic origin was proposed by Panayiotou, 1980 whilst a later hydrothermal origin is proposed by Thalhammer et al., 1986. Ni-Co-Cu mineralization in ultramafic assemblages elsewhere has largely been interpreted in terms of orthomagmatic origins (e.g. Naldrett, 1981); the model embraced for the Limassol Forest by Panayiotou, 1980. However, Thalhammer et al., 1986 note the likely hydrothermal origin for the mineralization based on mineral texture and association, consistent with the observations of the present authors based on the visit to Pevkos. Significantly, it has been noted in other ophiolite sequences that the ultramafic parts of the succession can host seafloor hydrothermal Ni-Co-Cu mineralization, notable examples being the Proterozoic deposits of Outukumpu in Finland (Loukola-Ruskeeniemi, 1999) and Palaeozoic deposits in the southern Urals (Nimis et al., 2004; Herrington et al., 2005). Similarly, active seafloor hydrothermal systems on exposed ultramafic oceanic crust are known from the Atlantic ocean (Murphy and Meyer, 1998) In extensional zones in either mid-ocean ridge or forearc settings, the basal crustal section may become exposed and hydrothermal activity may develop on the ultramafic sequence exposed on the seafloor. This observation suggests a re-examination of the Limassol Forest deposits is warranted to investigate the possibility of such a model for the mineralization.



Figure 9 Pevkos showing: A—View from gossanous outcrop southwest towards coast. Showing comprises rubbly gossanous outcrops next to field pack with small reclaimed dumps; B—Closeup of altered serpentinite with gossanous material after pyrrhotite?

### 3 Mineral deposit models and prospectivity analysis

The main tools used in taking a new look at VHMS mineralization on Cyprus was to create, using a GIS and spatial digital data, mineral potential maps. The first step in this process is to review and revise conceptual models for the target mineral deposit types—in this case Cyprus-type VHMS deposits and formulate a mineral deposit model. Second, the characteristics and data that may be useful to exploration—the exploration model—must also be identified. Third, the other important factor in identifying a useful exploration model, is the availability and applicability of available spatial digital data for the statistical analysis—not all data that can be used in exploration will be in digital format, and also not all data will be useful for certain mineral deposits. The exploration model, as shown in Figure 10, is a combination between the general deposit model and the available data.

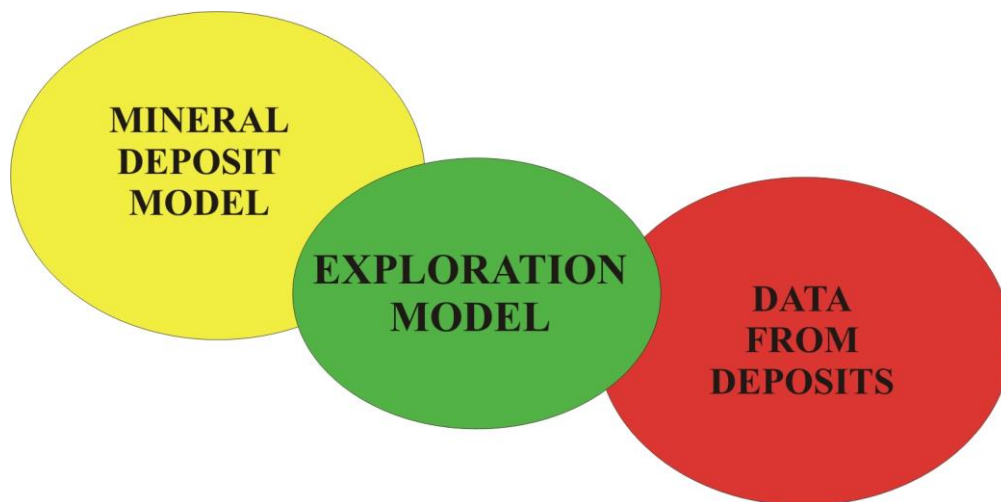


Figure 10 Conceptual diagram of an exploration model.

Also it is important to stress that exploration models are dynamic—they change as new research into the deposit model and techniques for exploration are identified, and as new exploration data becomes available.

First, a mineral deposit model is a summary of the state of knowledge about a given mineral deposit—a description of the characteristics of a mineral deposit, with information arranged systematically, and describing often only the essential attributes of the deposit. Two main types of mineral deposit are encountered (i) empirical (descriptive). Here various attributes are considered to be essential to the deposit, even though their various relationships may be unknown (ii) theoretical (genetic). Here mineral deposit attributes are interrelated through fundamental mineralization concepts (Cox and Singer, 1986).

According to Cox and Singer, 1986 the following information comprise the minimum specifications for a useful mineral deposit model:

- Deposit type—Name of type and sub-type, commodities and examples.
- Economic characteristics—relative importance, grade and tonnage (with or without grade-tonnage curves), production figures.

- Geological features—setting, host rocks, morphology, mineralogy, alteration assemblages, paragenesis, relative and actual ages of host rocks and mineral deposits, geochemical signatures and distributions, geophysical features.
- Genetic aspects—sources of metal, fluids, mineral deposits, etc., controls on sites of mineralization.
- Exploration methodology—linking to the mineral deposit model to be used for exploration potential maps.

Mineral deposit models are extremely valuable for several reasons. Firstly, they allow easy comparisons between deposits and facilitate the classification of new discoveries. Typical deposit fingerprints or signatures can also be identified, allowing the prediction of new exploration target areas. Exploration methodologies and strategies can be tailored to search for certain mineral deposits with characteristic signatures. Finally, these deposit models can be easily revised and updated, giving these models a dynamic nature (Cox and Singer, 1986).

### 3.1 VHMS MINERALIZATION

VHMS Deposits are widespread throughout the world. Figure 11 shows the locations of some of the more important deposits around the world.



Figure 11 Major VHMS deposits and provinces around the world. 1 = Troodos, Cyprus, 2 = Iberian Pyrite Belt, Spain/Portugal, 3-5 = Central and Southern Urals, Russia and Kazakhstan, 6 = Windy Craggy, British Columbia, 7 = N Cordillera, Canada, including Eskay Creek, 8 = Abitibi-Superior, Canada, including Kidd Creek, 9 = Big Stubby, Mons Cupri and Whim Creek, Australia, 10 = Scuddles – Golden Grove, Australia, 11 = Benambra – Woodlawn, Australia, 12 = Mt. Read, Tasmania, Australia, 13 = Kuroko Japan. Adapted from Barrie and Hannington, 1999).

They occur in a wide variety of settings and throughout the geological record, from the Archaean (e.g. deposits in the Slave Province and Abitibi-Superior Province, Canada) to the Mesozoic (e.g. Troodos deposits, Cyprus) and the modern day (e.g. contemporary sea-floor vent settings such as the TAG mound in the Atlantic). Deposits have been traditionally categorised into groups based on geographical occurrences namely: Besshi-type, Kuroko-type, Cyprus-type, Urals-type etc. More

useful classifications have been the five-fold categorisation proposed by Barrie and Hannington, 1999, modified by Franklin et al., 2005, which classifies VHMS deposits according to lithostratigraphic types. Classes in this modelling system consist of bimodal-mafic (ultramafic, most Precambrian deposits), mafic (ophiolitic or mid-ocean ridge, Cyprus-type), mafic-siliclastic (or pelite-mafic) (Windy Craggy or Besshi-type), bimodal-felsic (Kuroko-type) and bimodal-siliclastic (or siliclastic-felsic) (Iberian Pyrite belt-style) (Barrie et al., 1999a). Given the largely interchangeable nature of the classifications, reference to both types of classification will be given where applicable, to ensure clarity. Figure 12 shows suggested typical tectonic settings for Cyprus/Ophiolite Hosted, Besshi, and Kuroko/Noranda VHMS deposits.

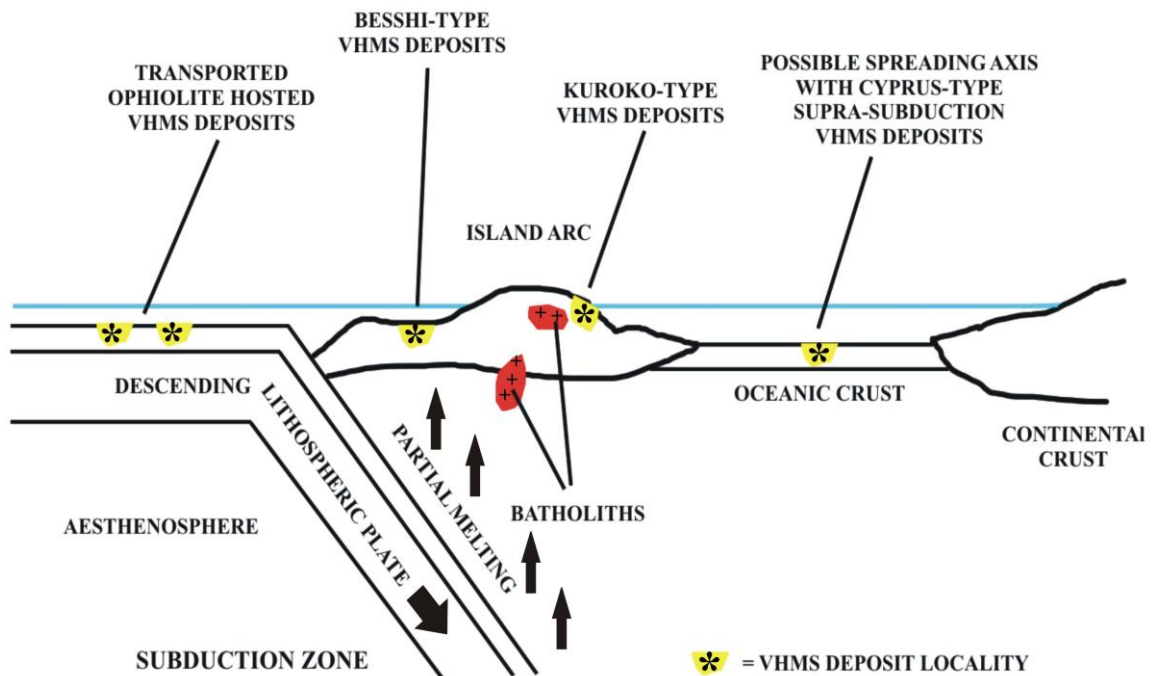


Figure 12 Examples of tectonic settings for the formation of Cyprus/ophiolite-hosted, Besshi and Kuroko/Noranda-type VHMS deposits. Adapted from Evans, 1980.

As can be gathered by the three-fold deposit classification, VHMS deposits are typically found in one of three settings. Cyprus-type deposits are typically found in ophiolite complexes, formed at oceanic ridges or back-arc spreading centres (Hoy, 1995a). Besshi-type deposits are found at extensional oceanic settings, such as back-arc basins, oceanic ridges close to continental margins, or rift basins in the early stages of spreading and continental separation. Kuroko-type deposits, sometimes known as Noranda-type deposits, are found in Island arc settings, typically in a localised extensional or rift setting, within or associated with an oceanic or continental margin arc (Hoy, 1995b). VHMS deposits also occur in a wide variety of volcanic environments within these tectonic settings. Two general volcanic end members can be envisaged, namely those primarily associated with volcanic flows to those contained within successions of primary and redeposited pyroclastic deposits, corresponding roughly to deep and shallow water environments respectively (Gibson et al., 1999).

Heat and fluid flow are the main fundamental processes in the formation of all VHMS deposits. All VHMS deposits are marine, and form by the venting of high

temperature fluids at or near the seafloor, seen today at localities such as the TAG mound on the Mid-Atlantic ridge, where black smokers are venting high temperature metal-bearing fluids. These black smokers, and their unique communities of fauna, have been found in the geological record, giving us a link between ancient and modern ore-forming processes (Hannington et al., 1998). These high temperature fluids are produced by underlying hydrothermal systems, heated by underlying heat sources, such as magma chambers associated with ocean spreading as seen on the Troodos, and forming a circulatory system flowing from the hot magma chamber to the surface. These hot, buoyant and reactive fluids strip metals from the lower parts of the crust and transport them towards the surface (Richardson et al., 1987). At or near the seafloor surface, massive sulphides are precipitated where non-boiling fluids are vented and come into contact with cold seawater, or are cooled by the steep near-surface thermal gradient. The steep thermal gradient near the seafloor also induces precipitation of ore minerals into a stockwork zone, found beneath the massive sulphide deposit. This stockwork deposit marks the upflow zone of the hydrothermal fluid, and forms directly beneath the hydrothermal vent (Adamides, 1990). If boiling occurs, metal precipitation is rapid, in turn inducing subsurface metal precipitation in the form of vein deposits not associated with VHMS deposits. For this reason, VHMS deposits must be formed at a suitable water depth to prevent this boiling (~1.5km for fluids ~350°C) (Barrie et al., 1999a).

Type	Number of Deposits	Total Tonnage (Bt)	Average Size (Mt)	Average Cu Grade (%)	Average Zn Grade (%)	Average Pb Grade (%)	Average Au Grade (g/t)	Number of Deposits >100Mt
Mafic, Cyprus-type	62	0.18	2.8	2.04	1.82	0.10	2.56	0
Bimodal-mafic, Precambrian-type	284	1.45	5.1	1.88	4.22	0.75	1.52	1
Mafic-Siliciclastic, Besshi-type	113	1.24	11.0	1.74	2.43	1.83	0.84	3
Bimodal Felsic, Kuroko/Noranda-type	255	1.29	5.2	1.44	5.63	1.34	2.06	0
Bimodal-Siliciclastic, Iberian Pyrite Belt-type	97	2.50	23.7	1.10	4.16	1.84	1.13	9
Total	811	6.66	–	–	–	–	–	13
Average	–	–	9.56	1.64	3.652	1.172	1.622	–

Table 4 Total and average grades and tonnages for worldwide (excluding former USSR and Chinese deposits) VHMS deposits. Adapted from Barrie and Hannington, 1999.

The main controls on the nature and pattern of the hydrothermal circulation that forms VHMS deposits are the source of heat driving the hydrothermal system, and the permeability of the host rocks.. These factors are very broadly related to the geological setting and host-rock composition of the VHMS deposits, and therefore related to the classification of the deposit (Barrie and Hannington, 1999). The thickness of underlying crust also plays a significant role in the deposition of VHMS deposits. bimodal-felsic and bimodal-siliciclastic deposits are often underlain by

~10-30km of rifted continental crust, whereas pelitic-mafic (Besshi) and mafic (Cyprus) types are generally underlain by thinner, rifted oceanic crust 3-10km thick. This difference in thickness changes the underlying thermal gradient, with heat sources that drive the hydrothermal system in thicker crust remaining at a higher temperature for longer when compared to heat sources underlying thinner crust. This implies that hydrothermal circulation would last longer in thicker crust, creating larger numbers of deposits, and these deposits may well be larger in size (Barrie et al., 1999a).

VHMS deposits, as seen in Figure 11, are found in many locations over the world. Deposit sizes range from insignificant to giant, with world class deposits such as Kidd Creek in Ontario (>138.7 Mt at 2.35% Cu, 6.5% Zn, 0.23% Pb and 89g/t Ag) and Windy Craggy in British Columbia (the world's largest Besshi-type deposit, at 297.4 Mt at 1.38% Cu, with a cut-off grade of 0.5% Cu) (Barrie et al., 1999b, Peter and Scott, 1999). Table 4 gives some average grades and tonnages for worldwide (except former USSR and China) VHMS deposits.

As can clearly be seen in Table 4, the five different classes of deposit have their own individual characteristics in terms of size and grade of deposit.

### 3.2 OPHIOLITE-HOSTED VHMS DEPOSITS

Ophiolite-hosted VHMS deposits, also known as Cyprus-type VHMS deposits, are seen in at least 25 of the world's more than 200 known ophiolite terranes. The term Cyprus-type is not restricted to typical Mid-ocean ridge ophiolite settings since many of this deposit type are considered to have formed in a supra-subduction zone setting, similar to the present day Mariana-Bonin arc. Thus the Cyprus-type VHMS deposits form a subdivision of the wider Ophiolite-hosted VHMS deposits (Galley and Koski, 1999), a group within the mafic deposit class of Barrie and Hannington, 1999. Figure 13 shows some well-known ophiolite-hosted VHMS deposits, both at MOR and supra-subduction settings.

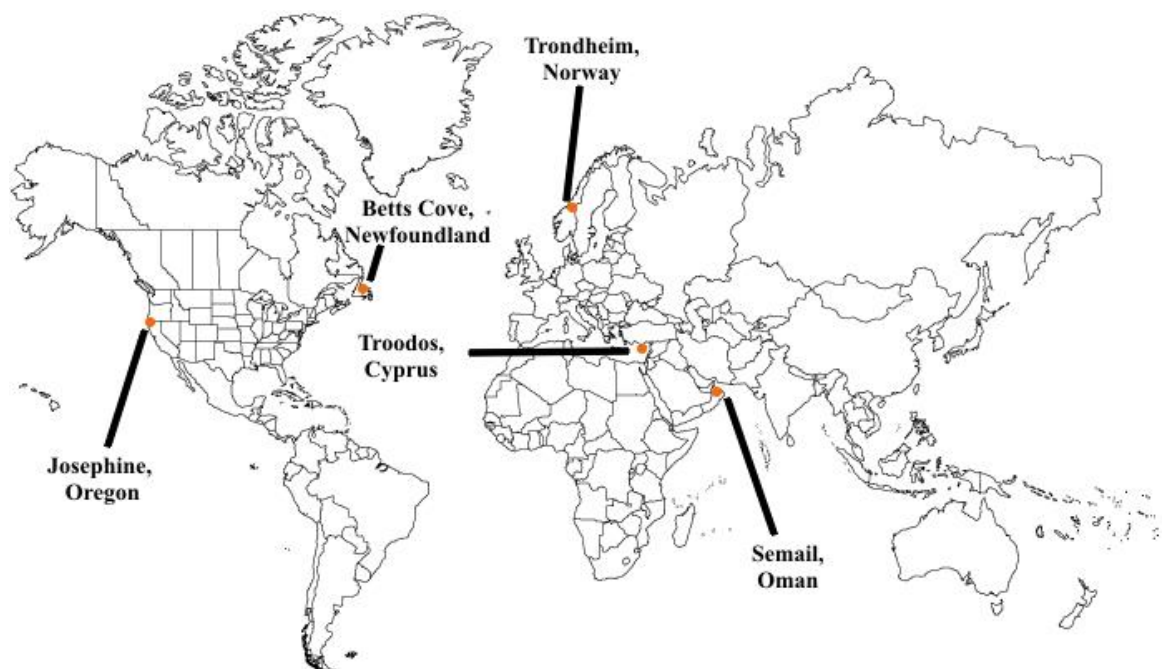


Figure 13 Some well-known ophiolite related VHMS deposits.

Ophiolite-hosted VHMS deposits of both types form a significant worldwide base metal resource. These deposits are copper and copper-zinc rich, compared to other VHMS deposit types; individual deposits can reach up to 30Mt, although the average deposit size is around 5 Mt (Galley and Koski, 1999). Gold is usually present in the oxidised sulphide caps of these deposits—particularly those associated with the Tethyan Ocean, as seen on Cyprus (Constantinou, 1980).

As with all other VHMS deposit types, ophiolite hosted deposits are formed as a consequence of hydrothermal circulation. The primary heat source that drives the hydrothermal circulation at the ocean ridge axis are layered ultramafic-mafic plutonic magma chambers that are found below sea-floor spreading axes. These chambers are formed of layered peridotite grading up into gabbros and plagiogranites, with the overlying Sheeted Dyke Complex representing fossilized conduits for magma ascending to the ocean floor. Overlying the Sheeted Dyke Complex is a volcanic section formed of massive and thinner lava flows, pillow lavas, lava breccias and hyaloclastites, with feeder sills and dykes, and interstitial sediments, all usually overlain by a thick marine sedimentary cover sequence (Galley and Koski, 1999).

Spreading rates are key to the formation of VHMS deposits associated with ophiolites. Ophiolite sea-floor spreading centres known to host larger VHMS deposits, for example, the Troodos ophiolite, Cyprus, the Josephine ophiolite, Oregon, and the Semail ophiolite, Oman, are known to have had alterations in spreading rate over time. Intense magmatic activity is required to initiate large-scale seawater convection and resultant high-temperature fluid/rock interactions, within reaction zones where metals are stripped from the rocks by the hydrothermal fluids. Intercalated sediments within the upper volcanic sequence provide evidence for slower rates of spreading later in the life of the spreading ridge, during which significant hydrothermal activity would produce large volumes of massive sulphide and stockwork mineralization. These large volumes of ore would not have accumulated if the fast spreading rate had been sustained, as the hydrothermal circulation system would have been transported too quickly away from the driving force of the underlying heat of subsurface magma chambers. Slower spreading rates would have enabled far more ore to be formed and deposited than would be the case in a faster spreading regime (Galley and Koski, 1999).

Massive sulphides in ophiolite-hosted VHMS deposits are commonly clustered in groups along the exposed strike length of the ophiolite. Within these clusters of deposits and mining districts, base metal mineralization can occur at any stratigraphic level, from the top of the magma chamber to the overlying sedimentary cover sequences (Harper, 1999). However, massive sulphide deposits and associated stockwork mineralization are usually only found throughout the volcanic strata above the Sheeted Dyke Complex. Indeed, in many ophiolites, stratiform massive sulphide deposits are most commonly located along a major contact, between differing suites of lavas, or between lavas and the overlying sediments, implying a hiatus in magmatism, allowing a hydrothermal circulation system to initiate during fast spreading, and propagate throughout a period of slower spreading. Deposits themselves consist of a stratiform massive sulphide lens and a proximal sulphide vein stockwork zone. These may be seen together or one component may be missing, due to displacement by faulting or deformation, or simply due to lack of preservation. The stockwork mineralization itself may be up to several hundred metres wide and may be traceable through several hundred metres of depth into the Sheeted Dyke Complex. A clear example of this is provided by the Aarja VHMS

deposit, Oman, where a diffuse stockwork zone can be traced vertically over 3 km, and in places is up to 500m wide (Galley and Koski, 1999).

The massive sulphide deposits themselves are all pyrite-rich, commonly having a massive base, overlain by sandy-textured and brecciated ore, with the pyrite-rich massive core being cemented by base metal sulphides, for example chalcopyrite and sphalerite. The underlying stockwork zone is generally formed of a mixture of quartz and pyrite, with minor amounts of base metal mineralization.

### 3.3 MINERAL DEPOSIT MODEL—CYPRUS-TYPE VHMS DEPOSITS

Mine	Type	Original Ore Reserves (Mt)	Cu (%)	Zn (%)	Pb (%)	Ag (ppm)	Au (ppm)	S (%)
Kalavassos A-E	Massive and Stockwork	1.9	1.0	0.5	0.01	6	1.7	35
Petra	—	0.526	—	—	—	—	—	—
Mavri Sykia	— (Underground)	0.269	—	—	—	—	—	—
Mavri Sykia	— (Open-cast)	0.697	—	—	—	—	—	—
Landaria	—	0.3155	—	—	—	—	—	—
Platies	Massive and Stockwork	.0439	2.8	—	—	—	—	46
Mousoulos	Massive and Stockwork	2.6	1.0	0.5	0.01	6	1.7	35
Mavridia	—	0.600	—	—	—	—	—	—
Skouriotissa	Massive and Stockwork	5.44	2.3	0.06	—	69	—	48
Phoenix	Stockwork	15	0.5	—	—	—	—	—
Limni	Massive	0.422	1.4	—	—	3	3.4	—
Limni	Stockwork	16	1.0	0.2	—	—	—	14
Mavrovouni	—	15	3.8	0.5	—	39	0.3	49
Apliki	—	1.65	1.8	0.2	—	5	—	40
Ambelikou	—	0.016	1.0	—	—	—	—	—
Memi	Stockwork	1.5	0.1	—	—	—	—	26
Alestos	—	0.100	—	—	—	—	—	—
Kokkinoyia	Massive and Stockwork	1.5	~3.0	—	—	—	—	—
Kokkinopezoula	Massive and Stockwork	3.5	0.2	—	—	—	—	24
Agrokipia A and B	Massive and Stockwork	5.265	~0.6	~0.6	—	—	—	~40
Kambia	Stockwork?	1.5	—	—	—	—	—	30
Mathiati	Massive and Stockwork	2.8	0.2	1.0	—	—	—	33
Sha	Massive and Stockwork	0.350	1.0	—	—	—	—	25
Klirou East	Massive and Stockwork	0.420	1.1	1.4	—	—	—	23
Klirou West	Massive and Stockwork	0.077	0.5	0.5	—	—	—	21
Troulli	—	0.270	1.0	—	—	—	—	8
Peravasa	—	0.090	0.8	—	—	—	—	—

Table 5 Resources and grades for selected orebodies on Cyprus. Data taken from Adamides, 1980 and Hannington et al., 1998, — = no information.

The typical view of a Cyprus-type copper deposit is a sulphide deposit formed at the spreading zone of a mid-oceanic ridge. All the copper deposits on Cyprus are VHMS deposits, with massive sulphides having formed at the seawater-lava interface, as indicated by the presence of a fossil record within many of the sulphides (Herrington et al. 1999). These massive sulphides are formed from metal-bearing exhalative fluids, typically from black smokers, as seen in Mid-Ocean Ridge settings today (e.g. the TAG mound, on the Mid-Atlantic Ridge). The seawater-rock interface was presumed, in most orebody cases, to be represented by the junction between the Upper and Lower Pillow Lavas, representing a hiatus in magmatic activity that allowed the hydrothermal circulation system, needed for the formation of these orebodies, to develop (Constantinou, 1980). Below the massive sulphide bodies are

lower grade stockwork bodies; these bodies are presumed to fossilised routes for the hot mineralizing fluids as they flowed towards the surface after interacting with the lower Sheeted Dykes, stripping them of metals (Richardson et al., 1987). This overall model has not been re-examined in detail but it is apparent that not all deposits are formed at the contact between Upper and Lower Pillow Lavas as was presumed. Current work, both on Cyprus and in areas such as the Ural Mountains where Cyprus-type sulphide deposits have been the focus of a recent multinational geological investigation, has created a better understanding of how these deposits formed in an evolving arc system. The mineral deposit model described in this section aims to combine the older views with more recent work to create a better outline for exploration for copper on Cyprus. A deposit model for Cyprus-type copper deposits is outlined below.

Zone	Phenocryst Mineral Alteration		Groundmass Alteration		Glassy Margins Alteration		Void Filling Alteration	
<b>Seafloor Weathering Zone</b>	Goethite, calcite, spinel	Hematite, smectite,	Smectite, Maghemite, calcite	K-Fsp, smectite,	Smectite, phillipsite		Smectite, Fe-hydroxide, adularia, palygorskite	analcite, calcite,
<b>Low Temperature Zone</b>	Goethite, smectite, calcite, titanomagnetite	calcite, celadonite, spinel,	Smectite, celadonite, calcite, maghemite,		Smectite, phillipsite, analcite, clinoptilolite		Smectite, celadonite, Na-Ca zeolites, quartz, chalcedony, palygorskite	calcite,
<b>Transition Zone</b>	Smectite, smectite/chlorite mix, albite, titanomagnetite		Smectite, smectite/chlorite mix, albite, quartz		Smectite, smectite/chlorite mix, laumontite, quartz, pyrite		Smectite, smectite/chlorite mix, laumontite, quartz, pyrite, calcite	
<b>Upper Dyke Zone</b>	Chlorite, calcite, chlorite	albite, epidote,	Chlorite, epidote, sphene, pyrite	albite, quartz,	Chlorite, quartz, pyrite, epidote		Chlorite, quartz, pyrite, calcite	epidote,
<b>Mineralized Zone (Stockwork Zone)</b>	Illite, quartz, sphene		Chlorite, pyrite, sphene	quartz,	Chlorite, quartz, pyrite		Jasper, pyrite, quartz, chalcedony, pyrrhotite	

Table 6 Alteration facies associated with mineralization in the Troodos ophiolite—adapted from Gillis and Robinson, 1990a.

- *Mineral Deposit Model:* Cyprus-type VHMS Deposits, Troodos Ophiolite, Cyprus
- *Deposit Type:* Ophiolite-hosted VHMS Deposit, subtype Cyprus-type, locality Troodos Ophiolite, Cyprus
- *Metals Present:* Cu (Au, Zn, Ag, Co) (Deposits were also previously mined for sulphur, obtained from pyrite)

Examples: Selected orebodies from the Troodos ophiolite.

The average size of Cyprus-type deposits is 1.6 Mt containing 1.7 % Cu, 0-33 g/t Ag, 0-1.9 g/t Au, and 0-2.1 % Zn (Singer and Mosier, 1986).

- *Tectonic Setting:* Supra-subduction zone, fore-arc (Mariana-Bonin Arc-type)
- *Geological Setting:* Lenses of massive sulphides, and the often-mineralized underlying stockwork zone, are associated with the upper parts of the Troodos ophiolite – the Upper and Lower Pillow Lavas, the Basal Group transitional unit, and the Sheeted Dyke Complex.
- *Host Rocks:* Diabase sheeted dykes, Basal Group (transition from Sheeted Dykes to Pillow Lavas), Pillow Lavas – of island arc tholeiite, depleted tholeiite and highly depleted boninite composition, and mixed lava/volcaniclastic sediment piles.

- *Age of Host Rocks:* Triassic – Early Cretaceous
- *Deposit Form:* Stratiform layered massive sulphide pods originally overlying veinlet and disseminated stockwork ore zone that acted as a preferential flow conduit for ore forming fluids.
- *Ore Controls:* Orebodies are associated with the upper parts of the Ophiolite sequence only – the Pillow Lavas and associated sediments, the Basal Group, rarely in the Sheeted Dyke unit and very rarely within the Gabbro and Plagiogranite units. Orebodies can be associated with steeply dipping faults – which may have acted as conduits for upflowing hydrothermal fluids.
- *Alteration:* 5 major zones of alteration surrounding mineralization as described in Table 6, with three distinct types of stockwork alteration, described in Table 6.

Facies	Layer Silicates	Other Minerals
<b>Smectitic</b>	Smectite (generally Saponitic, including phases with up to 20% Chlorite)	Fe-Hydroxides, quartz, zeolites, (relict Ca Plag, pyx, Fe-Ti oxides)
<b>Chlorite-Smectite Mixed Layer</b>	Chlorite/Smectite mixed layer minerals, over 20% chlorite	Albite, quartz, sphene, pyrite, (relict Ca Plag, pyx, Fe-Ti oxides)
<b>Chlorite-Albite</b>	Chlorite	Albite, quartz, sphene, pyrite (relict Ca Plag, Fe-Ti oxides)
<b>Chlorite-Illite</b>	Chlorite, Illite	Quartz, pyrite, anatase
<b>Leached</b>	Illite	Quartz, pyrite, anatase
<b>Chlorite-Rectorite</b>	Chlorite, Rectorite, or similar hydromica-smectite mixed layer phase	Quartz, pyrite, anatase

Table 7 Common mineralized stockwork alteration facies observed in the Troodos ophiolite, adapted from Richards et al., 1989.

It is also worth noting that post-depositional surface weathering may alter some of the primary alteration minerals, with hematite and goethite being converted to limonite, etc.

- *Source of Mineralization:* Recharge zones in the lower Sheeted Dykes and upper gabbros and plagiogranites, with hot hydrothermal fluids – heated by underlying magma chambers – stripping metals from the recharge zones and transporting them to higher stratigraphic levels – the Pillow Lava extrusive sequences.
- *Genetic Model:* Seafloor deposition of massive sulphide deposits from venting of underlying hydrothermal circulation systems, with mineralization of hydrothermal passageways beneath massive sulphides – as stockwork mineral deposits.
- *Associated Mineral Deposits:* Metalliferous umbers (Mn), ochre deposits, gold deposits.
- *Preservation:* Moderate subsidence combined with low dyke density is needed. In order to be preserved in the geological record, orebodies need to be sufficiently buried to prevent the dissolution of ore minerals by seawater, but rapid and substantial subsidence of an orebody would cause break up by abundant dyking.
- *Geochemical Signature:* Depleted in Mg, Ca, Na and Si. Zn is enriched close to sulphide deposits, but depleted away from mineralized areas. Sheeted Dykes are depleted in Ba, with deposits showing locally enriched Ba values

in soils and rock samples. Enriched in Cu, Zn, Pb, Ag, Mo, Co, As, Hg, Bi, Cd, Au, Sb and Mn, although local Mn-rich sediments and umbers may affect Mn values.

- *Geophysical Signature:* Inverse Polarisation can be used to locate orebodies, but anomalies may be obscured when survey lines cross the Upper Pillow Lavas, or Basal group units. Magnetic surveys show that most sulphide mines lie on the flanks of broad areas of low magnetic intensity (possibly corresponding to Basal group rock types at the surface or at shallow depth), also lying on or close to magnetic structures, lineations or boundaries. Microgravity and gravity anomalies may show the presence of massive sulphides.
- *Other Exploration Guides:* Often associated with boundaries in the ophiolite volcanic sequence - as a hiatus in magmatic activity is needed to form large ore deposits.

The tectonic setting of Cyprus, and in particular the Troodos ophiolite, is the first major point to examine. As explained elsewhere in this report, modern thinking on the formation of the Troodos has indicated that the ophiolite most probably formed in a supra-subduction zone setting, much like the Mariana-Bonin arc in the present day Western Pacific. This, therefore, should also be taken as the setting for the formation of the massive sulphide and stockwork deposits seen on Cyprus, as magmatism and spreading had not ceased after the formation of the later series of Pillow Lavas and other extrusive igneous rocks, seen to cover many orebodies on the island (Adamides, 1990).

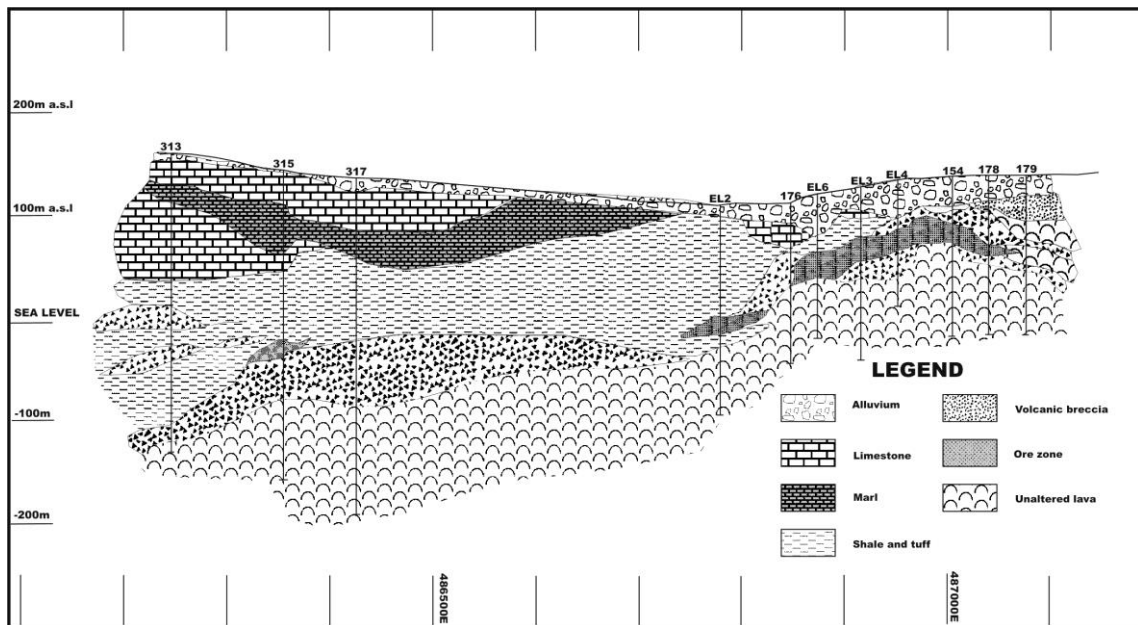


Figure 14 Cross section through the East Lefka VHMS deposit (from Adamides, 2004).

Orebodies on Cyprus are generally limited to the Pillow Lavas and Basal Group units, with rare mineralization occurring in the Sheeted Dykes and Gabbros. Originally thought to form on the contact between the Upper and Lower Pillow Lavas, recent geochemical work has identified three distinct units of Pillow Lavas, rather than the two previously proposed. Since orebodies are known spanning the stratigraphic range from the Basal Group, to the Upper Pillow Lavas, the theory that the Lower to Upper Pillow Lava contact is one of the primary controls to the

distribution of mineralization is somewhat flawed (Constantinou, 1980). Mavrovouni is by far the largest of the Cyprus deposits, amounting to 15 million tons of 4.0 % copper (Bear, 1963) and is located at a very high stratigraphic level within the Upper Pillow Lava sequence. The East Lefka deposit, located a few hundred metres east of Mavrovouni, is poorly studied but drill logs clearly indicate the presence of massive sulphides within sediments at the top of the volcanic pile (Figure 14).

Nevertheless, the bulk of economically important mineralization is found in specific units, namely the Pillow Lavas and associated sediments, the Basal Group, and the Sheeted Dyke Complex. There is a suggestion that hydrothermal sulphides may even be developed in the ultramafic parts of the sequence (see later discussion on the Limassol Forest mineralization) but to date no economically important deposits have been located.

Mineralization-hosting rocks are part of the Troodos ophiolite, which was originally formed during the Jurassic–Early Cretaceous. However, no Jurassic crust is preserved on Cyprus, with the ophiolite having formed between the start of the Triassic and the Early Cretaceous, where subduction started due to the convergence of the African and Eurasian plates. After the subduction of any young Cretaceous crust, older and denser Triassic crust entered the trench, causing roll-back of the subduction zone, and the hinge of the subduction zone to migrate backwards—causing the mantle wedge above the young subduction zone to extend. This allowed asthenospheric material to well up, forming the 200 km wide spreading fabric of the Troodos ophiolite, which continued to spread and form new crust until Turonian times (92–90 Ma). Ages of host rocks for the copper deposits on Cyprus, therefore, range from the Triassic to Turonian, ceasing at least by the Eocene, with the orebodies necessarily forming within this time period, as the heat generated by the spreading ridge drove the hydrothermal system that formed the ore (Robertson, 1998).

Massive sulphide deposits on Cyprus take the form of layered deposits containing generally more than 60 % pyrite, with comparatively minor amounts of chalcopyrite and sphalerite. Deposited on, or close to, the seafloor, the orebodies can be found anywhere within the volcanic sequence, although mineralization usually occurs upon a surface showing the cessation in magmatism that is required to generate large tonnage orebodies. Post-mineralization magmatism is usually, but not always, seen, with orebodies often originally being covered by pillow lavas and many being cut by later dyke intrusions, possibly following the same lines of weakness as the mineralizing fluids (Constantinou, 1980). Some deposits show an ochreous layer between the sulphides and the overlying Pillow Lavas, suggesting submarine oxidation of the orebody took place (Boyle, 1990).

The massive sulphide deposits are, except where displacement or deformation has taken place, underlain by a mineralized stockwork zone, formed of mineralized and hydrothermally altered volcanics extending to considerable depths. These stockworks have a core of pyritic mineralization, with traces of cobalt, lead and molybdenum, with an outer layer of remobilised copper and zinc minerals at the periphery of the pyritic mineralization. Minerals found in the stockwork and massive sulphide orebodies include pyrite (the majority of the orebody), chalcopyrite and sphalerite, with less common minerals, such as copper secondary minerals for example bornite, as well as marcasite, galena, pyrrhotite, cubanite, stannite-besterite and hematite (Richards et al., 1989).

A complex history of hydrothermal alteration, crustal aging, uplift and emplacement is recorded in the Troodos dykes and lavas. General wall rock alteration around stockwork deposits is found to be generally smectitic or chlorite-smectite mixed facies in grade, as seen in Table 6. However, alteration associated with stockwork mineralization can be divided into three different types, namely P-, K- and M-type alteration ‘pipes’, so called due to the pipe-like nature of the stockwork mineralization (Gillis and Robinson, 1990a).

P-type Pipes, named after the Pitharokhoma deposit, have sulphide mineralization associated with chlorite-illite, smectite and chlorite-smectite mixed layer alteration. Possible leached-facies alteration may also be present. K-type pipes, named after the Kokkinopezoula mine, have smectitic and chlorite-smectite mixed layer alteration, as seen in P-type alteration. However, no chlorite-albite alteration is present, and a continuous alteration sequence from smectitic through chlorite-smectite to chlorite-rectorite facies is present. K-type pipes may well have formed through partial retrogression of P-type pipes. M-type pipes, however, have an entirely different type of alteration. Named after the Mathiati orebody, the central stockwork zone host rocks are altered to a chlorite-quartz-pyrite-anatase assemblage not seen in other types of pipe alteration, with chlorites of a comparatively distinct Fe-rich composition. Intermediate stockwork zones include chlorite-rectorite and chlorite-smectite mixed facies, with chlorites in the intermediate zone being more Mg-rich than in the central stockwork zone (Richards et al., 1989).

The source of the massive sulphide mineralization is seen within the Sheeted Dyke Complex and upper gabbros, below the extrusive sequences of the Pillow Lavas and volcanics. Within the Sheeted Dyke Complex, zones of epidote-quartz-magnetite rocks up to 900m wide are found, having sharp contrasts with the background ‘normal’ diabase dykes. These epidosite zones are thought to form the hydrothermal reaction zones of the major hydrothermal systems that produced the massive sulphide and stockwork deposits of the Troodos ophiolite. These areas have been stripped of copper, zinc and manganese, as well as removing some sodium, and several are seen to lie along strike from major mining districts in Cyprus. These zones form the base of the recharge zone of the hydrothermal ore-forming systems, where metals were leached from the host rocks by the hydrothermal fluids, before flowing towards the surface along fissures and faults, eventually forming the ‘pipes’ of the stockwork deposit and the overlying exhalative massive sulphides (Richardson et al., 1987). Isotopic evidence, from Sr, H, S and O isotopes, has also suggested a basement sourcing for the metals found in the massive sulphide and stockwork deposits (Bickle et al., 1998). This is further confirmed by Pb isotopic evidence, which also details the alteration history of the Sheeted Dykes, with hydrothermal alteration being overprinted by a later secondary alteration event in the Sheeted Dyke Complex. This is probably due to the later stage low-grade zeolite facies metamorphism, widespread and clearly visible across the Sheeted Dyke Complex (Booij et al., 2000).

### **3.4 EXPLORATION MODEL**

The exploration model derived for this project is based available data for use in the project. The data used in the project is described in Chapter 4.

- *Host Rocks:* Mineralization is hosted by or associated with Upper and Lower Pillow Lavas, Basal Group, Lavas and Volcaniclastic Sediment, Gabbro and

Intrusive Plutonic rock units. Deposits may be covered by autochthonous sedimentary cover.

- *Age of Host Rocks:* Triassic to Late Cretaceous (Turonian)
- *Ore Controls:* Mineralization is only associated with certain host rocks, as mentioned previously. Mineralization is preferentially associated with faults, acting as fluid conduits, and with contacts between the host rock units, representing magmatic inactivity during which hydrothermal activity could commence.
- *Alteration:* PIMA analyses used in the project determined that alteration is complex, and assemblages are highly varied, but alteration assemblages appear to be dominated by mixtures of jarosite, halloysite, alunite, chlorite, montmorillonite, kaolinite, opal, diaspore, palygorskite, paragonite, epidote, illite, muscovite, ankerite, calcite, and celadonite.
- *Associated Mineral Deposits:* Mineralization is associated with umber, gold and ochre deposits, as well as ancient slag heaps.
- *Geophysical Signature:* This project determined that mineralization is associated with specific gravity levels, shown by Bouguer Anomaly levels, between 118.8-166.4 mGal.
- *Other Exploration Guides:* This project determined that mineralized gossans are potentially highlighted using certain ASTER Band ratios – SWIR 1/3, 1/5, 2/3, 2/5, 4/5, 6/1, and LandSat TM composite band ratio images, using ratios 5/7, 5/7, and 3/1. Satellite lineations trending NW-SE and E-W, derived from ASTER data, were also determined to be associated with mineralization.

## 4 Assessment of previous work and data used in the study

Many of the higher-grade volcanic hosted massive sulphide copper deposits exposed at the surface are exhausted and at the start of the project, in 2002, only one deposit, at Skouriotissa, was being actively exploited. Though the massive sulphide deposit is largely exhausted, two satellite disseminated low-grade (~0.5 % Cu) deposits (Phoenix and Three Hills), with supergene enrichment, provided ore for a copper-leaching, solvent extraction, and electro winning plant, which provides high quality (> 99.99 % pure) copper plate. Activities at Skouriotissa ceased during the project, but with the current high price of copper (> \$7 000 US/tonne) mining and processing of ore is scheduled to restart in the near future.

Previous, publicly available, Cu exploration programmes are centred on two large United Nations (UN) funded research and development projects, these were:

- UN Development Programme (UNDP) 1970: Survey of Groundwater and Mineral Resources.
- UN Revolving Fund For Natural Resource Evaluation (UNRFNRE) 1983: *Mineral Exploration in Western Cyprus*.

### 4.1 EXPLORATION CONCEPTS USED IN UNITED NATIONS WORK

The UNDP project (April 1963–March 1969) recognised VHMS and supergene mineralization styles and explored three terrains: (i) in and near existing deposits, (ii) on volcanic rocks with shallow cover and (iii) on volcanics with no expression of mineralization. It recognised that any new large Cu deposit would be buried beneath cover and explored 80 prospects using detailed and regional mapping, geophysical surveys and geochemical surveys. In addition, 245 boreholes (~31 000 m) were drilled with an average depth of 120 m (maximum 300 m). Virtually all targets were explored with geophysics and thirty-eight were drilled. Weak to moderate mineralization was located in twenty-four of the thirty-eight drilled targets and six of these contained significant copper with moderate pyrite concentration (c. 10% S). It identified Kokkinovounaros as a potential deposit with 100 000 tonnes of ore with Cu at 0.5%, and Petra with a potential 350 000 t grading 6% Cu. The UNDP suggested two phases of mineralization associated with the volcanic rocks and emphasised the importance of structure in the exploration model. It recommended further detailed geological mapping at 1:10 560, especially focussing on structure and alteration, and an extension of geochemical methods of exploration. Drilling was generally on the basis of geophysical survey data, although all of the detailed gravity data are without terrain corrections. It also recommended more Induced Polarisation (IP) work. Over 52 000 Cu–Zn assays were made on drill core samples.

The UNRFNRE Project (April 1979–July 1982) focused on two areas in western Cyprus. It included geological mapping at 1:10 000 to 1:31 680, geochemical sampling and geophysics, especially IP and gravity. It drilled 63 boreholes to a cumulative depth of 6 650 m. Chip samples from 5 m intervals in these boreholes are stored at GSD. The project recognised the sea floor nature of the massive VHMS deposits and the potential for mineralized propylitic zones beneath. It also

realised that several deposits exposed at the surface contained no massive sulphides. The structural control was again emphasised. It developed the following exploration model:

- Deposits are spatially related to the trace of major faults on old rift systems.
- Deposits are focussed on these structures at intersections with cross-faults.
- Solution pathways are most likely to be the rejuvenated faults.
- Massive sulphides will only exist in Pillow Lava terrain, but disseminated ores can occur in the diabase and the extrusive rocks.
- Most favourable location for massive ores is at the Upper Pillow Lavas (UPL)–Lower Pillow Lavas (LPL) contact and at the Basal Group (BG)–LPL contact, both of which represent breaks in volcanic activity.
- A broad aureole of high metal values will occur around massive ores and can be detected by interstitial and fault gouge geochemistry.
- Dykes may contain high levels of ore metals
- Propylitic alteration beneath massive ores is likely to be relatively thin except above stockwork root zones, so that the gravity response will vary markedly.

## **4.2 GEOLOGICAL DATA**

Currently the GSD has digital geology and structure as attributed polygons and lines at scales of 1:250 000 (digitised from Bear, 1995) and 1:31 860. At the 1:31 860 scale, for this project the relevant Memoirs are 1–9 inclusive (Bagnall, 1960; Bear and Morel, 1960; Carr and Bear, 1960; Gass, 1960; Moore, 1960; Gass et al., 1994; Pantazis, 1967; Wilson and Ingham, 1959; Bear, 1960). In addition to geology and structure, these reports and maps contain valuable information on mineral occurrences, distribution of gossans and alteration.

The UNDP and UNRFNRE research programmes also include large-scale (~ 1:10 000 and smaller scale) geological maps.

## **4.3 GEOPHYSICAL DATA**

### **4.3.1 Regional surveys**

Largely because of the invasion of 1974 and the continued partition and occupation of the island, Cyprus lacks in modern national regional coverage of basic geophysical and geochemical data. There is effectively no complete island coverage of gravity data, airborne magnetic, radiometric or EM data and no regional baseline geochemical data.

1. The survey of the southern part of the island by Gass and Masson-Smith, 1951 is still the main source of regional gravity data for the Troodos region. This survey provided 770 validated gravity observations with complete terrain corrections. These data were incorporated into the GIS.
2. As part of the UNDP research programme, about 620 regional gravity observations were made along roads and tracks on the north side of the Troodos. These data have been located in GSD in gravity field book 1. As yet no location

maps for the stations have been identified. None of these data have been terrain corrected.

3. Regional magnetic data were collected by Hunting Group (HG) in 1965–66. These data included airborne total magnetic field and an EM system. Data were collected in analogue form and compiled as worksheets and the survey area covers most of the northeast Troodos region. There are a total of 21 worksheets at a scale of 1:31 680. Each worksheet has 5 maps: (i) radio altimeter, (ii) EM profiles 1, (iii) EM profiles 2, (iv) total magnetic field and (v) EM–Magnetic interpretation. Original transparent masters of these maps are held at GSD. The flight lines were orientated NE and spaced approximately 400 m apart. The flying height was approximately 100 m above ground level. These data were digitised by the Hellenic Mining Company Ltd and, after agreement about confidentiality, incorporated into the GIS
4. The Hunting Group also flew a high level barometric survey at 8 500 feet (2 591 m) above mean sea level in November 1969, in the region south of UTM grid line 3 900 kmN. This was flown on behalf of the Universities of Leeds and Princeton, supported by NERC and the US National Science Foundation. The flight lines were spaced at intervals of 1 and 3 miles (1 609 and 4828 m), but no flight line map is available. GSD has a transparent master of the compiled contours for this survey at 1:250 000. These data were not digitised nor used in the GIS
5. Digital airborne Magnetic–EM data have been collected across 5 blocks on the north side of the Troodos by Eastern Mediterranean Minerals (EMM), a consortium formed by Hellenic Mining Company Ltd. and Oxiana Resources. The flight lines were east–west and spaced 200 m apart (100 m over Skouriotissa). The flying height was 60 m with a bird at 30 m above ground level. The survey collected EM data at 5 frequencies using a Geotrex–Dighem system and total magnetic field data. The EM coil separation was 8m for 900, 5 500 and 7 200 Hz and 6.3 m for 56 000 Hz. After agreement about confidentiality, these data were incorporated into the GIS

#### **4.3.2 GSD local survey data**

GSD was involved in survey operations for both the UNDP and the UNRFNRE projects and, in addition, carried out its own ground surveys over mineral targets using IP, magnetic and gravity methods primarily, together with Turam EM. The largest part of these surveys appears to be detailed gravity data and detailed magnetic surveys. Much of the GSD IP data is Frequency Domain (FD) data, collected with a dipole–dipole array. Most of the commercial IP data collected by the Hellenic Mining Company Ltd. is Time Domain pole–dipole data.

The UNDP programme collected magnetic (38 000), gravity (23 500), EM (32 500), resistivity (4 700) and SP (260) sample point data at 80 prospects and drilled about 245 boreholes in the mineral exploration phase of the project with a total depth of 31 000 m. The prospects, survey results and mineral boreholes are referenced in a series of included maps within the report, However, these maps are based on a local grid system, with one axis representing the line number and the other axis representing the distance along the line. The line numbers started at 1 and generally increased by odd integer numbers to allow infill lines if required. The origin and bearing of these local grids is not given so that exact location of the survey data is difficult to determine. Simple descriptions of the UNDP mineral boreholes are

included in the text of the report. GSD do have the UTM grid locations of the UNDP water and mineral boreholes so that some geo-referencing of the local survey maps might be possible. There was a tendency to drill local positive gravity anomalies although none of the detailed gravity stations appear to have any terrain correction. The data were collected mostly with Worden gravity meters.

The UNRFNRE carried out IP (82 km), gravity (563) and minor magnetic surveys at about 36 sites and drilled about 60 boreholes at 11 sites. Volume two of the UNRFNRE report gives text and graphic details of the drilling. The gravity data were collected with a La Coste and Romberg Gravity meter but it is not clear if any terrain corrections were made to the data. The boreholes are located by reference to a local grid origin and a line number. These boreholes are not listed in the GSD borehole database so at present there are no accurate locations of these data. The locations of many of these boreholes can probably be captured from the set of maps supplied with the UNRFNRE report.

GSD have IP data forms and maps for 6 main survey areas:

- 1 *Troulli*: 1–72 lines of FD IP on a UTM grid collected during 1980–84.
- 2 *Lythrodontas*: Lines 01–15 collected by GSD as FD IP with 60 m dipoles, line 0–6 by HMC.
- 3 *Mathiati*: Lines 1–29 collected with FD IP at 60 and 100 m dipoles.
- 4 *Philari (Kyprovasi)*: 8 lines of dipole–dipole IP at 60 and 50 m.
- 5 *Klirou*: Dipole–dipole IP along 14 lines and one test line at 200 feet dipoles.
- 6 *Agios Ioanis*: Dipole–dipole IP at 100 feet dipoles on line 16S to L28N at 400 m line spacing.

#### **4.4 REMOTE SENSING DATA**

There are several existing structural interpretations based on satellite and photo-geology. The UNRFNRE report includes a map of West Cyprus showing main lineaments derived from satellite images and the frequency of these structures, although the map is at a small scale and is poorly referenced to a grid.

GSD have paper and possibly film masters of a lineament map derived from LandSat images by Hoppe (1979) based on a project with the German Geological Survey (BER) at Hanover. This map also indicates smaller regions that have photo-geological lineament interpretations.

For the project, Advanced Spaceborne Thermal Emission and Reflection Radiometer (ASTER) imagery were incorporated into the GIS to look for regional alteration patterns and structure.

#### **4.5 GEOCHEMICAL DATA**

Significant amounts of geochemical data (rocks, soils, fault gouge, etc) are presented in the two UN reports. However, this is held in analogue format as paper records. To get this data into a format suitable for prospectivity mapping required resources outside the scope of the current project. In addition, this data is locality–prospect specific and is not regionally extensive. Therefore, it is not of use in a regional or district prospectivity model—for this regional geochemical data, at a resolution of approximately one sample per square kilometre are required.

Along with the geophysical data described above, Eastern Mediterranean minerals also supplied extensive geochemical data spatially resolved and in digital format. These comprised a regional data set comprising over 1000 samples

The analysis and results of the geochemical data are discussed in Chapter 6.

## 5 Alteration mineralogy and putative epithermal-style mineralization

### 5.1 BACKGROUND INFORMATION AND INTRODUCTION

Recent reinvestigations of Au-rich sulphide deposits by Eastern Mediterranean Minerals (EMM) prompted the suggestion that their genesis may be more akin to epithermal style mineralization (Maliotis and Herzig, 2000; Nillos and Elipane, 1998; Nillos et al., 1998a; Nillos et al., 1998d; Nillos et al., 1998b). This was based on the high Au content of the deposits, which show elevated gold grades averaging up to 13.5 ppm at Tourounjia (Nillos et al., 1998d) and 10.7 ppm at Alestos (Maliotis and Herzig, 2000). In addition, brecciation associated with mineralization is interpreted to be of explosive hydrothermal origin. As the alteration assemblages found in typical Cyprus-type VHMS deposits are markedly different from the alteration commonly linked to epithermal mineralization it should be possible to compare, using techniques such as portable infrared mineral analysis (PIMA) and X-Ray diffraction to compare and contrast the alteration found at typical Cyprus VHMS mineralization with the putative epithermal style deposits. To test this five deposits (Figure 15) were subject to an alteration study using PIMA and XRD. The supposed epithermal deposits (Kokkinovounaros, Papoutsi, Alestos and Tourounjia) were analysed and compared to the alteration found in the Agrokipia B orebody, which is interpreted as a typical Cyprus-type VHMS deposit. XRD analysis was undertaken at two of these deposits—Tourounjia and Alestos—with the highest gold grades.

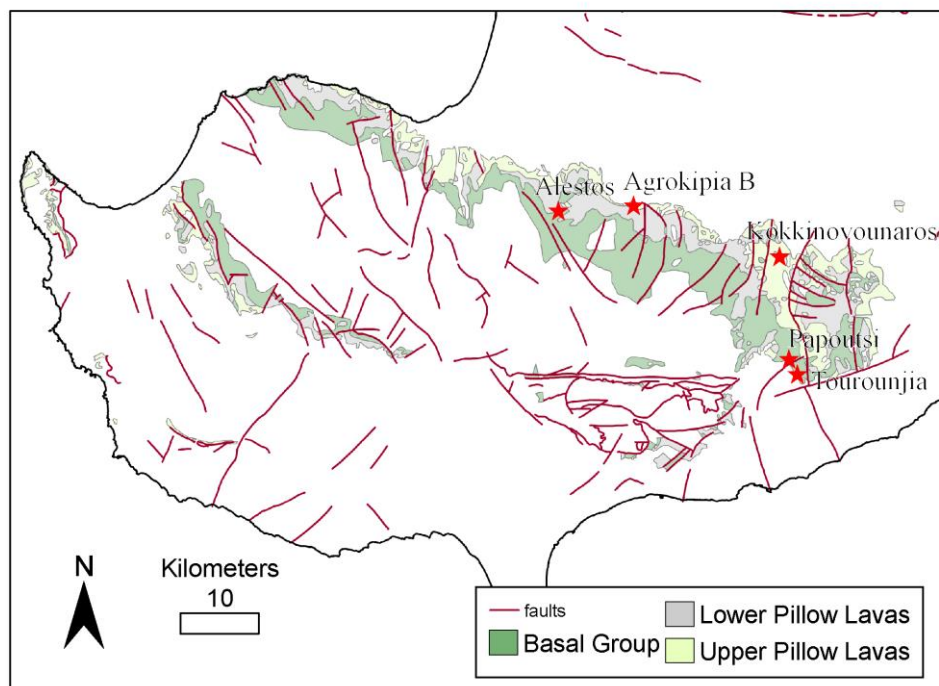


Figure 15 A map of south-west Cyprus showing the locations of the five deposits in relation to lithologies.

PIMA spectra were collected from drill-core material (either diamond or reverse circulation) and compared with spectral measurements from the CY-2a borehole that intersects the Agropia B orebody. The assay data used to support the findings were provided by EMM (Kokkinovounaros, Papoutsi, Alestos and Tourounjia) and Bednarz et al., 1987 (Agropia B).

Below, the geological background relevant to the epithermal-style VHMS deposits on Cyprus is described. A description of how the PIMA can distinguish alteration minerals is also included and the materials and methods used in this study are explained. The results obtained from the spectral and geochemical analysis are discussed within a framework that relates observed alteration to the genesis of the deposits.

## **5.2 BACKGROUND ALTERATION OF THE TROODOS OPHIOLITE**

The Troodos ophiolite lacks a pervasive emplacement-related metamorphic sole found in most ophiolites, which means that even the low temperature alteration has been preserved. Gillis and Robinson, 1990b identified five distinct alteration zones in the Troodos ophiolite based on mineralogical, geochemical and hydrologic characteristics. These zones have been interpreted to represent a seafloor-weathering zone, a low temperature zone, a transition zone, an upper dyke zone and a mineralized zone. The alteration zones generally display a consistent vertical pattern although they are laterally discontinuous.

The seafloor-weathering zone is characterised by pervasive oxidative alteration with abundant calcareous sediment between the pillows. The pillow margins and interpillow hyaloclastite are pervasively altered to mixtures of green smectite, Fe-hydroxide, phillipsite, analcime and calcite (Gillis and Robinson, 1990b).

The low temperature alteration zone is distinguished from the seafloor-weathered zone by non-pervasive alteration. The volcanic glass is variably altered to smectite, phillipsite and analcime. Zones of intense weathering frequently occur along the edges of massive flows and are represented by celadonite, mixed with smectite, clinoptilolite, mordenite and calcite (Gillis and Robinson, 1990b).

The transition zone displays a mixture of characteristics shown in the overlying low temperature zone and the underlying upper dyke zone. The upper boundary of this zone is marked by the presence of laumontite and quartz and the lower boundary is defined by the dominance of chlorite, quartz and pyrite.

The mesostasis of the upper dyke zone is recrystallised to chlorite and quartz with occasional pyrite and patchy epidote. Zones of intense alteration are marked by the development of epidotes.

The mineralized zone refers to the massive sulphide deposits, mineralized stockwork zones and smaller zones of mineralization (Gillis and Robinson, 1990b). The mineralized zones can be further subdivided into three types and more detailed information about the alteration underlying the Cyprus massive sulphides is given below.

## **5.3 ALTERATION ASSOCIATED WITH VHMS DEPOSITS**

Three different styles of alteration affecting the stockworks and alteration pipes in the footwall of the Cyprus massive sulphide deposits are recognised (Richards et al.,

1989). These have been named P-type, K-type and M-type after the type localities Pitharokhoma, Kokkinopezoula and Mathiati respectively (Table 8). All three types of pipes exhibit similar peripheral alteration although the alteration assemblage of the central zones, corresponding to higher water–rock ratios, varies.

The outer alteration zones of all three types of deposit are characterised by smectitic and chlorite–smectite mixed layer facies. This often grades into a chlorite–albite facies, which is characterised by the assemblage chlorite, albite, quartz and sphene. These peripheral alteration zones are enriched in Mg and Na but generally depleted in Ca, K, Rb and Ba.

The smectitic facies is indistinguishable from the relatively widespread low temperature alteration that affects the volcanics. This alteration is believed to be later than the alteration associated with mineralization.

The chlorite–smectite mixed layer facies forms a distinct halo around the mineralized zone but is itself unmineralized. This zone is characterised by the variable alteration of plagioclase to albite and almost complete alteration of mesostasis to various chlorite-smectite mixed layer minerals and occasionally discrete phases of chlorite and/or smectite. The inner zone of the chlorite-smectite facies shows complete albitisation of plagioclase, an increase in the abundance of discrete chlorite and groundmass quartz, and the development of sphene at the expense of Fe-Ti oxides (Richards et al., 1989).

The chlorite-albite facies commonly forms inside the chlorite-smectite alteration zone and is represented by the almost complete alteration of the primary phases to chlorite, albite, quartz and sphene. This zone is relatively unmineralized and disseminated pyrite generally occurs only in the pillow margins. In the pillow interiors the primary igneous texture is well preserved. The plagioclase is often replaced by albite and the mesostasis is altered to chlorite and quartz (Richards et al., 1989).

The outer alteration zones for all three types of pipes are similar but the inner alteration assemblages vary.

### **5.3.1 P-type pipes**

P-type pipes are characterised by the presence of a chlorite-illite facies and often have a leached core. These zones represent the most intensely altered areas of the pipe.

The chlorite-illite facies is defined by the presence of both chlorite and illite. Chlorites are more Mg-rich than those of the chlorite-albite facies and pillow margins are frequently very friable and show no primary igneous texture apart from relict vesicles. The pillow interiors display the alteration of plagioclase to illite and quartz and the replacement of the mesostasis with chlorite and quartz. Clusters of anatase occur and commonly pseudomorph Fe-Ti oxides. Also pyrite occurs as subhedral to euhedral crystals and thin sub-millimetric veins. However, the majority of the pyrite occurs in the inner regions of this zone in the fine-grained interpillow material and is associated with quartz.

The leached facies is represented by the total alteration of the lava to the assemblage illite, quartz, pyrite and anatase. The alteration minerals have largely overprinted the original igneous textures and replaced primary minerals. The interiors of the pillows are very low density, white, soft and porous compared to the surrounding, less

altered lavas. The pillow margins are silicified but still friable. This zone generally contains the highest mineralization with pyrite contents occasionally exceeding 40 % in the pillow margins and vein aureoles (Richards et al., 1989).

### 5.3.2 K-type pipes

The K-type pipes are similar to the P-type pipes and intermediate pipe-types have been found. The inner zone of the K-type pipe is represented by a chlorite-rectorite facies instead of the chlorite-illite facies recorded in P-type pipes. The majority of the rectorite forms in the place of plagioclase and chlorite plus quartz replace the mesostasis. The chlorite compositions and bulk rock geochemistry are very similar to those seen in the chlorite-illite facies. However, as rectorite forms at lower temperatures (100–230 °C) than the main mineralizing temperatures (c. 300 °C) it is inferred that the K-type pipes result from low temperature overprinting of P-type pipes (Richards et al., 1989)

### 5.3.3 M-type pipes

The absence of illite or rectorite from the central zone of the M-type pipes distinguishes them from P and K-types. The central zone comprises the assemblage chlorite, quartz, pyrite and anatase and is referred to in the literature as chlorite-quartz-pyrite facies alteration. In addition, the chlorite is more Fe rich than corresponding chlorites in the other two pipe types (Richards et al., 1989).

Facies	Layer silicates	Other minerals
Smectitic facies <b>P, K, M</b>	Smectite* (generally saponitic and including phases with up to 20% chlorite)	Fe hydroxides, quartz, zeolites (Ca plagioclase, pyroxene, Fe-Ti oxides)
Chlorite-smectite mixed layer facies <b>P, K, M</b>	Chlorite*/smectite mixed layer minerals with over 20% chlorite and usually showing 1:1 ordering	Albite, quartz, sphene, pyrite (Ca plagioclase, pyroxene, Fe-Ti oxides)
Chlorite-albite facies <b>P, K</b>	Chlorite*	Albite*, quartz*, sphene*, pyrite (Ca plagioclase, Fe-Ti oxides)
Chlorite-illite facies	Chlorite*, illite*	Quartz*, pyrite*, anatase*
Leached facies <b>P</b>	Illite*	Quartz*, pyrite*, anatase*
Chlorite-rectorite facies <b>K</b>	Chlorite*, rectorite* or similar hydromica-smectite mixed layer phase	Quartz*, pyrite*, anatase*
Chlorite-quartz-pyrite facies <b>M</b>	Chlorite*	Quartz*, pyrite*, anatase*

Table 8 A table summarising the alteration assemblages of the alteration facies associated with P, K and M-type pipes. Letters in bold indicate the alteration pipe style in which this facies occurs. \* indicates that the mineral is always present. (Modified from Richards et al., 1989).

## 5.4 EPITHERMAL ORE DEPOSITS

Nowadays the term epithermal ore deposit has a narrow implication and is generally applied to ore deposits that formed from large-scale hydrothermal convection systems driven by magmatic heat, which are generally associated with subaerial volcanism and intrusion of calc-alkalic magmas. Two main styles are recognised—low sulphidation (also known as adularia–sericite) and high sulphidation (also referred to as gold–alunite or alunite–kaolinite) (Cooke and Simmons, 2000).

Low sulphidation epithermal mineralization precipitates from fluids that are predominantly of meteoric origin with a magmatic volatile source for the sulphur and carbon. The meteoric fluids percolate downwards and are heated up by proximity to an intrusion. The fluids are then channelled up a structural discontinuity in similar ways to the fluids that form VHMS deposits. There is strong evidence for fluid boiling in low sulphidation epithermal systems, which is interpreted to be the cause of metal deposition.

The alteration mineral assemblages indicate that mineralizing fluids are of near neutral pH composition with  $H_2S$  as the dominant sulphur species (Cooke and Simmons, 2000). Boiling of the fluids commonly produces advanced argillic alteration and silicification in a zone above the site of ore deposition as the acidic vapour phase condenses.

The fluids associated with high sulphidation epithermal mineralization are predominately magmatic in origin and have oxidising and acidic compositions. The major sulphur species is  $H_2SO_4$  with only minor  $H_2S$ . These are supplied by the disproportionation of magmatic  $SO_2$ . Most high sulphidation epithermal deposits contain two-phase (liquid and vapour) fluid inclusions, although most workers do not interpret boiling as an important depositional mechanism (Cooke and Simmons, 2000).

It is generally accepted that rising magmatic fluids and gases mix with meteoric water and form an acidic fluid that causes intense acid leaching and the development of advanced argillic assemblages.

The advanced argillic alteration that commonly hosts the ore is characterised by alunite, kaolinite, dickite, pyrophyllite and diaspore. This alteration zone commonly grades out into argillic assemblages dominated by mixed layer smectite-illite and then to a pyrolytic alteration zone (Gunn and Rollin, 2000).

### 5.4.1 Epithermal-style gold deposits in VHMS districts

Since the late 1980s Au-rich VHMS deposits have been recognised and received a relatively large amount of attention. The Au-rich deposits can generally be split into three groups depending on whether the Au is associated with Cu or Zn or pyrite. The Au-Cu association (also referred to as high sulphidation by Sillitoe et al., 1996) is commonly coupled to advanced argillic alteration assemblages and are inferred to have formed from acidic, high temperature ( $>300^\circ C$ ), oxidising fluids. The Au-Zn rich types (also known as auriferous polymetallic deposits) are associated with K-feldspar or carbonate alteration and are interpreted to have formed from lower-temperature ( $\sim 200^\circ C$ ), near-neutral fluids. The deposits that do not fit into the two groups outlined above are referred to as pyritic Au deposits, as the Au is concentrated in pyritic zones (Poulsen and Hannington, 1995). The following discussion will focus on the Au-Cu metallogenic assemblage.

Au-Cu deposits have been identified in Japan, Fiji, Indonesia, Sweden, Turkey, Wisconsin, Alaska, Quebec, Queensland and Tasmania. The Au-Cu association in modern black smokers was not discovered until 1993 but has since been identified at Logatchev hydrothermal field (Mid-Atlantic Ridge), Hine Hina (Valu Fa Ridge, Lau Basin) and Pacmanus and Suzette (Eastern Manus basin) (Huston, 2000).

The Au-Cu alteration assemblages include quartz, kaolinite, pyrophyllite, diaspore, alunite, barite and native sulphur. This commonly grades out to intermediate argillic and then to chloritic alteration. The deposits that exhibit this advanced argillic style alteration all appear to be in Kuroko type VHMS deposits. The modern black smokers listed above are active near oceanic spreading centres analogous to those that formed the Troodos ophiolite. The Hine Hina hydrothermal field occurs at depths of 1,850 to 2000 m. Furthermore, it is well below the depth of boiling for normal seawater and the acidic fluids probably result from the condensation of magmatic volatiles into circulating seawater (Sillitoe et al., 1996).

## **5.5 GEOLOGY OF THE STUDIED PROSPECTS**

### **5.5.1 Agrokipia B**

The Agrokipia B orebody is hosted by the Lower Pillow Lavas and displays an asymmetrical pyramidal shape 150 m high and 150 m wide. It is located on the Agrokipia Fault, which strikes roughly northwest and offsets the orebody (Malpas, 1987). It is underlain by medium to fine-grained basalts that are interpreted as dikes. The contact between this unit and the overlying lithologies of the orebody is represented by a thin fault breccia (Robinson and Gibson, 1987). Immediately above the fault breccia is a 15 m thick zone of highly brecciated, altered and bleached basalt with many zones of red jasper. The rocks are pervasively bleached and variably replaced by mixtures of argillic material, grey silica, jasper and quartz. This zone is weakly vesicular and sporadically veined with infills of both consisting of quartz and pyrite (Robinson and Gibson, 1987).

The overlying lithology is a 127 m thick unit of highly altered massive lava flows, the protolith to this is interpreted to be alternating layers of crystalline basalt and massive glass. The original groundmass of this unit is pervasively replaced by cream coloured argillic material, quartz, pyrite and minor sphalerite. Above the highly altered basalt is a 5m thick unit representing a single lava flow that is relatively unaltered but contains veins of argillic and zeolitic material. This is the stratigraphically highest lithology to show evidence of hydrothermal alteration.

The rocks overlying the hydrothermally veined basalt retain layers of fresh glass intercalated with layers of massive crystalline basalt. The origin of this lithology is interpreted to be similar to that of the highly altered basalt, although it has remained unaffected by hydrothermal alteration (Robinson and Gibson, 1987).

### **5.5.2 Kokkinovounaros**

The Kokkinovounaros prospect is located in the northeastern part of the Troodos ophiolite. The Romans carried out small-scale underground gold mining in ancient times, but modern extraction began in the 1930s with the north-trending adits following the gold-rich bleached zone. Here grades averaged 6 ppm Au (Hedenquist, 2000). The workings were subsequently enlarged to form a small open pit operation (Nillos and Elipane, 1998). Records of the gold analyses from the open

pit operation in 1937 show average values of 8.8 ppm Au and 56.9 ppm Ag (Maliotis and Herzig, 2000).



Figure 16 A photograph looking south at the bleached mill breccia that was mined during the 1930s.

The Kokkinovounaros prospect is hosted by the Lower Pillow Lavas, which locally dip gently towards the northwest. The lavas are massive, brecciated, fractured or jointed and pillow structures are occasionally discernable. The mineralization occurs in the brecciated, fractured and jointed volcanics where it is commonly associated with jasper or sometimes calcite-gypsum stockworks (Nillos and Elipane, 1998).

The excavated area is centred on a ~10 m wide, NNW trending, sub-vertical breccia that extends for around 100m. This area contains highly bleached sub-angular to angular clasts of vesicular volcanics supported in a rock flour matrix (> 50%). The bleaching is accompanied by a yellow halo, probably jarosite, which often forms veins extending beyond the breccia boundary (Nillos and Elipane, 1998). The brecciation is interpreted to be tectonic in origin and was subsequently mineralized. In addition, it is suggested that the breccias formed in a sub-aerial environment and interpret the mineralization to be of either high or low sulphidation epithermal origin (Nillos and Elipane, 1998). However, the brecciation has been described as explosive (Maliotis and Herzig, 2000).

The main breccia zone is bound to east and west along its length by a clast-supported breccia—to the east of this zone it is ~2m wide, but on the west it extends for ~15m. It is composed of highly bleached sub-rounded to rounded clasts with an interstitial rock flour matrix (Nillos and Elipane, 1998).

To the west of the main breccia zone is an extensive northwest trending jasper stockwork around 50 m wide and 200 m long. Bleaching decreases westward and the stockwork grades into locally silicified massive and fractured basalt. To the eastern side, the host rocks to the breccia comprise a zone of jointed volcanics with calcite-gypsum infills. The amount of calcite-gypsum infilling decreases towards the east (Nillos and Elipane, 1998).

To the south of the excavated area is an extension of the system that was discovered and drilled in the 1960s. This area is approximately six times the size of the original Kokkinovounaros prospect but was not investigated in this report.

### 5.5.3 Papoutsi

The Papoutsi prospect is located approximately 2 km east of the village of Kato Lefkara and around 3 km northwest of the Tourounjia prospect and was utilised for gold extraction in ancient times. Slag dumps in the vicinity led the Hellenic Mining Company to explore the area in the 1930s (Nillos et al., 1998b). Several of the exploration pits exploited gold in layers averaging 27 ppm Au (Hedenquist, 2000) and mineralization appears to be confined to a northeast trending jasper-jarosite vein, which is located entirely within the mafic volcanism (Nillos et al., 1998b).

Two rock types occur in the area. A cherty-marlstone of the Lefkara Formation unconformably overlies fine to medium-grained, locally vesicular mafic volcanics. Alteration has a strong structural control and areas of slight to moderate silicification occur with fracture filling saccharoidal to crustiform quartz. In the southwest a calcite  $\pm$  quartz stockwork is developed (Nillos et al., 1998b).

The mineralized jasper-jarosite vein is around a metre wide and is bound on its hanging wall by the fractured and silicified volcanics while the footwall is comprises volcanic-hosted calcite stockwork (Nillos et al., 1998b).

### 5.5.4 Alestos

The Alestos prospect, located on the northern flank of the Troodos ophiolite, is part of a circular 3 km diameter hill rising 300 m above its surroundings. It was discovered in 1938 when high concentrations of gold prompted small-scale surface mining. Records of the Hellenic Mining Company show that the small open pits and trenches operated at an average grade of 10 ppm Au (max. 309 ppm) and 10.7 ppm Ag (max. 112.5 ppm) (Maliotis and Herzig, 2000).



Figure 17 Photograph looking east at the open cast pit that was mined at the end of the 1930s. Alestos hill rises to the north.

Fluid inclusion data (Janissen, 1988) show an early widespread high-temperature fluid (340–360°C) was responsible for VHMS mineralization. This was subsequently overprinted by a cooler phase (260–290°C) centred on the inner deposit area. The salinity of the fluids ranges from 2.8–5.4 wt %. Salinities less than seawater may indicate that the fluids boiled.

The deposit is hosted by the upper Pillow Lavas (Nillos et al., 1998a). Adjacent to the main workings (Figure 17) is a roughly circular, 70 m diameter, outcrop of quartz breccia (Figure 18), which consists of angular quartz clasts with an interstitial quartz-chalcedony matrix. It has very fine-grained disseminated pyrite and possible magnetite (Nillos et al., 1998a). The presence of pyrite suggests that bleaching is hypogene (Hedenquist, 2000). The EAD-2 drill hole suggests that this area is underlain by a quartz-magnetite stockwork. The quartz-breccia is interpreted to be a fault-generated breccia-pipe complex (Nillos et al., 1998a).



Figure 18 A photograph of the quartz-breccia showing the sub-angular to rounded clasts supported by an Fe-rich silicic matrix.



Figure 19 A close up photograph of the quartz-breccia as it grades into the hematite–quartz–jasper breccia. Note the sub-rounded variably altered clasts.

The quartz breccia grades outwards into a hematite–quartz–jasper brecciated pillow lava (Figure 19), which is largely composed of < 60 cm pillows with the interstitial material being similar fine-grained volcanics. The rock mass is highly silicified,

moderately chloritised and held in a fine quartz-veined stockwork (Nillos et al., 1998a). The intensity of stockworking and silicification decreases outwards.

### 5.5.5 Tourounjia

Tourounjia, a gold prospect, with no massive sulphide zone, is located on the eastern flank of the Troodos ophiolite and was mined from the surface in ancient times. It was investigated by the Hellenic Mining Company in the 1930s and around 50 exploration pits and relatively extensive percussion drilling indicate the gold mineralization to be largely confined to two types of breccia with average Au values of 5.6 ppm, which locally increase to 10.7 ppm in opal layers (Maliotis and Herzig, 2000). The highest gold grades, at an average of 13.5 ppm, occur in breccias comprising silicified volcanics in a silica matrix (Figure 20). Breccias with silicified clasts in a rock flour/jarositic matrix have lower grades (2.5 ppm—Nillos et al., 1998c).

Mineralization is hosted in the upper part of the basal group, near the unconformable boundary with the overlying marlstone of the Lefkara Formation. The sediments dip gently and thicken towards the WSW (Nillos et al., 1998c). The volcanic rocks of the area are fine to medium grained basalt to diabase and are highly bleached near the boundary with the Lefkara Formation (Nillos et al., 1998c). Towards the east, the bleached zone decreases intensity and grades into a highly silicified zone followed by a zone of chloritisation and finally a zone with calcite fills along fractures and joints.

A map of the deposit, modified after Nillos *et al.* (1998) is attached in Figure 21. The prospect consists of an upper zone of silicified breccias, which show the highest gold values. Underlying this is a zone of intense argillic alteration with minerals of the kaolin group. Outside the argillic zone, propylitic alteration is quite extensive containing abundant chlorite and some pyrite. Silicification is intense in the breccias but also extends into the surrounding volcanics. Silicification is also seen as banded opaline silica. The alteration is highlighted in Figure 22.

The mineralized breccias at Tourounjia consist of two units. The Volcanics Breccia; (Nillos *et al.* 1998) and brecciated, silicified clasts of this breccia, within a silicified matrix, termed the Silica Volcanics Breccia (Nillos *et al.* 1998). These units form a continuous sheet that extends to the west under the overlying cherty-marlstone. The Silica Volcanics Breccia appears to be the core to this sheet, grading out into Volcanics Breccia. Here, the Volcanics Breccia is interpreted to be a hyaloclastite (Thomas, 2005), formed above a lava flow due to quenching by seawater. This highly permeable hyaloclastite appears to have been utilised as a conduit for the mineralizing fluid, during which time a high degree of silicification occurred. Less intense silicification is seen in the less permeable, underlying bleached volcanics. The silicification affected the clasts of hyaloclastite as well as forming a matrix of amorphous silica between the clast. Blocks of the Volcanics Breccia can be found within a further silicic matrix, in the Silica Volcanics Breccia. This is interpreted to form where episodic hydrothermal brecciation occurs, with silicification and mineralization continuing throughout.

The breccias occur within the bleached zone at the intersection between older, presumably ridge-parallel, northwest trending graben faults and younger northeast trending sinistral faults.



Figure 20 A photograph of a boulder of the silica volcanics breccia. The clasts are sub-angular to rounded and supported in a silicic matrix.

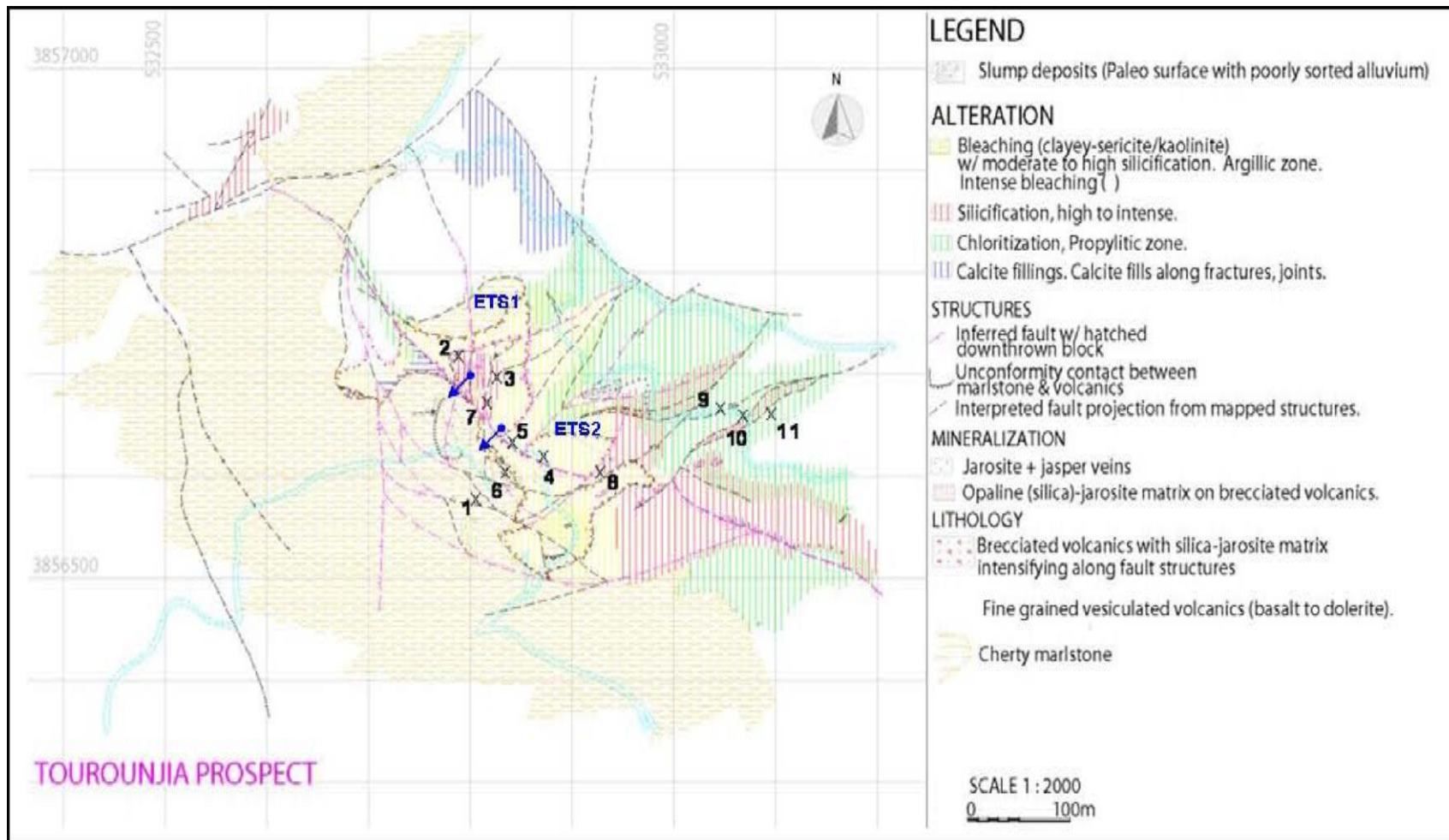


Figure 21 Geological map of Tourounjia with the locations of samples shown as black crosses with numbers. Drill collars shown with blue circles, plunge directions shown with arrows. (From Osborn, 2004).

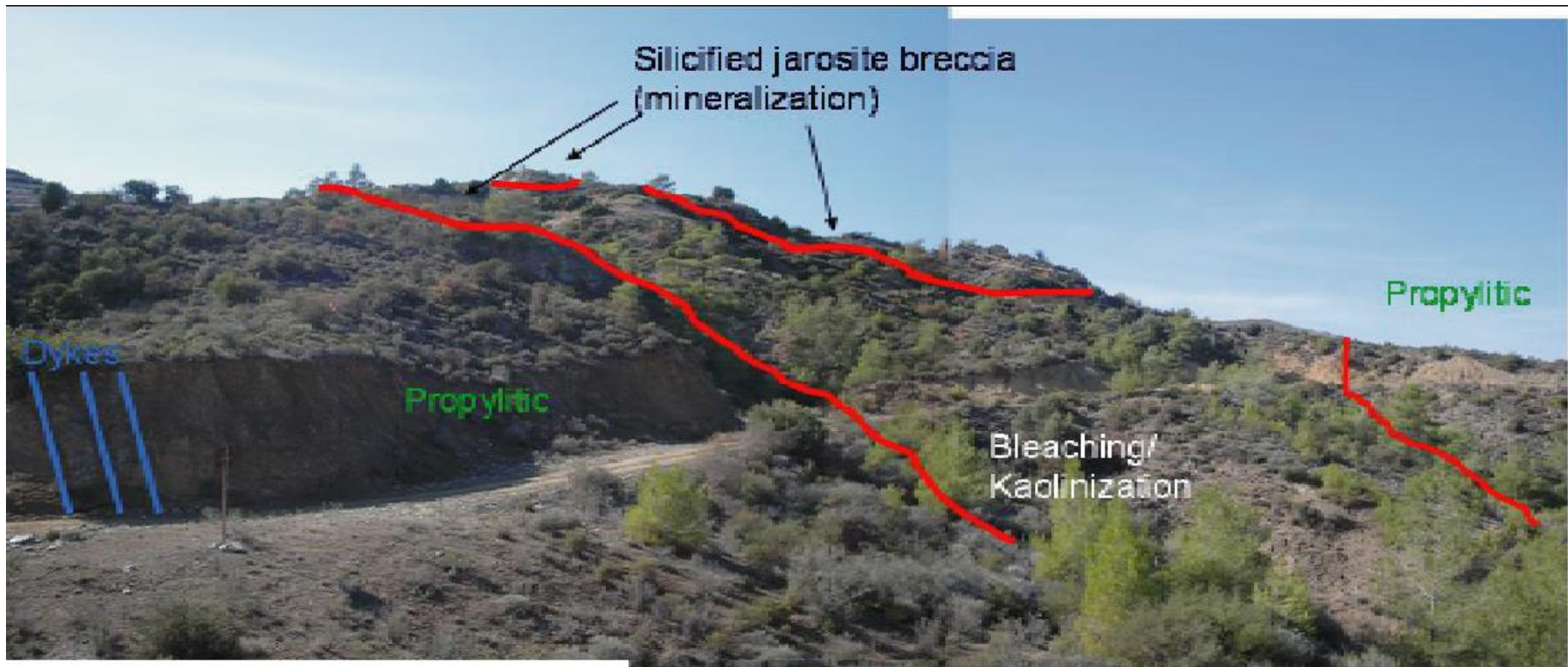


Figure 22 View of Tourounjia looking west.

## 5.6 PORTABLE INFRARED MINERAL ANALYSER (PIMA)

### 5.6.1 Background

The Portable Infrared Mineral Analyser (PIMA) is small shoebox-sized instrument. It is mains or battery powered and spectra are recorded onto a small palmtop or laptop computer. It can be used to analyse many types of samples including diamond drill core, RC and RAB chips, outcrops and soils. Very little sample preparation is needed and each spectral measurement takes between 30 and 60 seconds. The PIMA uses an internal light source to emit light in the short wavelength infrared range (SWIR) onto the surface of a sample. An area of 10mm by 2mm is monitored using a laboratory class spectrometer to measure the amount of light reflected over the range of wavelengths.

The SWIR spectral range is useful for the investigation of alteration minerals as it picks up absorption features attributed to OH, H<sub>2</sub>O, CO<sub>3</sub>, NH<sub>4</sub>AlOH, FeOH and MgOH molecular bonds. The affected molecular bonds may be found in a range of mineral groups including phyllosilicates (including clay, chlorite and serpentine minerals), hydroxylated silicates (such as epidotes and amphiboles), hydrated sulphates (such as alunite, jarosite and gypsum), carbonates and ammonium bearing minerals (Pontual et al., 1995).

#### 5.6.1.1 MINERAL IDENTIFICATION

Although the whole spectrum is important, mineral identification is based on characteristic absorption at or near specific wavelengths. The majority of different silicates may be distinguished in SWIR due to vibrational transitions associated with hydroxyl plus water near 1400 nm and water near 1900 nm. The bending and stretching of the bonds between Al-OH, Fe-OH and Mg-OH are also important diagnostic absorption features and occur at or near 2200, 2250 and 2330 nm respectively.

The sulphates are relatively easy to distinguish from the silicates as they have diagnostic OH absorptions that are quite different from those of the silicates. The carbonates display significantly different spectra and contain a strong diagnostic absorption feature between 2300 and 2350 nm (Pontual et al., 1995). The wavelengths of the absorption features are shown in Figure 23

The spectral analysis software—*The Spectral Geologist*—can attribute the spectra to a mixture of up to three minerals and provide a semi-quantitative although often unreliable estimate of their relative abundances. The software also gives an estimate on the reliability of the mineral identification.

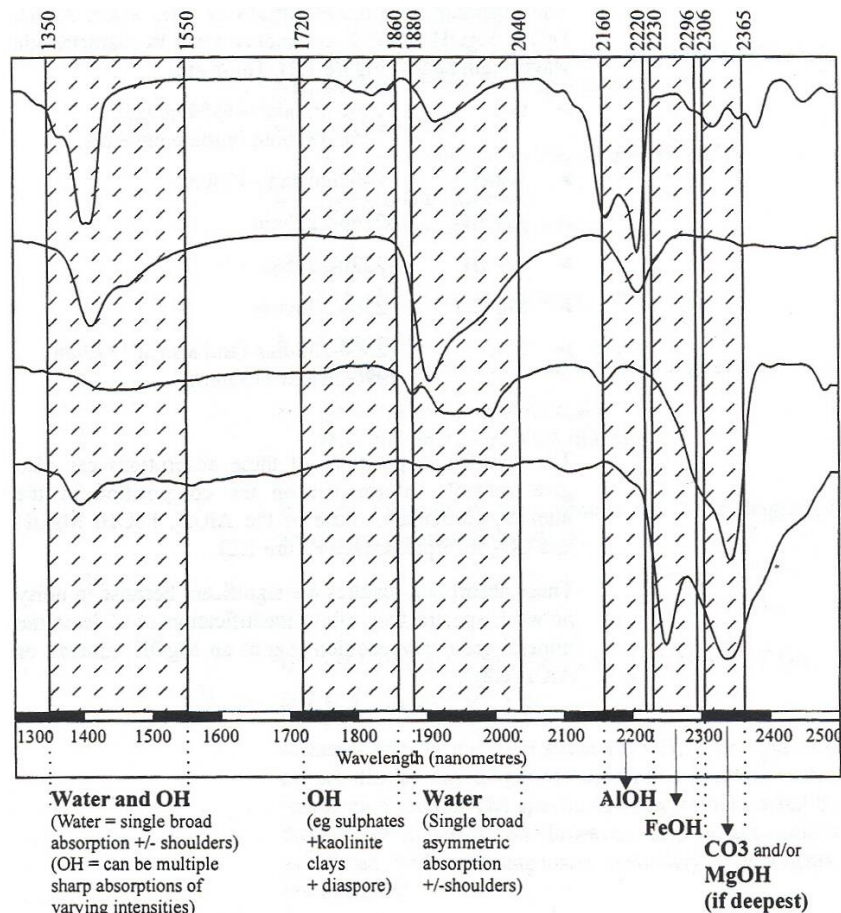


Figure 23 A plot showing the major spectral absorption bands in SWIR from which the minerals producing the spectra can be identified (Modified from Pontual et al., 1997b).

### 5.6.1.2 CRYSTALLINITY AND COMPOSITIONAL VARIATIONS

The PIMA can also provide qualitative information on the degree of crystallinity of a mineral. The variations in crystallinity may have been brought about by temperature and chemical variations within an alteration system and can be used to delineate these zones or distinguish weathering from alteration-related clays.

The shapes of the diagnostic absorption features reflect variations in the crystallinity and typically sharpen up with increasing crystallinity. This function may be parameterised in a similar way to the crystallinity indexes used in XRD (Fraser et al., 1990; Pontual et al., 1995).

The spectra measured by the PIMA can also be used to distinguish compositional variations within mineral groups. The composition of an alteration mineral in a hydrothermal system may vary systematically as a function of temperature and composition of the altering fluids, fluid to rock ratios and the proximity to mineralized zones. The systematic variation of mineral compositions is a useful parameter, as mineralization–alteration relationships may be evaluated and alteration zones may further be delineated to allow positioning of oneself within the system and producing vectors towards zones of increased alteration (and therefore possible increased mineralization).

The compositional variations are represented by slight shifts in the wavelengths of diagnostic absorption features although the overall spectral signature remains largely unchanged.

## 5.7 RESULTS OF THE PIMA INVESTIGATION

### 5.7.1 Mineral identification overview

Fe-rich chlorite, Mg-rich chlorite, intermediate chlorite, illite, montmorillonite, epidote, gypsum, muscovite, phengite, paragonite, biotite, Mg-clays, palygorskite, gypsum, jarosite, epidote, calcite, ankerite, zoisite, halloysite, kaolinite, dickite and nacrite were identified by the PIMA. Of these minerals chlorite and illite are important primary alteration minerals in terms of classifying the alteration zones into the P and M-type pipes. The identification of kaolinite, dickite and nacrite is also important as these indicate acidic alteration. Chlorite is the most common mineral to be found in this study and it shows significant variations in composition within the deposits. Illite is a common primary alteration mineral although it is most frequently found as the second most abundant alteration mineral in the samples. Lastly, kaolinite, dickite and nacrite were found to be very abundant in the two boreholes from Tourounjia and dickite was recorded in three samples from Alestos.

### 5.7.2 Data presentation

In total, data were acquired from six boreholes: One each from Agrokipia B, Alestos, Kokkinovounaros and Papoutsi plus two from Tourounjia (Table 9).

Deposit	Borehole	Type	Investigated interval (m)	Sampling interval (m)	Borehole log
Agrokipia B	CY2A	Diamond	140–306	variable	Figure 24
					Figure 25
Alestos	EAD-2	Diamond	0–100	6 <sup>¶</sup> and 3 <sup>#</sup>	Figure 28
					Figure 29
Kokkinovounaros	ERD-2	Diamond	0–100	5 <sup>¶</sup> and 2 <sup>#</sup>	Figure 26
Papoutsi	EPS-2	Reverse circulation	0–85	2	Figure 27
	ETS-1	Reverse circulation	0–75	2	Figure 31
Tourounjia	ETS-2	Reverse circulation	0–75	2	Figure 30

<sup>¶</sup>sampling interval in non-mineralized zones; <sup>#</sup>sampling interval in mineralized zones

Table 9 Summary of investigated boreholes, showing type of core, amount of core analysed, sampling intervals and reference to borehole log Figures .

The PIMA mineral identification software—*The Spectral Geologist*—characterises the analysed spectra in terms of the two most abundant SWIR sensitive minerals, gives an approximation of their relative abundance plus an indication that the identifications are correct. The data are illustrated as a sequence of down-hole logs (Figure 24 to Figure 31) that compare alteration mineral identifications with geological geochemical and geophysical information and where appropriate qualitative information on chlorite composition and kaolinite crystallinity are also given. A guide to the headings in each of the borehole logs is given in Table 10.

<b>Mineral identification</b> <i>Headings: Mineral 1 and Mineral 2</i>	<b>Relative abundance</b> <i>Heading: Mineral 1 weight</i>
<i>The Spectral Geologist</i> software can identify up to two minerals with the most abundant mineral referred to here as Mineral 1 and the less abundant mineral referred to as Mineral 2	<i>The Spectral Geologist</i> software produces a semi-quantitative estimation of the relative abundance of Minerals 1 and 2. It is based on the relative contribution that each mineral makes to a spectrum. A value of 1 means the spectrum is entirely accounted for by Mineral 1 and a value of 0.5 indicates that the spectrum is produced by equal mixes of Minerals 1 and 2
<b>Identification certainty</b> <i>Heading: Identification certainty</i>	<b>Compositional and crystallinity parameters</b> <i>Headings: FeOH, MgOH &amp; K1/K2</i>
The identification error is a value produced by <i>The Spectral Geologist</i> software that attempts to quantify the certainty of mineral identification. A high value indicates that the identification cannot be totally relied upon. High identification error values are produced when there are more than two alteration minerals making a significant contribution to a spectrum or when the absorption features are either very weak or obscured by noise. Weak spectral features can be produced when there is a relatively low abundance of the minerals that vibrate in SWIR. Noisy spectra are also produced when there is a high abundance of sulphides, a large gap between the sample and the measurement window or the sample is dark. Where the identification error is too high for any minerals to be reliably identified, Mineral 1 in the downhole logs is represented as <i>NULL</i>	The composition of chlorite is indicated by the wavelengths of the FeOH and MgOH absorption features. In the logs, these are headed FeOH and MgOH and the scale is in nanometres. With increasing iron content the FeOH feature in chlorite increases in wavelength and the MgOH shows a corresponding decrease. An increase in FeOH from 2250 to 2260 equates approximately to a decrease in Mg# from 0.8 to 0.2. The K1/K2 is the ratio between the intensities of the AlOH absorption features at 2206nm (K1) and 2162nm (K2). This ratio provides information on the crystallinity of kaolinite with larger ratios generally equating to less crystalline kaolinite. <i>Note:</i> this parameter is only shown for the Tourounjia boreholes
<b>Geophysical information</b> <i>Heading: Magnetic susceptibility</i>	<b>Geochemical parameters</b> <i>Headings: Au (ppm), Ag (ppm), As (ppm), Pb (ppm), Cu (ppm), Zn (ppm), Mn (ppm)</i>
The magnetic susceptibility is a unit-less parameter comparing the Earth's magnetic field and the induced magnetic field of the sample. It is commonly referred to as the k-value. The results shown in the downhole logs are 100 times their true value to decrease the need to use very small numbers. The magnetic susceptibility of the samples was taken to provide a semi-quantitative indication of the extent of alteration. The magnetic susceptibility of a rock usually depends on its magnetite content and generally decreases in altered basalts as magnetite is oxidised to hematite or removed completely. The range of k values of unaltered basalts is 0.1 to 10 (Milsom, 1989).	For comparison geochemical data (Au, Ag, Pd, Cu, Zn & Mn) are presented as downhole barcharts. Data were derived from EMM assay information for boreholes from Tourounjia, Alestos, Papoutsi and Kokkinovounaros. Data for Agrokippia B are from Bednarz et al., 1987, but only includes Cu, Pb and Zn as there are no information for Au, Ag and Mn.

Table 10 Key to headings in borehole logs given in Figure 24 to Figure 31.

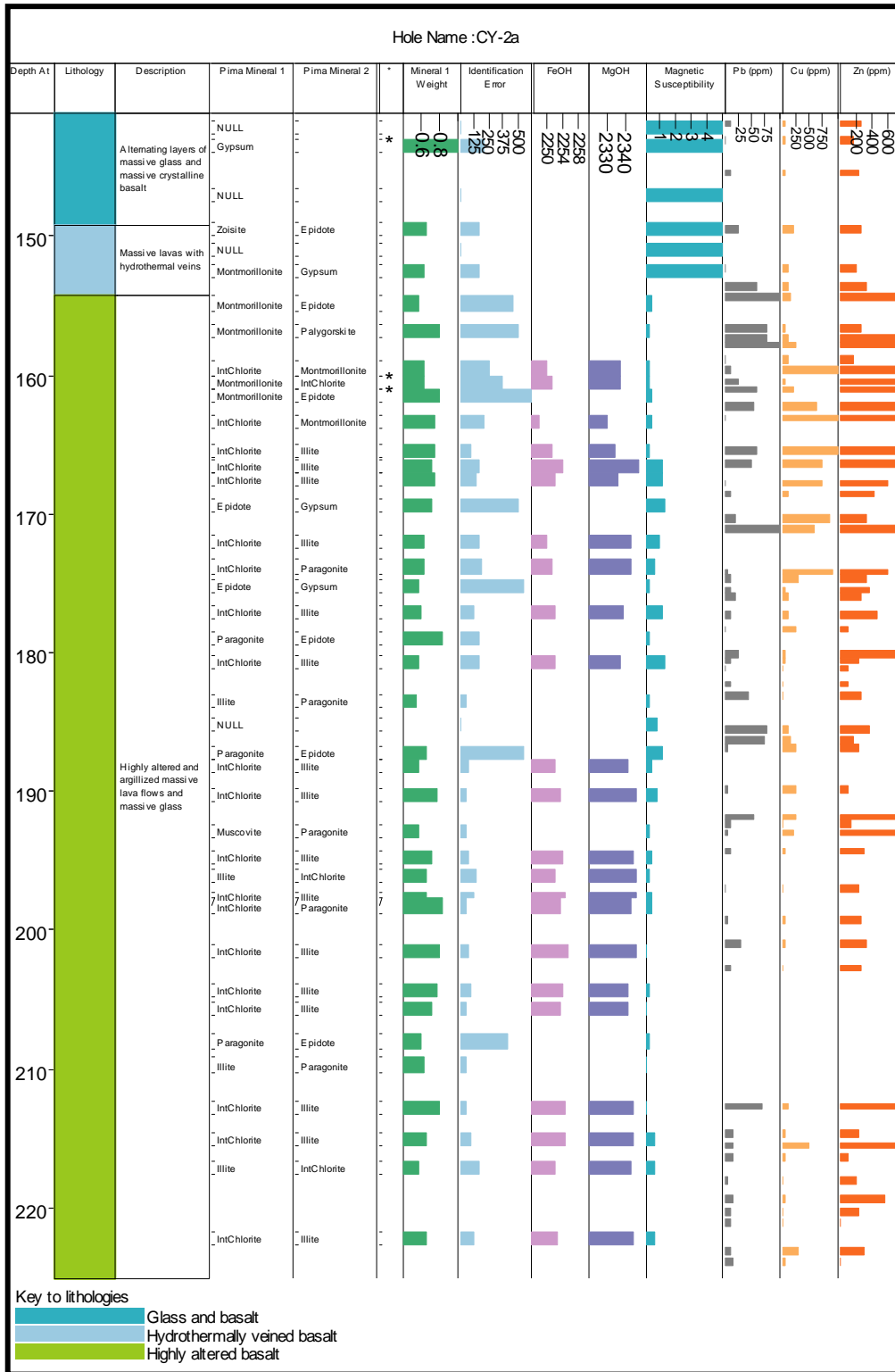


Figure 24 Downhole log for borehole CY2A (140 to 226m) from the Agrokipia Mine comparing PIMA, geological, geochemical and geophysical data.

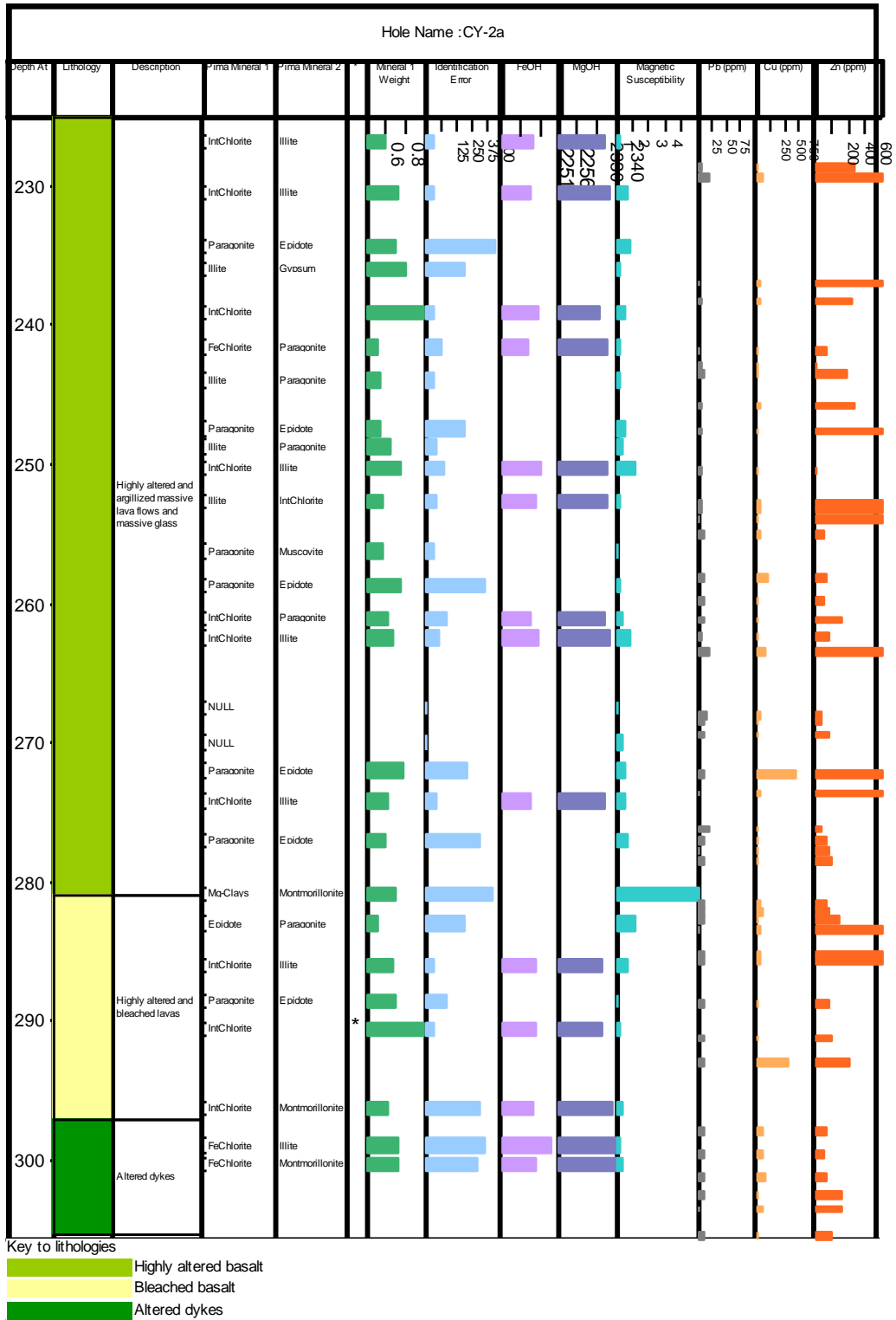


Figure 25 Downhole log for borehole CY2A (226 to 306 m) from the Agrokipia Mine comparing PIMA, geological, geochemical and geophysical data.

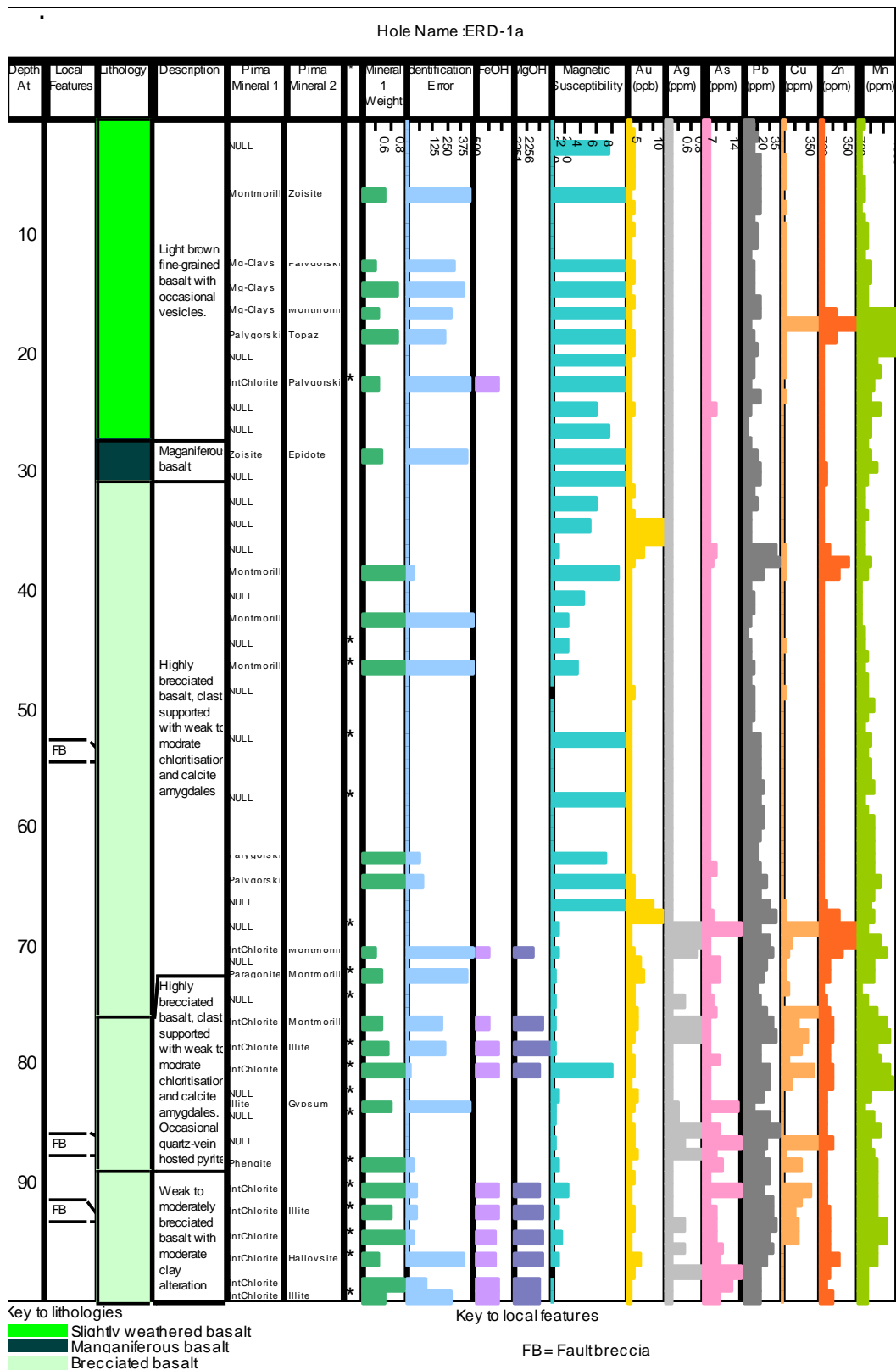


Figure 26 Downhole log of the data from ERD-1a borehole. \* indicates that multiple spectral measurements were taken (lithological division and assay data were adapted from EMM log sheets).

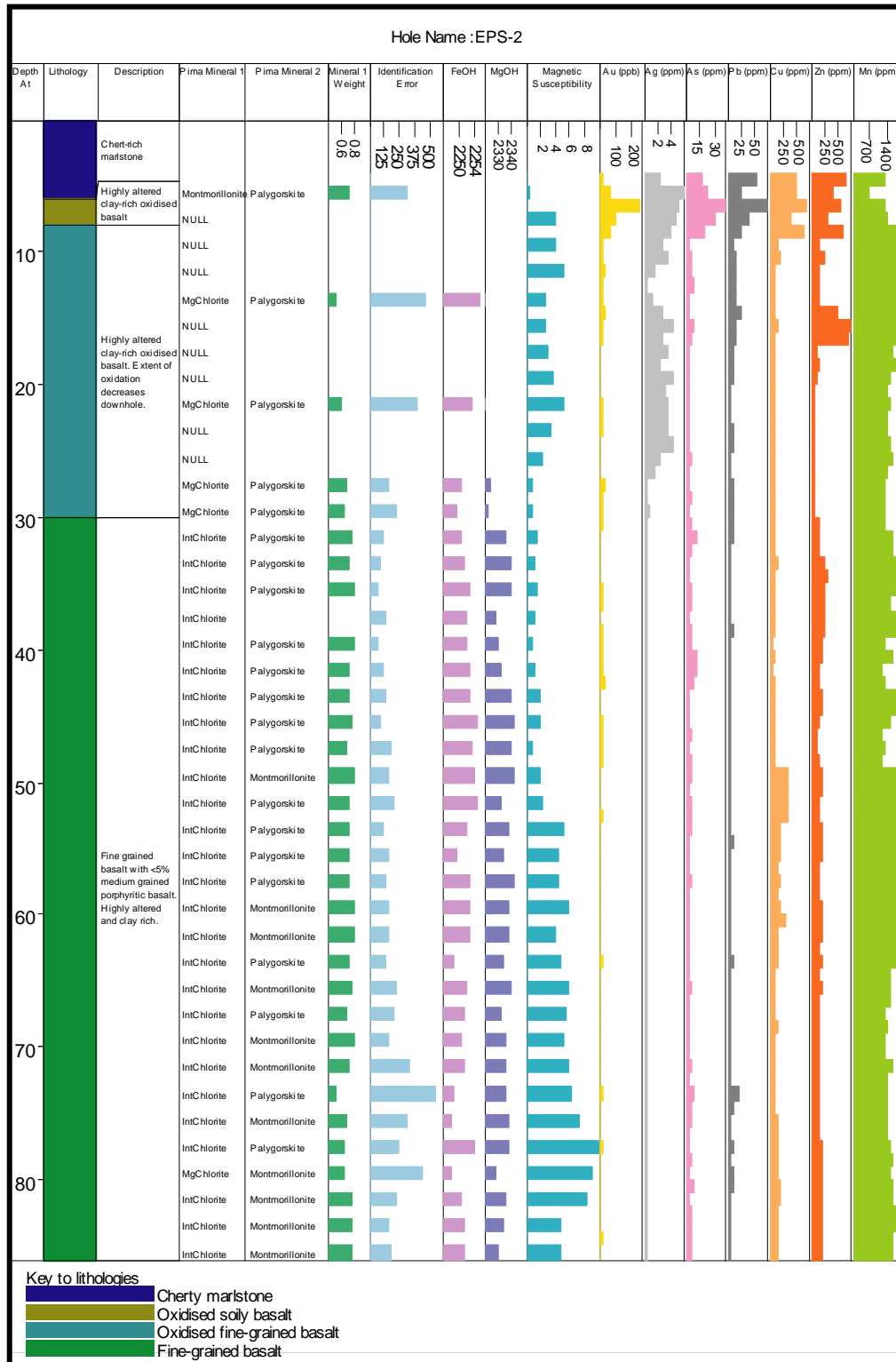


Figure 27 Downhole log of the data from the EPS-2 borehole (lithological division and assay data were adapted from EMM log sheets).



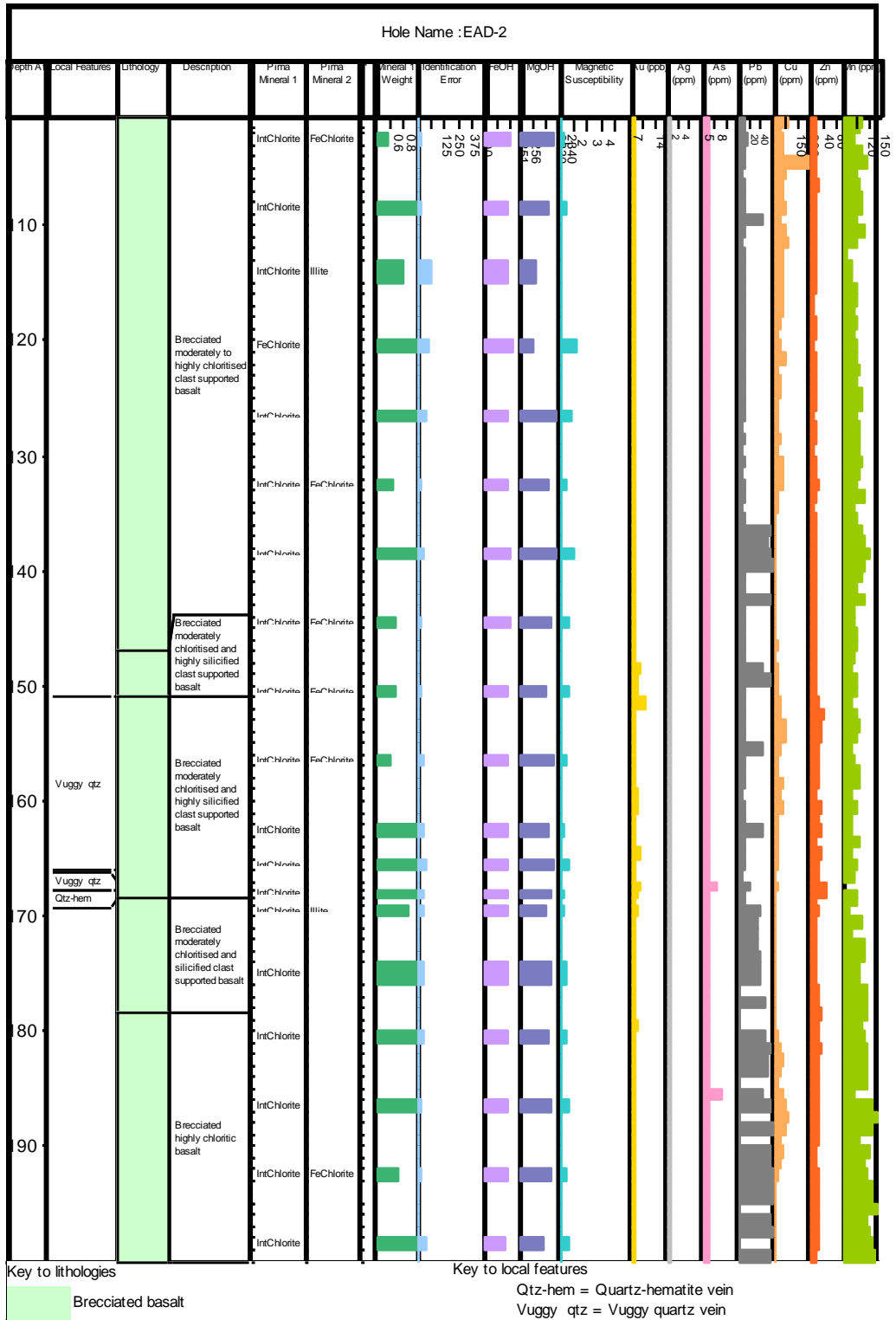


Figure 29 Downhole log of the data from EAD-2 borehole (100 to 200 m). \* indicates that multiple spectral measurements were taken (lithological division and assay data were adapted from EMM log sheets).

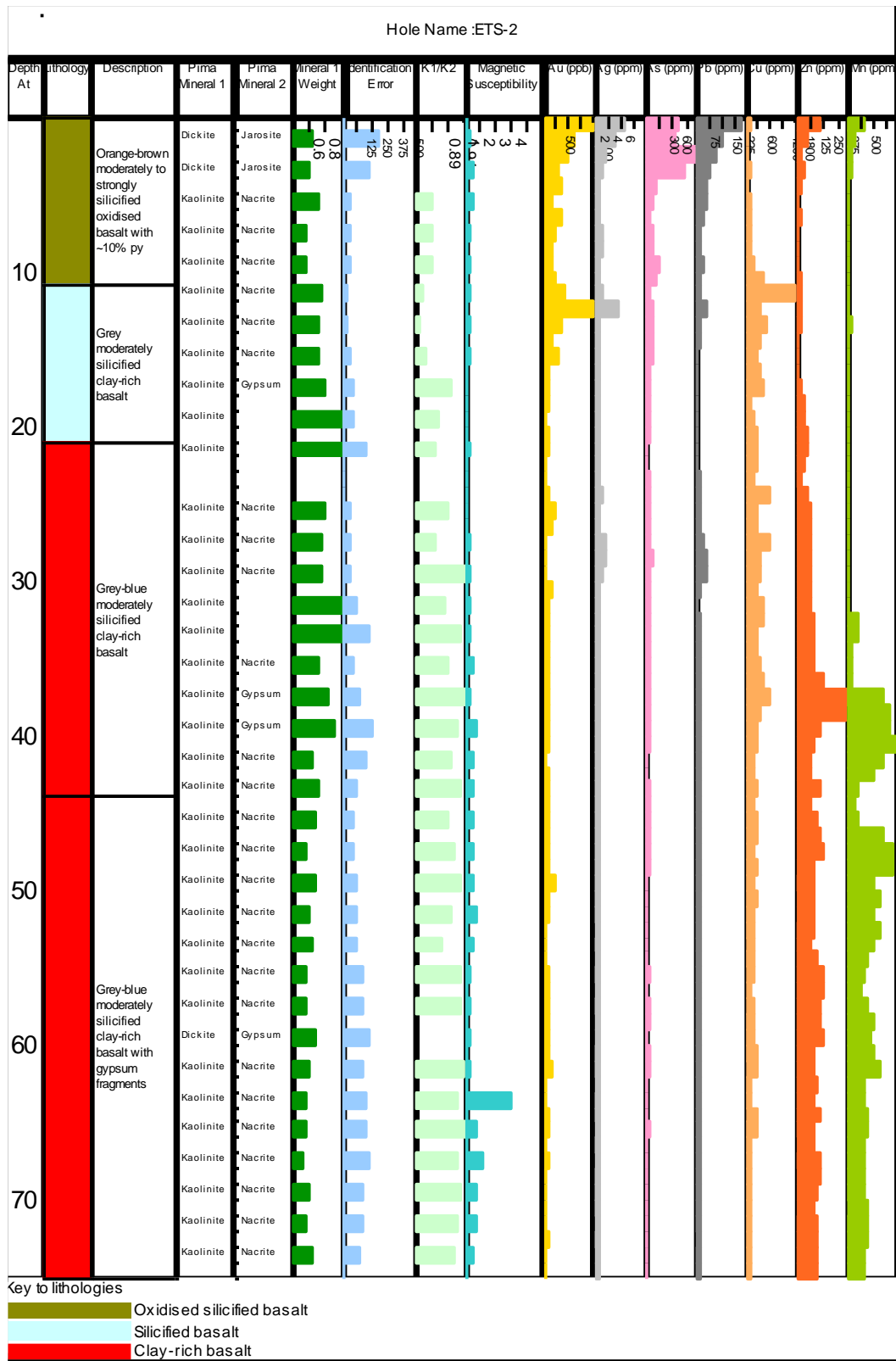


Figure 30 Downhole log of the data from the ETS-2 borehole (lithological division and assay data were adapted from EMM log sheets).

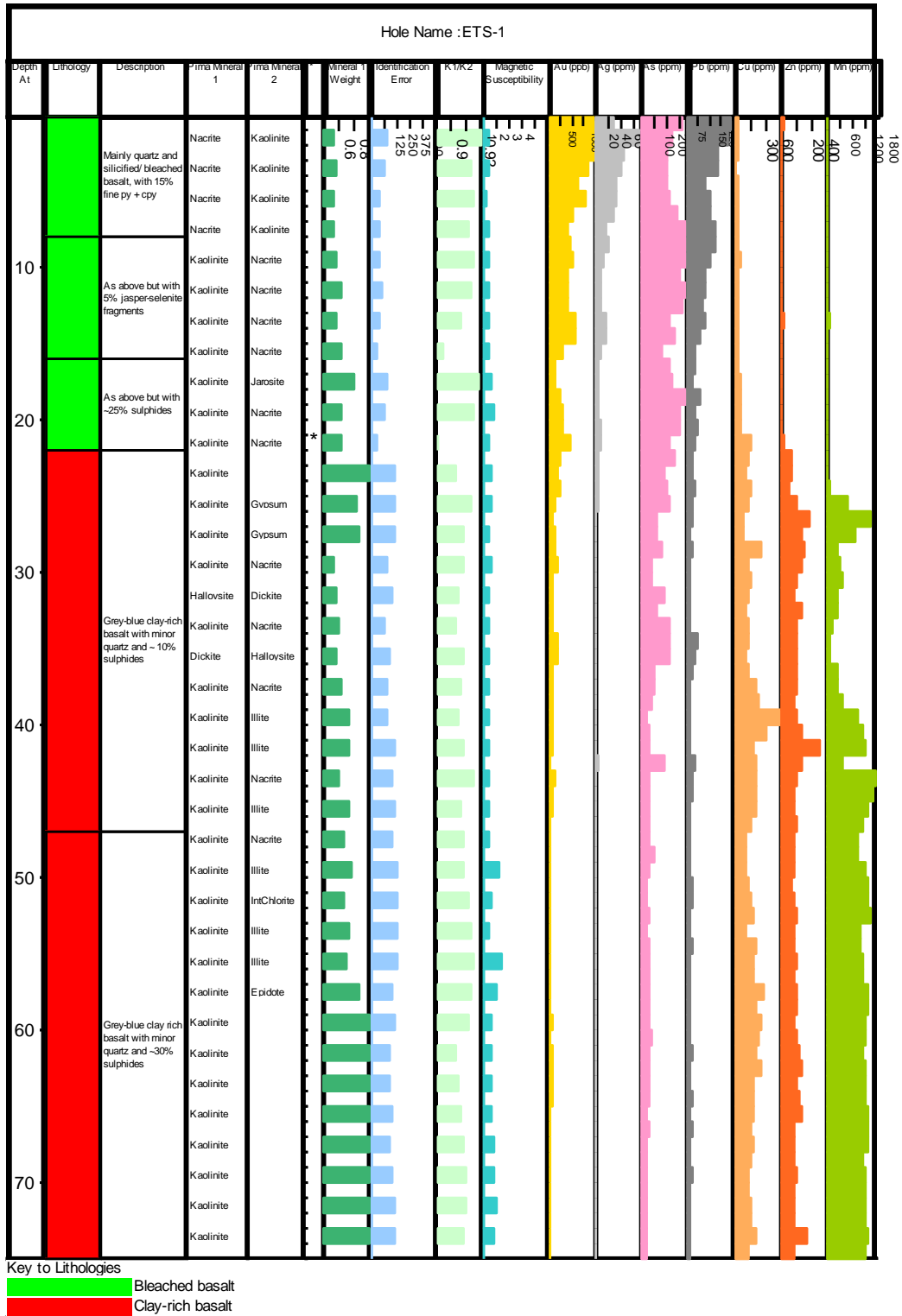


Figure 31 Downhole log of the data from the ETS-1 borehole (surface to 100 m). \* indicates that multiple spectral measurements were taken (lithological division and assay data were adapted from EMM log sheets).

### 5.7.3 Agropikia B—borehole CY-2a

Chlorite is the most commonly identified mineral and the majority occurs with illite although samples associated with paragonite, montmorillonite and gypsum can also be found (Figure 24 and Figure 25). Fe-chlorite is rare and restricted to

deepest 60m. When illite is identified as the main alteration phase intermediate-chlorite, paragonite, montmorillonite or gypsum are in association with it. Samples with epidote are spread relatively evenly down the hole. Muscovite is rare (two identifications) and both are associated with paragonite. However, paragonite and muscovite have very similar spectra and the identification of muscovite should be considered dubious. The highest concentration of low temperature alteration minerals is found in the uppermost 20m of the sampled drill hole. This corresponds to the less altered basalts termed ‘glass and basalt’ and ‘hydrothermal veined basalt’ in the down hole logs. Montmorillonite is the most common alteration mineral in this zone and all but one of the highest magnetic susceptibility readings (over 8.3) occur here.

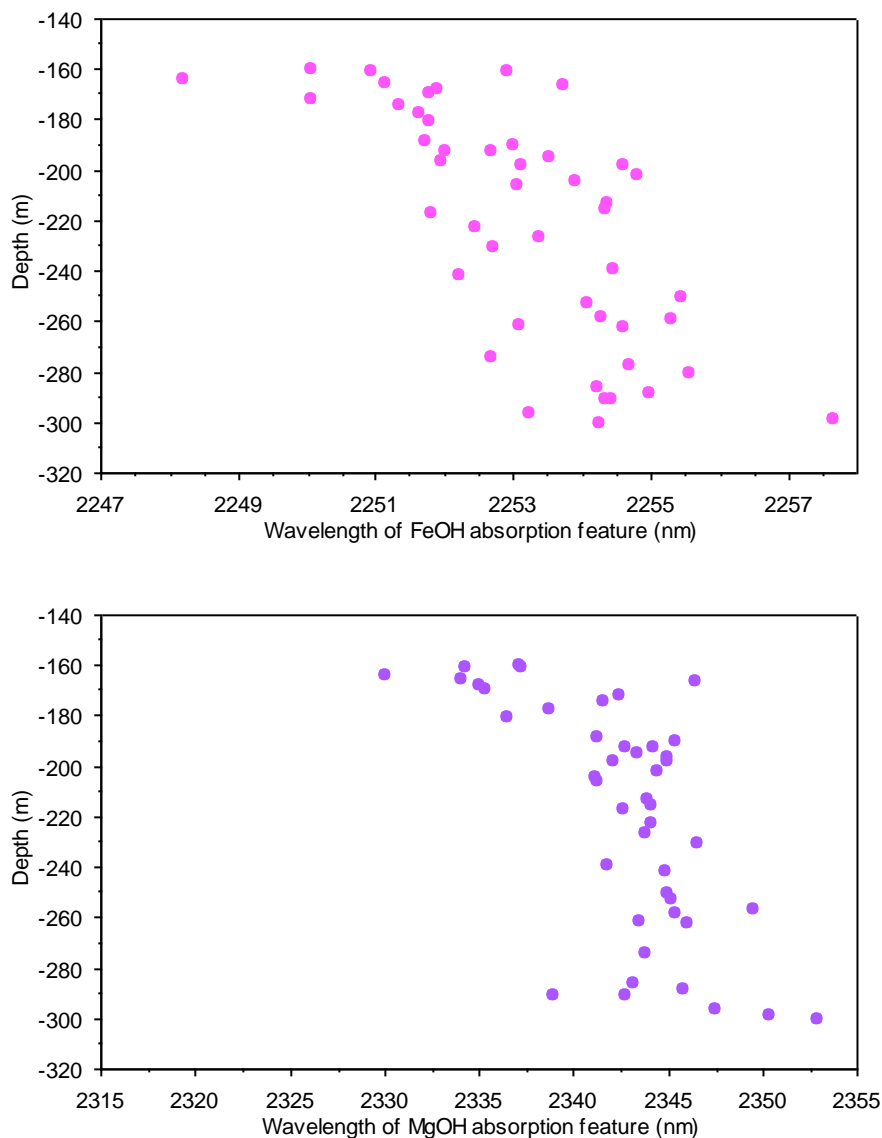


Figure 32 Graphs showing the variation in the wavelength of the FeOH and MgOH absorption features for chlorites in the CY-2a borehole.

The range of the wavelengths of the FeOH and MgOH absorption features are 2248 to 2258 nm and 2330 to 2352 nm respectively. These ranges of wavelengths correspond roughly to chlorites with a Mg number of 0.8 to 0.17 (Pontual et al., 1997b). The average wavelengths for the FeOH and MgOH absorption features are around 2253 and 2342 nm respectively although there is a

clear systematic variation with depth. This relationship is illustrated in Figure 32. From these graphs it is clear that the wavelengths of both absorption features increase sharply to a depth of around 192 m after which a less sharp increase is observed with increasing depth. These relationships imply that the chlorites are becoming more Fe-rich with depth. This is exemplified by the identification of Fe-chlorite in the two deepest samples analysed.

The magnetic susceptibility values show a considerable downhole variation ranging from 16.2 to 0.03. All but one of the high values, above 8, occur in the top 15 m of the hole. This corresponds with lithological divisions—the start of the highly altered basalt heralds a large drop in magnetic susceptibility. It should be noted, however, that the elevated Cu, Pb and Zn values only occur in areas where the magnetic susceptibility is below 1.

#### 5.7.4 Kokinnovounaros—borehole ERD-1a

The downhole variation in alteration mineralogy for ERD-1a is shown in Figure 26. Most of the chlorite is located below 70 m, in the lower part of the brecciated basalt. It is the dominant alteration mineral and occurs in association with illite, montmorillonite, paragonite or halloysite. No Fe-chlorite was identified. Illite is also restricted to the lower parts of the brecciated basalt. It is mainly associated with intermediate-chlorite. In addition, illite is only recorded in samples with a magnetic susceptibility value of less than 1. Epidote is uncommon (three identifications) and spread relatively evenly down the hole. It is found in association with montmorillonite, illite and zoisite. Low temperature alteration minerals are found throughout the drill core. Palygorskite is the most common. It is mainly located in thin (1–5 mm) white clay-filled veinlets that are pervasive throughout the drill core (Figure 33). The majority of the palygorskite in these veins is associated with montmorillonite.



Figure 33 A photograph of the ERD-1a drill core at a depth of 57.5m showing the late stage white clay filled veins that host most of the palygorskite. Montmorillonite is also commonly identified from spectra taken from these veins.

Montmorillonite is the second most abundant low temperature alteration mineral and is common in the pervasive alteration throughout the drill core, although at

depth it is mainly confined to white clay veins. It is commonly found in association with intermediate-chlorite, palygorskite and magnesium clays. Halloysite is minor in occurrence and restricted to the deepest 10 m of the borehole where it mainly occurs in association with intermediate-chlorite. Magnesium clays are restricted to the shallowest 17 m of the borehole and are therefore only found in the slightly weathered basalt.

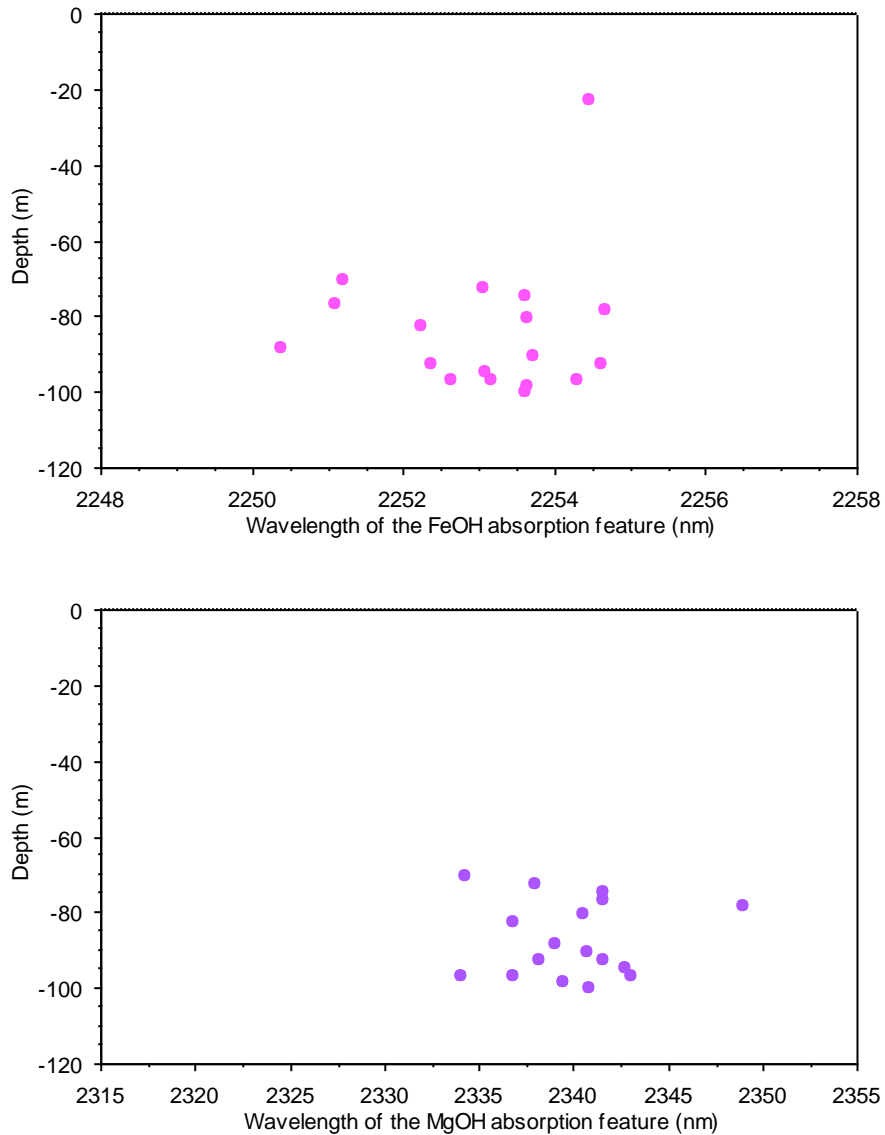


Figure 34 Graphs showing the variation in the wavelength of FeOH and MgOH absorption features for the chlorites in the ERD-1a borehole. The range of the wavelengths of the FeOH and MgOH absorption features are 2250 to 2255nm and 2334 to 2348 nm respectively. Both these ranges of wavelengths correspond roughly to chlorites with a Mg number of 0.65 to 0.3 (Pontual et al., 1997b). The average wavelength of the FeOH and MgOH absorption features are approximately 2253 and 2338 nm respectively and there is no systematic variation with depth (Figure 34).

The magnetic susceptibility values are very variable, ranging from 28.5 to 0.01 with a median average value of 1.44. All of the magnetic susceptibility values above 8 occur in the top 67 m of the drill core. The onset of the low magnetic

susceptibility readings at 67 m correlates well with the start of the chlorite and illite identifications and elevated Au, Ag, As, Cu and Zn grades.

### 5.7.5 Papoutsi—borehole EPS-2

Intermediate-chlorite is the dominant alteration mineral and is mostly associated with either palygorskite or montmorillonite (Figure 27). Most of the samples identified as Mg-chlorite are located between depths 14 and 30 m and are associated with palygorskite, which correlate well with the distribution of oxidised fine-grained basalt. None of the low temperature alteration minerals are the dominant alteration mineral. Palygorskite occurs throughout the hole but tends to be more common in the top 48 m. Below about 50 m montmorillonite is the dominant low temperature alteration mineral.

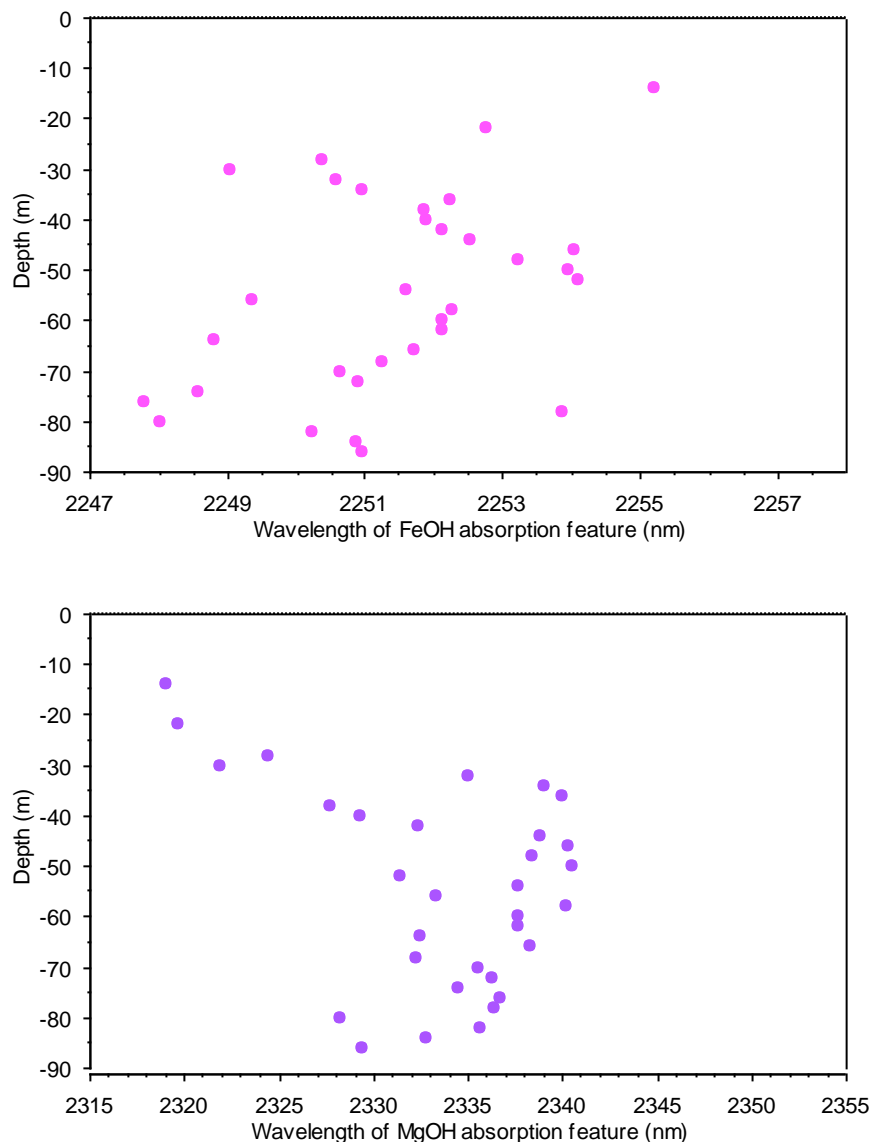


Figure 35 Graphs showing the variation in wavelength of the FeOH and MgOH absorption features for chlorites in the EPS-2 borehole.

The range of the wavelengths of the FeOH and MgOH absorption features are 2248 to 2255 nm and 2319 to 2341 nm respectively. The variation in wavelength of the FeOH absorption feature does not correlate very well with that of the

MgOH feature (Figure 35). The range of wavelengths of the FeOH feature corresponds roughly to chlorites with a Mg number of 0.8 Mg to 0.3 whereas the range in wavelengths of the MgOH feature fits those expected from chlorites with a Mg number ranging from near 1 to 0.55 (Pontual et al., 1997b). The accuracy of the FeOH absorption feature in predicting chlorite composition appears to fall with decreasing Fe contents (Pontual et al. 1997). If the values of the FeOH feature are discounted for the two samples with the shortest MgOH feature wavelength (at depths of 14 and 22 m—Figure 27) the correlation between the FeOH and MgOH features and depth is much better (Figure 35). The wavelengths of the absorption features increase with depth, indicating a shift to higher Fe compositions, until a depth of around 50 m where the wavelengths of the absorption features progressively shorten with depth.

k-values, for magnetic susceptibility, vary from 0.51 to 14.5 and show a systematic variation with depth. The shallowest sample analysed has the lowest k-value and correspond to an oxidised soil-like basalt. The k-values of the oxidised fine-grained basalt beneath this (8–30 m) are significantly higher but decrease towards the lithology's lower boundary. Beyond this, the k-values at the top of the fine-grained basalt remain relatively low until ~52 m where they rise steadily, reaching the maximum at 78 m. The change from the EPS-2 average k-values in the oxidised fine-grained basalt to the low values of the fine-grained basalt correlates roughly with the change of Mg-chlorite to intermediate-chlorite. The highest k-values, near the bottom of the hole also correlate roughly with the identification of Mg-chlorite. This relationship is supported by the fact that the zone of low k values (between 27 and 52 m) is associated with samples with the longest (more Fe-rich) FeOH and MgOH absorption feature wavelengths.

#### 5.7.6 Alestos—borehole EAD-2



Figure 36 A photograph of the pebble breccia zone from a depth of 18.5m in the EAD-2 borehole. The spectrum identified as dickite was produced by one of the less silicified clasts.

For the Alestos borehole, Figure 28 and Figure 29 illustrate the downhole variation in alteration mineralogy. Intermediate-chlorite is present in most of the

analysed samples from the EAD-2. Fe-chlorite is the dominant alteration minerals in approximately a third of the samples in the top 44.5 m of the borehole. In this zone, which is dominantly brecciated basalt with a rock flour matrix, it is commonly associated with intermediate-chlorite. Illite is a minor phase and is restricted to brecciated basalt below 56.5 m. It occurs in association with intermediate-chlorite. Dickite was recorded as a minor alteration phase in three samples where it occurs with intermediate-chlorite. Furthermore, all of these samples occur in areas that have been hydraulically brecciated (pebble breccia in downhole logs—Figure 28 and Figure 29). Figure 36 illustrates a pebble breccia where dickite was identified as an alteration mineral. Halloysite is the only recorded low temperature alteration mineral to be found, is minor in abundance and is restricted to shallow samples within the stockworked basalt.

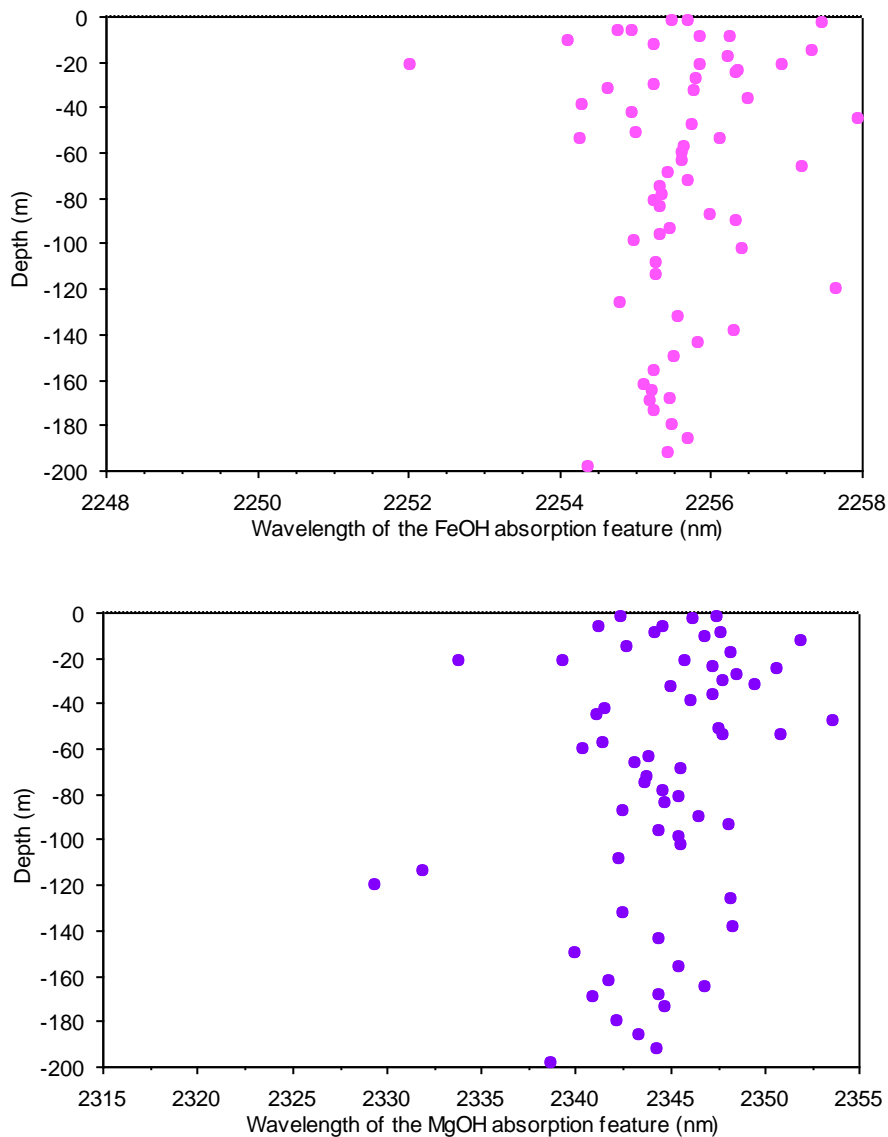


Figure 37 Graphs showing the variation in the wavelength of the FeOH and MgOH absorption feature for the chlorites of the EAD-2 borehole.

The wavelengths of the FeOH and MgOH absorption features of the samples containing chlorite vary from 2252 to 2258 nm and 2329 to 2354 nm respectively. The wavelengths of the FeOH absorption feature correspond to chlorites with a Mg number ranging from 0.6 to 0.2 while the MgOH absorption feature

wavelengths correspond to chlorites with a Mg number ranging from 0.85 to 0.20 (Pontual et al., 1997a). This difference can be explained by the reduction in the ability of the MgOH absorption feature to determine Mg number with increasing Fe contents in chlorite. A weak correlation of decreasing wavelength of the FeOH and MgOH absorption features with depth can be discerned (Figure 37). This relationship correlates to the lower number of Fe-chlorite identifications with increasing depth.

The magnetic susceptibility of the EAD-2 borehole varies from 0.09 to 46.3. The vast majority of these values are below 2 but there are a few samples with exceptionally high values that indicate the presence of vein-hosted magnetite. These high values all lie in a zone between depths of 21.5 and 39.5 m. The low values do not show any significant variation down hole.

## **5.7.7 Tourounjia**

### **5.7.7.1 BOREHOLE ETS-1**

Kaolinite is dominant alteration phase in the borehole and is found in association with nacrite, illite, dickite, gypsum, intermediate-chlorite and epidote (Figure 31). However, nacrite is a major alteration mineral in the uppermost (<8 m) part of the hole. This distribution corresponds to the uppermost division of the bleached basalt, which is distinguished from the lower sections by the absence of jasper-selenite fragments. Below 8 m the abundance and frequency of identification of nacrite decrease to depths of 47.5m, below which it is not found. Nacrite only occurs in association with kaolinite. Illite is a subsidiary alteration phase and occurs between 39.5 and 55.5 m and is restricted to a clay-rich basalt. It is always associated with kaolinite. Dickite occurs as a major alteration phase in one sample (35.5 m) and as a subsidiary in two others (21.5 and 31.5 m). Two spectral analyses were taken of samples from a depth of 21.5 m—one using a Petri dish and another on a single chip. The spectral analyses of the chip produced a spectrum that was identified as being produced from kaolinite and dickite. Both the other samples identified as containing dickite are associated with halloysite. Only one sample (51.5 m) contained intermediate-chlorite. It is worth noting that the wavelengths of the FeOH and MgOH absorption features of the spectra from this sample are 2250 and 2338 nm respectively, which correspond to a chlorite with a Mg number of 0.65 (Pontual et al., 1997a). Epidote was identified in one sample at a depth of 57.5 m where it is associated with kaolinite.

K1/K2 varies from 0.881 to 0.938 and indicates that kaolinite is probably poorly crystalline (Pontual et al., 1997a). The correlation between depth and K1/K2 is not as clear as that seen in the ETS-2 borehole. Figure 38 illustrates the trend. Here, the samples in which nacrite is dominant over kaolinite are shown in red. In addition, the samples above 20 m have all been identified as containing less than 62% kaolinite. If these samples are ignored then a similar pattern to ETS-2 borehole is seen where the K1/K2 ratio generally increases with depth (Figure 38).



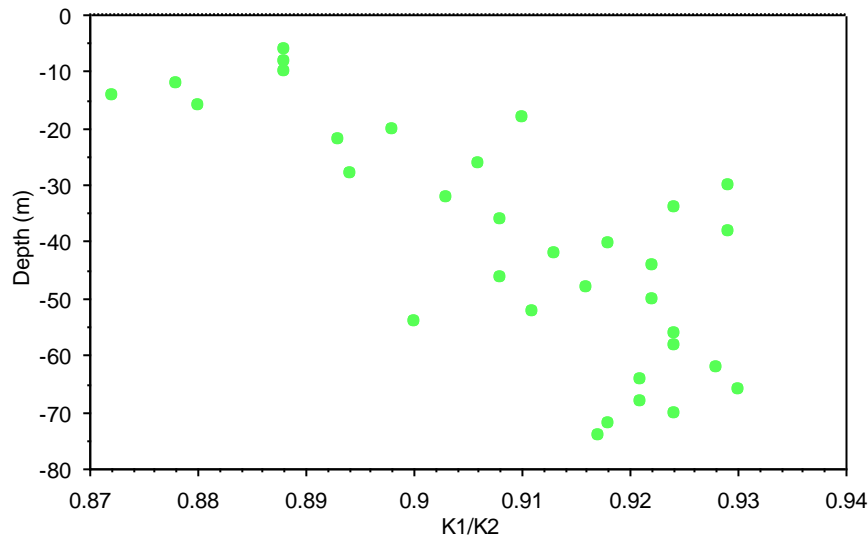


Figure 39 A plot showing the variation of the ratio of absorption intensities between the K1 absorption feature (at 2206nm) and the K2 absorption feature (at 2162nm) from sample containing kaolinite with depth.

K1/K2 provides information on the crystallinity of kaolinite with larger ratios generally corresponding with less crystalline kaolinite. However, the real K1/K2 of the kaolinite in the analysed samples may be masked, as nearly all samples contain nacrite. Nacrite and kaolinite share spectral features and consequently increasing nacrite contents have the effect of increasing K1/K2. It is however worth examining the K1/K2 ratio as systematic variations can be seen. K1/K2 for samples containing kaolinite varies from 0.87 to 0.93. This implies that all of the kaolinite is probably poorly crystalline (Pontual et al., 1997a) although K1/K2 generally increases with increasing depth (Figure 39). However, the reasons for this correlation are not fully understood. Also, the ratio displays a positive correlation with identification error. This indicates that the samples with the lower K1/K2, i.e. more crystalline, are identified by *The Spectral Geologist* software with a higher certainty.

The magnetic susceptibility of the samples from the ETS-2 borehole vary from 0.09 to 2.87 with very low median and mean values of 0.3 and 0.41 respectively. At the top of the borehole the k-values are average but they drop steadily, reaching a zone of minimum values at between depths of 17.5 and 25.5 m, the centre of which corresponds to the boundary between a silicified and a clay-rich basalt.

### 5.7.8 Data summary

A summary of the alteration mineralogy by prospect is presented in Table 11. It is clear that there are major differences between the high temperature alteration assemblages associated with some of the prospects. The significant differences between Papoutsi compared to Agrokipia B and Kokkinovounaros is the absence of illite and more Mg-rich chlorites. Alestos has a similar assemblage to Agrokipia B although dickite is found occasionally in zones of hydraulic brecciation. Tourounjia displays a markedly different alteration style with kaolinite and nacrite dominating.

Deposit	Agrokipia B	Kokkinovounaros	Papoutsi	Alestos	Tourounjia	
Borehole	<i>CY-2a</i>	<i>ERD-1a</i>	<i>EPS-2</i>	<i>EAD-2</i>	<i>ETS-2</i>	<i>ETS-1</i>
High temperature alteration minerals	Int-chlorite, Illite, Epidote, Fe-chlorite	Int-chlorite, Illite, Epidote	Int-chlorite, Mg-chlorite	Int-chlorite, Fe-chlorite, Illite, Dickite	Kaolinite, Nacrite <sup>7</sup> , Dickite	Kaolinite, Nacrite, Dickite, Illite, Int-chlorite, Epidote

Table 11. A table showing the main high-temperature alteration minerals identified by the PIMA according to prospect and borehole.

The chlorites of the Papoutsi prospect exhibit more Mg-rich spectral characteristics than those of the other prospects while the spectra of the chlorites from Alestos indicate more Fe-rich compositions than the other deposits.

The average magnetic susceptibility of the boreholes varies from 0.3 to 3.8. The two highest average magnetic susceptibility values are found in the Papoutsi and Kokkinovounaros prospects and it is interesting to note that no Fe-chlorite was found in these deposits. Papoutsi has the highest magnetic susceptibility and the most Mg-rich chlorites. The identification of kandite (kaolinite-group) minerals, in the Tourounjia and Alestos prospects, is limited to deposits with relatively low k-values.

## 5.8 X-RAY DIFFRACTION ANALYSIS OF ALTERATION MINERALS

### 5.8.1 Introduction and methodology

The PIMA investigation potentially identified high temperature polytypes of the kaolin group (dickite and nacrite) at Alestos and Tourounjia. Therefore to confirm this and to identify other alteration phases X-Ray Diffraction (XRD) analysis was undertaken, performed in the laboratories at the Natural History Museum, London. Samples were taken of chips from two reverse circulation boreholes from Tourounjia (ETS-1 and ETS-2) and one diamond core drill-hole from Alestos (EAD-2). Samples were selected to target the areas where the PIMA identified nacrite or dickite.

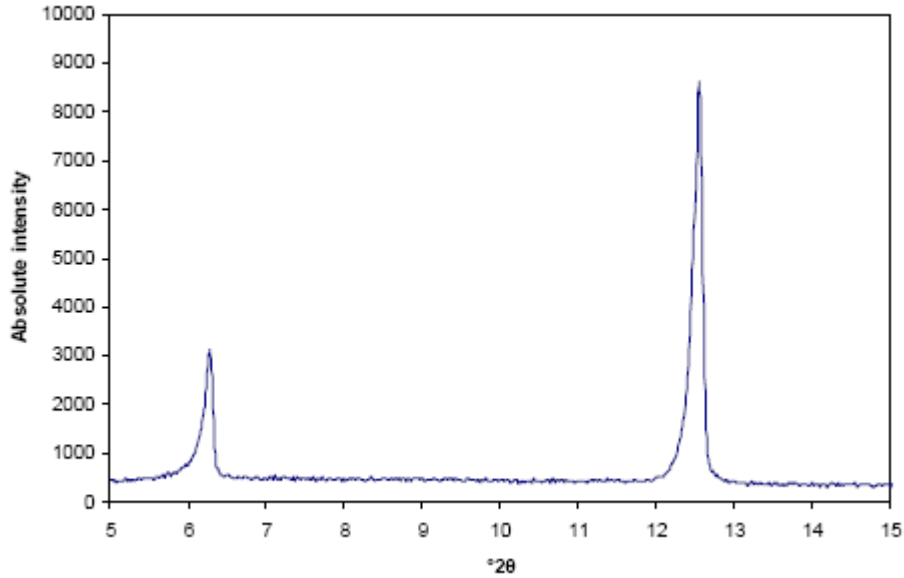


Figure 40 XRD patterns for EAD-2 (Alestos) at a depth of 18 m. The peaks at  $6.3^\circ$  and  $12.6^\circ$   $2\theta$  show the same shape, giving a good indication that they are both produced by the same phase, clinochlore. The PIMA detected dickite and chlorite in the same sample.

Kaolin group minerals can easily be confused with clinochlore (of the chlorite group) as distinctive peaks overlap. To overcome this problem it was necessary to look at the relative shapes and sizes of the peaks at  $6.3^\circ$  and  $12.6^\circ$   $2\theta$ .

If the shapes of these two peaks are the same, and their heights are in the same proportion as those of the standard for clinochlore, then clinochlore is the only phase responsible for these, and kaolin group minerals are not present. This was the case in borehole EAD-2 from Alestos where PIMA analysis identified dickite as being present. Figure 40 gives an example of this. Where these peaks appear markedly different in shape or the heights do not correspond well with the standards, multiple phases are responsible for them, allowing identification of kaolin group minerals (Figure 41).

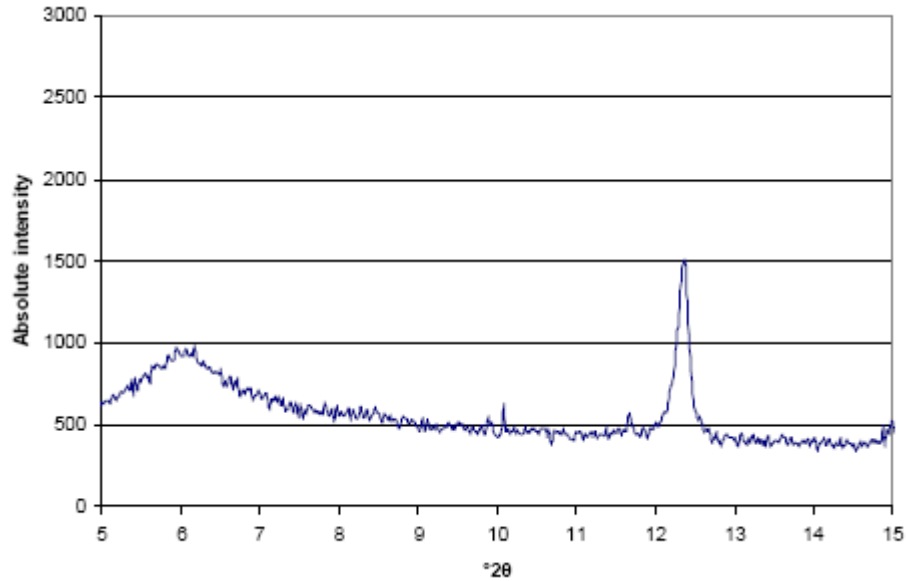


Figure 41 XRD patterns for ETS-2 (Tourounjia) at a depth of 1 m. The peak at 12.6° 2θ is markedly different from the broad peak at around 6° 2θ which is from a mixed-layer clay. The sharp peak at 12.6° 2θ indicates the presence of a mineral of the kaolin group.

The kaolin group minerals have very similar patterns. Confirmation that high temperature acidic alteration has occurred relies on the identification of the polytypes of the kaolin group that are interpreted to form at high temperatures: dickite and nacrite (Marumo, 1989). The crucial range of the spectra for identifying whether the kaolin group mineral is kaolinite, dickite or nacrite is between 36° and 40° 2θ. The peaks primarily used for identification have been selected from Bailey (1980). These peaks were used because they show the largest intensities of the diagnostic XRD lines and they are distinguishable from the other phases present. They are shown below in Table 12.

Kaolinite			Dickite			Nacrite		
d (Å)	°2θ	I	d (Å)	°2θ	I	d (Å)	°2θ	I
2.340	38.42	9	2.324	38.70	9.5	2.432	36.92	
						2.404	37.36	10
						2.395	37.51	

Table 12 The main peaks used to identify between the polytypes of the kaolin group minerals. Note that the nacrite peak is a broad peak over a range of 2θ angles. In the table d is the lattice spacing in ångstroms, θ is the angle of diffraction in degrees, and I is the intensity. Data from Bailey, 1980.

## 5.8.2 Results

### 5.8.2.1 ALESTOS

Table 13 shows a summary of the identified phases at depths indicated and a comparison with what the PIMA identified at these depths.

EAD-2 (Diamond core)		
Depth (m)	XRD	PIMA
5	Quartz Fe-Clinochlore Pyrite	IntChlorite
15	Quartz Fe-Clinochlore Pyrite	FeChlorite IntChlorite
18	Quartz Fe-Clinochlore Natro-alunite	IntChlorite Dickite

25	Quartz Fe-Clinochlore Pyrite Natro-alunite	FeChlorite IntChlorite
32	Quartz Fe-Clinochlore (Pyrite) (Natro-alunite)	IntChlorite Dickite
39	Quartz Fe-Clinochlore Pyrite	IntChlorite Dickite
50	Quartz Fe-Clinochlore (Pyrite)	IntChlorite FeChlorite
60	Quartz Fe-Clinochlore (Pyrite)	IntChlorite
63	Quartz Fe-Clinochlore (Pyrite)	Na_Alunite
70	Quartz Fe-Clinochlore (Pyrite)	IntChlorite

Table 13 Phases identified in the EAD-2 borehole at Alestos through XRD compared with those identified by a PIMA. Brackets indicate that only a trace of the mineral was identified.

### 5.8.2.2 TOUROUNDJIA XRD–PIMA COMPARISON

Table 14 shows a summary of the identified phases at depths indicated and a comparison with what the PIMA identified at these depths.

Depth (m)	ETS-1 (RC chips)			ETS-2 (RC chips)		
	Powder XRD		PIMA	Powder XRD		PIMA
1	Quartz Nacrite Mixed-layer clay Jarosite (Epidote?) (1 other phase?)	Mixed-layer Calcite Pyrite		Quartz Mixed-layer Calcite Pyrite	Nacrite clay Jarosite	
2	Quartz Nacrite Mixed-layer clay Jarosite Pyrite (1 other phase?)	Mixed-layer Calcite (1 other phase?)	Nacrite Kaolinite	Quartz Mixed-layer Calcite Andalusite Gypsum	Nacrite clay Jarosite	Dickite Jarosite
3	Quartz Nacrite Mixed-layer clay Jarosite Pyrite	Mixed-layer Calcite		Quartz Mixed-layer Calcite Andalusite Gypsum	Nacrite clay Jarosite	
12	Quartz Mixed-layer Jarosite Pyrite	Kaolinite Nacrite clay	Kaolinite Nacrite	Quartz Nacrite Mixed-layer Natro-alunite Gypsum Pyrite	Kaolinite Dickite? clay	Kaolinite Nacrite
21	Quartz Mixed-layer Jarosite Pyrite Gypsum	Kaolinite Nacrite clay Natro-alunite				
22	Quartz Mixed-layer Jarosite Pyrite Gypsum	Kaolinite Nacrite clay Natro-alunite	Kaolinite Nacrite/Dickite			
23	Quartz Mixed-layer Natro-alunite Pyrite Gypsum	Kaolinite Nacrite clay	Kaolinite			
29	Quartz Mixed-layer clay/Clinochlore Natro-alunite Pyrite Gypsum	Kaolinite Nacrite	Kaolinite Nacrite			
31				Quartz Dickite clay	Kaolinite Mixed-layer Natro-alunite	

ETS-1 (RC chips)				ETS-2 (RC chips)		
				Gypsum Pyrite		
32				Quartz	Kaolinite	Kaolinite
				Dickite	Mixed-layer clay	
				Natro-alunite	Pyrite	
				Gypsum (Clinochlore)		
35	Quartz	Kaolinite	Dickite			
	Dickite?	Mixed-layer clay/ Clinochlore	Halloysite			
	Natro-alunite	Jarosite				
	Gypsum	Pyrite				
36	Quartz	Kaolinite				
	Dickite?	Mixed-layer clay/ Clinochlore				
	Natro-alunite	Jarosite				
	Gypsum	Albite				
37	Quartz	Kaolinite	Kaolinite			Nacrite
	Dickite?	Mixed-layer clay/ Clinochlore				
	Natro-alunite	Jarosite				
	Gypsum	Albite				
42	Quartz	Albite	Kaolinite	Quartz	Kaolinite	Kaolinite
	Clinochlore	Gypsum	Illite	Dickite?	Mixed-layer clay	Nacrite
	Calcite	Pyrite		Natro-alunite	Pyrite	
				Gypsum	Clinochlore	
52	Quartz	Albite	Kaolinite	Quartz	Kaolinite	Kaolinite
	Clinochlore	Gypsum	IntChlorite	Dickite?	Mixed-layer clay	Nacrite
	Epidote?			Natro-alunite	Pyrite	
				Gypsum	Clinochlore	

Table 14 Phases identified in the ETS-1 and ETS-2 boreholes at Tourounjia through XRD compared with those identified by a PIMA. Brackets indicate that only a trace of the mineral was identified.

## 5.9 PETROLOGICAL ANALYSIS

Samples were collected from Tourounjia at the locations shown on Figure 21. They include silicified propylitically altered volcanics, bleached silicified volcanics, and a number of samples of mineralized, variably silicified breccias, including both the Volcanics Breccia and the Silica Volcanics Breccia.

In the silicified propylitically altered volcanics (Sample T09) the presence of abundant orthopyroxene laths replaced by finely crystalline biotite (Figure 42), which subsequently alters to chlorite (Figure 42) confirms boninitic pillow lavas host the prospect. Where chlorite is most abundant, pyrite is also present in larger quantities.

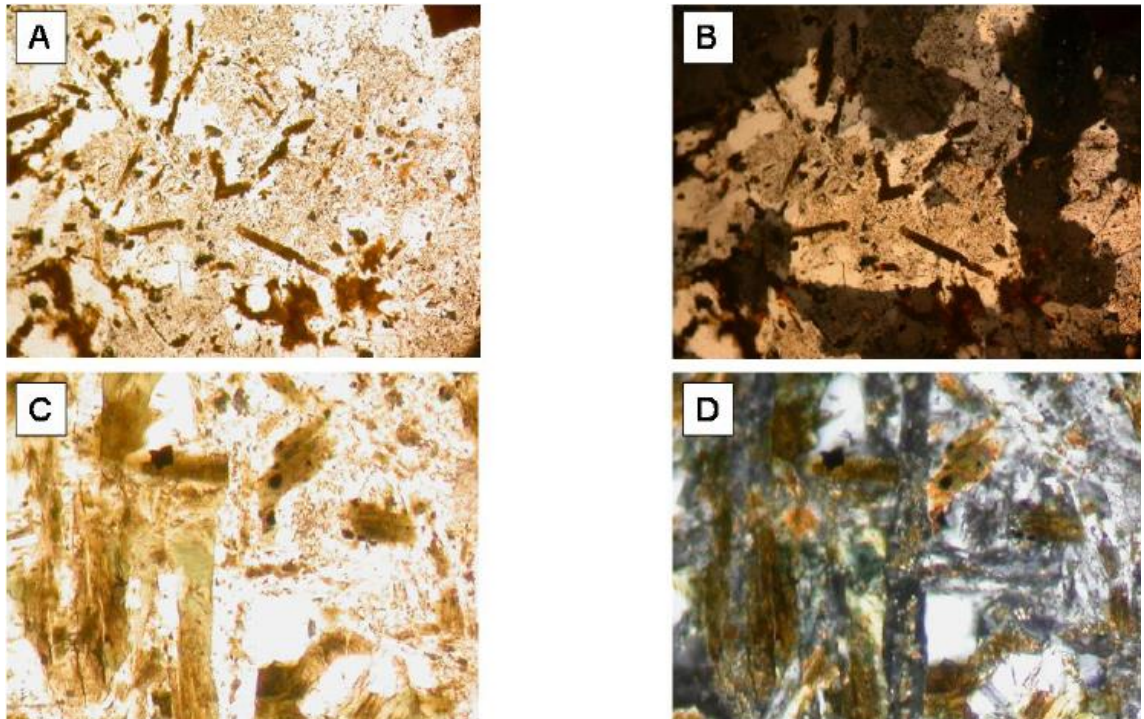


Figure 42 Transmitted light photographs of T09 from the silicified propylitically altered volcanics. A and B: PPL and XPL respectively of a view of the textures with biotite laths after orthopyroxene and a silica rich groundmass. Field of view: 2 mm. C and D: PPL and XPL respectively of a N-S trending orthopyroxene crystal with straight extinction being replaced by a finely crystalline brown phase. Biotite altering to chlorite can be seen to the left of this crystal. Field of view: 0.7 mm.

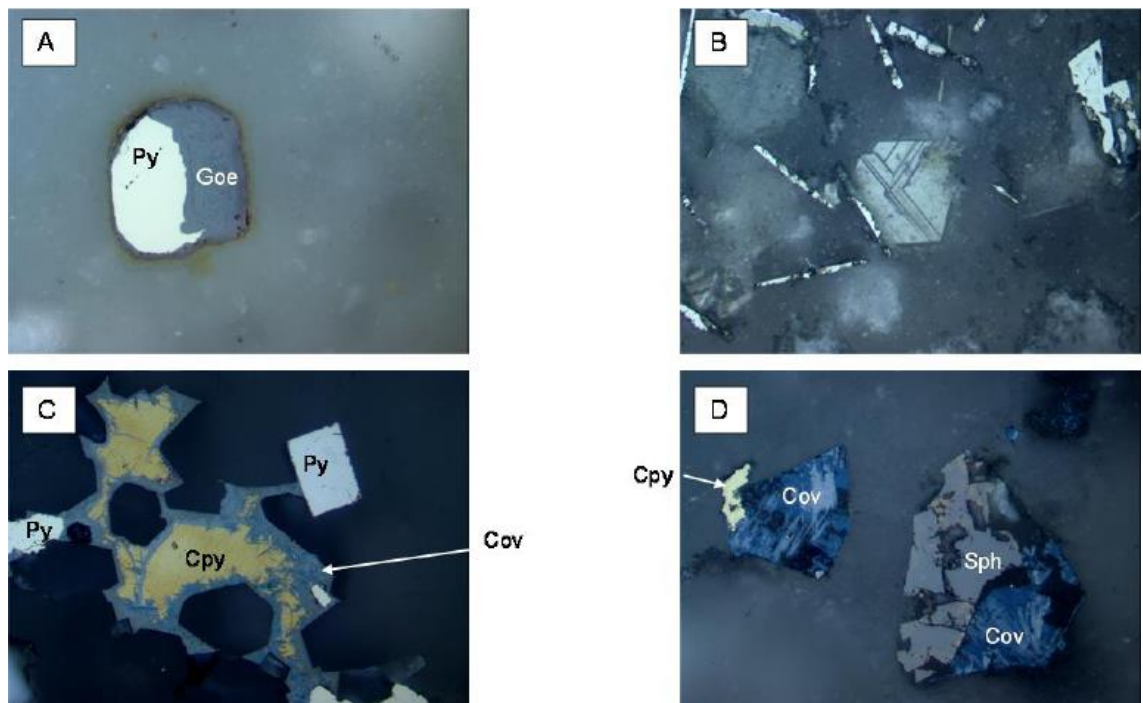


Figure 43 Reflected light photographs of mineralization. Py- pyrite, Cpy- chalcopyrite, Cov- covellite, Sph- sphalerite. A: Pyrite grain in silica weathering to goethite. B: Platy pyrite grains in silica. C: A sulphide assemblage typical of Cyprus-type mineralization. D: Covellite after sphalerite and chalcopyrite. All fields of view: 275  $\mu$ m.

The main mineralization is hosted by the silicified breccias, though sulphide assemblage makes up <5% of these units and is dominated by pyrite. Pyrite

occurs as anhedral to euhedral crystals, both within the silica matrix and within partially silicified clasts. It can be seen weathering to goethite in many samples (Figure 43A). Pyrite also occurs as plates (Figure 43B), which were investigated using scanning electron microscopy (SEM)—see below.

The remaining sulphides identified through microscopy consist of covellite, chalcopyrite and sphalerite. Chalcopyrite and sphalerite are seen as early phases with covellite coating pyrite, and replacing and coating chalcopyrite and sphalerite (Figure 43C+D).

### 5.9.1 Scanning Electron Microscopy

The platy pyrite occurs within the silicic matrix of the Silica Volcanics Breccia and can be seen associated with morphologically similar plates of non-sulphide (Figure 44). This non-sulphide mineral is replaced by the pyrite during mineralization, implying that the plates formed early within the mineralization process.

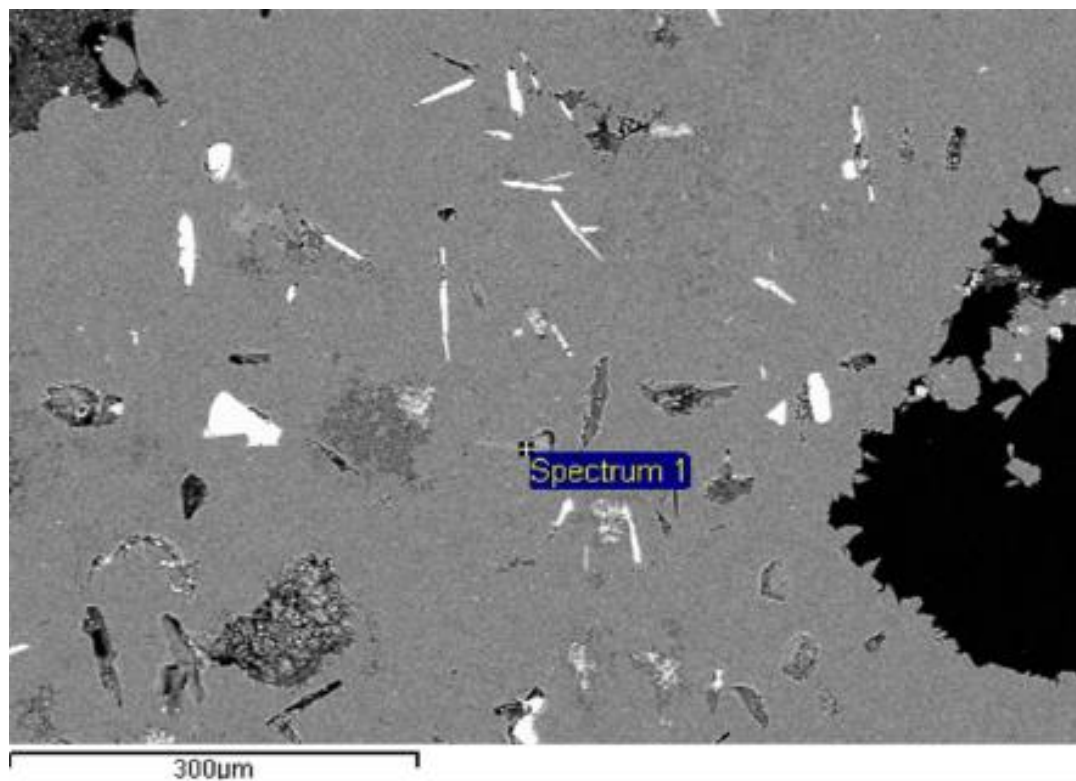


Figure 44 Back scattered electron micrograph, showing blades of pyrite and non sulphide in sample T06.

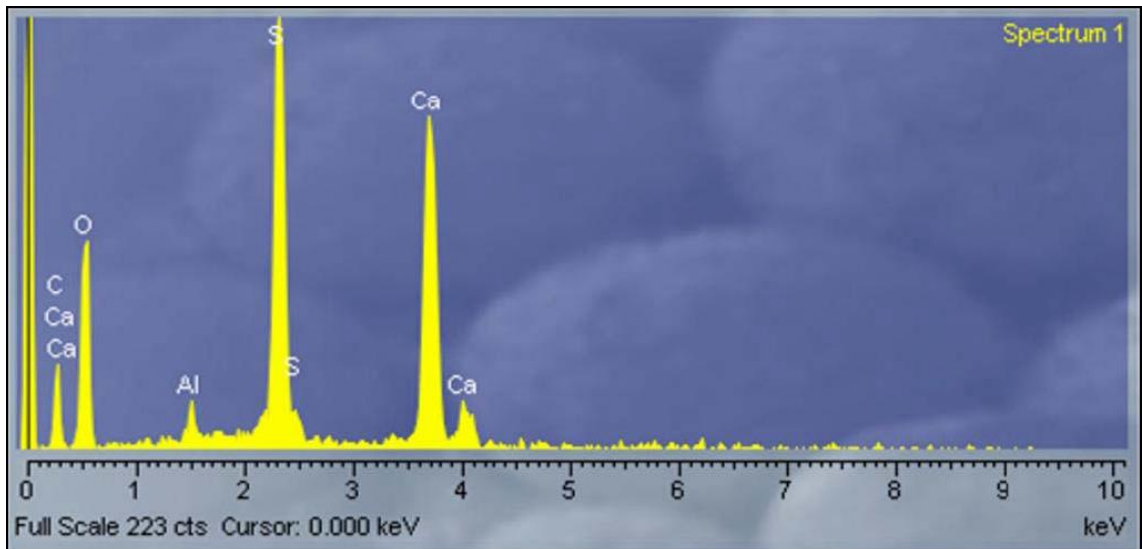


Figure 45 Spectrum detected over a 10 second period showing the phases detected which are compatible with the elements found in gypsum.

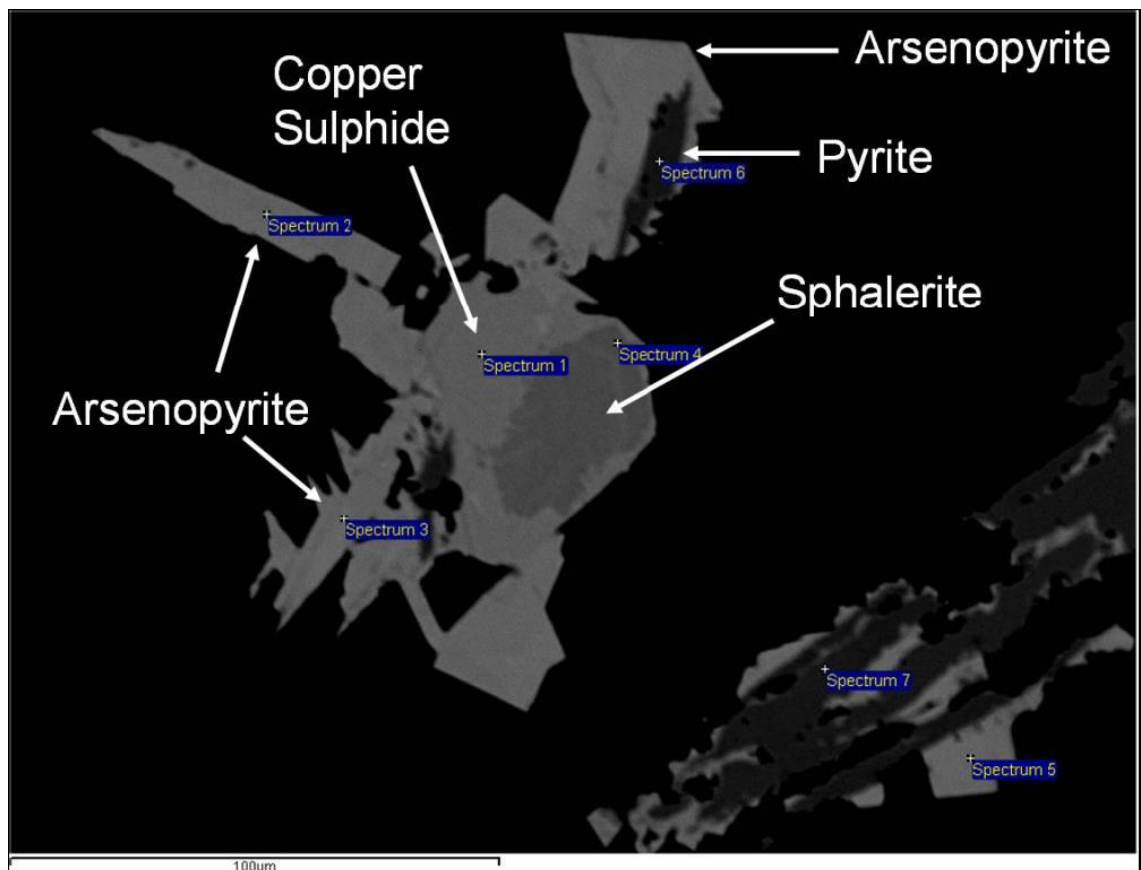


Figure 46 Back scattered electron micrograph, showing arsenopyrite in T03 with pyrite, sphalerite and copper sulphide.

## 5.9.2 Fluid Inclusion Study

### 5.9.3 Introduction

During the precipitation of crystals from fluids, defects in the crystal lattice trap samples of the fluid during crystal growth. These pockets of trapped fluid are

known as fluid inclusions. In order to gain an understanding of the nature of the fluid that was responsible for the mineralization, silicification and alteration at Tourounjia, micro-thermometry of fluid inclusions in quartz has been carried out. This should constrain the minimum temperature of the fluids at the time of formation of the crystals. The salinity of the mineralizing fluid can also be interpreted.

Fluid inclusions are often well preserved in well crystalline quartz. Most of the silicification at Tourounjia however consists of very finely crystalline, amorphous silica. It was anticipated that finding inclusions large enough to be analysed might be problematic. From the samples collected, doubly polished fluid inclusion wafers were prepared to a thickness of 100  $\mu\text{m}$  from three samples of the Silica Volcanics Breccia (T02, T03, and T06). These were chosen as the quartz appeared to be less amorphous than in other samples. Examination of the three fluid inclusion wafers with a transmitted light microscope led to the identification of suitable inclusions ( $>20 \mu\text{m}$ ) in only T06. These inclusions were found in two clusters within a clast of silicified jarositic material as shown in Figure 47.

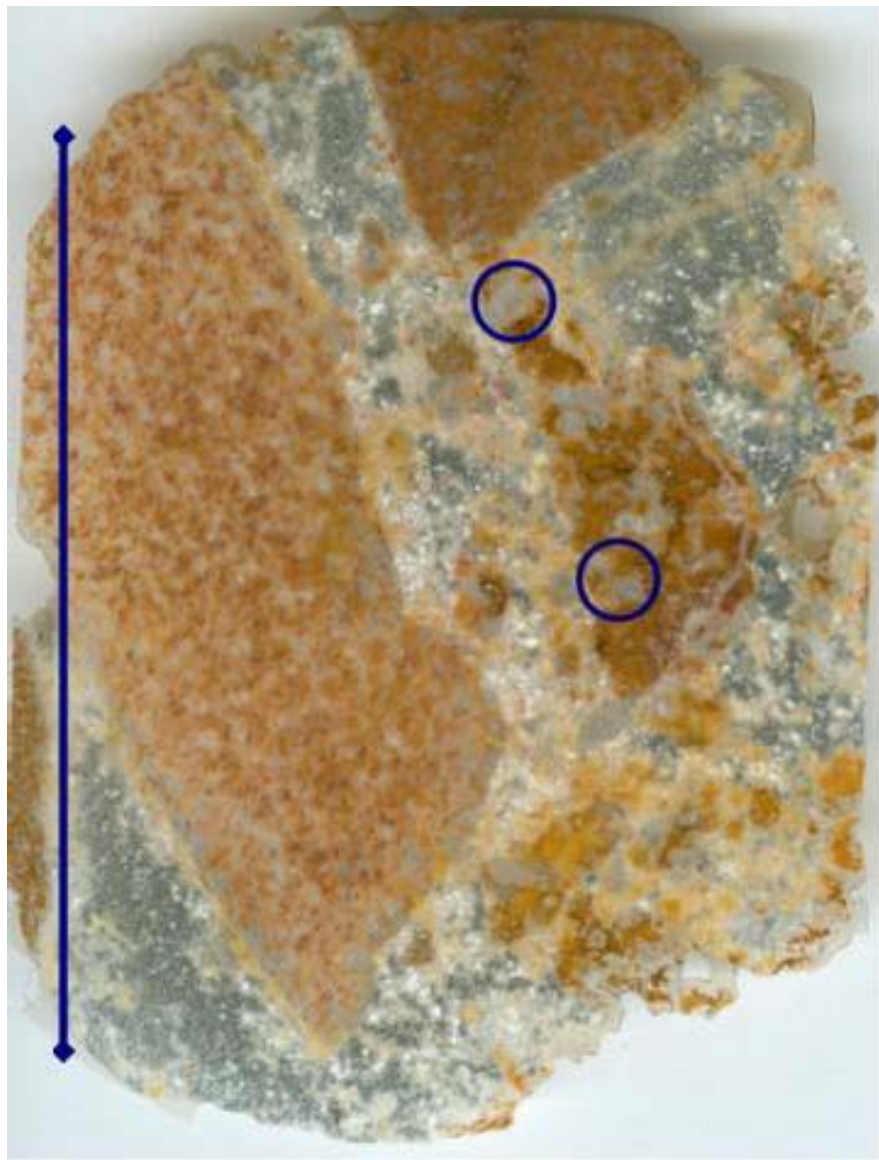


Figure 47 Fluid inclusion wafer from sample T06 with the two areas that contained the fluid inclusions analysed marked. Scale bar = 30mm.

The fluid inclusions in the sample are liquid rich two-phase fluid inclusions. They have a degree of fill (F, defined as the volume of liquid as a proportion of total inclusion volume) of 0.9 to 0.95. The number of inclusions of a size where phase changes could be seen was highly limited, tending to occur in growth zones of quartz fairly close to crystal boundaries. Individual inclusions were selected for analysis from those of a suitable size that appeared to be primary (criteria from Shepherd *et al.* 1985).

Temperatures of freezing ( $T_{FR}$ ), first ice melting ( $T_{FM}$ ), last ice melting ( $T_M$ ) and homogenization ( $T_H$ ) were sought for individual inclusions during freezing and heating cycles.

$T_M$  can be used to estimate the salinity of the fluid in weight percent NaCl equivalent using the equation (Bodnar, 1993):

$$\text{Salinity (wt\% NaCl equivalent)} = (-1.78 T_M) - (0.0442 T_M^2) - (0.000557 T_M^3)$$

#### 5.9.4 Results

A summary of the results corrected for stage calibration is shown below in Table 15.

<b>Inclusion</b>	<b><math>T_{FR}</math> (°C)</b>	<b><math>T_{FM}</math> (°C)</b>	<b><math>T_M</math> (°C)</b>	<b>Salinity (wt% NaCl equiv)</b>	<b><math>T_H</math> (°C)</b>
<b>1</b>	-45.0	-11.5	-3.6	5.88	110.9
<b>2</b>	-34.9		-4.1	6.61	237.8
<b>3</b>	-44.2	-13.2	-2.3	3.92	207.6
<b>4</b>	-39.3		-1.6	2.81	170.1
<b>5</b>	-37.3		-2.3	3.92	248.9
<b>6</b>	-44.8	-13.2	-1.7	2.97	209.1
<b>7</b>	-43.4		-1.8	3.13	207.5
<b>8</b>			-1.9	3.29	217.3
<b>9</b>	-42.7	-13.4	-1.8	3.13	247.8
<b>10</b>	-56.4	-15.0	-1.6	2.81	231.6
<b>11</b>	-44.7		-1.9	3.29	211.5
<b>12</b>					205.1

Table 15 Table showing the results of the fluid inclusion analysis. The temperatures have been corrected according to stage calibration.

Temperatures of first ice melting were very hard to observe and the temperatures given represent the first observed movement of the vapour bubble. They are not suitably accurate for interpretations to be made. No daughter minerals were observed during the cooling or heating of the inclusions. The temperatures of last ice melting range from -4.1 to -1.6°C with a mean of -2.08°C. Their distribution is shown in

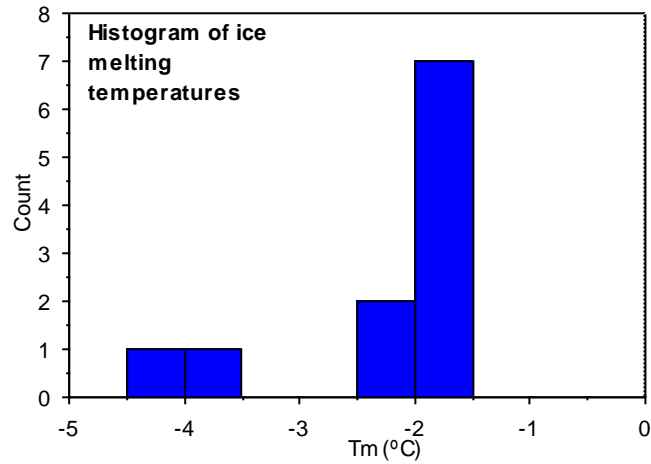


Figure 48. This mean correlates to a salinity of 3.52 wt % NaCl equivalent.

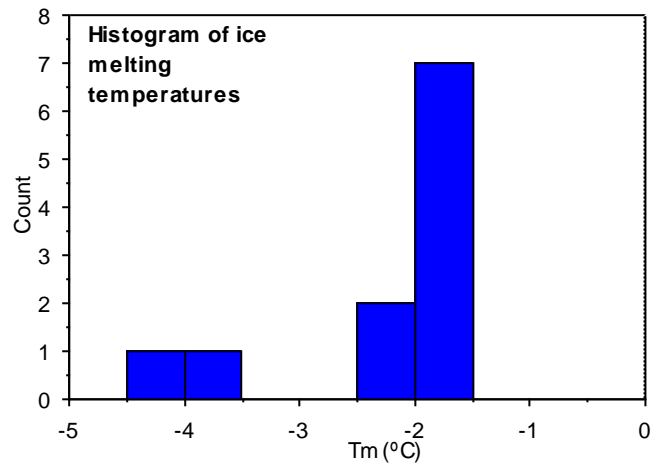


Figure 48 Histogram showing the distributions of last ice melting temperatures ( $T_m$ ) in 0.5 °C groupings.

Homogenization temperatures for the inclusions had a range from 110 to 249°C, with the lowest of these values showing signs of necking. Excluding these values the range of 205 to 249°C with a mean of 222°C, as shown by the histogram in Figure 49.

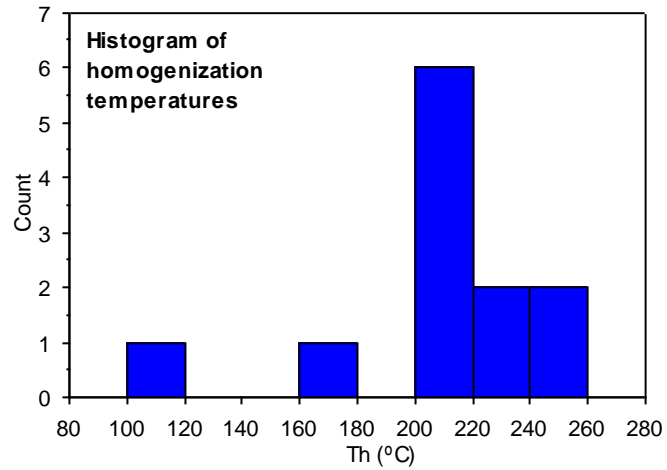


Figure 49 Histogram showing the distributions of homogenization temperatures (Th) in 20 °C groupings.

Homogenization temperature is plotted against salinity in Figure 50. The salinity of seawater, and the extremes of salinities of fluid inclusions from the TAG hydrothermal field on the Mid-Atlantic Ridge (Peterson et al., 2000; Tivey et al., 1998) are also shown for comparison.

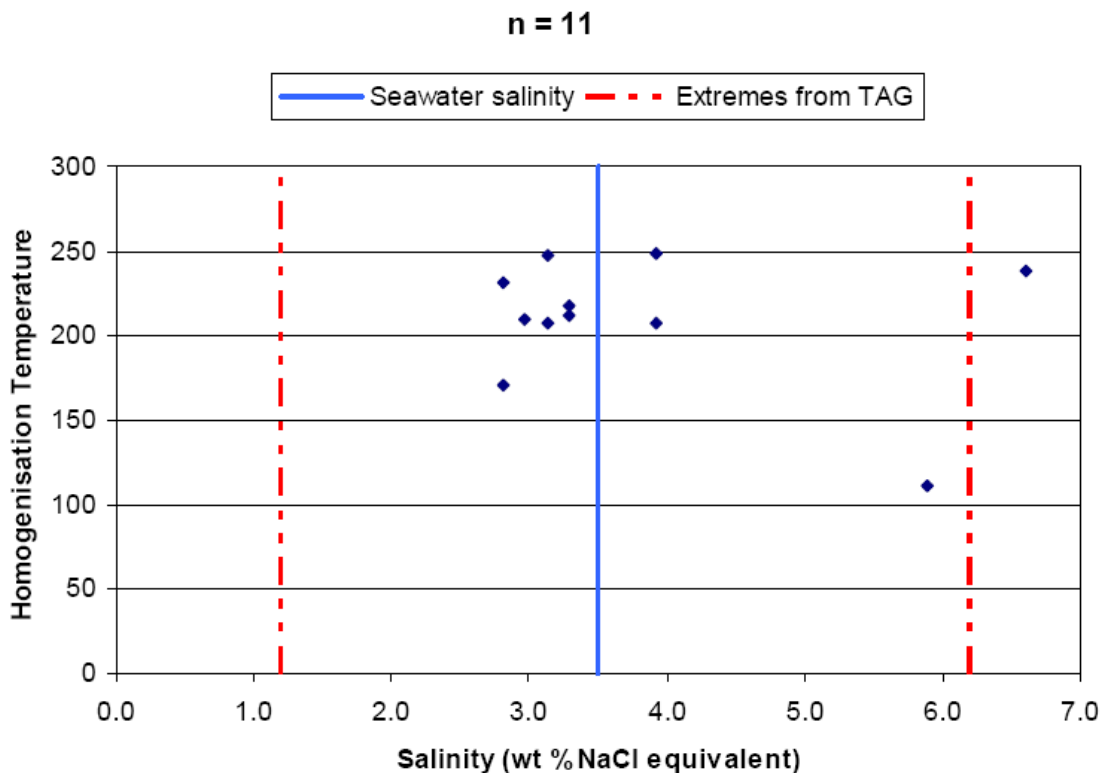


Figure 50 Graph showing fluid inclusion data for Tourounjia, including salinities of seawater and the range of those found at the TAG hydrothermal mound. From Peterson et al., 2000; Tivey et al., 1998.

## 5.10 DISCUSSION

### 5.10.1.1 ALTERATION MINERALOGY

Significant differences in the alteration assemblages of the deposits have been found. The Agrokipia B deposit, described as a P-type alteration pipe (Richards et al., 1989), shares a similar alteration assemblage to the Kokkinovounaros deposit. Both exhibit the characteristics of chlorite-illite facies of P-type alteration pipes as they contain both chlorite and illite. The lack of illite in the samples from Papoutsi indicates that it may be classed as a M-type alteration pipe with the EPS-2 borehole cutting through the chlorite-quartz-pyrite facies. The higher average magnetic susceptibility values of the EPS-2 borehole may imply that hydrothermal alteration was not as intense.

Kaolinite, nacrite and dickite are found in the two boreholes from Tourounjia. This alteration assemblage has not previously been found in the alteration pipes of Cyprus VHMS deposits and is referred to here as T-type alteration pipe (after the Tourounjia prospect). The kandite minerals are the only high temperature alteration minerals found in the ETS-2 borehole although ETS-1 also contains intermediate chlorite, illite and epidote. The ETS-1 borehole is possibly intermediate between the T-type alteration of ETS-2 and the P-type alteration of Agrokipia B or Kokkinovounaros.

The EAD-2 borehole from Alestos can also be fit into this spectrum of alteration styles as it displays predominately P-type alteration but also contains three samples identified as containing dickite in zones of explosive hydraulic brecciation.

### 5.10.1.2 ORIGIN OF ACIDIC-STYLE ALTERATION

Kaolinite, dickite and nacrite are polymorphs of  $\text{Al}_2\text{Si}_2\text{O}_5(\text{OH})_4$  and typically form in acidic conditions. In hydrothermal systems kaolinite, dickite and nacrite have been interpreted to form at progressively higher temperatures, this is based on oxygen isotope data (Marumo, 1989). Kaolinite and occasionally dickite can form as the weathering products from the breakdown of aluminosilicates. It is therefore possible that the formation of the kaolin group minerals was a low temperature supergene effect. However a hydrothermal origin is supported by the fact that putative high-temperature acidic alteration minerals (dickite and nacrite) are only recorded associated with silica-cemented breccias at the Tourounjia and Alestos prospects.

If the kaolin minerals are indeed of hypogene origin, the question of how to generate acidic hydrothermal fluids is presented. There are three ways to generate acidic fluids under the conditions that the Cyprus VHMS deposits formed. The simplest is the oxidation of abundant  $\text{H}_2\text{S}$  in the fluids by mixing with oxidised seawater. The other two are analogous to the genesis of the high and low sulphidation epithermal deposits where magmatic input or boiling is the cause of low pH fluids.

The genesis of acidic fluids through the oxidation of  $\text{H}_2\text{S}$  requires a S content higher than the  $\text{S}_2:\text{Fe}$  ratio and more oxidising conditions than those in which the other Cyprus VHMS deposits formed. The S to Fe ratios are seen to vary significantly at modern black smokers. The P-type pipes are interpreted to represent zones enriched in S relative to pyrite composition ( $\text{FeS}_2$ ) whereas the

M-type pipes show S to Fe ratios lower than pyrite composition. If this were the case then the T-type alteration found at Tourounjia and Alestos may represent the oxidised equivalent to the P-type alteration.

The genesis of high-sulphidation epithermal deposits requires the input of magmatic fluids to provide SO<sub>2</sub> to create the acidic fluids. This is the model proposed by Sillitoe et al., 1996 to explain the acidic alteration found at shallow Kuroko-style VHMS deposits and the deep (1850-2000m), presently active, Hine Hina hydrothermal field of the Lau basin. The Lau basin is situated in a supra-subduction zone and is an analogous setting to the Troodos ophiolite. The alteration assemblage found there is advanced argillic and is characterised by quartz, kaolinite, pyrophyllite, alunite and native sulphur. Alunite, pyrophyllite and native sulphur indicate fluids were rich in SO<sub>2</sub> but these have not been found at Tourounjia.

All the stable isotope studies on the Cyprus VHMS deposits point to a seawater source of the fluids, although none of the studies have included Tourounjia or Alestos where the T-type alteration is found.

The high sulphidation model of Sillitoe et al., 1996 does not explain the formation of the explosive hydrothermal breccias found at Tourounjia and Alestos. The most likely way to produce such brecciation is by a sudden increase in volume of the hydrothermal fluids through subcritical phase separation. This boiling can create conditions of lower pH than the original fluid as acidic gases (e.g. H<sub>2</sub>, HCl, H<sub>2</sub>S and SO<sub>2</sub>) are preferentially partitioned into the vapour phase. This is somewhat analogous to the steam heated alteration zone in on-land low-sulphidation epithermal deposits

Boiling is well documented in Kuroko-type deposits, but was not thought to be an applicable process in the Cyprus VHMS deposits, as the depth inferred from the overlying sediments and modern analogues (2000–2500 m) is too deep for 350° C mineralizing fluids to boil. Figure 51 shows the pressure–temperature phase diagram of seawater salinity and the normal temperature and pressure conditions under which the Cyprus VHMS deposits are interpreted to have formed.

There are two ways to get the ascending fluids to boil, namely reduce the pressure or increase the temperature of the fluids. The only way that the pressure would be reduced is if the fluids were venting at shallower water depths. Tourounjia and Alestos would have to be uplifted by at least 500 m from the depth of 2000 m inferred as the depth of ophiolite formation. It is possible that local uplift of the two prospects occurred through the process of seafloor faulting. Alternatively, the fluids that produced the acidic alteration and hydrothermal brecciation could have occurred at a later stage than the other VHMS deposits, as the Troodos ophiolite shallowed.

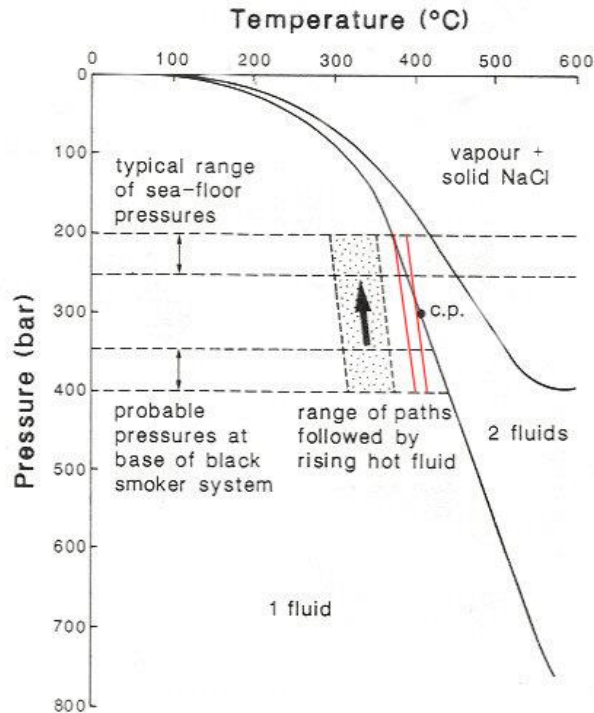


Figure 51 A P-T diagram for a NaCl-H<sub>2</sub>O solution of seawater salinity (3.2wt%). c.p. is the critical point for seawater which represents the termination of the phase boundary. The typical range of seafloor pressures corresponds to normal mid-ocean ridge depths of 2000 to 2500 m. The probable pressures at the base of the hydrothermal system correspond to hydrostatic pressure 1500 to 2000 m below the seafloor. The path of normal Cyprus type mineralizing fluids rising from the base of the system to the seafloor is plotted in the stippled region. The path of the raised temperature fluids needed to produce boiling is outlined in red (Adapted from Cowan and Cann, 1988).

The other way to produce conditions suitable for boiling is to raise the temperature of the ascending fluids. It can be seen from Figure 51 that a fluid venting at a temperature of between 380 and 395°C would be hot enough to produce subcritical phase separation. Fluids at around these temperatures have been found at modern black smokers such as the Vai Lili field in the Lau basin (Herzig et al., 1993), and the North Fiji basin (Luders et al., 2002). Sub-seafloor boiling is interpreted to be related to mineralization in these areas and (Herzig et al., 1993) postulate that it was the cause of the alteration at Hine Hina described above.

The condensation of the acidic vapour phase would allow the progressive formation of nacrite, dickite and then kaolinite as the fluids cooled. If the vapour phase mixed with too much cold seawater the pH would rise due to dilution and would reach a stage at which the kaolin minerals would no longer form. The fact that the all the kaolinite exhibited low crystalline characteristics may indicate that the metastable polymorphs of nacrite and dickite have broken down to form kaolinite.

The enrichment of Au in the Tourounjia prospect can also be explained by boiling. Gold is mainly transported as Au(HS)<sub>2</sub> in hydrothermal systems. However, it is not often found in Cyrus-type VHMS deposits as the typical high temperatures associated with their formation inhibit Au(HS)<sub>2</sub> saturation until after the fluids have been released from the vent (Hannington et al., 1995). If the fluids boiled before reaching the seafloor, then the Au would be deposited along

with the other metals. It is feasible that Ag and As were also enriched in Tourounjia in this way. Earlier phases of mineralization are included in some of the veins and included as clasts within the volcanics breccia, which is interpreted as a hyaloclastite. This indicates a multiple origin for brecciation, at least in part volcanic, and at least one event of mineralization predating the formation of the hyaloclastite. This is normal where a fresh lava flow can rip-up previously altered and mineralized material which formed during an earlier phase of 'normal' VHMS-style mineralization. Successive phases of hydrothermal activity are interpreted to be a fundamental part of the formation of Cyprus-type VHMS deposits. Thus a fresh heat source is needed to increase the temperatures at the base of the hydrothermal system or even near the site of deposition. This is conceivable, as the Troodos is interpreted to have formed from multiple magma chambers and the injection of dykes is seen to have continued after the first few phases of hydrothermal activity. A similar process may be applicable to the formation of the hydrothermal breccia found at Tourounjia.

#### 5.10.1.3 FLUID INCLUSIONS AND MINERALOGY

The XRD analyses of Alestos show that minerals of the kaolin group were not present in the samples (Thomas, 2005). This is contrary to the interpretation of Osborn, 2004 who identified dickite in three of the samples using a PIMA. This may be due to the presence of Fe-rich chlorite and the dark colour of the samples. PIMA identifications are known to be unreliable under these conditions (R. Armstrong, pers. comm. 2005). However, the identification of kaolin group minerals using XRD analysis was confirmed at Tourounjia. Furthermore, XRD analysis led to the identification of the high temperature polytypes of the kaolin group, nacrite and dickite (Marumo, 1989), as identified by Osborn, 2004 using a PIMA. The polytypes identified by the two methods correlate well in most samples. Differences can be partially attributed to the fact that the similarity of the dickite and nacrite spectra does cast doubt on the identification of one or the other when using the PIMA.

The use of XRD has allowed the positive identification of nacrite, the highest temperature polytype of the kaolin group. This confirms that high temperature, acidic alteration has occurred, proving that the alteration at Tourounjia is not simply a weathering effect. Such high temperature acidic alteration is not observed in association with Cyprus-type VHMS deposits but can be found as the result of both LS and HS epithermal deposits in the steam-heated overprint (Hedenquist et al., 1996). The presence of Na-alunite in some of the samples supports this interpretation. A steam-heated overprint is clear evidence of boiling.

The salinities derived from the temperatures of last ice melting of fluid inclusions clustered around the salinity of seawater. Some, however, were notably lower or higher than this. Comparison of the salinity of these inclusions with those found at a modern hydrothermal vent is possible due to work done by (Peterson et al., 2000; Tivey et al., 1998) on the TAG hydrothermal field on the Mid-Atlantic Ridge (Figure 50). Comparison shows that this variation away from the salinity of seawater appears to be a natural consequence of hydrothermal circulation through oceanic crust. This suggests that seawater is the dominant fluid involved, but that the presence of small amounts of a second fluid cannot be discounted. This contrasts with sub-aerial epithermal deposits, which have a salinity much lower than that of seawater, usually <1 wt% NaCl equivalent (Hedenquist et al., 1996),

as the fluids are mainly derived from meteoric water. This implies that if an epithermal model is most appropriate, the setting was marine.

The homogenization temperatures of the fluid inclusions, which range up to 249°C, are a minimum temperature of trapping. This suggests that the mineralization at Tourounjia is not the result of low-temperature off-axis fluid circulation as proposed by Prichard and Maliotis, 1998 to account for the high gold values found in silicified umbers. The  $T_H$  is lower than that found in two Cyprus VHMS deposits (~350°C) by Spooner et al., 1977, but does, however, sit within the range of 182-437°C for liquid dominated low salinity inclusions examined by Kelley *et al.* (1992) through a cross section of the Troodos ophiolite. The  $T_H$  is also broadly consistent with the temperature of formation of epithermal deposits (<300°C).

The platy pyrite (Figure 44B) appears to be replacing gypsum, which often shows a platy habit and is commonly found as gangue in Cyprus-type VHMS deposits. The fact that the other plates appear to have been replaced by silica is not surprising due to the high degree of silicification of the sample as a whole.

The mineralization includes a number of sulphide phases typical of Cyprus VHMS deposits (mostly copper sulphides and sphalerite) but also a number that are not. Arsenic is not found in Cyprus-type VHMS deposits, but is often present in epithermal deposits. Arsenopyrite, however, is not found in HS deposits, and is a clear indication of a LS epithermal system. The many metals found as impurities within the arsenopyrite are slightly ambiguous. Ni and Co are seen in Cyprus VHMS systems (Constantinou and Govett, 1973) but Sb is much more indicative of epithermal deposits (Hedenquist et al., 1996).

Arsenopyrite is found in mineral assemblages of a number of gold-rich VHMS deposits in other parts of the world including the Cu-Au-As Boliden deposit of northern Sweden (Hannington et al., 1999). Boliden is, however, heavily metamorphosed and its classification as a VHMS deposit is debated.

Cinnabar is another mineral not found in Cyprus-type VHMS deposits, but it is not unusual in epithermal deposits, and has even been mined from sinters of LS epithermal systems (Sillitoe, 1993). Cinnabar is found in the Eskay Creek gold-rich polymetallic VHMS deposit in British Columbia in a mineral assemblage which also includes arsenopyrite (Hannington et al., 1999).

## 6 Whole rock geochemistry

Three whole rock geochemical datasets were available to the project:

- Data from the Cyprus Crustal Study boreholes—in particular boreholes CY2 and CY2a were useful as they penetrated the Agrokippia B sulphide deposit and provide a comparative backdrop against which the surface samples could be compared. The CY2 boreholes cored a section through the Upper and Lower Pillow Lava sequences (after Gass, 1960), probably straddling the Upper and Middle zones as described by Robinson and Hall, 1983
- Data from Adamides, 1990 comprise a series of stratigraphical traverses across the north-eastern limb of the ophiolite.
- Data provided by Eastern Mediterranean Minerals comprising analyses of regional rock chip samples analysed by ICP (semi-quantitative?). These consisted of 1133 samples analysed for 8 major elements and 25 trace elements and were located across the northern Troodos.

The rocks in all datasets are entirely igneous, comprising suites belonging to the high MgO and high SiO<sub>2</sub> suite of depleted tholeiites, which have been described as having somewhat boninitic affinities. The comprehensive geochemical datasets include major and trace elements, analysed in a variety of laboratories. The data were incorporated into the GIS as a series of spatially resolved data tables. The lithogeochemical datasets were reprocessed to see whether discriminant functions could be constructed from the datasets in order to recognise (i) favourable rock types and (ii) alteration styles and display these parameters in a graphical format within the GIS.

### 6.1 DISCRIMINANT PLOTS

Simple classification of volcanics is possible using a variety of compatible and incompatible, immobile (or more correctly conserved) elements. The CY2, 2a and Adamides datasets have clear potential in this area.

Figure 52 shows a plot of zirconium versus yttrium for the complete dataset, which is one of many useful diagrams for igneous classification. The data are coherent, particularly with respect to useful elements and the plot clearly confirms the largely tholeiitic affinity of the Upper and Middle zone rocks. Rocks showing very low Y and Zr are likely to be highly altered and these are the ones displaced more into the calc-alkaline field due to alteration effects.

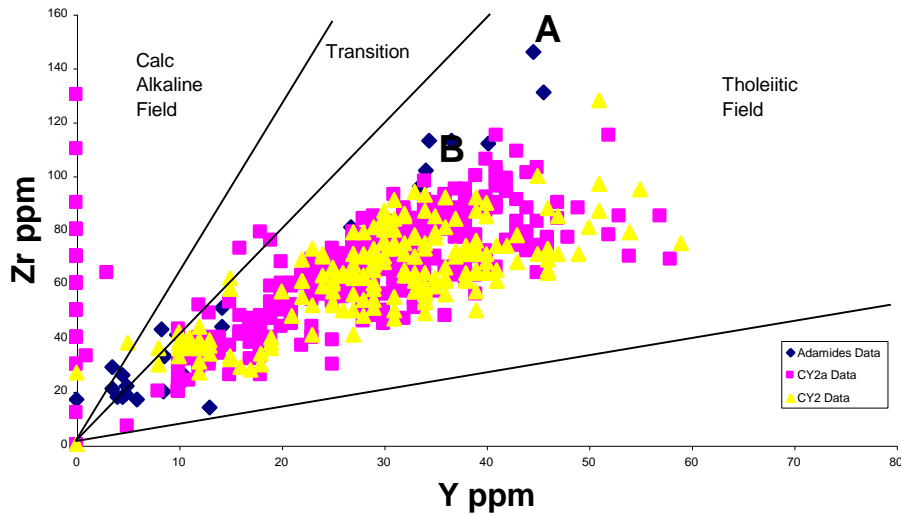


Figure 52 Zirconium versus yttrium values for CY and Adamides datasets.

It is important to note that in these immobile-compatible-incompatible plots, straight lines that pass through the origin define igneous field boundaries. Data that are displaced up and down parallel to these lines are probably altered since alteration causes either covariant dilution or concentration effects. An example of this is shown by the positions of samples A and B on Figure 52. They have identical Zr to Y ratios but the analytical values of both elements in sample B are lower, possibly due to the addition of silica, for example, to the rock which dilutes both component A and B by the same ratio.

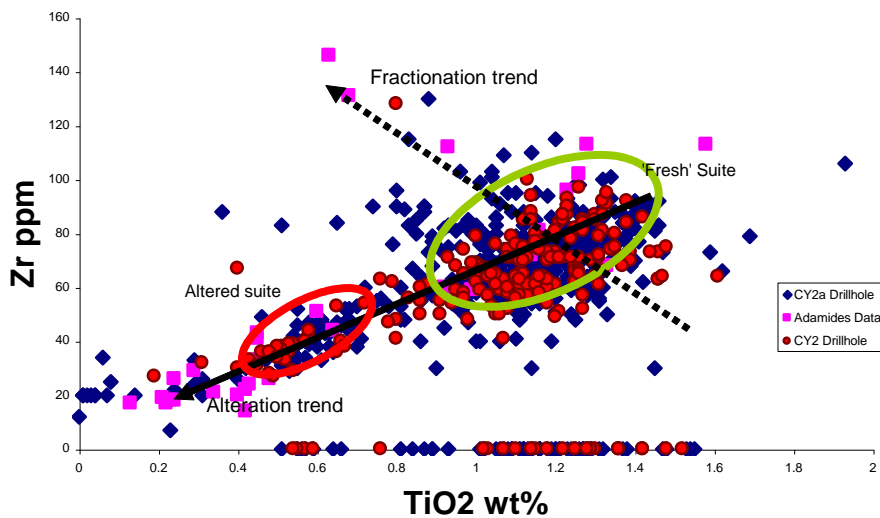


Figure 53 Plot of zirconium versus titanium for the dataset.

Other simple plots of the preliminary dataset indicate that both alteration and fractionation effects may be apparent. Figure 53 shows a compiled plot of the zirconium and titanium data for the same rocks. There are two broad clusters of data that lie on a line subtending the origin. The spread along this line shows the effect of covariant dilution due to alteration already suspected in Figure 52. However, an additional feature is the spread of data from the upper cluster towards the top-left of the graph. This marks an increase in zirconium with a

concomitant decrease in titanium, which is likely to be a function of igneous fractionation.

Discriminant plots, using immobile elements, suggest that sub-classification of the volcanics may be possible. Figure 54 shows a plot of  $\text{Al}_2\text{O}_3$  versus  $\text{TiO}_2$ . Both elements may be considered immobile in VHMS systems. There is clear evidence of alteration with again a strong distribution of data along lines subtending the origin. In addition, there are clearly two clusters of data broadly connected by a line shown by the solid arrow. This trend is not alteration but can be equated to igneous fractionation. This indicates that there may be two sub-groups of igneous rocks (marked by oval fields), defined petrochemically and linked by fractionation processes from a parent source. This sort of subdivision may be a useful lithogeochemical discriminator for volcanic units, even when they are altered.

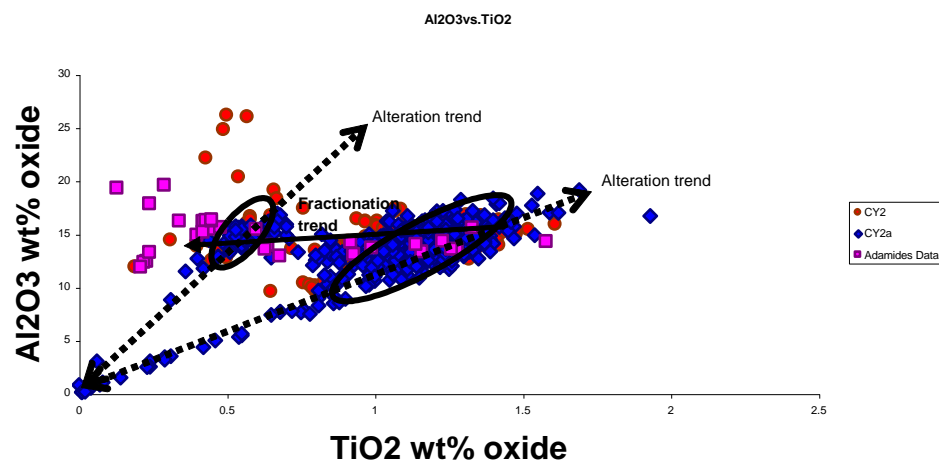


Figure 54 Aluminium versus titanium data plotted for the dataset.

## 6.2 HYDROTHERMAL ALTERATION

VHMS deposits are generally associated with distinctive mineralogical and geochemical alteration envelopes, usually expressed as major variations in mobile major and trace elements in the adjacent host rocks. Such alteration halos are often regional or sub-regional in scale and hence may be useful for prospecting in new or covered prospective terrain. The literature on the subject is vast, but the wealth of studies has yielded a few useful universal patterns to alteration, which may be applicable to Cyprus. Whilst trace element data are useful to screen alteration versus fractionation effects (e.g. Figure 53), it is more common to assess alteration in terms of major element data.

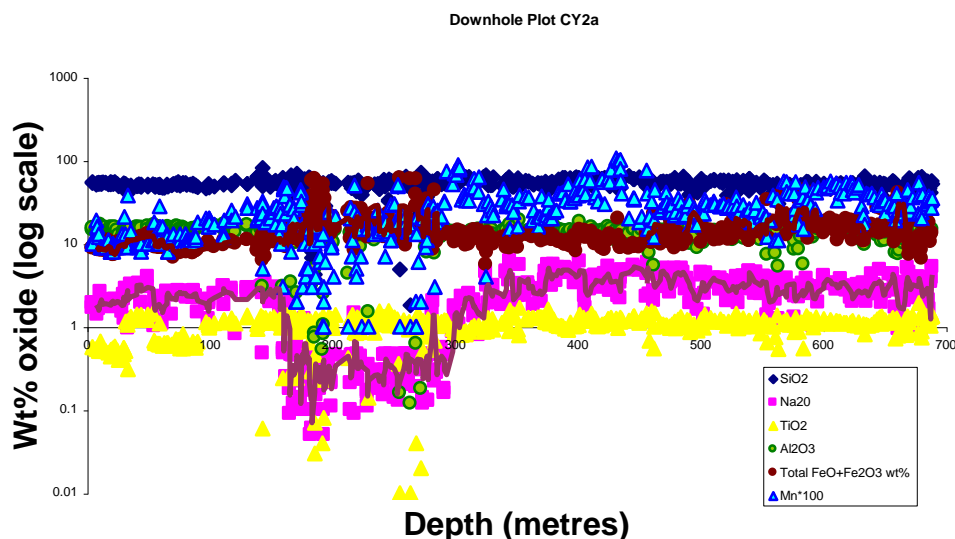


Figure 55 Down-hole graphical log of CY2a showing selected oxide variation

With this in mind, the borehole dataset were been processed to test some of the simple patterns observed elsewhere. Holes CY2 and 2a are particularly useful since they drill through a mineralized package of rocks and there is a comprehensive systematic whole rock dataset for the entire lengths of both holes. Figure 55 is a simple down-hole plot with increasing depth shown on the x-axis for some of the major elements in CY2a. There are major changes in the mineralized interval from 170 to 300 m. The presence of abundant pyrite is expressed as the total iron content (brown symbols). More interesting is the trace for Na<sub>2</sub>O where strong depletion is linked to the mineralization, but more significantly for a significant depth down the hole below the massive sulphide body.

### 6.3 HYDROTHERMAL ALTERATION INDICES

The simple plot in

Figure 55 suggests that lithogeochemistry might be useful so the data was treated using some of the published alteration indices tried elsewhere. These are:

1. Sericite index ( $K_2O/[K_2O+Na_2O]$ )—linked to the formation of sericite, particularly typical in felsic-hosted VHMS deposits
2. Chlorite index (CAI) ( $[MgO+Fe_2O_3]/[MgO+Fe_2O_3]$ )—linked to elements present in chlorite, a key alteration mineral in mafic systems
3. Ishikawa index (II) ( $100*[MgO+K_2O]/[Na_2O+K_2O+CaO+MgO]$ )—developed for the Kuroko district of a range of mafic to felsic host volcanics (see Date et al., 1983; Ishikawa et al., 1976)

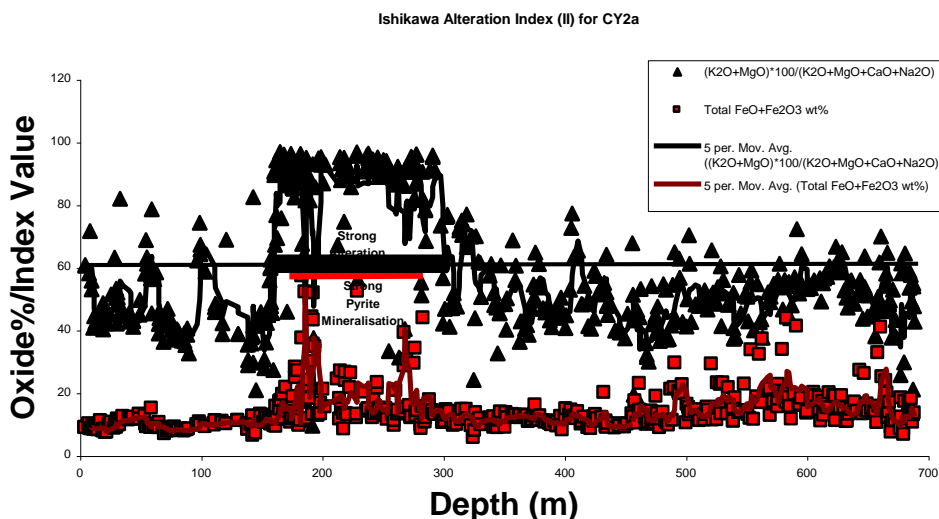


Figure 56 Down-hole plot of CY2a showing calculated Ishikawa alteration index and total iron as a graphical log (II=60 marked as a horizontal line).

Figure 56 shows the down-hole plot of CY2a with the Ishikawa alteration index and total iron plotted. It is clear that the strong alteration pattern is seen both in the hanging wall and more strongly in the footwall of the massive sulphide body. It would appear that this index might be a useful exploration parameter to plot for regional lithogeochemical datasets.

To progress the study of alteration recorded in the regional lithogeochemistry further the analyses undertaken on the CY boreholes were duplicated for the two major whole rock databases, namely:

- Whole rock geochemistry in a series of traverses across the gabbro to UPL series in the northern Troodos, generated by N. Adamides (179 samples, 10 major elements, 13 trace elements)—the *Adamides dataset*
- Regional rock chip ICP geochemistry (semi-quantitative?) by EMM (1133 samples with 8 major elements and 25 trace elements) across the northern Troodos—the *Eastern Mediterranean Minerals dataset*

Initially the data was screened for compatibility with the test sets. This was carried out largely by compiling bivariate plots of incompatible elements and comparing the results with the test data that was high precision data from the complete section of the Troodos volcanics.

### 6.3.1 Adamides dataset

The initial plot of Zr against Y (Figure 57) shows a very strong correlation pattern, very similar to the bulk of the data from the CY2 and CY2a drill cores. Likewise a plot of Zr against TiO<sub>2</sub> (Figure 58) shows identical patterns to the CY2 dataset with the bulk of the data plotting as one comagmatic group bracketed by the red lines with a minor indication of more fractionated rocks shown by the arrow trend (identical to the trend shown in CY2). The dataset thus appears to be of comparable quality to the CY2 data.

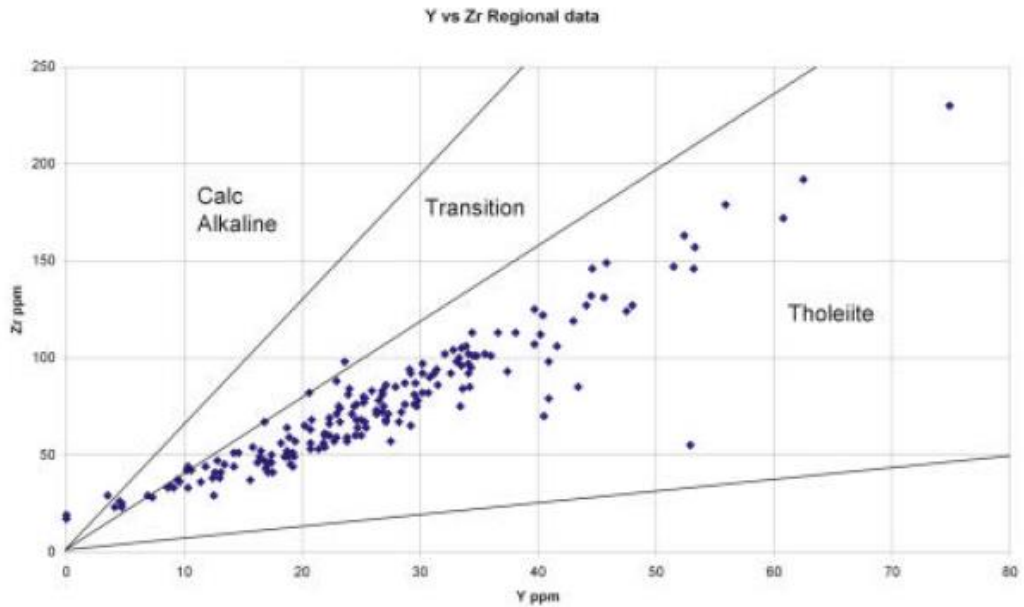


Figure 57 Yttrium versus zirconium for the Adamides data set.

Alteration indices were then calculated from the major element data, both CAI and II. CAI ranges from 0.22 to 0.93 and II from 5.68 to 93.76. The alteration index data were then incorporated into the project GIS and the results shown in Figure 59 (CAI) and Figure 60 (II). There is apparently good correlation between the indices with anomalies in the CAI coincident with known mineralization associated alteration but also several anomalies that are more subtle. These require further investigation and show that geochemical data are important for exploration models and should be used in any future prospectivity mapping.

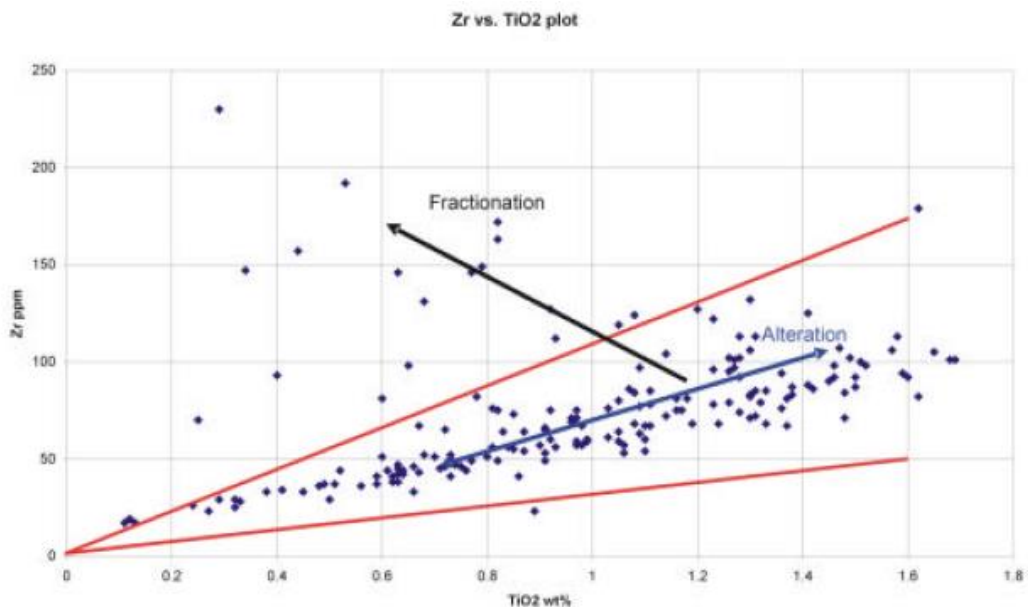


Figure 58. Titanium oxide versus zirconium for the Adamides data set

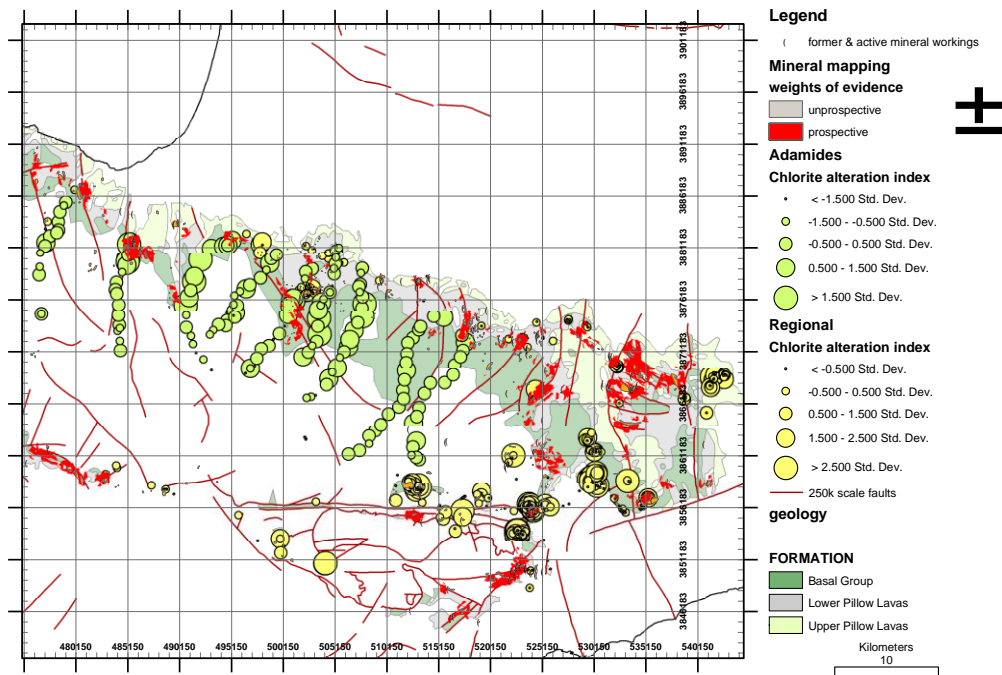


Figure 59 Comparison of chlorite alteration index against digital 1:250,000 geology and mineral prospectivity.

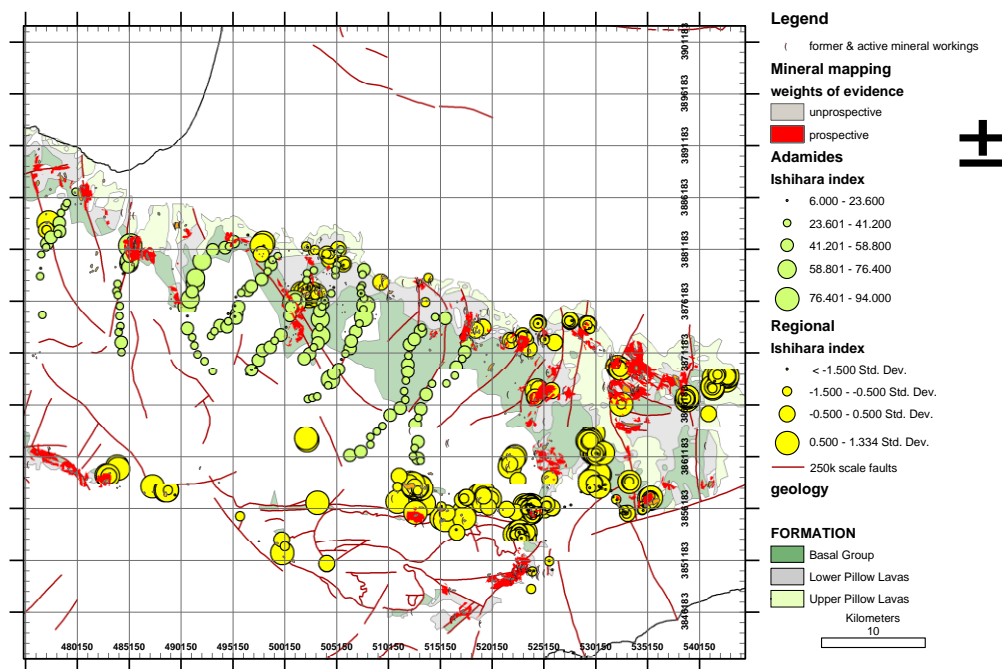


Figure 60 Comparison of Ishihara alteration index against digital 1:250,000 geology and mineral prospectivity.

### 6.3.2 The East Mediterranean Minerals dataset

This package of data is far more challenging both in terms of data volume and possibly data quality. Analyses are quoted as percent element not the usual oxide percentages, which may suggest they are only semi-quantitative. Nevertheless it is possible to calculate oxides from the data. Simple plots of Y versus Zr and

TiO<sub>2</sub> versus Zr (Figure 61 & Figure 62) indicate that there may be some problems with the data. Zircon is highly insoluble to many acid attacks routinely used in geochemical analysis and the low Zr here may be due to incomplete digestion. TiO<sub>2</sub> values also may be a little low given the fact that these are largely mafic rocks which although altered would be expected to maintain titanium as a ‘conserved’ element.

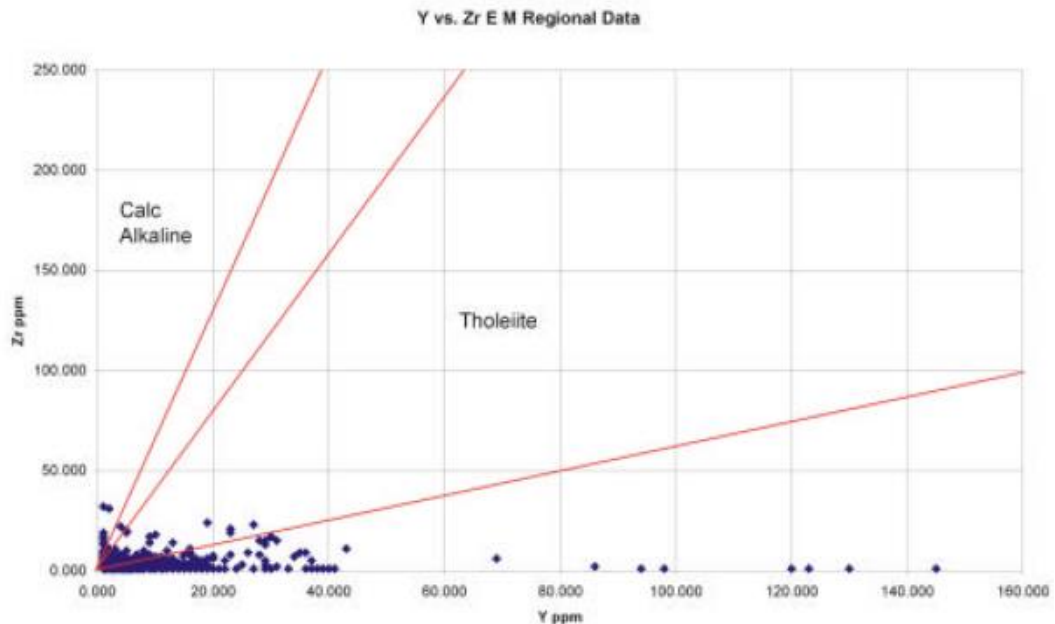


Figure 61 Yttrium versus zirconium for the EMM regional data set.

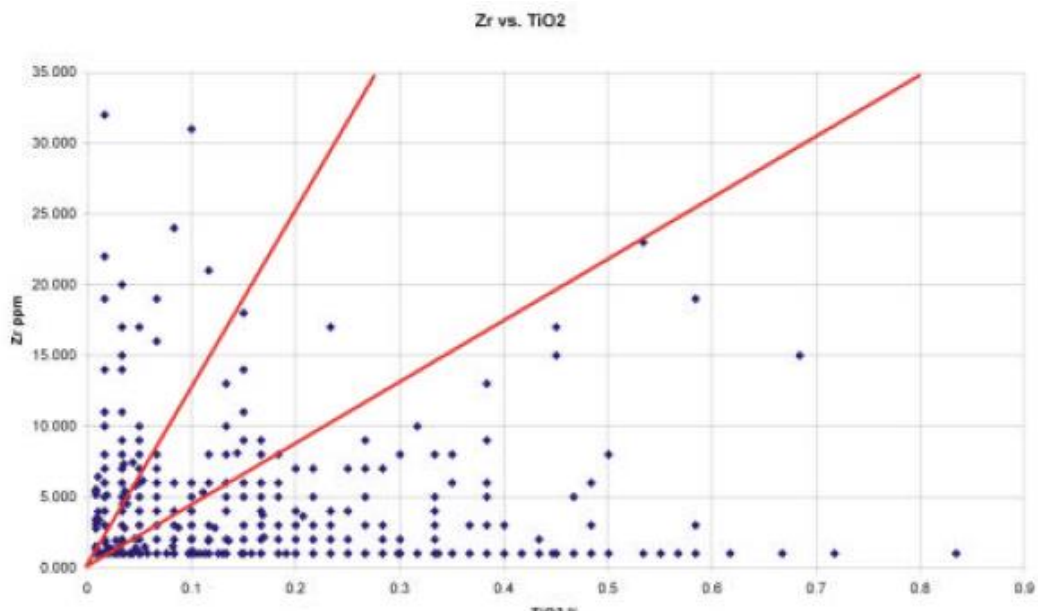


Figure 62 Titanium oxide versus zirconium for the EMM regional data set.

Nevertheless, the data was processed to produce major oxide data to enable CAI and II to be calculated. It is clear that most of the rocks are highly altered with CAI ranging from 0.22 to over 9 (1 is highly anomalous). These results are again plotted as bubble plots in the project GIS (Figure 59 & Figure 60). The plots show the area of the Adamides dataset discussed above with the East Mediterranean data clearly useful on a more regional basis. However, as the data are highly irregularly distributed in terms of their spatial location it would not be

prudent, using geostatistical or other gridding techniques, to construct maps of element distribution or alteration index. Therefore, this data was not used in the prospectivity analysis as this requires that data are presented as raster (gridded) maps.

## 7 Mineralogical research

The bulk of recent, post WWII copper production from Cyprus has focused on the massive and disseminated sulphide bodies, with production of both sulphide concentrates from which copper, zinc and sulphuric acid have been produced. However, more recently, the focus has been on copper extraction using SX-EW techniques applied directly to secondary copper ores suitable for acid leaching. Given that the variability of leach efficiency by this process is determined by mineralogy, it was decided to focus a small research effort into mineralogical research on three secondary sulphide occurrences in the Troodos.

### 7.1 PROCESSES OF SUPERGENE UPGRADE IN VHMS SYSTEMS

Work on modern VHMS systems has established that the primary composition of massive sulphide deposits can be later modified by high-temperature metasomatism, low-temperature hydrothermal oxidation, submarine weathering, and degradation by mass wasting to oxides before the deposits are finally preserved in stratigraphic record. Subsequent to this, deposits can be further modified by subaerial oxidation processes following uplift, exposure and erosion.

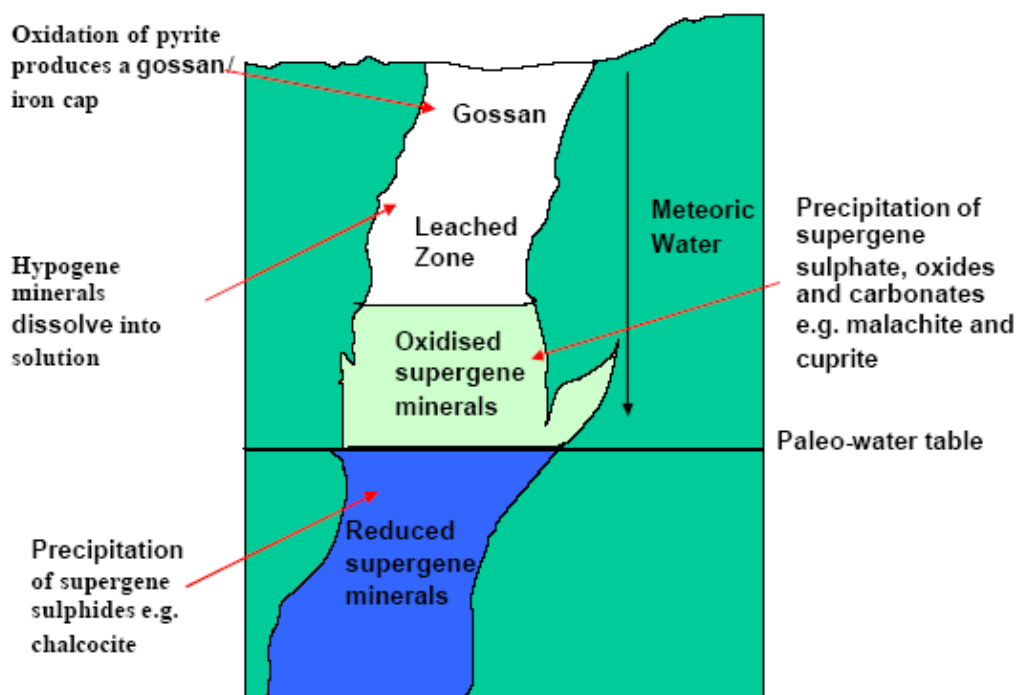
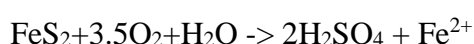


Figure 63 Schematic diagram for the formation of supergene mineralization by meteoric water

The process of subaerial supergene enrichment of VHMS deposits on Cyprus, like many deposits elsewhere is controlled by the oxidation of pyrite by supergene fluids passing down through the deposit: The presence of many iron oxide-rich gossans is testament to the major process of iron oxidation during terrestrial weathering. The key reaction in the process is:



This reaction effectively creates sulphuric acid through pyrite oxidation leading to a dramatic decrease in pH in the meteoric fluid as this dissociates to produce hydrogen ions. If the pH drops sufficiently then the fluid will be capable of dissolving chalcopyrite, with copper sulphates being the most soluble complex for the metal. The fluid descends under gravity utilising available porosity and permeability. Near the water table, mixing of low pH surficial water with groundwater produces dilution, pH and redox changes, encouraging the precipitation of supergene copper minerals. In the wet, but oxidising region above the water table dilution causes the precipitation of oxidised minerals like malachite, cuprite and jarosite. Whilst below the water table reducing conditions favour the precipitation of sulphides like chalcocite, digenite, djurleite, bornite and covellite. The precipitation of sulphides will preferentially occur on the edges of, and fractures within chalcopyrite where both copper and sulphur are readily available. The process is summarized in Figure 63

### **7.1.1 Mineralogical study of supergene orebodies—background and sampling strategy**

In order to investigate the supergene mineralogy of the Troodos deposits, an MSci post-graduate student project (Chris White) based at the Royal School of Mines, focused on a mineralogical study of material collected from four deposits in the western Troodos. These deposits are:

- Phoukassa-Skouriotissa
- Phoenix
- Three Hills
- West Apliki.

The Phoenix deposit comprises a zone of low-grade secondary sulphide mineralization developed structurally lower than previously worked massive sulphides at Phoukassa-Skouriotissa (see Figure 65). The massive sulphides at Phoukassa have clearly suffered weathering both on the seafloor to form umbers (Figure 66) and probably more latterly by downward migrating meteoric waters. The working hypothesis for the secondary sulphide deposit is that the zone developed as a transported supergene sulphide zone. Acidic, copper-bearing solutions generated by meteoric water flow through the oxidising massive sulphide lens on the upper benches migrated down slope through the altered footwall volcanics to the disseminated pyrite within altered volcanics below at Phoenix. Copper sulphides were then reprecipitated on the low- grade disseminated pyrite within the altered volcanics forming the low-grade secondary sulphide body. Given this hypothesis, the strategy was to collect a series of samples from the massive sulphide, the leached lavas and the secondary sulphide zone down through the profile.

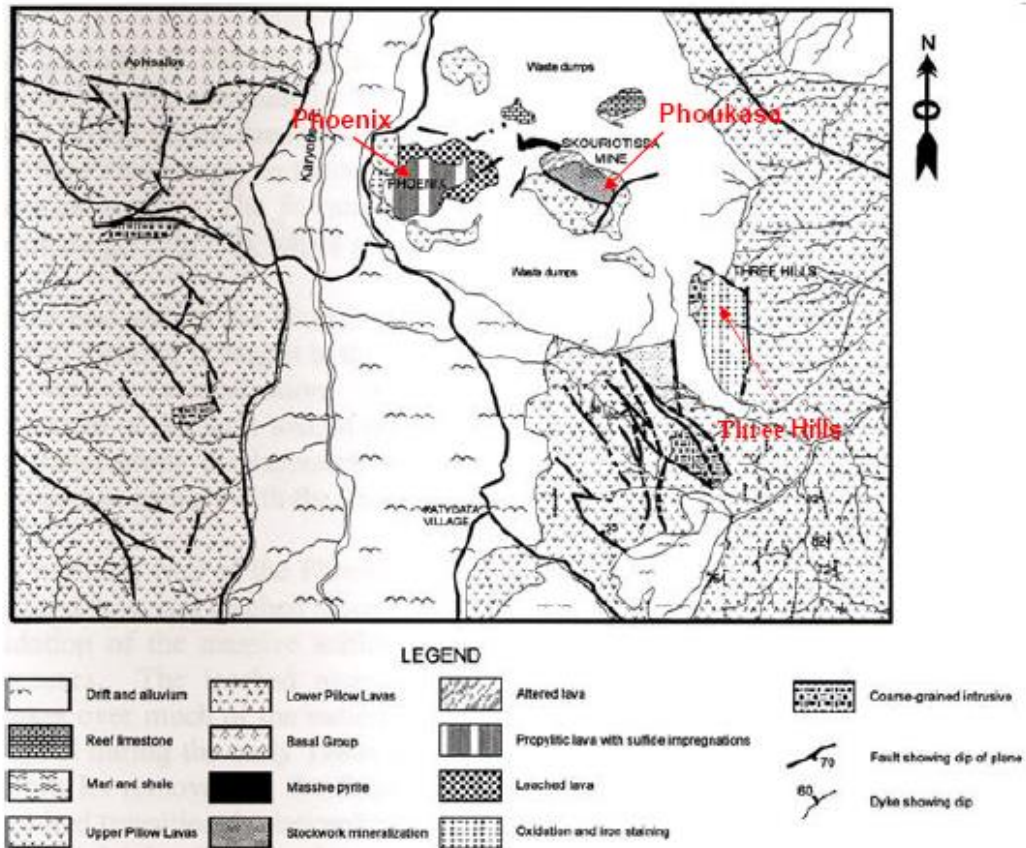


Figure 64 Geological Map of the Skouriotissa region, note Phoenix, Phoukassa and Three Hills orebodies. Scale 1:50 000, Phoenix Phoukassa Three Hills.

A set of samples was collected from the Three Hills pit for a similar study to that at Phoenix, although here the deposit appears to represent a simple oxidation zone above an exposed low-grade sulphide stockwork. Here it is speculated that the secondary sulphide zone is a simple in-situ oxidation upgrade to an existing chalcopyrite-pyrite stockwork mineralization (abundant primary chalcopyrite is obvious in hand specimen).

Lastly, a set of rock-chip samples from the West Apliki secondary sulphide prospect zone was submitted by N. Adamides for study, believed to be representative of potential undeveloped resources in the region.

### 7.1.2 Phoukassa (Skouriotissa) and Phoenix orebodies

The Skouriotissa mine initially exploited the substantial stockwork zone and overlying primary massive sulphide lens of hypogene sulphide. Immediately overlying the sulphide lens is a layer of amber (Figure 66), indicating that a degree of pre-lithification seafloor alteration occurred. The Phoenix orebody is situated west and topographically below the Skouriotissa pit where the Phoukassa body was mined. Phoenix consists of predominantly disseminated and stockwork mineralization well below the remaining massive sulphide mineralization exposed on the upper rim of the pit. The host rocks exposed in the base of the pit are a distinctive green grey colour due to the dominant chlorite and smectite (propylitic) alteration. Above this, and below the massive sulphide layer, there is a distinctive oxide-stained bleached layer and the boundary between the bleached and grey-green alteration appears to mark the transition from oxidised (white) to

reduced (green grey) assemblages. This may well indicate the level of the paleo-water table during subaerial weathering.

From top to bottom the investigated profile is defined as a) massive sulphide; b) footwall stockwork; c) bleached volcanics (leached zone) and d) secondary (sulphide) enrichment zone (Figure 65)

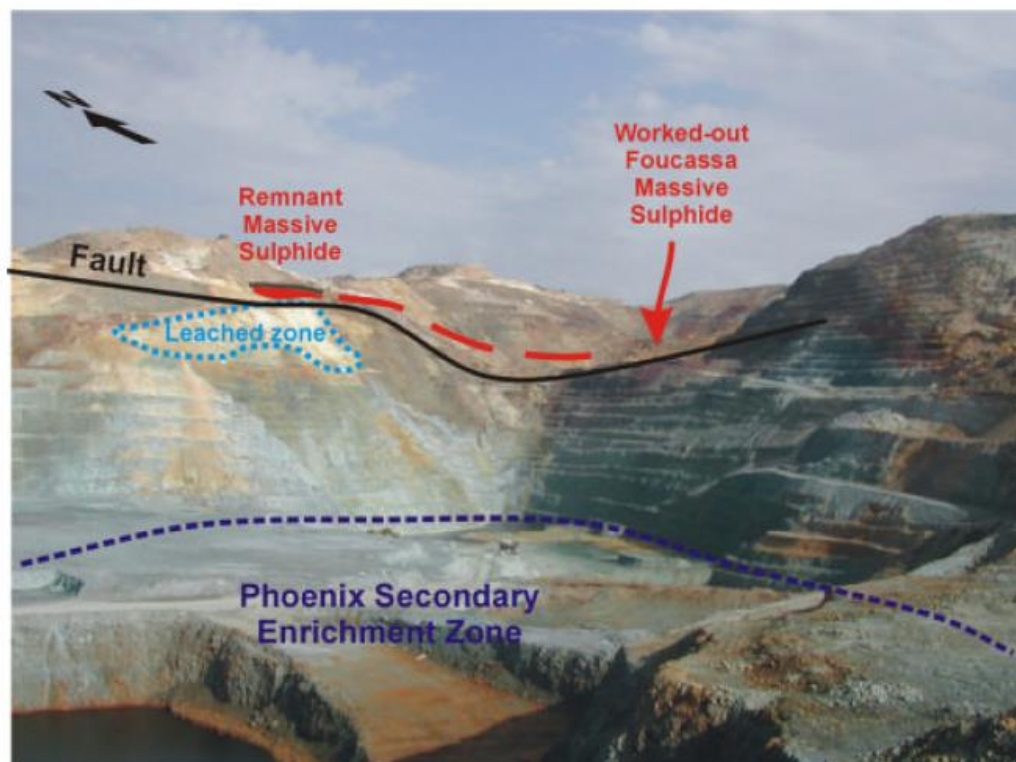
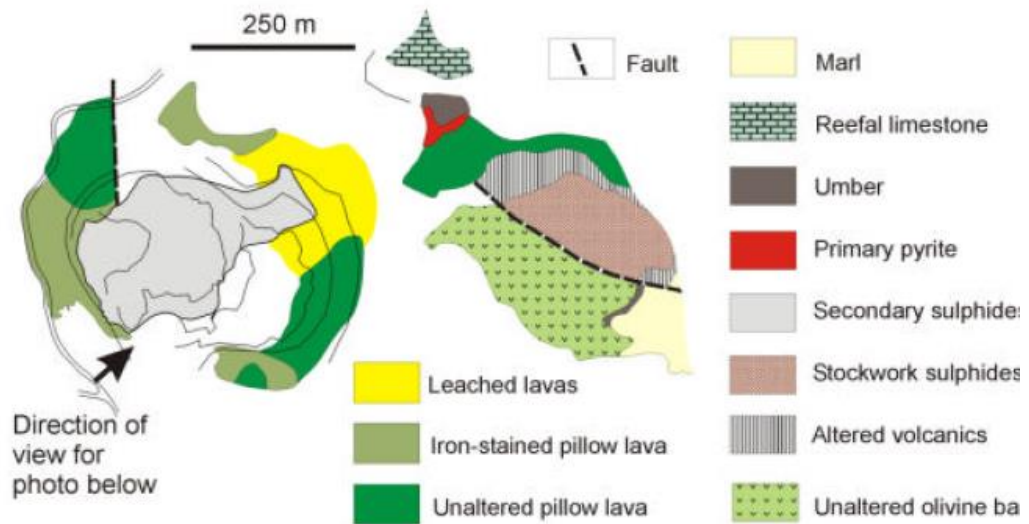


Figure 65 Simplified Geology of the Skouriotissa-Phoenix open pit—note as this a view of the pit that works the supergene sulphides the main stockwork zone is hidden from view

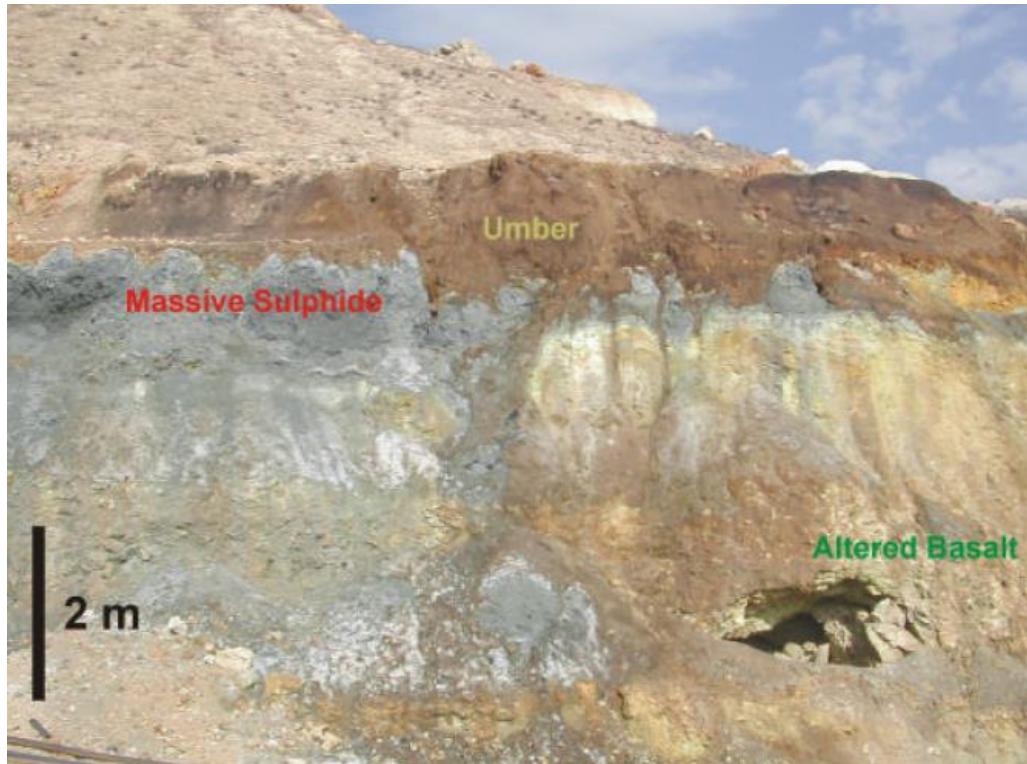


Figure 66 Detail of the massive sulphide–umber interface, Skouriotissa.

*Massive sulphide*

The massive pyrite lens overlying the stockwork shows a mixture of crystal sizes and shapes (Figure 67). The sulphides are very friable and the pyrite is somewhat oxidised, with goethite and limonite visible in hand specimen. Samples also contain abundant unidentified sulphate minerals (Figure 68), and some fine malachite veins. From this, it is likely that the remnant massive sulphide lens has been exposed to supergene processes in the form of oxidation reactions. Despite this, significant chalcopyrite is still visible in hand specimen indicating an incomplete oxidation process.



Figure 67 Hand specimen of massive pyrite from the Phoukassa deposit.



Figure 68 Hand specimen of supergene sulphate mineralization from the Phoukassa deposit.

Hypogene sulphides above and within the oxidised layer are characterised by the relatively low abundances of both chalcopyrite and sphalerite. The only abundant sulphide is pyrite, together with goethite, and limonite pseudomorphs (Figure 69).

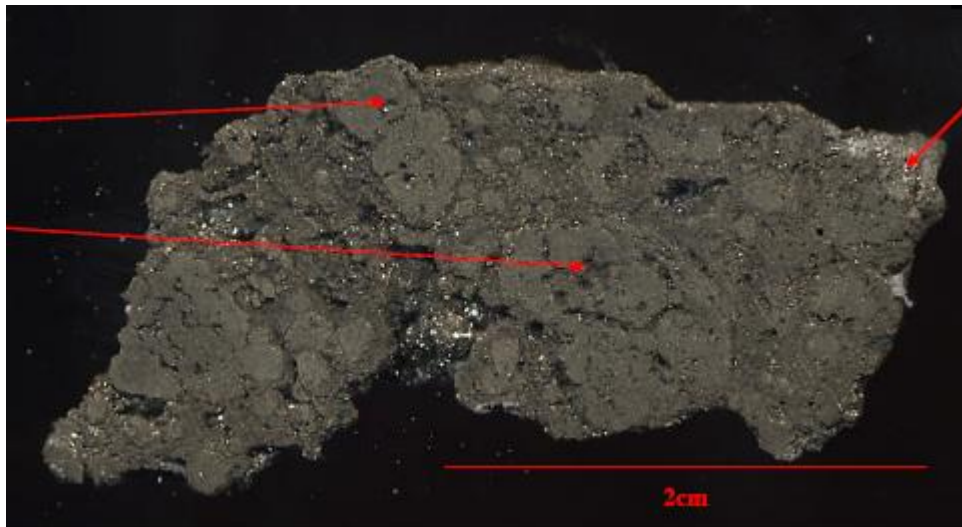


Figure 69 Sugary pyrite showing oxidation to hydrated iron oxides.

#### *Footwall stockwork*

The stockwork zone present at Phoukassa consists of veins ~1cm in thickness, consisting of pyrite, chalcopyrite, and some chalcocite, along with iron oxide staining (Figure 70). Reflected light microscopy shows that the veins contain some euhedral pyrite crystals (~3mm). Chalcopyrite crystals within the veins are largely subhedral and commonly completely pseudomorphed by digenite and chalcocite, and in some cases djurleite. Some fractures within chalcopyrite show alteration to bornite plus covellite, although this is rare. Quartz is the most common gangue phase in the veins.

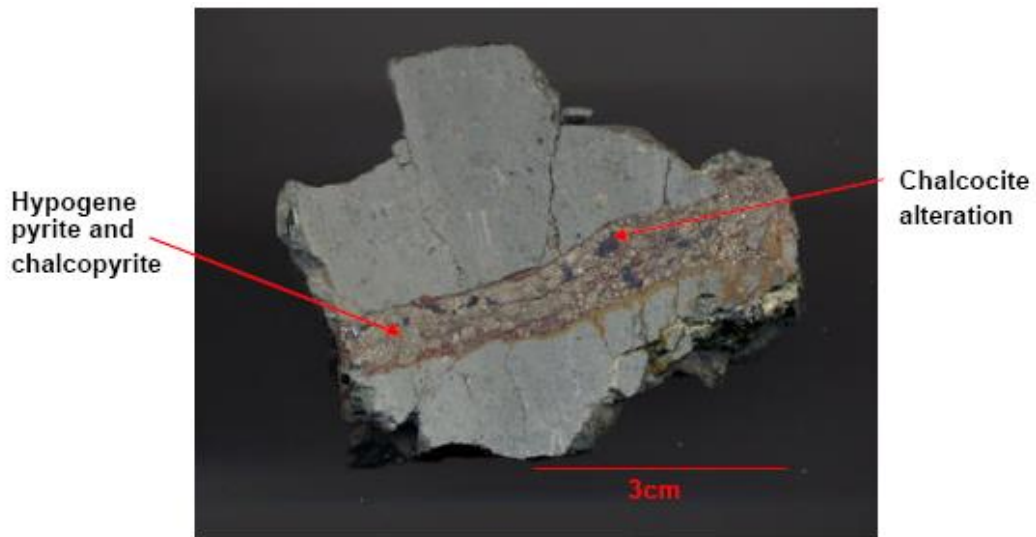


Figure 70 Hand specimen from Phoukassa showing stockwork vein cutting through the chlorite, smectite host rock.

Disseminated mineralization from footwall altered volcanics at Phoukassa shows the presence of (~0.5mm) euhedral crystals of pyrite and chalcopyrite (Figure 71). Supergene mineralization is observed on crystal edges and reflected light microscopy shows that chalcocite, digenite and minor covellite are the main minerals, no bornite was observed. Alteration rims on the chalcopyrite crystals are thin (<0.15 mm) The mineralization sequence for the Phoukassa deposit is shown in Figure 72.



Figure 71 Hand specimen from the Phoukassa deposit showing disseminated mineralization.

Hypogene	Supergene
Pyrite	
Marcasite	
Chalcopyrite	
Digenite	
Chalcocite	
Djurleite	
Bornite	
Covellite	

Figure 72 Mineralization paragenesis for the Phoukassa deposit.

*Bleached zone*

Copper mineralization is evident within the bleached zone in the road section below the small sulphide lens (Figure 73) where fine veins of malachite along with isolated crystals of cuprite (Figure 75 and Figure 74), are found. Vuggy altered rocks this zone contain cavities lined with jarosite and a number of unidentified iron sulphates.



Figure 73 Position in Phoenix pit showing supergene malachite veins, photo viewing north, December 2003.

The precipitation of these carbonates, oxides and sulphates requires oxidising conditions and so it must have occurred above the interpreted paleo-water table.

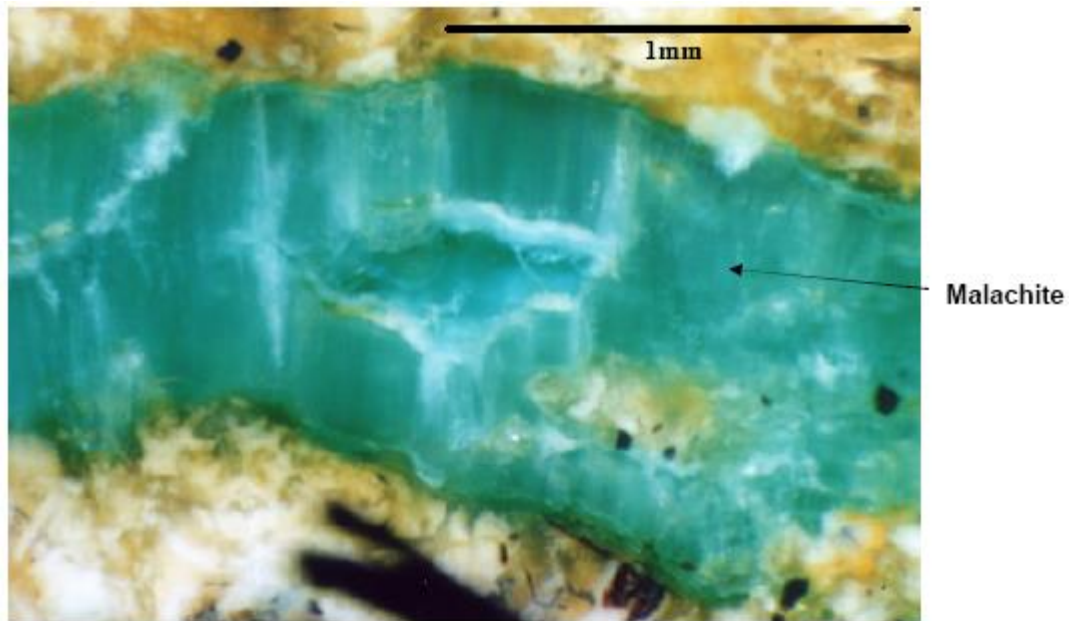


Figure 74 Reflected light microscopy photograph (x5 mag.) of malachite vein.

At the base of this bleached zone, sulphide material was collected illustrating a more complex formation history. The sample shown in Figure 75 clearly shows the overprinting of malachite veining by later black chalcocite, indicative of a secondary sulphide overprint onto an oxidised assemblage. This may be indicative of fluctuations in the height of the water table through the weathering history.

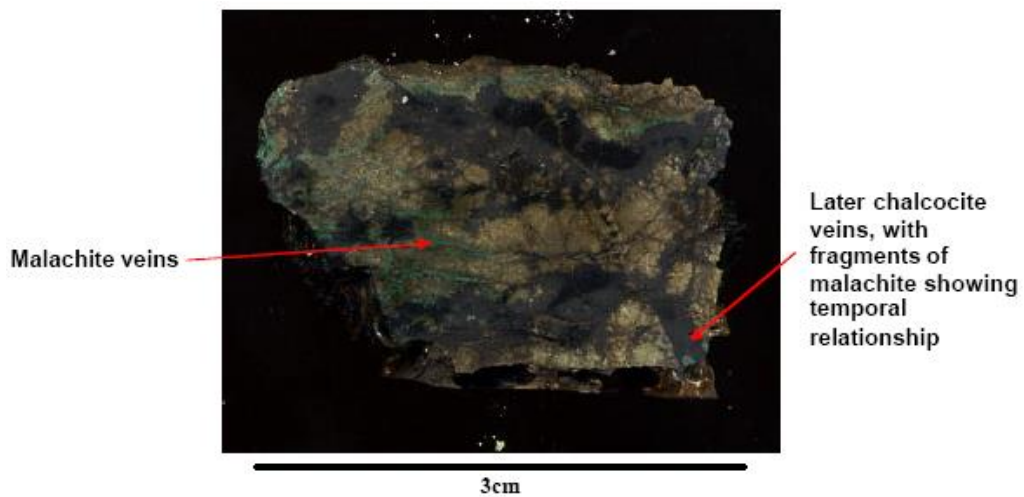


Figure 75 Hand specimen showing veins of supergene malachite (green), with later chalcocite veins (black).

### *Secondary sulphide zone*

At the base of the open pit investigated in 2003, the main mineralization being mined forms a 'stockwork' and disseminated orebody developed in highly fractured, propylitised volcanics. The fracture types show three distinctly different associations (hypogene, mixed hypogene-supergene and wholly supergene mineralized fractures), suggestive of a rather complex formation history which likely relates to both networks developed on the seafloor and

fractures developed in response to post-Miocene uplift of the Troodos ophiolite. Some of the fractures host hypogene sulphide veins which likely formed a sub-seafloor stockwork whilst others are clearly mineralized by post uplift, secondary sulphide assemblages.



Figure 76 Face in Phoenix Pit showing fracture network, red lines superimposed over fracture network for clarity.

Hypogene sulphide veins (Figure 77) have distinctly layered large euhedral pyrite crystals with quartz crystal orientation showing growth into fractures—features symptomatic of a hypogene stockwork vein. The lack of chalcopyrite or even evidence for the former presence of this mineral points to them representing a largely barren propylitic stockwork zone initially.

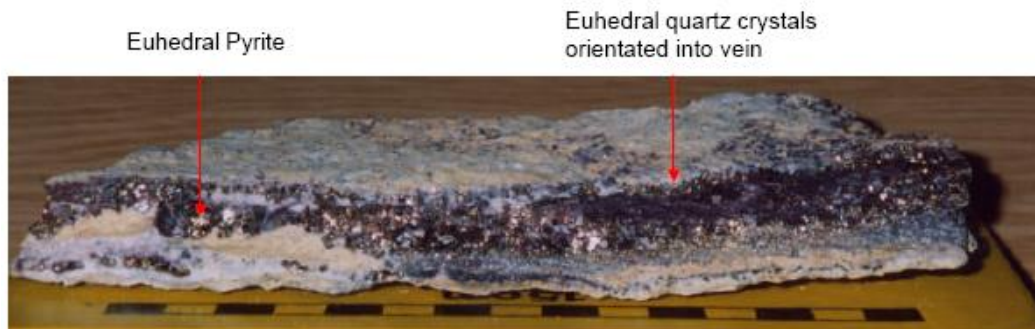


Figure 77 Hand specimen from Phoenix stockwork. Scale = 15cm.

Mixed hypogene-supergene veins (Figure 78) also contain large euhedral pyrite crystals, also lack chalcopyrite, which suggests a similar origin to the hypogene veins described above. However, the highly fractured (Figure 79) nature of minerals in the veins suggests they have been subject to post-mineralization brecciation, probably during post-depositional uplift. These fractures are also seen to be developed at low angles, suggesting a clearer relationship to low angle faulting to be expected during the uplift history.



Figure 78 Intermediate vein. Note variation in pyrite crystal size and shape.

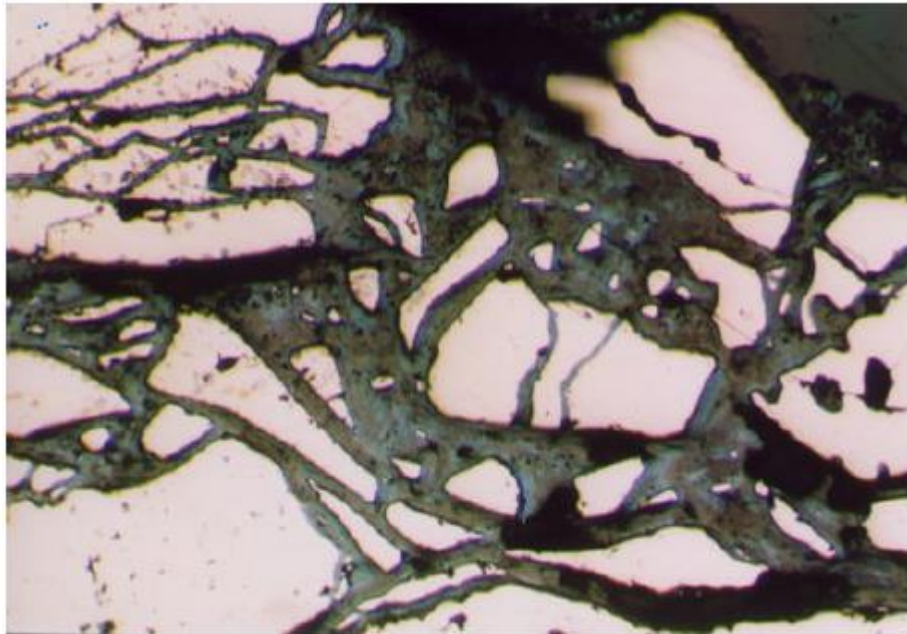


Figure 79 Heavily fractured pyrite crystals. Note chalcocite on, but not altering the pyrite (FOV 2cm).

Supergene veins occupy many of the less well-developed fractures. These contain fractured and comminuted pyrite and chalcopyrite (Figure 80 and Figure 81). The fractures still for active conduits for groundwater, indicating that they could also acted as conduits for older supergene fluids. Supergene enrichment in the Phoenix deposit comprises both alteration to primary chalcopyrite and a neo-mineralization developed on the surfaces of pyrite grains.

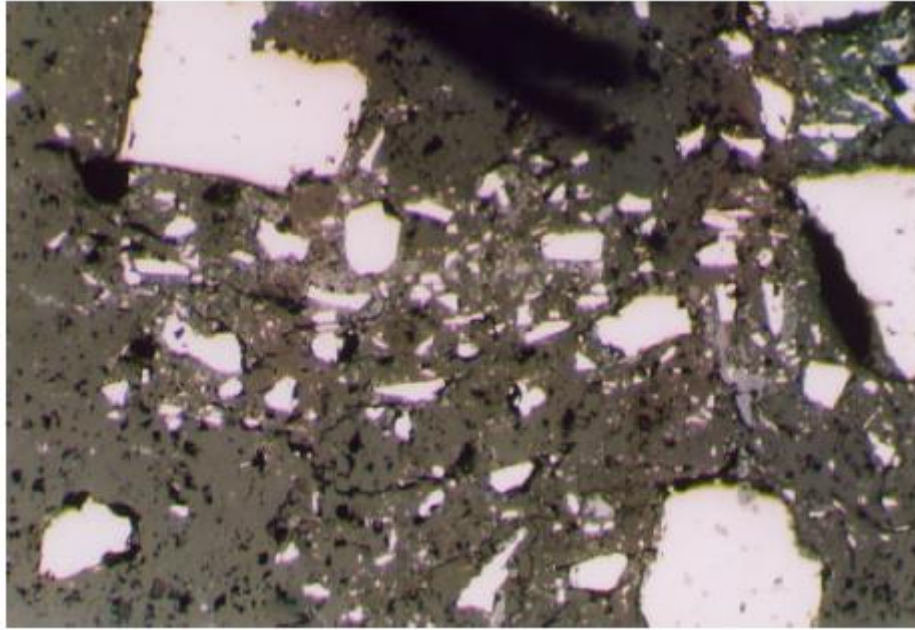


Figure 80 Small anhedral pyrite crystals



Figure 81 Hand specimen of vein showing anhedral pyrite and supergene sulphates.

The chalcopyrite is altered to digenite located on crystal edges and along fractures, with later alteration of digenite to chalcocite. Areas of digenite enclose chalcocite plus bornite and covellite filled fractures cut chalcocite and digenite. This confirms the relative timing of these supergene phases as chalcocite->digenite->bornite->covellite (Figure 82).

Chalcocite forms distinct overgrowths to fractured pyrite grains (Figure 79) which are clearly themselves not altered. This indicates that the chalcocite precipitated directly from percolating groundwaters on the surface of the fractured pyrite.

Hypogene	Supergene
Pyrite	
Chalcopyrite	
Sphalerite	
Digenite	
Chalcocite	
Bornite	
Covellite	

Figure 82 Mineralization paragenesis for the Phoenix deposit.

### 7.1.3 Three Hills pit

The Three Hills Pit is situated southeast of Phoukassa. It was a small mine with an original ore reserve of ~1.5Mt at an uncertain Cu grade and was operational until 2002. The pit has been in a stockwork zone beneath a massive sulphide lens, the relics of which were inaccessible in an unstable pit wall.

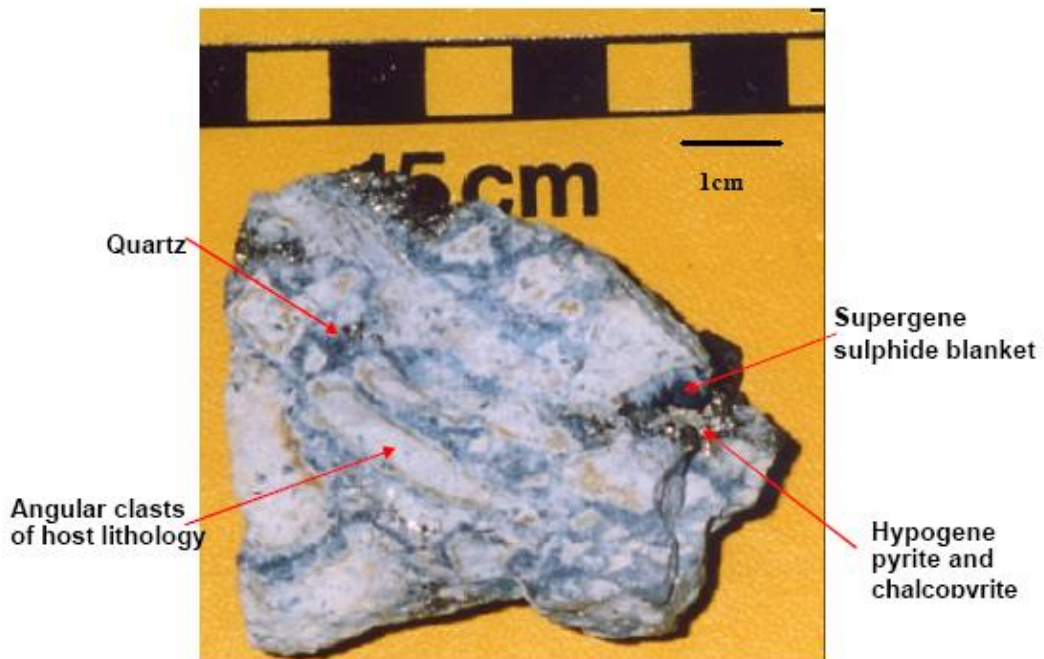


Figure 83 Stockwork mineralization from the Three Hills deposit.

Samples from Three Hills show mineralization to be a highly brecciated, highly silicified stockwork (Figure 83) with hypogene mineralization consisting of predominantly vug filling pyrite and chalcopyrite. Crystals are euhedral and range in size from 0.05–5mm and can be seen to have precipitated simultaneously with the quartz. Angular host rock clasts, within the stockwork zone are held in a

siliceous matrix and have altered to clay minerals. The clasts show a cream colouration indicative of illitic alteration, which is unlike the distinct green colouration of the main host rocks to the deposit caused by the presence of chlorite,. Some clasts show orange brown colour due to the oxidation pyrite.

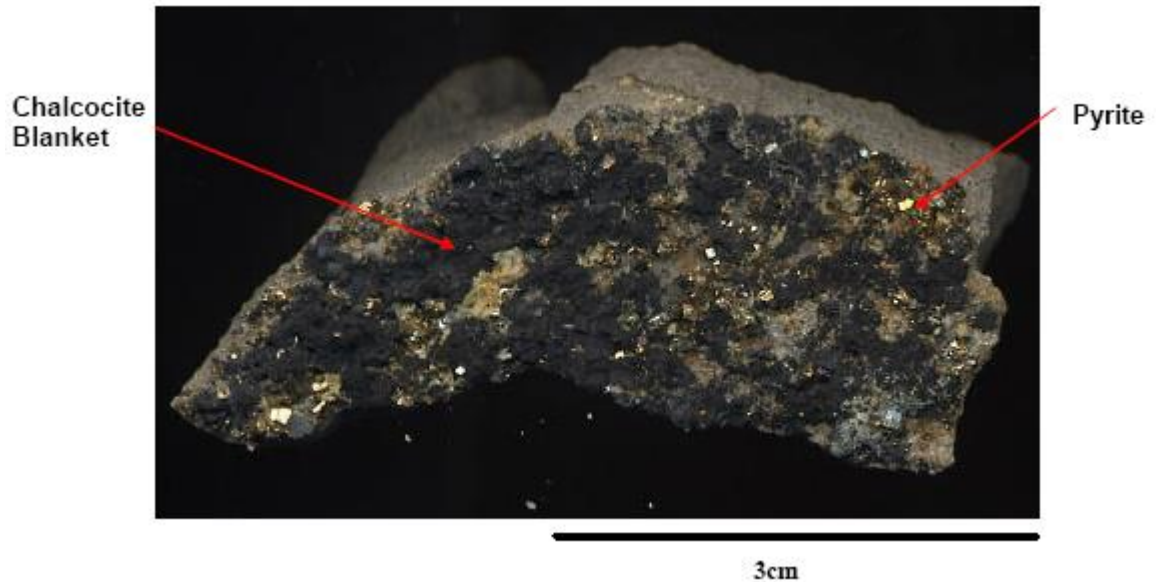


Figure 84 Chalcocite blanket in stockwork. Note pyrite, but little visible chalcopyrite.

The Three Hills material sampled contains a well-developed supergene mineralogy. Hand specimens show that the bulk of supergene sulphide consists of chalcocite. This can be seen to partially or completely pseudomorph chalcopyrite crystals and, in some cases, form fine rims on pyrite crystals, producing a chalcocite “blanket” over the walls of broken cavities in the host rocks (Figure 84). The chalcocite grades into bornite, which is visible as a colour change from blue to purple, and this in turn grades to individual crystals of covellite. Reflected light microscopy shows that the earliest supergene sulphide is digenite. This alters to chalcocite, which grades into bornite and finally covellite (Figure 85).

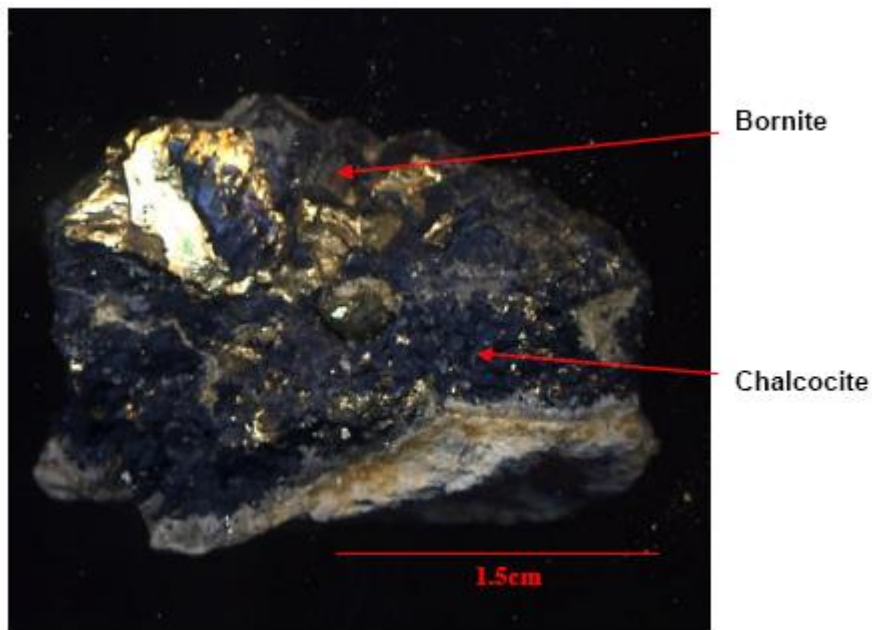


Figure 85 Supergene chalcocite grading into bornite.

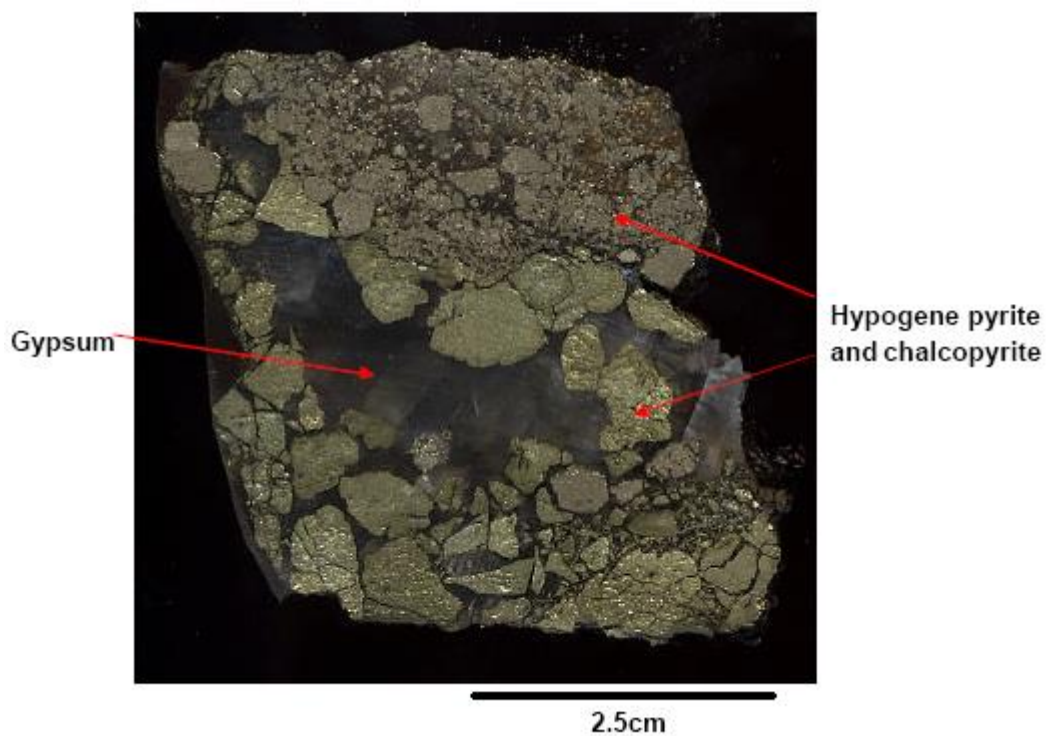


Figure 86 Hand specimen of Three Hills stockwork showing hypogene sulphide minerals and later gypsum.

The thickness of supergene mineralization suggests that alteration occurred in-situ with the fluid being retained in the stockwork for a long period of time. This allowed a significant thickness of supergene sulphides to develop on the existing hypogene assemblage (Figure 85).

A layer of later gypsum, blankets the supergene mineralization. Gypsum precipitation occluded porosity and permeability, blocking fluid migration, and undoubtedly resulted the cessation of supergene alteration (Figure 86 and Figure 87).

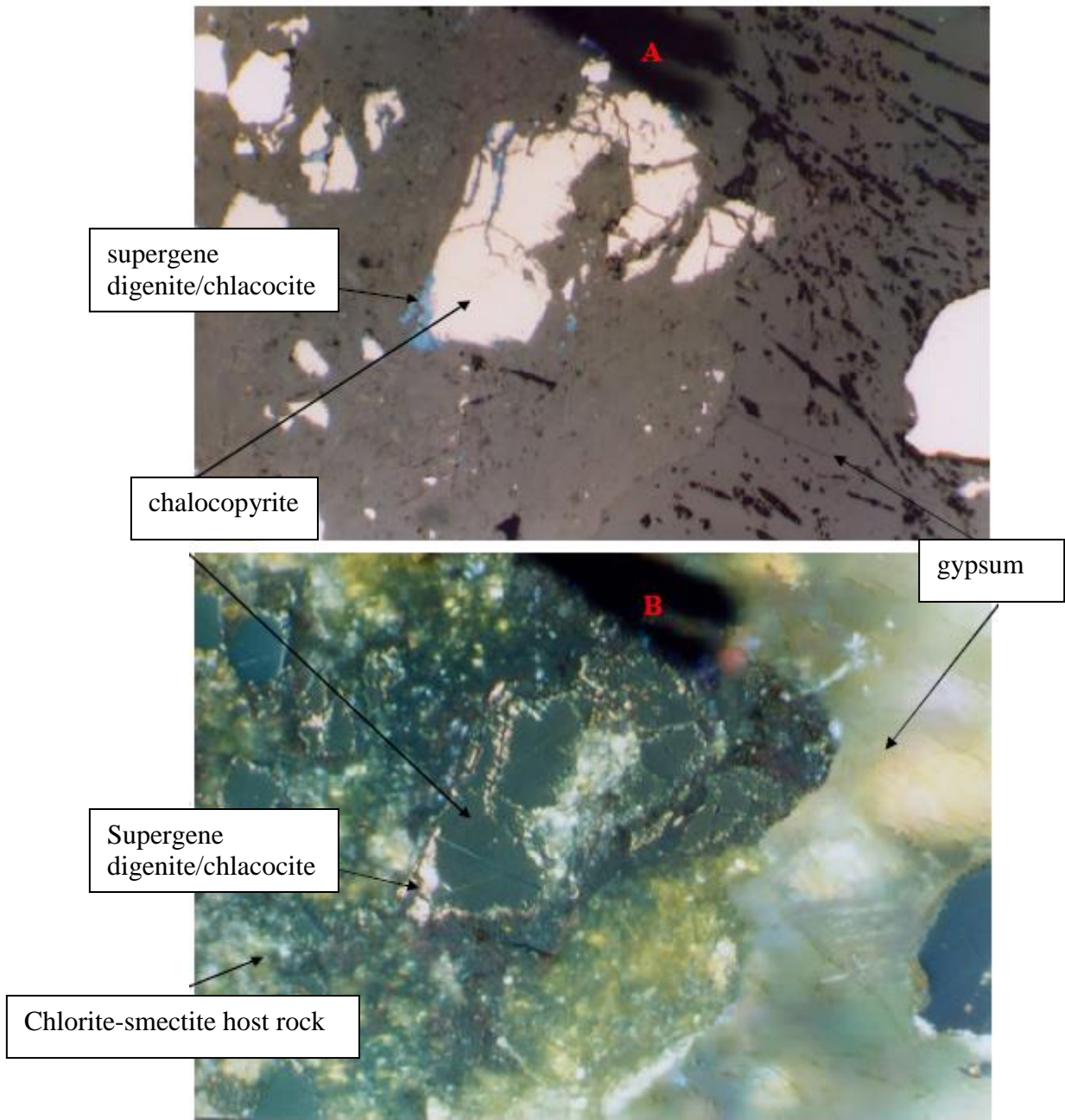


Figure 87 Reflected light section of Three Hills stockwork, photo A shows section in reflected light, Photo B shows transmitted light. Note that hypogene and supergene mineralization is covered by gypsum.

The mineralization paragenetic sequence for Three Hills is given in Figure 88.

	Hypogene	Supergene
Pyrite	—————	
Marcasite	—————	
Chalcopyrite	—————	
Digenite		—————
Chalcocite		—————
Bornite		—————
Covellite		—————

Figure 88 Mineralization paragenesis for the Three Hills Pit.

#### 7.1.4 West Apliki

Samples for the West Apliki prospect were provided by the Hellenic Mining company. The samples consisted of drill cuttings from different depths through the deposit and represented a cut through the ochre horizon (supra water table?) and the supergene sulphide region beneath the water table. No samples were available for the leached region which is indicated between these two zones.

##### *Ochre*

Samples from the upper ochre horizon show the distinctive orange brown colouration of oxidised iron. However, the sample size was too small to determine whether the ochre was layered or allow macroscopic mineral identification. Reflected light microscopy identified small quantities of highly corroded pyrite. The most commonly occurring minerals in samples are goethite and limonite, which pseudomorph pyrite crystals or as colloform build-ups within vugs.



Figure 89 Digenite alteration exploiting fracture in chalcopyrite, note pseudomorphing of cleavage.

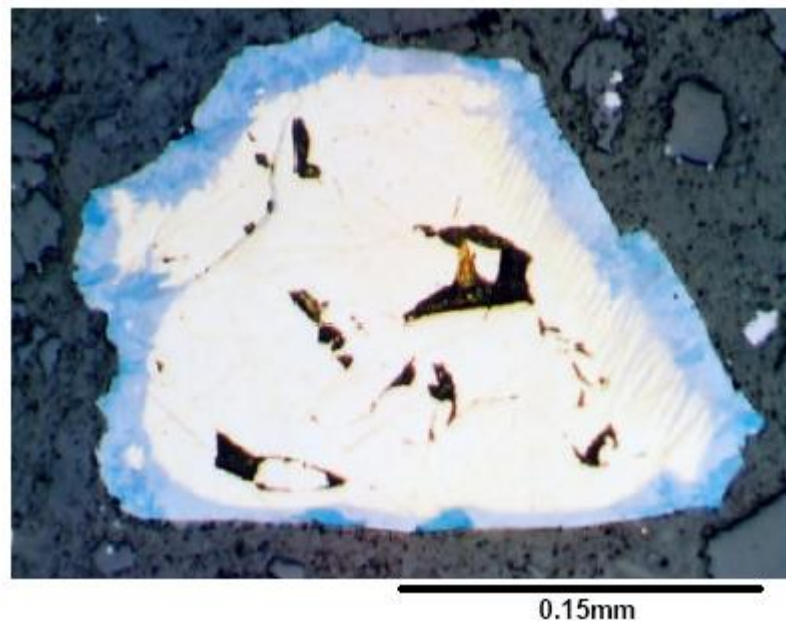


Figure 90 Digenite alteration exploiting chalcopyrite cleavage.

### *Supergene sulphides*

The supergene mineralization shows a number of recurring features—chalcopyrite alteration to digenite and chalcocite affects crystal edges and fractures. In addition, it can also be clearly seen to exploit the chalcopyrite cleavage (Figure 89 and Figure 90). There is also a size control—large chalcopyrite crystals (>0.25 mm) tend to show a rim of both digenite and chalcocite alteration (Figure 90), while smaller crystals (<0.25 mm) will tend to show only chalcocite (Figure 91).

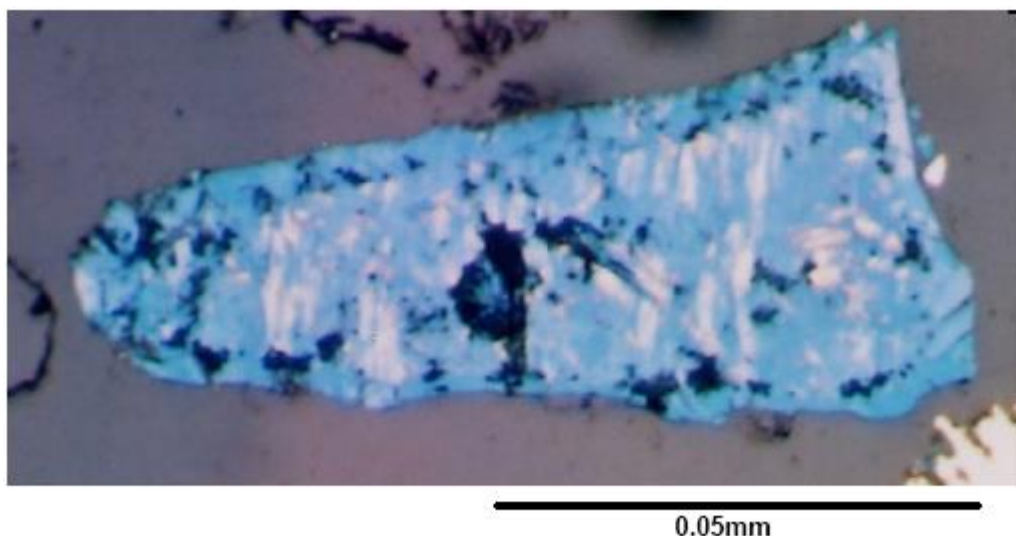


Figure 91 Chalcopyrite crystals fully pseudomorphed by chalcocite.

The mineralization paragenesis for West Apliki is shown in Figure 92

	Hypogene	Supergene
Pyrite	—————	
Marcasite	—————	
Chalcopyrite	—————	
Digenite		—————
Chalcocite		—————
Bornite		—————
Covellite		—————

Figure 92 Mineralization paragenesis for the West Apliki deposit.

## 7.2 DISCUSSION OF SUPERGENE MINERALIZATION

The study confirms the presence of distinctive and consistent supergene mineralogies, which can be related to the water table in the weathering profile in each case. In the specific case of the Phoenix deposit, the favourable interplay between the mineralization and topography is believed to have played an important role in the development of the large secondary orebody. This will be expanded in the discussion below.

In general, the supergene mineralogy consists of (i) malachite, cuprite and jarosite developed in the oxidised assemblages above the paleo-water table and (ii) digenite, chalcocite, bornite and covellite as coatings to oxidising chalcopyrite and in some cases as passive coatings to fractured pyrite in zones developed below the water table.

A distinctive leached region is developed in the profile at Skouriotissa where there is shown a distinct lack of the major sulphides pyrite and chalcopyrite, presumably as a result of acid dissolution by groundwaters. The absence of pyrite is compensated by the presence of goethite and limonite, which form as a result of pyrite oxidation. The lack of chalcopyrite is probably due to total leaching by low pH meteoric waters resulting from pyrite oxidation further up the profile. It is apparent in the case of Skouriotissa that this leached zone has resulted from the downward percolation of acidic groundwater generated by the oxidation of the pyritic massive sulphide lens, the remnant of which is seen exposed in the pit wall. This acidic groundwater would serve to both strip copper from the massive sulphide deposit and leach the bulk of metals from the bleached zone exposed beneath the massive sulphide. This copper-bearing groundwater would migrate by gravity driven through the fractured volcanic pile towards the hypogene pyretic stockwork seen at Phoenix. At this point the groundwater would both hit the water table and the reduced sulphide assemblage in the altered stockwork

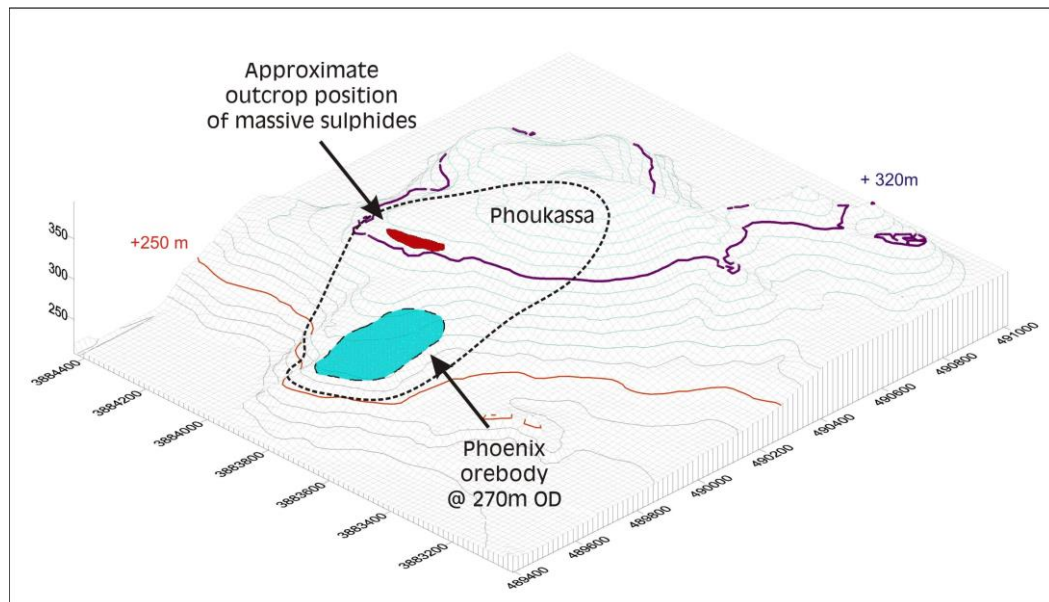


Figure 93 Topographic map of the pre-mining surface at the Skouriotissa deposit showing the relative elevations of the remnant massive sulphide (+320m OD) and the Phoenix secondary orebody (upper surface @ ca. 250m OD).

Figure 93 shows the topographic data for the deposit prior to mining where the massive sulphide lens is around 50 m vertically above the secondary sulphide blanket. Natural groundwater flow would have been driven downslope through the subcropping massive sulphide lens down to the Phoenix stockwork below, potentially at or close to the water table.

Precipitation of supergene minerals in all the deposits shows a consistent pattern. Digenite and chalcocite appear to have precipitated first, followed by a progressive alteration of digenite to chalcocite. Bornite and covellite replace earlier digenite and chalcocite but bornite more commonly occurs in fractures cutting chalcopyrite, chalcocite and digenite or in open-space fillings between and within chalcopyrite grains.

The controlling factor in formation of the supergene assemblage appears to be where mixing or dilution has occurred at the water table, leading to likely pH and redox changes in the solution. Furthermore, at Phoenix and West Apliki, chalcocite is more closely linked to the level of the water table itself, a scenario

analogous to the formation of chalcocite blankets seen in porphyry copper deposits.

Gypsum mineralization is clearly seen to post-date all the supergene sulphides.

From the study, it is apparent that supergene profiles are to be expected in a number of the VHMS deposits. Nevertheless, the Phoenix sample is considered to be a particularly favourable for a number of reasons:

1. A hypogene massive sulphide body containing primary copper-bearing sulphides was developed in a paleo-high, probably exposed to the atmosphere at the top of the section (evidence of a surface gossan) This oxidation produced a constant supply of sulphuric acid via oxidation into the groundwater, serving to decrease pH and strip copper from chalcopyrite into solution
2. A well-developed fracture network enhanced by uplift was developed through the footwall stockwork system
3. A zone of disseminated and fracture-hosted pyritic mineralization was already developed downslope, lower in the section at the water table, an ideal trap for reprecipitating the copper from solution.

Similar scenarios may exist elsewhere in Cyprus. Exploration strategy for this type of deposit would be to look for zones where a cupriferous massive sulphide may have oxidised at surface producing copper-bearing acid groundwaters that may have migrated to a suitable deposition site (such as a propylitic alteration zone). A substantial body of oxidising pyrite is needed to ensure the generation of acidic groundwaters for a significant period of time. Oxidation of a stockwork zone with a smaller volume of total sulphide is unlikely to result in a substantial secondary body. A strategy for exploring for such a supergene copper target would be to assess all surface gossans developed in topographic highs and seek potential downslope areas where reducing conditions may have developed to reprecipitate the copper.

## 8 Considerations on the application of recent advances in copper hydrometallurgy at the Hellenic Copper Mines Skouriotissa copper production plant.

### 8.1 Description of the Skouriotissa plant

Hellenic Copper Mines copper processing plant at Skouriotissa in western Cyprus utilizes solvent extraction-electrowinning (SX-EW) technology, which was first introduced into the copper industry in the late 1960s in the United States. The Skouriotissa plant was opened in June 1996, after a ten-year development period. The cost of the project was CYP10.7M and the construction period was 18 months. The plant is designed to produce 8000t/a high-grade (five 9s) cathode copper.

Oxidised copper ore is selectively mined from the Phoenix pit. The high-grade ore is  $>0.5\%$  Cu, with an average grade of  $0.8\%$  Cu. This crushed to  $<75\text{mm}$  and then screened and classified to separate the  $-0.3\text{mm}$  fines. The fines are agitation leached with sulphuric acid (pH 2, 2 hr retention) and then washed by 3-stage counter-current decantation, before being deposited in a tailings pond. The  $-75+0.3\text{mm}$  high grade ore is heap leached in 6m high benches (Figure 94) with acidified effluent from the low-grade heaps to produce a pregnant solution containing  $4.5\text{ gl}^{-1}\text{ Cu}$ .



Figure 94 High-grade leach heaps.

The low grade ore, which is  $< 0.5\%$  and  $> 0.1\%$  Cu, with an average of  $0.3\%$  Cu, is taken directly from the mine without crushing to the low-grade heaps, where it

is heap leached in 8 m benches with raffinate from the solvent extraction plant. The low-grade leach solution is then used to leach the high-grade ore heaps.

Copper is recovered from the pregnant leach solution in a conventional SX-EW plant. The solvent extraction section comprises two stages of extraction and one of stripping (Figure 95). Mount Isa technology is used in the tankhouse, where copper is electrowon on to stainless steel, instead of copper, starter sheets. Deposited copper is stripped from the stainless steel cathodes when it is 8 mm thick, to produce directly marketable copper sheets weighing approximately 50 kg each (Figure 96).



Figure 95 Stripping mixer-settler.



Figure 96 Finished cathodes being removed from cell.

Environmental impacts of the plant arise mainly from the mining operations, in the form of dust, noise, blasting vibrations and visual impact. There are the usual acid mist problems in the tankhouse and there is approximately 4 t/a of lead sludge, arising from the lead anodes, that has to be disposed of. The mining and leaching operations cover an area of about 3 km<sup>2</sup> and there are ill-defined seepages from this area, which can result in surface and ground water contamination during rainy periods.

The high-grade ore at Skouriotissa consists primarily of oxidized copper minerals, principally malachite and cuprite, together with minor amounts of supergene secondary copper minerals, namely chalcocite, digenite, bornite and covellite. The oxidized copper minerals and, to a lesser extent, the secondary sulphide minerals, are amenable to heap leaching with sulphuric acid. However, as the mining goes deeper, copper recoveries in heap leaching are decreasing, mainly

due to increasing proportions of primary chalcopyrite, which is refractory to heap leaching.

The objective of this report is to review recent developments in copper hydrometallurgy to examine whether changes can be made to the existing process to overcome the decline in metal recovery and hence to extend the life of the mine and the plant. The SX-EW plant at Skouriotissa is relatively modern and is still state-of-the-art. The declining production is due entirely to poor metal recoveries in leaching, which in turn is primarily caused by changing mineralogy in the ore as the mining goes deeper and moves into the unaltered primary sulphide ore zones. Thus this review will be mainly confined to advances in copper sulphide leaching technology and it will cover both heap leaching and agitation (tank) leaching processes. In order for copper sulphide minerals to dissolve, they must be oxidized. The oxidant used for this purpose is normally oxygen, either pure, or preferably as air. Usually, ferric iron ( $\text{Fe}^{3+}$ ) acts as an electron carrier between dissolved oxygen and the sulphide minerals and, often, these chemical reactions are speeded up many times (catalysed) by the action of certain bacteria. These various alternatives have all been exploited in leaching processes, as described in the following sections.

## 8.2 Overview of heap leaching-SX-EW

Currently about 15% of the world copper production is produced from heap leaching of oxide copper and, more recently, chalcocite ores. Typical cash operating costs for mine/heap leach-SX-EW operations are in the range \$0.40–0.55 US/lb Cu (Peacey et al., 2003), depending on:

- ore grade,
- mining costs ,
- Cu recovery,
- acid requirements, and
- power costs.

For operations in the 40,000 to 200,000 Mt/y Cu range, total capital costs vary between about \$4000 to \$5000 US/annual tonne Cu, with the higher level being more typical of the secondary copper sulphide operations. The capital costs for heap leach-SX-EW are split roughly one third each for:

- open-pit mining,
- ore crushing and heap construction,
- solution handling, solvent extraction and electrowinning.

For oxide ores, Cu recoveries are typically in the range 75–80 % within 50–100 days. Reusable leaching pads are now also used in the leaching of oxide ores as well as sulphide ores, rather than the original permanent heaps. Secondary sulphide heap leaching requires air injection into the heaps to promote bacterial oxidation and leaching rates are much slower and less predictable than oxide ores, with leach times typically in the range of 250 to 600 days to achieve 70–80 % Cu extraction.

### 8.3 Heap leaching of sulphide ores

The success of SX-EW for oxide and secondary sulphide copper ores has resulted in the initiation of research efforts to develop a heap leach process for chalcopyrite ores, which currently are generally recovered by flotation, followed by smelting and electro-refining. Chalcopyrite is much more difficult to leach than chalcocite and other secondary copper minerals, as shown in Table 16, which demonstrates that the secondary minerals, chalcocite and bornite leach very much more rapidly than the primary minerals, chalcopyrite and enargite, with covellite leaching at an intermediate rate. Based on evidence from secondary sulphide heap leaching operations, the development of high-temperature heap operations will be necessary to obtain acceptable copper recoveries from chalcopyrite ores in reasonable leach times. The issues of managing acid and iron generation are further complexities that need resolving.

Mineral		Solubility	Leach time (days)
Chalcocite	Cu <sub>2</sub> S	50%	8
Bornite	Cu <sub>5</sub> FeS <sub>4</sub>	45%	5
Covellite	CuS	35%	11 (35°C)
Chalcopyrite	CuFeS <sub>2</sub>	2%	43
Chalcopyrite (ultrafine)		39%	57
Enargite	Cu <sub>3</sub> FeS <sub>4</sub>	3%	60 (35°C)

Table 16 Relative solubilities of copper sulphide minerals.

Newmont have demonstrated that high-temperature heaps are feasible for refractory gold ore oxidation. Another interesting development is the use of high chloride and other lixivants in heap leaching. Several oxide heap leach operations in Chile, such as Michilla and Lomas Bayas, have naturally high levels of chloride and nitrate in their leach liquors. Antofagasta Minerals has patented a chloride-enhanced heap leach process called “Cuproclor” that uses NaCl or CaCl<sub>2</sub> additions to generate the lixiviant. It can only be a matter of time before chalcopyrite heap leaching becomes a commercial reality, but it is unlikely that such a development will make the treatment of very low-grade chalcopyrite ores (<0.5 % Cu) economic.

## 4. RECENT AGITATION LEACH PROCESSES FOR COPPER SULPHIDES

The first generation of copper hydrometallurgical processes for copper sulphide minerals were developed in the 1970's, but despite reasonable technical success, none of them proved economically viable. Over the next couple of decades, the success of heap leaching of copper oxide ores, with the commercial development of very efficient solvent extraction and electrowinning technology, led to renewed interest in copper sulphide leaching in the 1990's. Since then, many new innovative copper hydrometallurgical processes have been piloted and three of them have reached the stage of large demonstration plants ( 15–20,000 t/y Cu) - Placer Dome's pressure leach process and two bacterial leach processes—BHP Billiton's BioCop and the Bactech/Mintek process.

The main impetus for these developments has been the desire to develop a viable alternative to copper smelting to overcome the perceived drawbacks of smelting, which are:

- SO<sub>2</sub> emissions
- Sulphuric acid market saturation
- High capital cost
- Impurity limitations (As, Sb, Bi)
- Minimum economic size >100 kt/a

The advantages sought in the development of the new copper hydrometallurgical processes are:

- Elimination of SO<sub>2</sub> emissions, together with a sulphur product other than sulphuric acid, e.g.. elemental sulphur or gypsum.
- Ability to handle lower grade concentrates as well as higher levels of impurities, i.e. more effective for treating complex concentrates,
- Lower capital cost, especially at a smaller scale than smelters.

Sulphate-based processes, generally using oxygen as the oxidant, are the most extensively investigated technologies for the leaching of chalcopyrite concentrates. The main sulphate processes are listed in Table 17. It is generally necessary to use pressure leaching at high- temperatures (150–225 °C) to achieve rapid leaching rates (1-2 hours). Fine grinding to less than 20 microns is also effective at increasing leaching kinetics at lower temperatures. The atmospheric leaching processes with fine grinding require 12–24 hours for high Cu extraction whereas the lower temperature biological leaching processes typically require several days. In almost all processes, copper is recovered using the well-proven SX-EW combination. Precious metals recovery is a significant issue with most hydrometallurgical processes. Gold recovery from total oxidation leach residues by cyanidation is usually good, but silver recovery is more difficult due to the formation of argento-jarosite. A lime-boil or other step that destroys the jarosite is typically required for high silver recovery. Precious metal recovery from the sulphur-containing leach residues produced by partial oxidation processes is much more difficult.

Process	Leach pressure	Sulphur product	Proposed mechanism	Level of development	Note
Activox	Low,	S <sup>0</sup> , SO <sub>4</sub> <sup>2-</sup>	Direct	Laboratory	Fine grinding
Nenatch	Atmospheric	S <sup>0</sup> , SO <sub>4</sub> <sup>2-</sup>	Direct	Laboratory	Fine grinding
Dynatec	Pressure (medium)	S <sup>0</sup>	Direct	Laboratory	With coal
AAC/UBC	Pressure (medium)	S <sup>0</sup>	Direct	Pilot plant	With surfactant
Placer Dome Process	Pressure (high)	SO <sub>4</sub> <sup>2-</sup>	Direct.	Demo Plant Started 2003	High Temperature
BioCop	Atmospheric	SO <sub>4</sub> <sup>2-</sup>	Indirect	Commercial (underway)	Bacterial
Bactech/Mintek	Atmospheric	S <sup>0</sup> , SO <sub>4</sub> <sup>2-</sup>	Indirect	Demo.Plant	Bacterial
Geocoat	Atmospheric	SO <sub>4</sub> <sup>2-</sup>	Indirect	Pilot plant	Bacterial

Table 17 New sulphate processes for chalcopyrite concentrate leaching (Peacey et al., 2003).

The Placer Dome process, also called the total pressure oxidation process (King, 1997), uses the same conditions successfully used in the gold industry for refractory sulphide ore pressure leaching. In this process, copper sulphide minerals are decomposed by high temperature oxidation conditions (220 °C), resulting in rapid and complete copper leaching accompanied by hydrolytic precipitation of iron, mainly as hematite, and impurities. The features of the process are:

- High copper extraction and fast leaching kinetics without fine grinding
- Precious metal can be recovered by cyanidation of leaching residue
- Oxygen consumption is high because all the sulphur is converted to sulphate
- High lime consumption for acidic bleed solution neutralization unless the
- Acidic solutions are used for heap leaching.

A demonstration plant for this process treating 136 t/d of concentrate to produce about 16,000 t/a of copper cathode via conventional SX-EW was constructed at Bagdad, Arizona, by Phelps Dodge. A full-scale plant using this technology has recently been announced.

*Processes using fine grinding:* The processes using fine grinding are the Activox and Nenatech processes (Corrans and Angove, 1993; Horan, 1996). The particle size of concentrate for leaching is less than 20 microns after ultra-fine grinding. The features of these processes include:

- Leaching temperature is lower than sulphur melting temperature of 119°C.
- Element sulphur formed in the processes remains in the leach residue. This leads to difficulties in recovering precious metals from the residues.
- Some sulphate is produced, which is precipitated as gypsum
- Iron precipitation is as goethite and jarosite.

The Activox leaching temperature is around 110 °C and oxygen pressure is 1000 kPa. The Nenatech process uses atmospheric pressure and temperatures below at 100 °C.

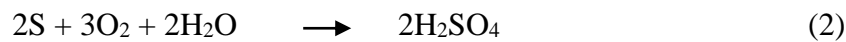
*Processessing surfactants/additives:* The best-known process in this category is the Dynatec process, which uses coal as the additive (Collins and Kofluk, 1998). This process is based on the well-proven Dynatec zinc leach process. The concentrate is ground to about 30–50 µm and oxidized under medium temperature (150 °C for chalcopyrite). Sulphur reports largely as elemental sulphur to the leach residue with about 25 % of the sulphur being oxidized to sulphate. The leach residue is floated to recover a sulphide fraction for recycle to the leach circuit and elemental sulphur is recovered by melting and hot filtration. The non-sulphidic residue is treated for gold and silver recovery by cyanidation. A lime boil is usually required for high silver recovery. Although pyrite is largely unreacted in the leach, it builds up in the recirculating sulphide fraction and is essentially totally oxidized. Iron is precipitated as hematite and jarosite.

Anglo American Corporation and UBC are developing a variant of the Dynatec and Activox processes, in which surfactants similar to those used in zinc pressure

leaching are added to disperse the molten sulphur. The feed is also finely ground to less than 20 µm. The leaching temperature is 150 °C. A pilot plant program is underway at the AARL facilities in South Africa.

*Bacterial Leaching:* There are two dominant views on the mechanisms involved in bioleaching. The first is that the overall leaching process occurs by the microbial oxidation of ferrous to ferric ions followed by the chemical oxidation of the sulphide mineral by the ferric ion. This is known as the indirect mechanism. The second view envisages the microbial catalysis of the overall dissolution of the mineral. It has been proposed that the microorganisms interact with the mineral directly, enhancing the rate of oxidation, over and above that achieved by chemical oxidation. This is known as the direct mechanism. Regardless of the mechanism, it is the enhanced oxidation of the mineral created by the microorganisms that creates the acid-solubility required for leaching to take place.

The overall chemical reactions for chalcopyrite oxidation are:



It should be noted that one of the problems that has had to be overcome in the leaching of chalcopyrite is that, when using natural bacteria, a passivating layer forms on the mineral surfaces that prevents further leaching. This passivating layer could come from one or both of two sources: (i)  $\text{Fe}(\text{OH})_3$  tends to form jarosite ( $\text{KFe}_3(\text{SO}_4)_2(\text{OH})_6$ ), which coats the unreacted material and/or, (ii) the elemental sulfur formed in reaction (1), which also tends to coat the surface. Covellite and chalcocite are much easier to leach.

In the past decade, copper bioleaching has been extensively applied in secondary copper heap leaching operations and in the dump leaching of marginal grade run-of-mine copper bearing rock. The bacteria employed widely in current heap leaching are *thiobacillus ferrooxidans* and *t. thiooxidans*. With further technical development, moderate *thermophiles* and *extreme thermophiles* may in future be used for extraction of copper in confined heap and *in-situ* environments

The BioCop process developed by BHP Billiton is the leading bioleaching process for copper concentrates. In this process, mesophiles (at 42-45°C) and/or thermophiles (at 70-80°C) are used for secondary sulphide copper leaching and chalcopyrite leaching, respectively. Pre-leaching ahead of oxidation leaching is helpful for copper recovery when treating secondary sulphide copper, but pre-leaching has little effect on chalcopyrite leaching. Sulphur is completely oxidized to sulphate, with the result that the oxygen consumption is high in this process. Alliance Copper (BHP Billiton and Codelco) has built a semi-commercial BioCop demonstration plant located near the Chuquicamata mine in northern Chile. The plant is designed to produce about 20,000 t/a Cu.

Bactech/Mintek has also developed a viable bioleaching process for various copper concentrates (Van Staden, 1998). The flowsheet consists of a moderate grind, two-stage ferric leach with air, followed by ferric regeneration with air. For chalcocite concentrates, mesophiles at 36–40 °C are used and the leaching and ferrous biooxidation are carried out in the same tank. For chalcopyrite concentrates, moderate to extreme thermophiles at 40–50 °C and 70 °C,

respectively, are used and ferrous biooxidation is done in a separate tank. The sulphur is converted to a mixture of elemental sulphur and sulphate and the latter is precipitated from a bleed stream as gypsum. Soluble iron is precipitated as hydronium jarosite. Pyrite is not attacked. Precious metals are recovered from the leach residue by cyanidation. Bactech and Mintek have jointly developed their tank bioleaching process up to demonstration plant level at the Peñoles operation at Monterrey, Mexico. The plant is designed to produce 500 kg/day of cathode copper. A 25,000 t/a copper–zinc commercial plant at Peñoles is under study.

Geocoat is an alternative approach to bioleaching. The process, which is being developed by GeoBiotics, involves the coating of concentrates on to a suitable substrate, usually barren rock, then stacking the coated material in a conventional heap fashion. The heap is irrigated with acidic solutions, containing iron and nutrients, while low-pressure ambient air is applied at the heap base.

#### **8.4 PRODUCTION OF COPPER CONCENTRATE USING FROTH FLOTATION TECHNOLOGY**

The production of copper concentrates from sulphidic copper-bearing ores is universally carried out by the froth flotation process and the quantity of copper concentrates produced by this process worldwide far exceeds that of any other metallic mineral.

Froth flotation has been used industrially to concentrate sulphide ores for nearly 100 years. The principles of the flotation process are well known. Briefly, the process involves crushing and grinding the ore to the particle size range required to achieve liberation, which means the physical detachment of the grains of the various sulphide minerals contained in the ore. Various surface active chemicals are then added to the ground ore pulp, which make the surfaces of the wanted sulphide mineral particles non-wettable, whilst the bulk of the gangue (unwanted minerals) remain wettable. Three types of chemical reagent are added to achieve the desired result:

(i) collectors: these function by attaching themselves to the sulphide mineral particles, creating an “oily” film on the surface, making the particles non-wettable. (ii) modifiers: these alter the behaviour of the collectors, helping them absorb selectively onto targeted sulphide minerals. (iii) frothers: these are soap-like molecules that create a stable froth in the flotation process. The ore pulp, together with the required flotation reagents, is passed through a series of flotation cells, which are agitated tanks in which swarms of air bubbles are continuously passed through the ore pulp. The non-wettable sulphide mineral particles attach themselves to air bubbles, which carry them to the surface, where they are trapped in the stable froth, which is continuously removed from the flotation cells.

All copper sulphide minerals respond readily to flotation using either the well-known xanthate collectors, or the dithiophosphate collectors. Xanthates have the chemical composition  $\text{ROCSSM}$ , whereas dithiophosphates are  $(\text{RO})_2\text{PSSM}$ , where R represents a hydrocarbon group, such as ethyl, isopropyl, or amyl, and M is an alkali metal ion, such as  $\text{Na}^+$  or  $\text{K}^+$ . An example of a widely used collector for copper sulphide flotation is potassium amyl xanthate, commonly abbreviated as KAX. Alkaline conditions are used in copper flotation pH 8–9, in order to

depress the flotation of pyrite, which is commonly present in copper sulphide ores. The effect of pH is shown in Figure 97, which illustrates the behaviour of common sulphide minerals with pH. Flotation of each mineral occurs at pH to the left of the labeled line, but not to the right. It may be seen that at pH above 8, out of the minerals shown, only chalcopyrite will float.

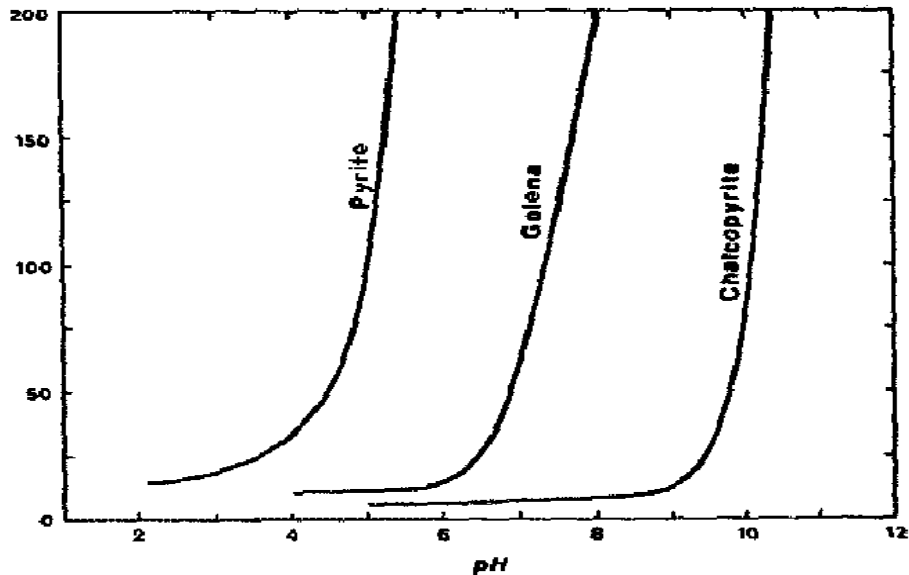


Figure 97 The effect of pH on flotation

In practice, lime is used to control the pH of the ore pulp at the desired value. Typical reagent consumptions in the flotation of copper ores are: 1–5 kg lime, 0.02–0.3 kg xanthate collector and 0.02–0.15 kg frother, per tonne of ore treated.

The cells in which flotation is carried out may be mechanically agitated or pneumatically agitated. There is much debate about which types of machines are better, but in general either type can give excellent performance, provided they are properly designed for the particular application. Mechanical cells use a large stirrer and diffuser mechanism at the bottom of the mixing tank to introduce air and provide mixing action. Flotation columns use air spargers to introduce air at the bottom of a tall column while introducing slurry above. The countercurrent motion of the slurry flowing down and the air flowing up provides mixing action. Mechanical cells generally have a higher throughput rate, but produce material that is of lower quality, while flotation columns generally have a low throughput rate but produce higher quality material. Figure 98 illustrates the principles of a mechanically-agitated flotation cell.

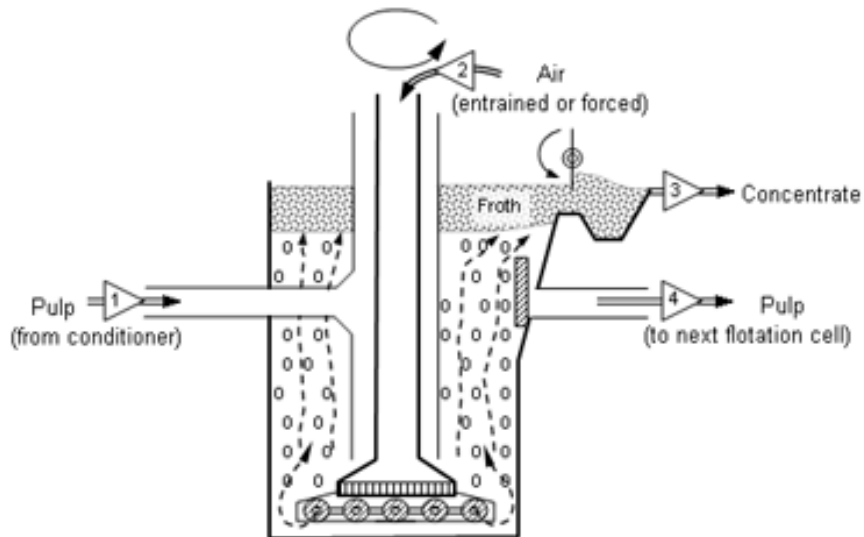


Figure 98 Illustration of the principles of a mechanically-agitated flotation cell

A typical simple flotation circuit is shown in Figure 99. After the addition of the flotation reagents in the conditioning tank, the ore pulp enters the first series of flotation cells, known as the roughers, where the most readily floating particles are collected. The product from the rougher cells is the final sulphide concentrate. The ore pulp moves on to a second series of cells, the scavengers, where the conditions are adjusted to be less selective so that all remaining sulphide-bearing particles are recovered, together with some unwanted particles. The product from the scavenger cells is recycled to the conditioner tank to go through the whole circuit again, whilst the unfloated tailings are discarded.

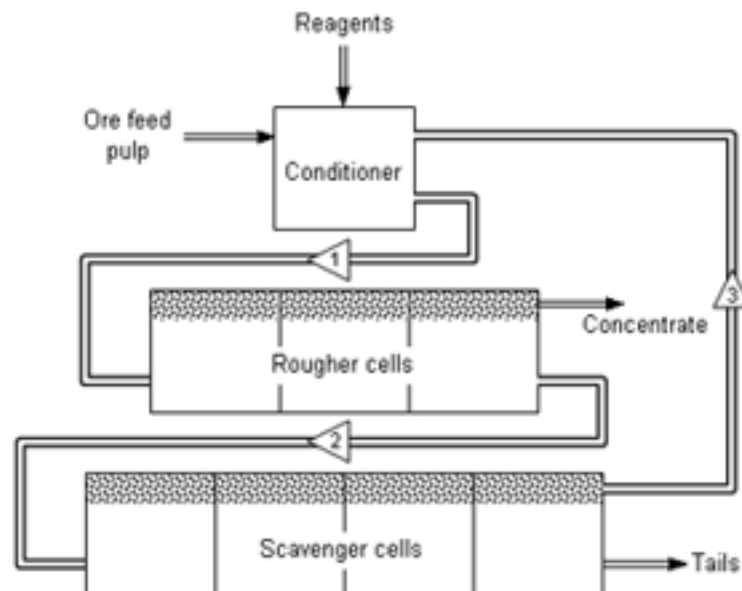


Figure 99 Illustration of a typical simple froth flotation circuit.

Whilst all copper sulphide flotation processes are based on the principles outlined above, the process has to be tailored to suit the characteristics of individual ore bodies. This involves a mineralogical study of representative samples of the ore to determine the minerals present, their associations and textures. This

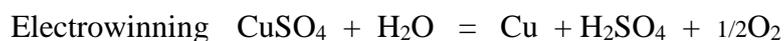
information is then used to devise a laboratory test programme to optimise all the possible variables in the flotation system, which include:

- Grind size
- Pulp density
- Reagent concentrations
- pH
- Flotation time
- Recycle loops

Once all this information has been collected, a full-scale flotation process can be designed and costed. This work is normally done by specialist consulting companies, who on completion of their design work, will often oversee, on behalf of their clients, the work of the equipment manufacture and plant construction companies, who will be involved in building the industrial flotation plant.

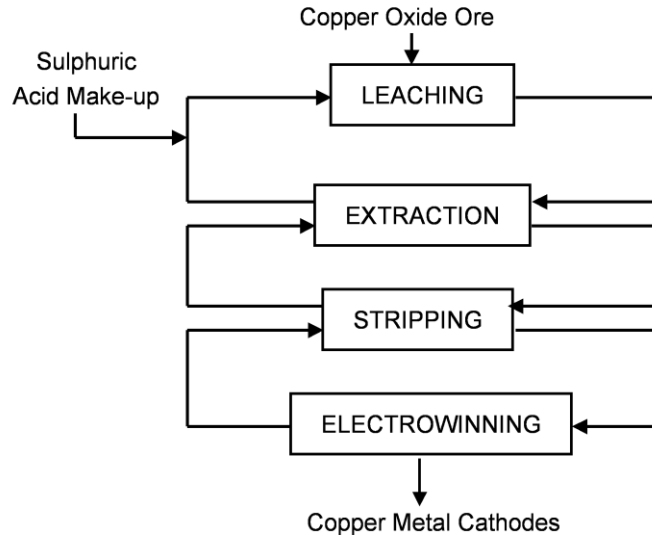
## 8.5 DISCUSSION

The success of the heap leach-solvent extraction-electrowinning process for copper oxide ores is largely due its elegant simplicity. This is illustrated in the simple flowsheet shown below. It can be seen from this diagram that the process comprises three counter-current closed-loop solution flows: (i) the leach solution, which flows from the leach heaps, through extraction and back to the heaps; (ii) the organic phase cycle, which flows from extraction to stripping and back to extraction, flowing in the opposite direction to the leach solution; (iii) the electrolyte cycle, which flows from stripping to electrowinning and back to stripping. The chemical reactions occurring at each stage are :



It can be seen by summing the above equations that the overall process is equivalent to simply splitting  $\text{CuO}$  into  $\text{Cu}$  and  $1/2\text{O}_2$ , i.e.





All other reactants and products are recycled within the process, which is totally closed cycle, except for the inputs of copper oxide ore into leaching and electric power to electrowinning and the outputs of copper metal cathodes, oxygen at the anodes, and barren leached ore. The sulphuric acid make-up shown in the diagram is necessary to replace acid lost during leaching by reaction with acid-soluble minerals in the ore, other than copper oxide.

The closed cycle nature of the process means that it has a minimal environmental footprint and this characteristic, together with the fact that high quality copper metal is produced at the mine-site, accounts for the world-wide success of the SX-EW process.

In order to use copper sulphide minerals in this process, these minerals have to be oxidized to become soluble. In the current heap leaching process used at Skouriotissa, nutrients are added to the leach solutions to encourage bacterial activity within the heaps. The bacteria catalyse the oxidation reactions, enabling acceptable copper recoveries to be achieved in reasonable time periods. However, this approach is only successful when the copper sulphides being leached in this manner are secondary supergene minerals, e.g. chalcocite or bornite. As illustrated in Table 2, the rates of leaching of these secondary minerals are orders of magnitude faster than that of the unaltered primary mineral, chalcopyrite. With present techniques, heap leaching of primary chalcopyrite ores is too slow and metal recoveries are too low to be economically viable. Thus in order to extend the life of the Skouriotissa plant, while retaining the current heap leach technology, it is essential to find further reserves of supergene altered copper mineralization. Simply deepening the Phoenix mine into the unaltered primary mineralization will rapidly lead to uneconomic metal recoveries in heap leaching, necessitating either a change in recovery technology, or closure of the mine.

Experience in other copper producing counties, in particular Chile, has shown that heap leaching of secondary copper sulphides can be commercially successful. The techniques already in use at Skouriotissa to encourage bacterial activity can be intensified to cope with a higher proportion of sulphides in the

feed, if this should prove necessary. For example, stirred tanks could be installed for pre-oxidation of the leach liquor under controlled conditions that are optimized for maximum bacterial activity, prior to discharge on to the heaps.

If after further geological exploration, it becomes evident that further reserves of oxidized/secondary copper ore are limited or non-existent, the result may be that the only option for continued production of copper in Cyprus is treatment of primary chalcopyrite ore. As discussed above, there are two bacterial leach processes capable of treating chalcopyrite minerals that are in advanced states of development. These are the BHP Billiton BioCop process and the Bactech/Mintek process. Both of these are agitated tank leaching processes that require finely ground copper concentrate feeds. Thus if either of these processes were to be introduced at Skouriotissa to provide feed solutions for the SX-EW plant, it would be necessary to install a flotation process, together with the associated crushing and grinding and tailings disposal facilities to produce a copper concentrate feed for the bacterial leaching tanks. If this process route is contemplated, it then becomes necessary to examine the relative merits of the alternatives available for copper concentrate processing, namely, smelting or leaching.

Copper concentrates can be sold in the open market to custom smelters, who produce copper by the traditional pyrometallurgical route of smelting and electrorefining. However, the specifications for smelter feeds are tightly drawn and heavy penalties are imposed for certain impurity elements, e.g. As, Sb, Te, Se, with the result that mines are rarely paid more than 60-70% of the metal value in the concentrate, unless it is exceptionally pure. Selecting this option at Skouriotissa would make the SX-EW plant redundant. This plant is not yet ten years old and should thus have a further life of at least 10 to 15 years. It may already be fully amortised, in which case scrapping the plant and salvaging saleable equipment may be the most economically attractive option. If not, the option of introducing one of the two new bacterial tank leaching processes to produce copper sulphate pregnant solutions to feed to the SX-EW plant should be investigated.

## **8.6 Conclusions from metallurgical studies**

The decline in copper recoveries in the heap leach process used at Skouriotissa is due to increasing amounts of primary chalcopyrite mineral in the run-of-mine ore as mining gets deeper.

Chalcopyrite is a refractory mineral that is very resistant to dissolution by oxidation. Recent processes developed for the hydrometallurgical treatment of chalcopyrite all involve the use of “extreme” conditions, such as high temperature pressure leaching, or ultra-fine grinding, or intensified bacterial leaching.

The best option for extending the life of the Skouriotissa plant would be the discovery and exploitation of further reserves of supergene altered copper ores containing leachable copper oxide and secondary sulphide minerals. This will allow production to continue using the heap leaching technology currently in use. If necessary, the effectiveness of this leaching method towards secondary copper sulphide minerals could be improved by introducing tanks for bacterially pre-oxidising the leach solutions under optimum conditions, prior to being sprayed on to the ore heaps.

If further reserves of secondary mineralization are not found and the only option is treatment of primary chalcopyrite ores, much detailed technical and economic analysis will be necessary. There are three courses of action available in these circumstances: (1) close the mine and plant, salvaging useful equipment for sale; (2) install mineral processing facilities to produce a chalcopyrite concentrate. This leads to two further options: (2a) sell the copper concentrates on the open market to custom smelters, or (2b) install an intensive leaching process on site to treat the copper concentrate to provide copper sulphate feed solution for the existing SX-EW plant.

It is suggested in the discussion above that if option (2b) is attractive, then the two most advanced bacterial leach processes (BioCop and Bactech/Mintek) should be considered, since these are more compatible with the existing technologies and skills at Skouriotissa, than the only alternative technology, which is pressure leaching.

A breakdown of direct cash production costs for a range of heap leach operations are given in Table 18.

Operation	Cost, UScents/lb of Cu produced			
	0.4 % Cu	0.6 % Cu	0.8 % Cu	1.2 % Cu
<b>Mining</b>	11.36	7.58	5.68	3.79
<b>Leaching</b>	18.75	12.50	9.38	6.25
<b>SX/EW</b>	14.00	14.00	14.00	14.00
<b>Maintenance</b>	3.20	3.20	3.20	3.20
<b>Sales</b>	2.00	2.00	2.00	2.00
<b>Total Cash Cost</b>	49.31	39.38	34.26	29.24

Table 18 Estimated heap leaching direct production costs as a function of ore grade (Assumptions: Mining costs — 1 US\$/ton; Leaching costs — 1.65 US\$/ton source: <http://www.copper.org/innovations>).

The low capital and operating costs of heap leach/SX/EW operations together with the relatively simple operation and the direct production of cathode copper close to the mine site make the economics of the process very attractive

Obviously, only a few of the multitude of new hydrometallurgical processes will become successful commercial operations. The Placer Dome process and BioCop are leading the race at the moment with large demonstration plants starting up in 2003. The other leading contenders are the CESL and Dynatec processes. The latter has the benefit of the successful track record of its similar zinc pressure leach process. Halide-based processes, such as Intec, are technically innovative and offer the attraction of atmospheric leaching and the potential to reduce power requirements but the drawbacks are corrosion issues, complex flowsheets and the copper product is not cathode. Outokumpu's recent HydroCopper process is another unique approach that offers a 30% potential reduction in power requirements versus conventional sulphate EW and its development will be followed with interest.

## 9 Geophysical modelling

### 9.1 GRAVITY DATA

The only geophysical information available for the pilot GIS were gravity data from the Overseas Geological Survey work that was undertaken in 1963. This survey was carried out using a Worden gravimeter, and a base station network of forty-three base stations. Measurements of observed gravity were converted to Bouguer gravity anomaly readings, using the gravity readings, with the height, latitude and topographic correction at each station. These anomaly readings were used in the pilot GIS, with measurements estimated to have a possible error of no more than 0.9 mGal. This relatively large possible error (~1% or less of the total fluctuation of anomalies on Cyprus) was due to the lack of trigonometric points, spot height or benchmarks, lack of detailed maps (1:50 000 contour maps were used), and errors attributed to the reading of the instrument and poor calibration Gass and Masson-Smith, 1963. 798 readings were taken on Cyprus, and 670 of these were contoured and used in the pilot GIS (Figure 100). The gravity data is generally low resolution, with occasional large gaps between sample points, meaning that that no gravity lineations could be derived.

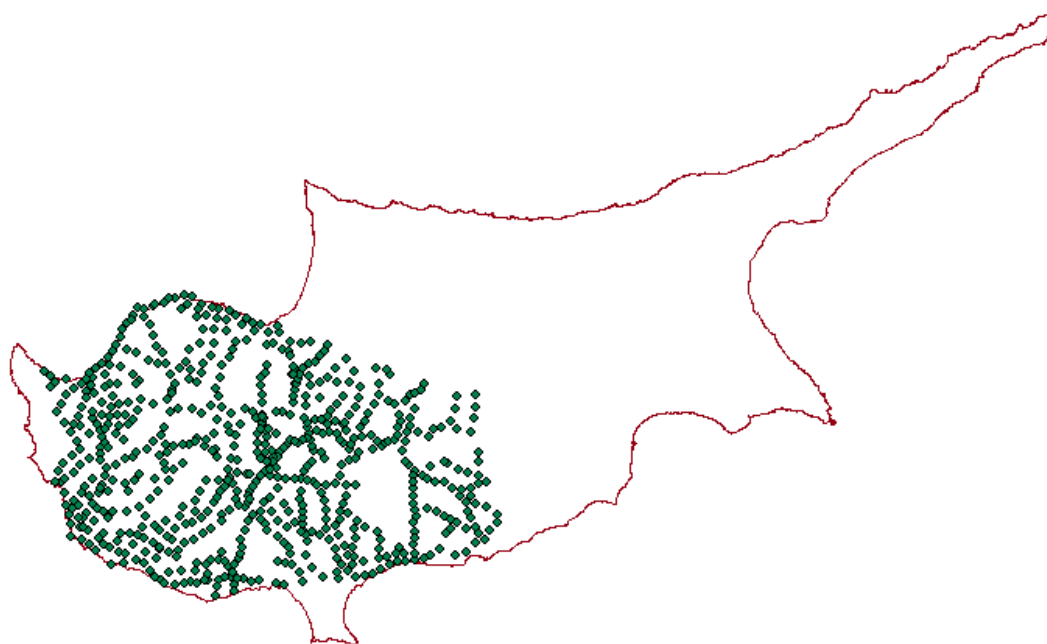


Figure 100 Gravity survey points used in mineralization potential modelling (data from Gass and Masson-Smith, 1963).

### 9.2 MAGNETIC DATA

As part of the collaborative nature of the project Eastern Mediterranean Minerals provide access to proprietary and public domain geophysical data sets in digital form. These comprised three generations of airborne magnetic data:

- A regional airborne survey on a 1 km grid covering the south of the island.

- The United Nations Development fund survey flown in 1970 on a 200 m grid
- Two helicopter surveys flown in 1998 on a 25 m grid

A detailed description of how the data were reprocessed and interpreted is given below.

### 9.2.1 Data sources

The project accessed three generations of airborne magnetic data as outlined below. The utility of each of the datasets is different, ranging from a regional overview to a tightly-focussed investigation at a target level.

#### 9.2.1.1 REGIONAL DATA

This data set is a 1 km grid that covers the south of the island (Figure 101). The date of acquisition of the source data and the flying height have yet to be identified, but it is possible to speculate that the flight height was relatively large. The anomalies are in gammas relative to an unknown geomagnetic reference field. This uncertainty precludes applying a reduction-to-pole operator, and the decision was taken to undertake no additional processing on these data. In any case, this dataset is of limited utility for detailed exploration, but is useful for giving an overview of the anomalies over the island.

#### 9.2.1.2 THE UNDP SURVEY

The ‘UN data’ were acquired as part of a United Nations programme to survey the groundwater and mineral resources of Cyprus (UnitedNationsDevelopmentFund, 1970). The survey was flown in 1966 by Hunting Geology and Geophysics Ltd, and covers approximately 1500 km<sup>2</sup> over the Pillow Lava complex and the northern edge of the Troodos Range, as well as an area of sedimentary rocks adjacent to the lavas (Figure 101). Flight lines were oriented NNE-SSW and were spaced at 400 m. Measurements were made at approximately 100 m above the ground surface. The data were made available as a grid of anomalies in gammas with a 200 m cell size.

The geomagnetic reference field that was used to generate the anomaly values of this survey had the following parameters: inclination 50°, declination 2.5° and magnitude 43500 gammas (G. Maliotis, pers. comm.). This may be compared with the values of the International Geomagnetic Reference Field (IGRF) for epoch 1966.5, evaluated at a representative point (33°E, 35°N, altitude 365 m), which are 51.8° inclination, 2.45° declination and total field strength 44847 nT. Clearly a slightly different model of the Earth’s field has been applied, and the *prima facie* evidence would suggest adding a value of -1347 nT to the UN data to bring it in line with the IGRF for the relevant date and location.

#### 9.2.1.3 DETAILED SURVEY DATA

Two areas surveyed by Eastern Mediterranean Minerals (EMM) were also available (Figure 101, areas AB and C). These data were acquired in December 1998 by helicopter, with a sensor height of 30 m above ground level. The orientation and separation of the flight lines are unknown to the author. The data grids have a cell size of 25 m.

The dataset consists of diurnally corrected total magnetic field (measured in nanoTesla [nT]) that may be reduced to magnetic anomaly by subtraction of a suitable reference field. A representative point for IGRF calculation was selected as 33°E, 35°N, altitude 368 m (for areas AB and C the mean terrain elevation is 406 m and 269 m respectively). We may therefore estimate the IGRF at the representative point as: magnitude 45340 nT, inclination 51.1 ° and declination 2.5 °. Uncertainties in the survey height are relatively unimportant, given that the IGRF has a vertical rate of variation of approximately 23 nT/km for epoch 1998.5.

### 9.2.2 Data processing

The individual surveys in the aeromagnetic dataset were flown at different heights, and the supplied grids each have a different cell size. Both of these factors can cause the data to have a different intrinsic frequency content, which can make the exact merging of the data sets difficult, and the presence of mismatches at the survey joins must therefore be expected. Furthermore, the use of different reference fields when calculating anomaly values is likely to lead to join errors at the edges of the individual surveys.

When merging the data, the decision was taken to use the EMM surveys as a reference because most is known about these data. Accordingly, anomaly values that were calculated by subtraction of the IGRF total field value were held as constant. The UN survey was shifted by -1347 nT in order to bring it into line with the expected IGRF as noted above; after this shift the dataset remained fixed. A level shift was applied to the regional data in order that the mean value of these data is equal to the mean value of the (shifted) UN magnetic data. A composite grid of data was produced from the adjusted data with a grid spacing of 25 m, chosen so that the full resolution of the EMM data is preserved. The final combined grid is shown in Figure 102.

#### 9.2.2.1 GEOPHYSICAL TRANSFORMATIONS

The combined data set (Figure 102) was used for geophysical interpretation in conjunction with the original grids. For each grid, a number of derived grids were computed by applying selected geophysical transformations, using software that was developed in-house and programs from the Generic Mapping Tools (GMT) package (Wessel and Smith, 1991). The derived grids included residual anomaly after upward continuation and the horizontal and vertical gradients. The reduction-to-pole transformation was not applied because it was judged that the likely presence of remnant magnetisation in the basalts, together with uncertainties in the reference fields, would make this too likely to introduce errors.

#### 9.2.2.2 IDENTIFICATION OF LINEAR AND AERIAL FEATURES

The grids and derived grids were loaded into the ArcView 3.2 GIS, where a BGS-developed extension was used to generate shaded-relief images. Linear features ('linears') were identified on the images by altering the illumination direction so as to highlight those features trending at a high-angle to the illumination direction. Features that were identified in this way were digitised into a GIS theme using the classification system given in Table 19. As well as recording the

linear type, a record was also kept of the interpreter, the map from which the linear was recognised and a comment.

Linear type	Characteristics
Minimum	Local anomaly minimum with pronounced character and / or extensive along-strike trend.
Maximum	Local anomaly maximum with pronounced character and / or extensive along-strike trend.
Minimum (discontinuous)	Local anomaly minimum with a more speculative character.
Maximum (discontinuous)	Local anomaly maximum with a more speculative character.
Inflection	A line of inflection in the total field, corresponding to a horizontal gradient maximum.
Offset	An line along which there is an offset in the anomaly pattern
Truncation	A line that truncates the anomaly pattern.
Speculative	A more speculative line that may be drawn to highlight a possible interpretation. These lines should be textually described.
Cultural	A linear whose source is of man-made origin, for example a road, railway line or pipeline. These may be recognised by their geometric regularity and / or their coincidence with mapped features.

Table 19 System of classification used for linear features.

As well as the identification of linear features described above, aerial features were identified from the combined grid by firstly upward continuing the data in order to smooth it, and then removing regional trends by subtraction of a low-order polynomial that was fitted by least-squares minimisation. The resulting residual anomalies were then contoured, and representative contour levels were chosen that illustrate features within the data. The purpose of this step is to indicate zones of low magnetic anomaly, which may be associated with areas that have been affected by alteration, with consequent destruction of primary magnetisation.

### 9.2.2.3 INTERPRETATION

A is presented here, based on the picked linears and polygonal features (Figure 103).

Three primary domains in the data are recognised on the basis of the orientation of linears. Domains one and two are separated by a line trending NNE through approximately [527000 3870000]. West of this line (domain one), the predominant trend is NNE, with important subsidiary trends of E and WNW. There are also a number of arcuate features, for example near [522000 3872000]. Contrastingly, to the E of the domain boundary (i.e. in domain 2), features with a NNE trend are absent, and the predominant trend is now approximately orthogonal (WNW). Because this is recognised in the area covered by the Eastern Mediterranean Minerals survey area AB, it is unlikely to be an artefact caused by the orientation and spacing of the flight lines. Preliminary interpretation of the line separating domains one and two is as a fault with an approximate NNE trend (sense of movement unknown). Note that there is also a

major dislocation near this location that is apparent in the interpretation of linears from satellite images.

Domains two and three are separated by an extensive linear feature that extends from about [525000 3858000] to [557000 3877000], a distance in excess of 30 km. Within domain two, as noted above, the predominant trends are approximately WNW and ENE. Contrastingly, in domain three, linears with a WNW trend are virtually absent, and within this domain the structural trend is predominantly ENE; the anomalies are also of lower amplitude. The nature of the boundary between domains two and three changes along strike, for example clearly truncating anomalies near [546000 3870000], but generally has the appearance of a discontinuous minimum. It appears to be offset along orthogonal linears near [531000 3862000] and [542000 3867000]. The preliminary interpretation of this feature is that it represents a significant fault (sense of movement unknown).

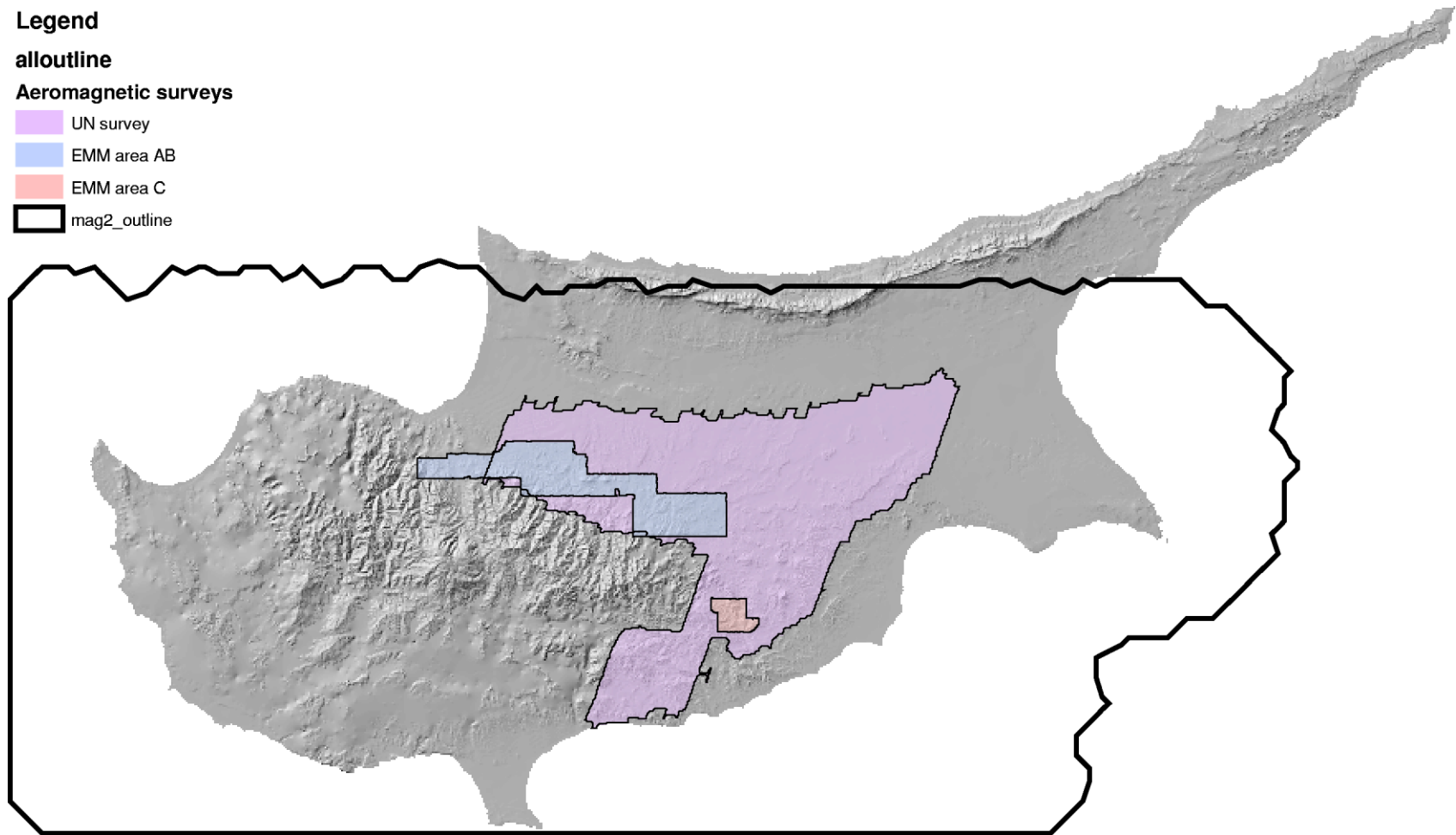


Figure 101 Locations of the three generations of survey that were available. The regional survey outline is shown by the thick bold line (mag2\_outline in the legend). The 1966 Hunting's data is shown in pink, Eastern Mediterranean Minerals (EMM) area AB in blue and EMM area C in orange.

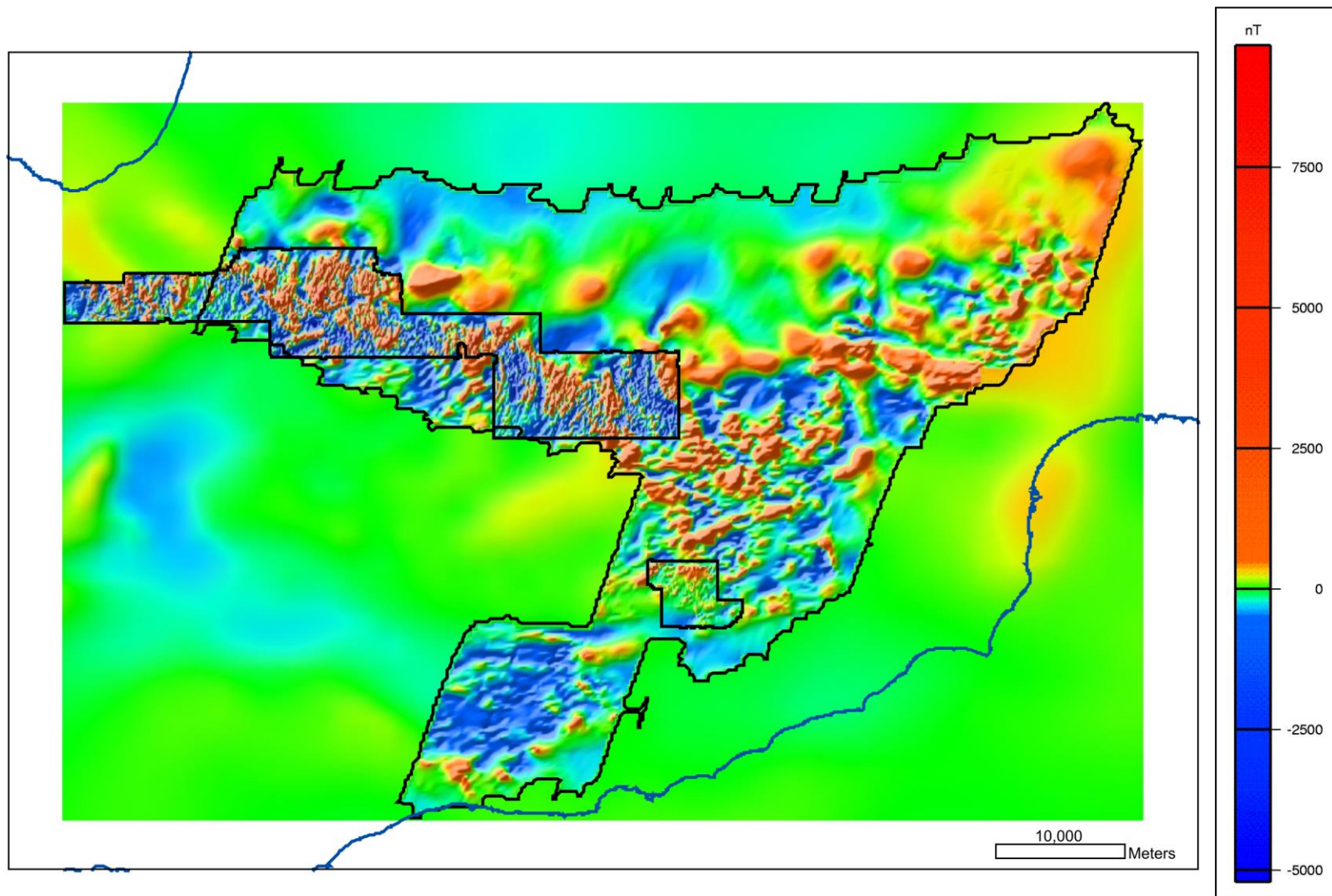


Figure 102 The combined aeromagnetic anomalies after merging the three generations of data as described in the text (NE illumination).

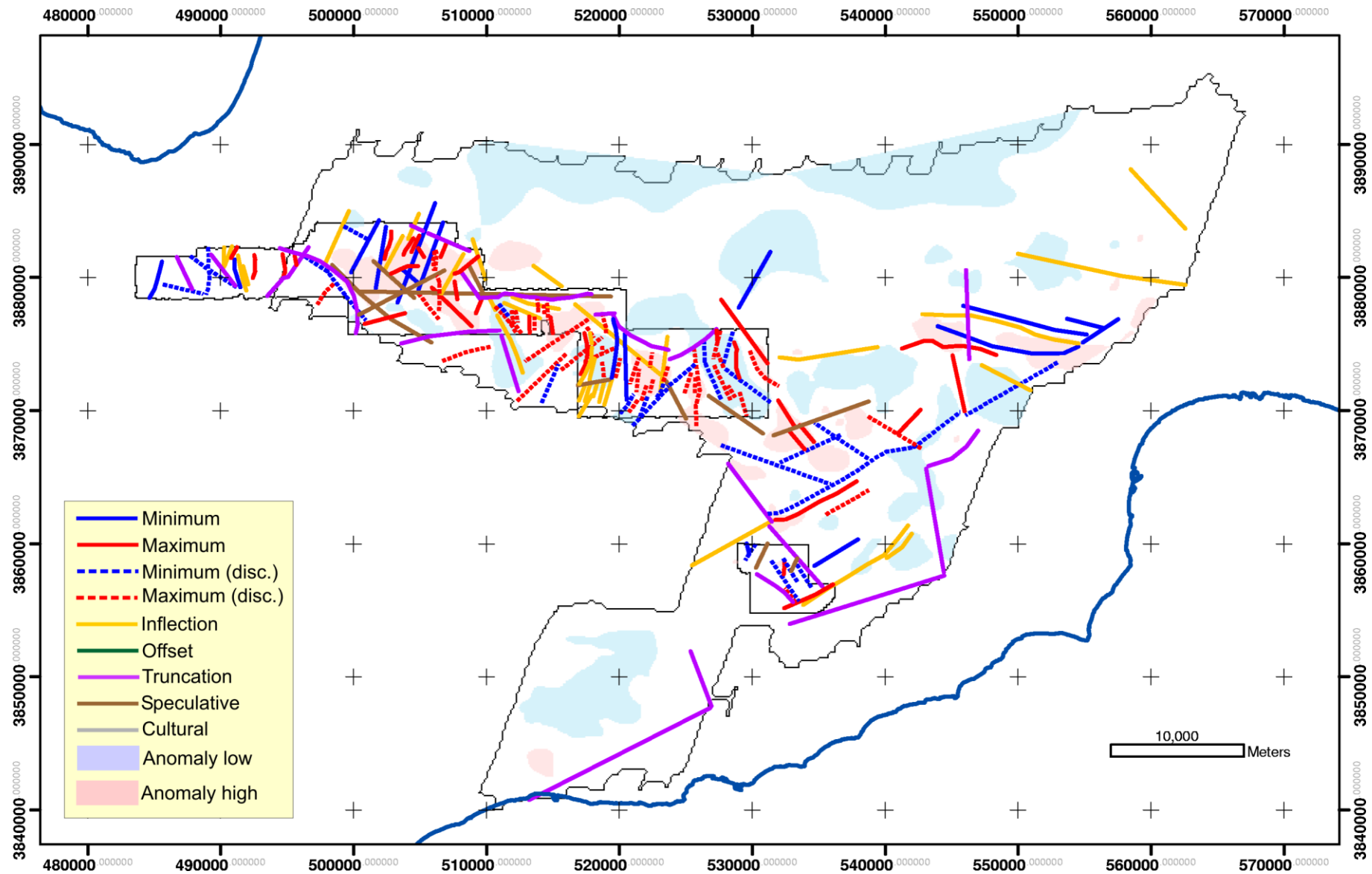


Figure 103 The preliminary geophysical interpretation of linear and polygonal features.

# 10 Remote sensing

## 10.1 PIMA

### 10.1.1 Background information

The PIMA is a field-portable spectrometer that measures reflectance in the short-wave infrared (SWIR) range of 1300–2500 nanometres. It allows quick and relatively easy identification of alteration minerals and can identify changes in the crystallinity of samples. Sample analysis requires no preparation, and each sample measurement usually takes around 30–60 seconds (Pontual et al., 1997a). Figure 104 shows a hull quotient PIMA spectrum taken on a jarosite sample from Phoenix mine. The sample is not 100% pure, as two of the characteristic absorptions are slightly masked or overprinted by another unidentified mineral, present in very small amounts. However, the main diagnostic absorption features are unaffected, and so the dominant Jarosite component of the mixture can easily be identified. Identification was done automatically using Spectral Geologist software. It should be understood that PIMA analysis does not always give interpretable results:

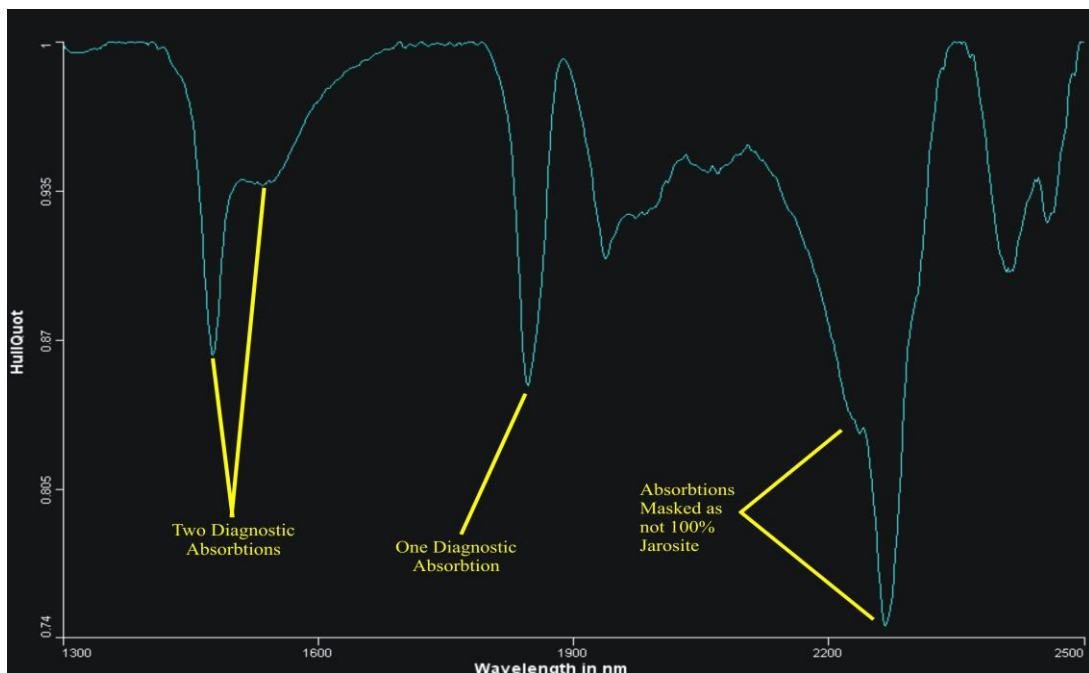


Figure 104 Hull quotient spectrum for a jarosite sample (CYR 011f) from Phoenix mine, showing diagnostic absorption troughs.

- It works well with single minerals and mixtures of minerals where one mineral dominates the rest, but more varied mixtures can provide confusing spectra, and no mineral species can be identified
- Only certain minerals with specific molecular bonds can be identified, meaning that its use is generally restricted to alteration minerals
- Spectra obtained in wet conditions and on wet samples can be dominated by water absorbance.

- Samples must also be clean and relatively dust-free, as dust or residues (e.g. drilling muds) may be sampled by the PIMA, giving spurious results.
- The colour of the sample being used may also cause problems—darker coloured samples give poorer results than lighter coloured ones. This is due to the lower reflectance and higher absorption in dark samples
- The Spectral Geologist software has a limited library of mineral spectra, so it may not identify any rare or unusual minerals encountered.

### 10.1.2 Pima data

Elevation (m)	Easting	Northing	Locality	Samples (# analyses)	Notes
1847	488323	3865474	Asbestos Mine	CYR 001 (3)	Former Asbestos Mine at Amiandos. General Troodos Overview—Background Sampling.
1827	488310	3865301	Dunite Pod	CYR 002 (4)	General Troodos Overview—Background Sampling.
1813	487353	3865364	Harzburgite Sequence	CYR 003 (4)	General Troodos Overview—Background Sampling.
1853	487379	3865472	Harzburgite Sequence	CYR 003 (1)	General Troodos Overview—Background Sampling.
1847	486994	3865454	Harzburgite Sequence	CYR 004 (2)	General Troodos Overview—Background Sampling.
1512	492046	3865595	Serpentinite	CYR 004 (1)	General Troodos Overview—Background Sampling.
1713	486763	3866949	Dunite-Harzburgite Sequence	CYR 005 (3)	General Troodos Overview—Background Sampling.
1706	486720	3866957	Dunite-Harzburgite Sequence	CYR 005 (1)	General Troodos Overview—Background Sampling.
1428	487181	3862495	Gabbro Sequence	CYR 006 (3)	Locality close to Gabbro—Mantle Sequence Boundary. General Troodos Overview—Background Sampling.
1294	493132	3865693	Gabbro Sequence	CYR 006 (1)	General Troodos Overview—Background Sampling.
800	490083	3870770	Plagiogranite (Top of Gabbro Sequence, Near Apliki)	CYR 007 (2)	Extensive pervasive alteration seen in road cutting. General Troodos Overview—Background Sampling.
654	491242	3872423	Sheeted Dyke - Gabbro Contact	CYR 008 (2)	Road Cutting, with dykes intruding into Gabbros and Plagiogranites—incoming of Dykes into ophiolite sequence. General Troodos Overview—Background Sampling.
252	495529	3882275	Lower Pillow Lavas	CYR 009 (5)	Road Cutting, General Troodos Overview—Background Sampling.
208	489565	3883479	Phoenix Pit Working Bench	CYR 010 (6)	Working Mine
280	489933	3883804	Skouriotissa Fault Overview, in Phoenix Pit	CYR 011 (10)	Working Mine
317	490870	3883134	Three Hills Pillow Lavas	CYR 012 (5)	Working Mine
396	484719	3881090	Apliki	CYR 013 (5)	Copper Sulphide Prospect
287	485599	3881106	W Apliki	CYR 014 (4)	Former Mine, currently being considered for reopening
474	525219	3872400	Red hills	CYR 015 (10)	Copper Sulphide Prospect
475	525186	3872400	Red hills	CYR 016 (2)	Copper Sulphide Prospect, CYR016 is inter-pillow material
417	524826	3872851	Kambia	CYR 017 (4)	Former Mine, abandoned in 1970's

Table 20 PIMA sampling localities, May 10th-17<sup>th</sup> 2003.

PIMA analyses were taken at various localities over the Troodos Ophiolite, using a PIMA-SP instrument. Table 20 shows sample details. At some sites, more than 1 sample was analysed, whilst at others, one sample may have been analysed 2 or 3

times, depending on uniformity of alteration. Veins and encrusting material were also sampled and analysed to give a better picture of any alteration.

In addition to the field sampling, PIMA analyses of two deep boreholes (CY-2 and CY-2a) from the Cyprus Crustal Study Project were undertaken. Where possible, samples were taken systematically in the alteration zones of each core, and above and below areas of mineralization. This, however, proved difficult, as the core had been sampled extensively for previous research, including the removal of ‘mini-core’ samples at 90° to the core-axis. However, analyses were taken, along with core descriptions and magnetic susceptibility readings from the same points as the PIMA analyses. A total of sixty-one readings were taken from Hole CY-2, from a depth of 5.00 m to 104.70 m, and eighty-two from Hole CY-2a, from a depth of 140.40 m to 300.30 m, as well as a solitary reading from 433.60 m for clarification reasons.

Data obtained from these analyses are presented in Appendix I and were used as a ground-truthing tool to aid processing of the ASTER imagery (see section 10.2.2 below)

## 10.2 SATELLITE IMAGERY

### 10.2.1 ASTER background information

Subsystem	Band Number	Spectral Range (µm)	Spatial Resolution (m)
Very Near Infrared (VNIR)	1	0.520–0.600	15
	2	0.630–0.690	
	3 Nadir	0.780–0.860	
	3 Backward	0.780–0.860	
Short-wave Infrared (SWIR)	4	1.600–1.700	30
	5	2.145–2.185	
	6	2.185–2.225	
	7	2.235–2.285	
	8	2.295–2.365	
	9	2.360–2.430	
Thermal Infrared (TIR)	10	8.125–8.475	90
	11	8.475–8.825	
	12	8.925–9.275	
	13	10.25–10.95	
	14	10.95–11.65	

Table 21 Characteristics of the three ASTER sensor systems (adapted from Abrams et al., 2002)

ASTER (Advanced Spaceborne Thermal Emission and Reflectance Radiometer) is an imaging instrument based on Terra, a satellite launched in December 1999 as part of NASA’s Earth Observing System and as a joint venture between NASA, Japan’s Ministry of Economy, Trade and Industry and the Earth Remote Sensing Data Analysis Center NASA, 2003. The instrument covers a wide spectral region, enveloping fourteen different wavelength bands from the visible to thermal infrared (Table 21). Each subsystem of the ASTER instrument has its own telescope, and the ASTER instrument, with its high resolution, acts as an aiming device for other instruments on the Terra satellite platform. The Terra satellite is in a sun-synchronous orbit, flying at an altitude of 705 km, and can gather data from the entire globe, covering around 8% of the earth’s surface in one day. Image resolution varies with wavelength, and each ASTER image, or scene, covers an area of 60 by

60 km, although multiple images can be joined together to form a mosaic image Abrams et al., 2002.

### 10.2.2 Aster data

The images of Cyprus were obtained from three different passes of the Terra satellite, creating slightly differing colours and shading according to the time of day that the satellite passed over, and also forming northeast-southwest trending artefacts (Figure 105). This may have created problems, but the main area of interest for the project was covered by two passes of the satellite (Figure 105—passes 1 and 2), meaning that any data discontinuity was minimal. However, if Pass 3 is to be used in any subsequent analysis continuity may cause problems. Though, as data manipulation was carried out by comparing pixels in the same place in two separate layers, creating a greyscale band ratio image, rather than using a mathematical function, means that the overall result should not be affected. Before image processing, the images were corrected for atmospheric absorption effects. This was done by using known black body reflectors, such as bodies of water, to correct the images.

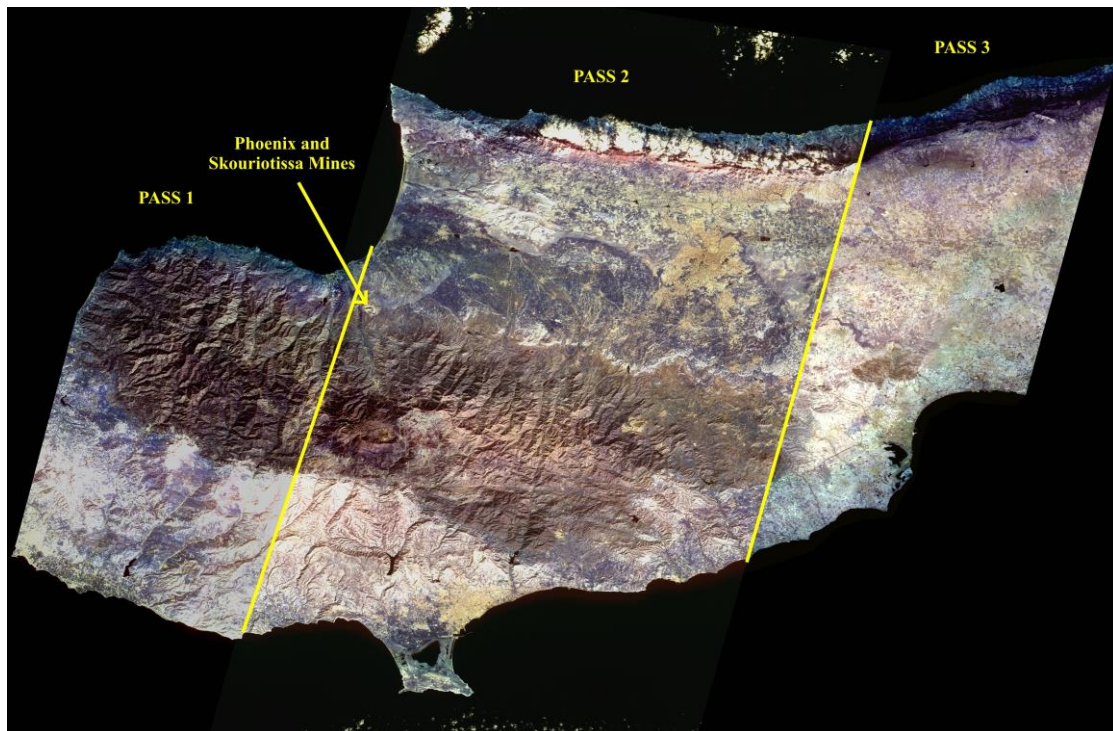


Figure 105 False-colour SWIR mosaic image of Cyprus, showing Phoenix and Skouriotissa mines for reference, and separate satellite overhead passages—notice the differences in colours and textures between passes.

After initial corrections, the ASTER images were processed using a technique employing ratios of individual spectral bands as this highlights the spectral differences between materials, whilst at the same time decreases the variations in surface brightness due to topographic effects. It involves dividing one ASTER layer by another—pixel values in one layer are divided by pixel values at the same location in another layer. In addition, spectra for mineralization-associated alteration assemblages were obtained from PIMA sample analysis, and used as to ground-truth the ASTER data. Figure 106 shows a PIMA spectrum, of a sample taken from the Phoenix open pit, with ASTER SWIR Bands superimposed. It shows the associations between distinctive absorption and higher reflectance features and

ASTER spectral bands 1–6 and these can be used to identify the minerals or mixture of minerals within ASTER images using the band-ratining technique. Suitable ASTER bands were identified using a scalar function within The Spectral Geologist software, enabling reflectance within ASTER wavelengths to be identified and compared, and allowing the deduction of suitable band ratios to be used in prospectivity analysis.

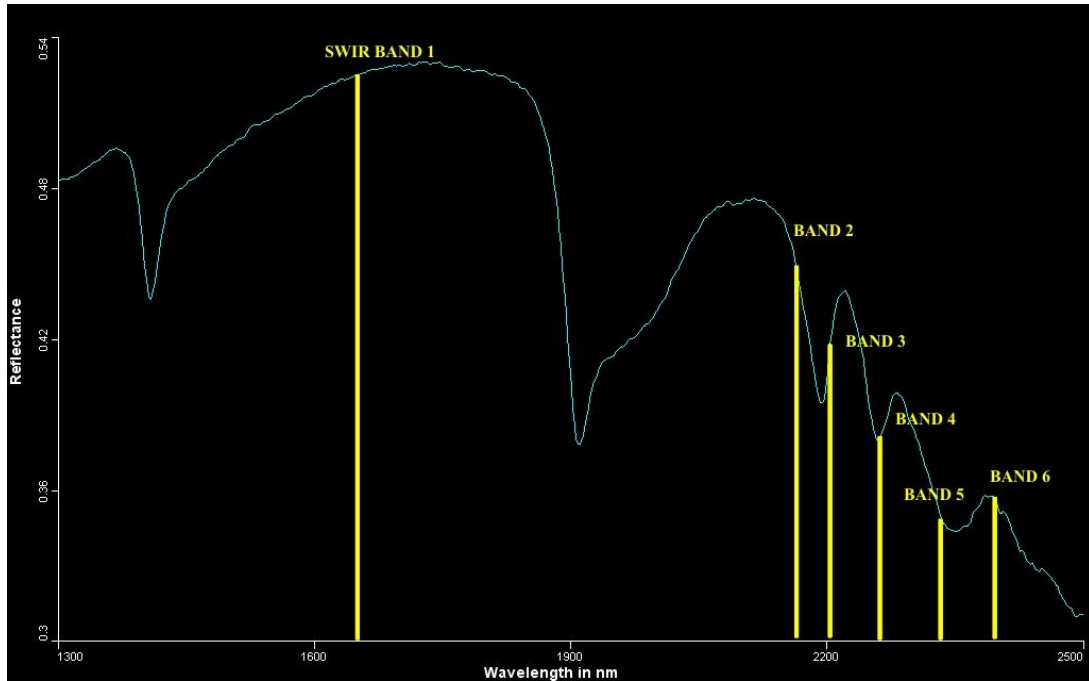


Figure 106 PIMA spectra for sample taken from Phoenix working pit, sample Cyr\_010b, showing mid-ranges for ASTER SWIR spectral bands 1-6.

Band ratio images have the effect of amplifying the reflectivity minima when compared to maximum values. Taking Figure 106 as an example, this graph shows (i) that this sample has a reflectance maximum for ASTER SWIR bands within Band 1, and a (ii) minimum within Band 5. Furthermore, this maximum and minimum are not seen in areas where this type of alteration is absent. Table 22 explains with arbitrary numbers how these maximum and minimum values are used. These are used as there are no typical values for altered or unaltered rocks—values change mainly according to the amount of alteration assemblage minerals contained in rocks and other surface material (Sabins, 1999). Therefore, the ratio image produced by ASTER SWIR bands 1/5 should highlight the mineral assemblage present in Figure 106.

Rock Type	Band 1 Reflectance (Pixel Value)	Band 5 Reflectance (Pixel Value)	Ratio 1/5	Pixel Value for Band Ratio Image
Altered Rocks containing the same assemblage as Cyr_010b (Figure 106)	100	50	2.0	200
Unaltered rocks	100	100	1	100

Table 22 Calculation of pixel values in band ratio images

In the pilot analysis, the main use of the PIMA data was to identify the highest and lowest reflectance values in the six ASTER SWIR band wavelengths. These can then be used to identify band ratios that best predict mineralization—greyscale mineral maps where the higher the pixel value is, the more alteration assemblage is present, and therefore the higher the possibility of mineralization underlying or adjacent to the alteration (Sabins, 1999). The only band ratio image used in any modelling that was not ground-truthed using PIMA data was a very near infrared (VNIR) band ratio image, where band 2 was divided by band 1 to try and give a limonite image— this is equivalent to a Landsat 3/1 image, which also highlights iron oxides. However, it did not show any clear relation to mineralization, and was not used in the subsequent prospectivity analysis. Figure 107 to Figure 112 show the greyscale band ratio images used for binary prospectivity mapping in the pilot GIS.

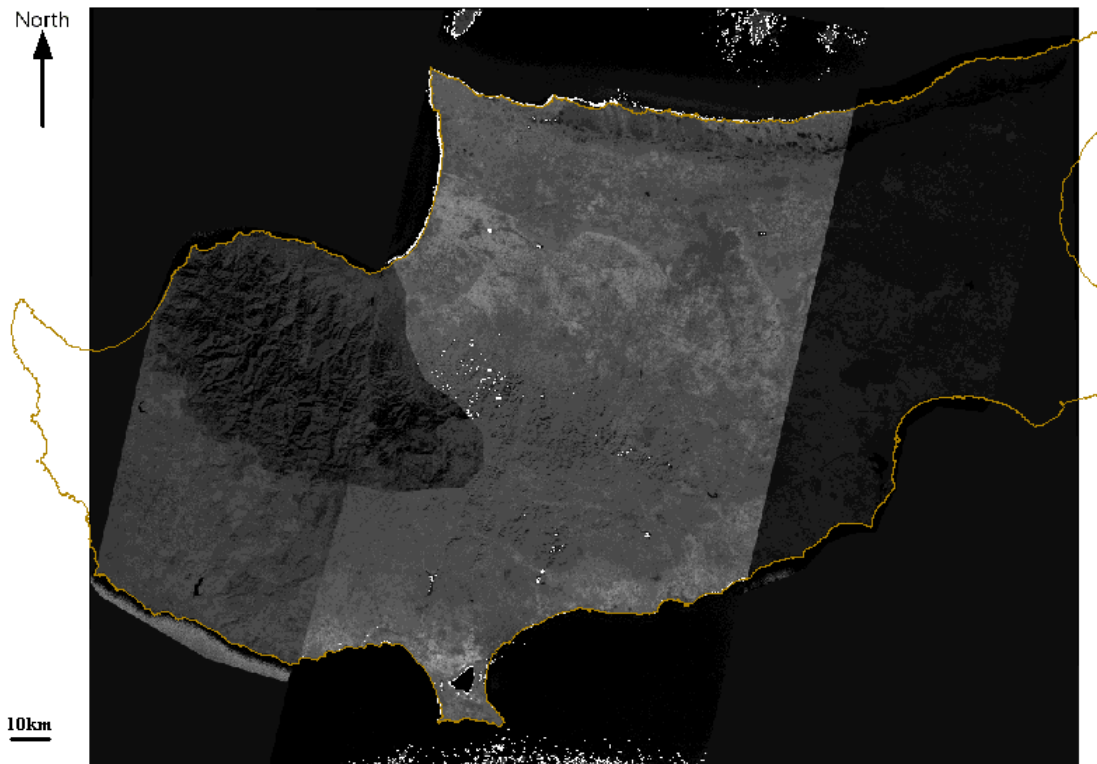


Figure 107 Greyscale band ratio image for ASTER SWIR Bands 1 / 3. Lighter areas indicate areas of high concentrations of mineralization-related alteration assemblages.

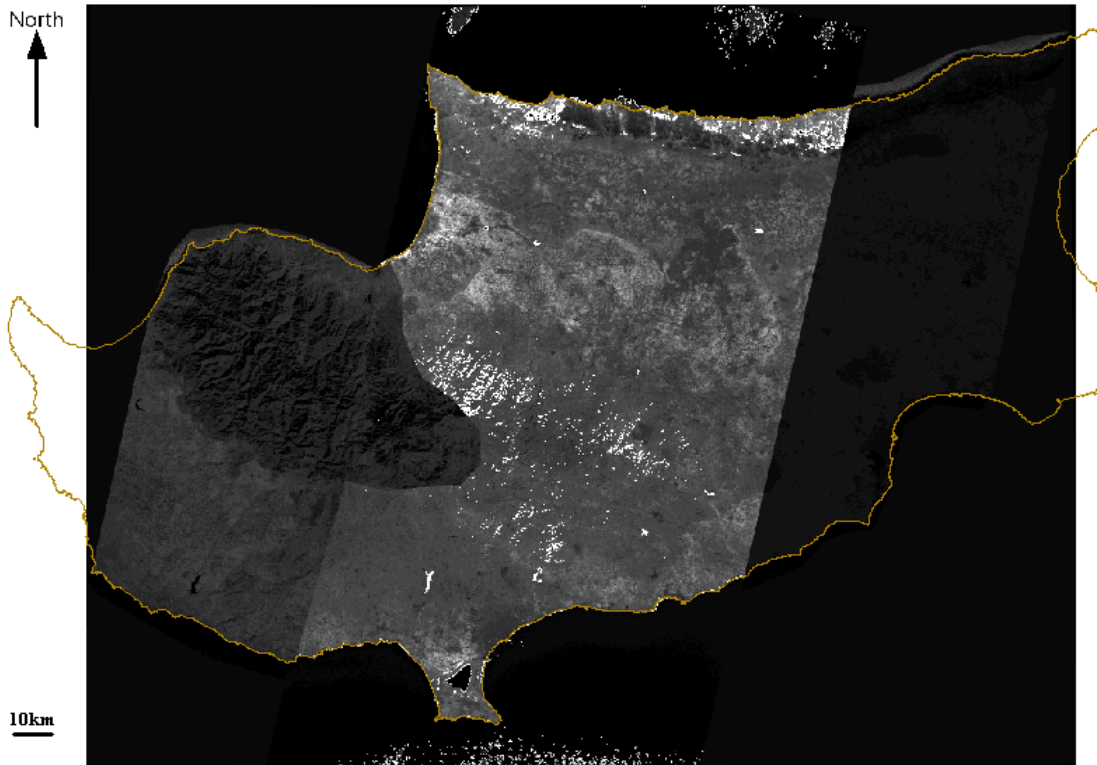


Figure 108 Greyscale band ratio image for ASTER SWIR bands 1 / 5. Lighter areas indicate areas of high concentrations of mineralization-related alteration assemblages.

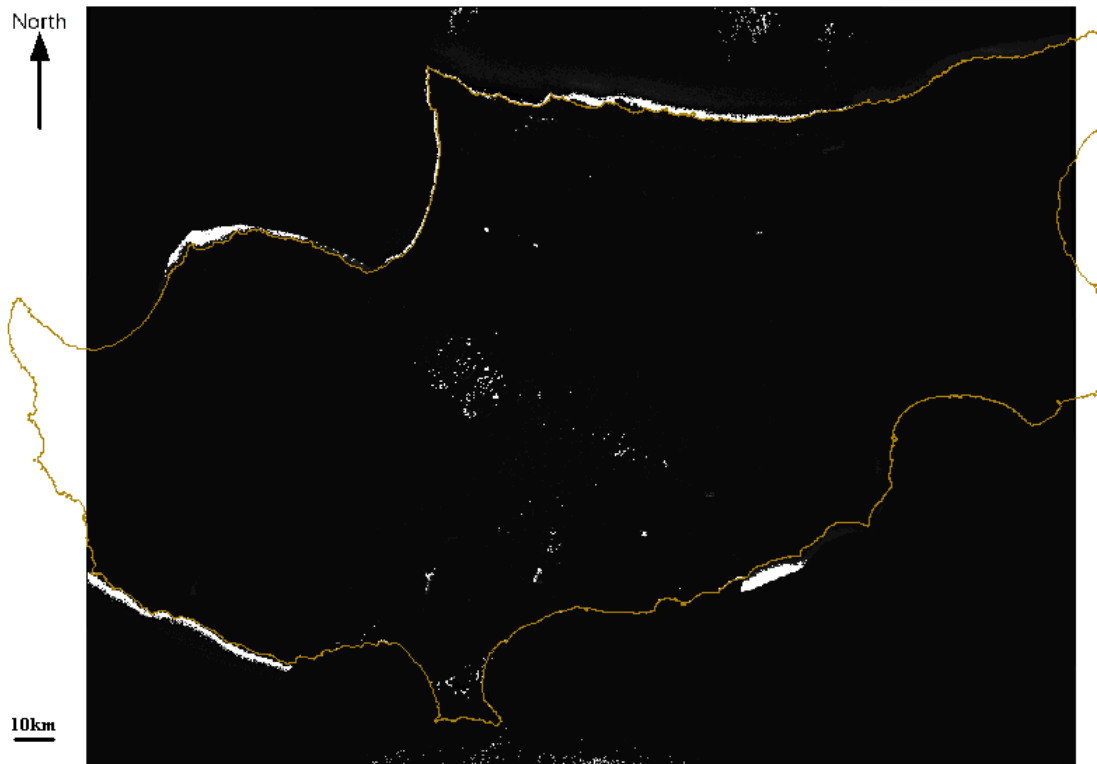


Figure 109 Greyscale band ratio image for ASTER SWIR bands 2 / 3. Lighter areas indicate areas of high concentrations of mineralization-related alteration assemblages.

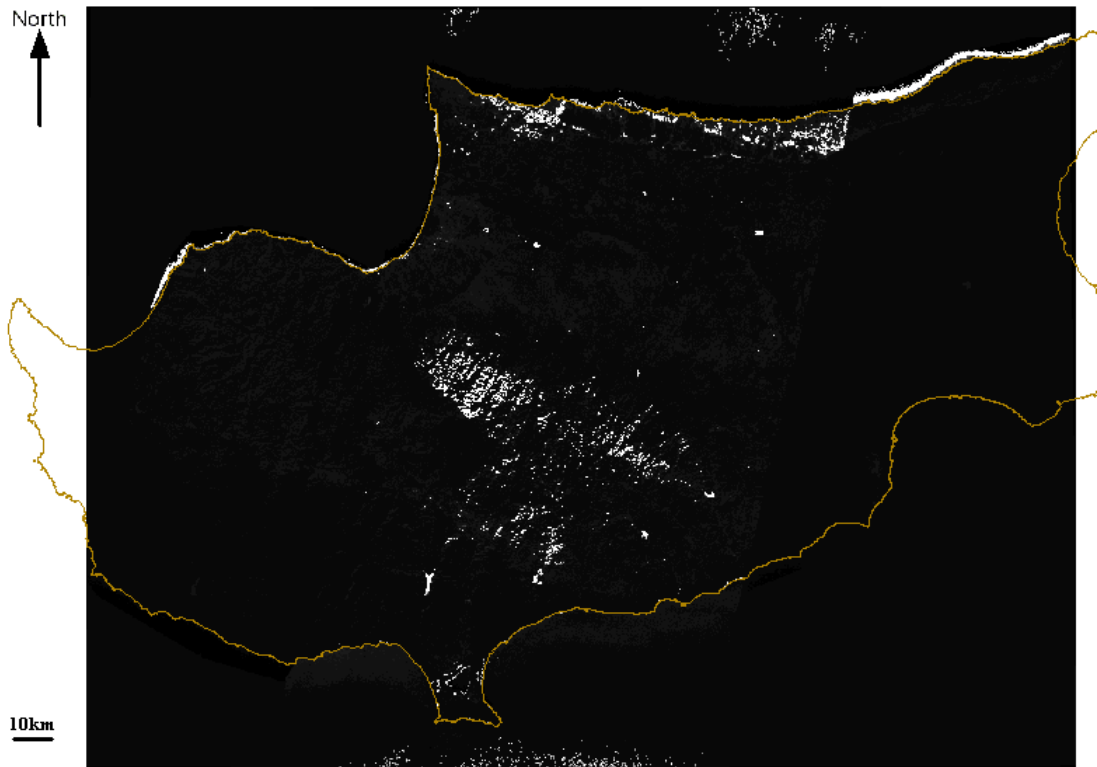


Figure 110 Greyscale band ratio image for ASTER SWIR bands 2 / 5. Lighter areas indicate areas of high concentrations of mineralization-related alteration assemblages.

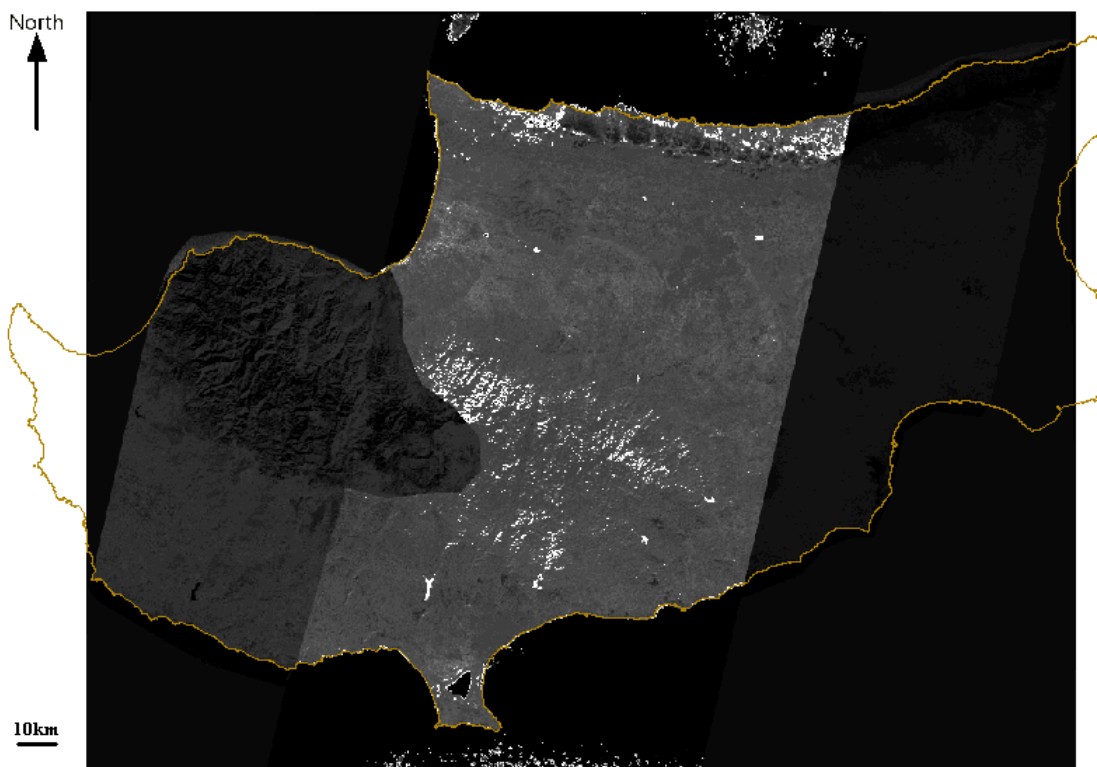


Figure 111 Greyscale band ratio image for ASTER SWIR bands 4 / 5. Lighter areas indicate areas of high concentrations of mineralization-related alteration assemblages.

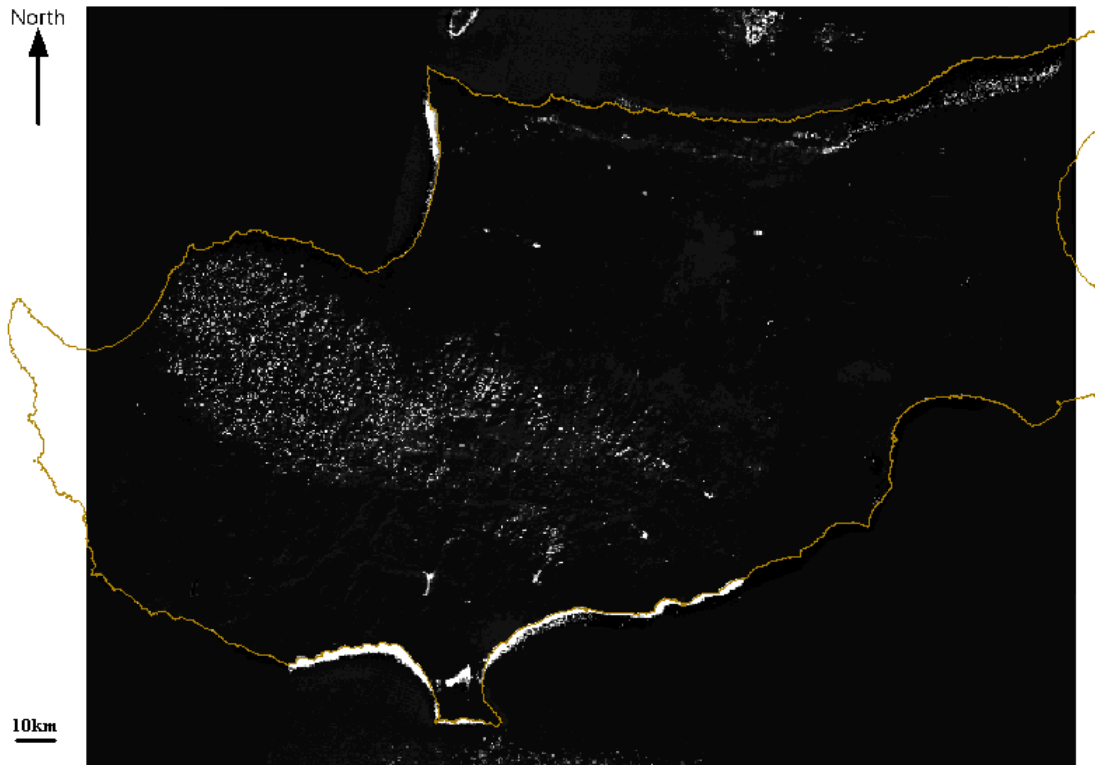


Figure 112 Greyscale band ratio image for ASTER SWIR bands 1 / 5. Lighter areas indicate areas of high concentrations of mineralization-related alteration assemblages.

In addition to the band ratio images, lineation analysis maps were created from ASTER derived digital elevation models (DEMs) of Cyprus. Figure 113 illustrates this and is artificially lit from an azimuth of  $225^{\circ}$  to highlight any NW–SE features or lineations. The lighting on the DEM can be rotated to highlight lineations in other directions, for example Figure 114 shows an image lit from  $315^{\circ}$ , which highlights NE–SW features. ERDAS–IMAGINE was used to pick lineations, which were then saved to a shape file.

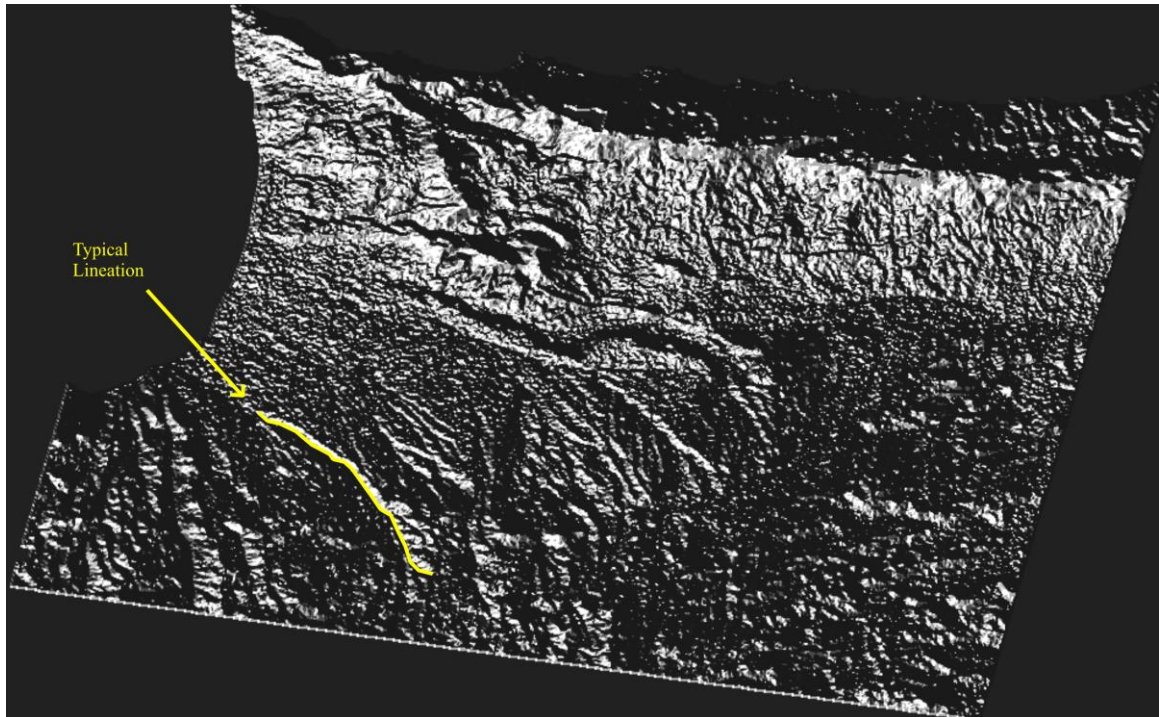


Figure 113 DEM of part of northern Cyprus, lit from an azimuth of 225° to show NW–SE trending lineations.

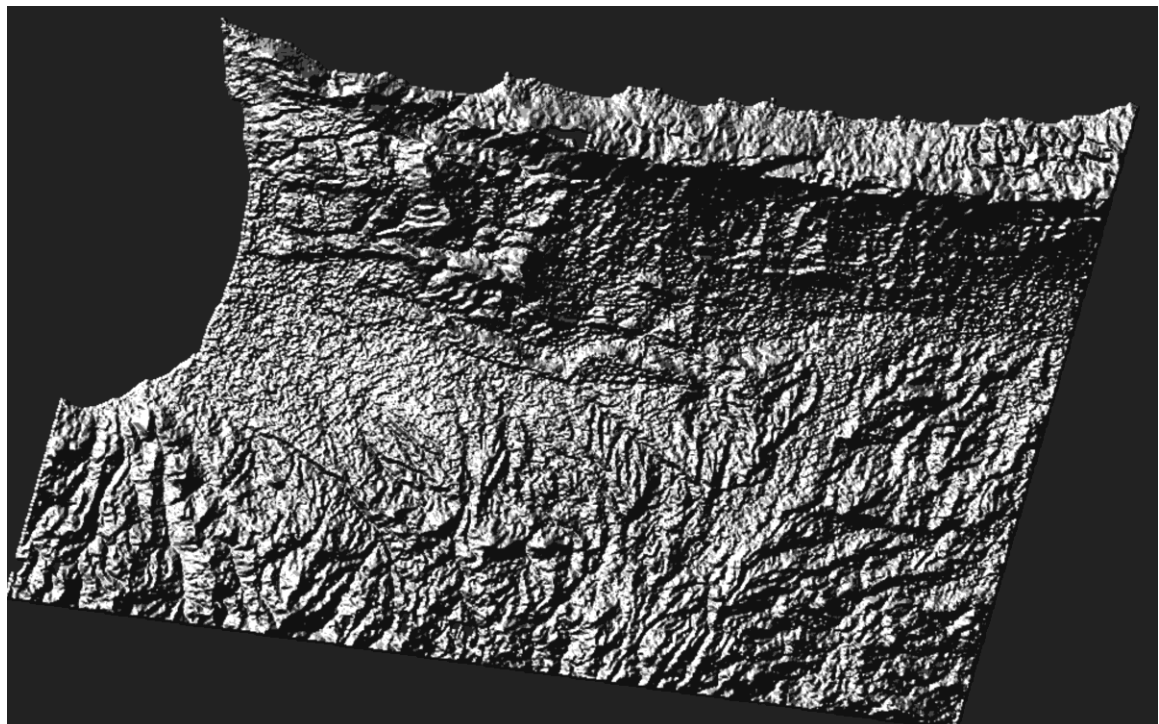


Figure 114 DEM of part of northern Cyprus, showing NE-SW trending lineations, at 90° to Figure 113.

### 10.2.3 LANDSAT: background information

The LandSat 5 satellite was launched in 1984, and orbits the earth at an altitude of 705 km, covering the earth every 16 days. The satellite carries two main imaging sensors, the Thematic Mapper (TM) and the Multi-Spectral Scanner (MSS). The

MSS sensor responds to earth-reflected sunlight in four spectral bands, with a resolution of 80 m. The Thematic Mapper sensor is an advanced, multi-spectral scanning Earth resource sensor designed to achieve higher image resolution, sharper spectral separation and greater radiometric accuracy and resolution than the MSS sensor. This sensor produced the TM images used in the pilot GIS. TM data are sensed in seven spectral bands, with each spectral band covering a much wider wavelength range than the ASTER data mentioned previously. Figure 115 shows a graphic comparison between sensors on the two platforms and shows that ASTER has far narrower wavelengths than TM, especially in the thermal infrared. Table 23 shows that the resolution for VNIR spectra on the Landsat-5 Platform is poorer than ASTER. However, the SWIR data for both platforms is at the same resolution. Image sizes produced by TM (185 by 172 km) are larger than ASTER images (60 by 60 km), meaning that most of Cyprus, including all of the study area, is included in one image. This means that no mosaicing of images was necessary and consequently no unwanted imaging artefacts are included in LandSat images. In addition, the longevity of the LandSat satellite programme means that far more research has been undertaken into band ratio image processing than for ASTER images. Three commonly used band ratios were used to create greyscale images:

- 5/4 for ferrous minerals
- 5/7 for clays
- 3/1 for iron oxides

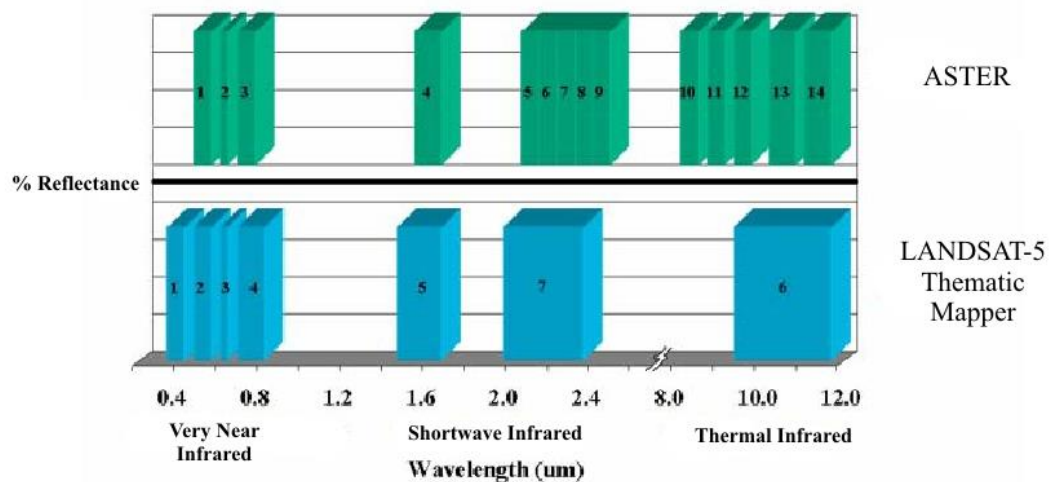


Figure 115 Graphical comparison between ASTER and Landsat-5 sensor imagery, adapted from Abrams et al., 2002.

These images were then combined to create a Red–Green–Blue image (Figure 116). However, the dominance of ferrous minerals (blue) makes interpretation very difficult. To avoid this, the images were combined, using pixel values only, into a single greyscale image to highlight areas of prospectivity. This greyscale image (Figure 117) was then used in the prospectivity mapping.

Subsystem	Band Number	Spectral Range ( $\mu\text{m}$ )	Spatial Resolution (m)
TM Very Near Infrared (VNIR)	1	0.45–0.53	30
	2	0.52–0.60	
	3	0.63–0.69	
	4	0.76–0.90	
TM Short-wave Infrared (SWIR)	5	1.55–1.75	30
	7	2.08–2.35	
TM Thermal Infrared (TIR)	6	10.40–12.50	120
MSS	1	0.50–0.60	80
	2	0.60–0.70	
	3	0.70–0.80	
	4	0.80–1.10	

Table 23 Characteristics of the TM and MSS sensors on the Landsat-5 platform

Before the images could be imported into the pilot GIS, they were converted from the ERDAS-IMAGINE \*.img format into shape files that could be used by the ARC-SDM modeller. The first stage in this process was to divide pixel intensity into ten ‘bins’ of equal value, to isolate the highest pixel values, representing the areas of highest concentration of alteration mineral assemblages. Once this was done, the image was converted into a shape file, for use within the pilot GIS. The shape file was edited to remove any interference from bodies of water, and to display only the highest pixel values, with subsequent buffering and generalisation carried out as for other datasets.

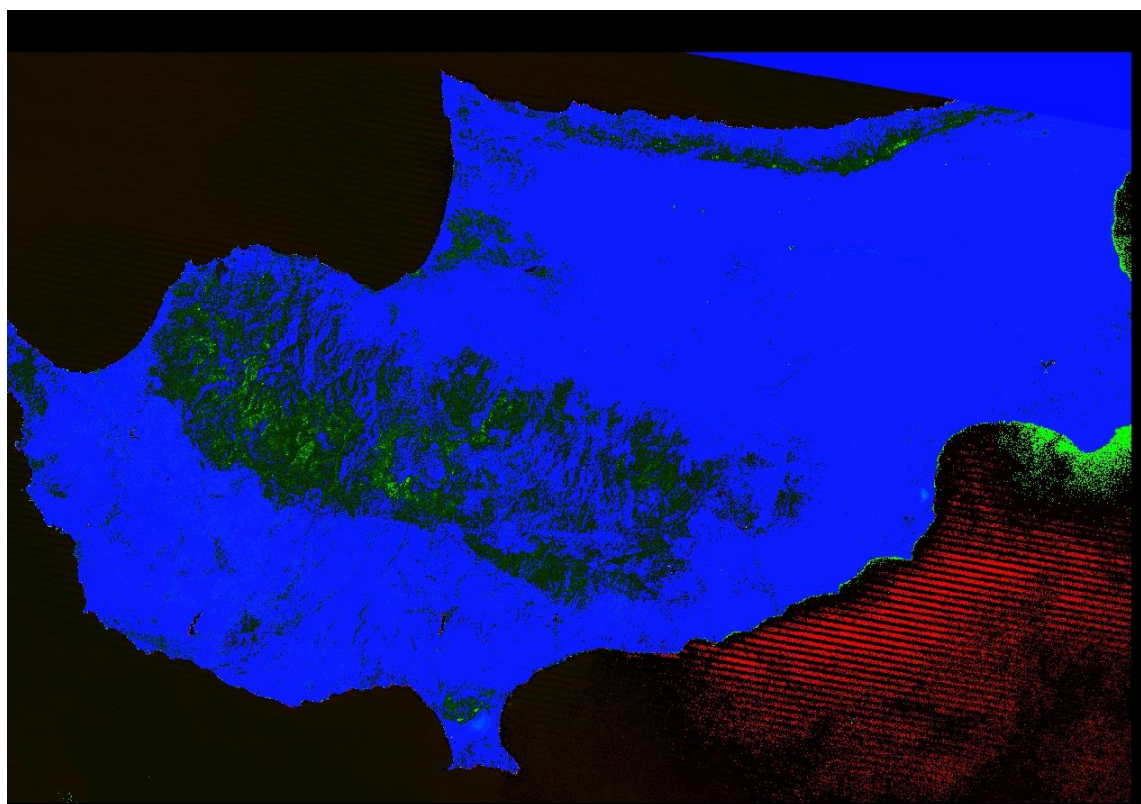


Figure 116 Stacked red-green-blue image formed from three LandSat TM band ratio images. Red = iron oxides, green = clay minerals, blue = ferrous minerals.

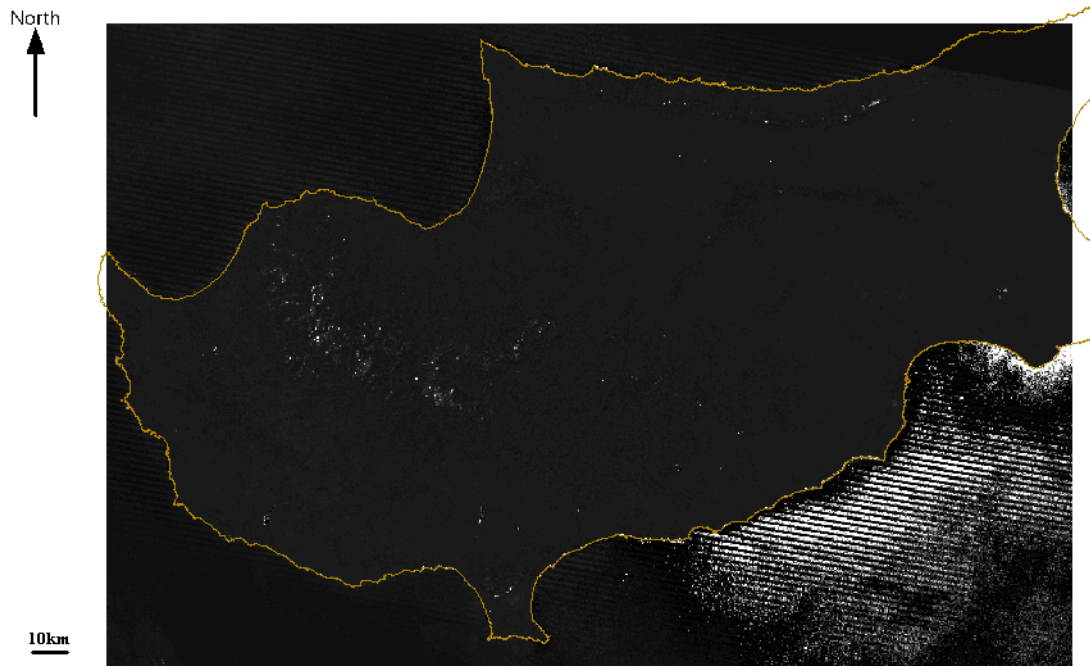


Figure 117 Greyscale combination image of three Landsat TM band ratio images, showing the distribution of areas of high concentrations of ferrous minerals, iron oxides and clay minerals associated with mineralization related alteration.

# 11 Prospectivity mapping

The process of forming maps of exploration potential for any deposit type falls into four key stages:

- Establishing a conceptual model—in this project, the deposit and exploration models.
- Building a spatial database—the compilation of available data and processing this data, producing map forms that can be used in a GIS system.
- Processing the data—formation of binary potential maps, used as layers in the GIS – showing areas of favourable or unfavourable characteristics for mineralization.
- Applying an integration model to generate a favourability map—the processing of the individual GIS layers or maps into one mineralization/exploration potential map.

These stages are fundamental in the creation of exploration potential maps for any deposit type—if the deposits being explored for are copper, gold, diamonds, or any other mineral or deposit type, the overall methodology behind the process is the same (Tangestani and Moore, 2001).

The method used to create exploration potential maps for copper on Cyprus is statistically based. Originally used for medical diagnosis, it has been altered and extended to deal with spatial prediction, identifying mineral deposits, or potential mineral deposits using the symptoms of geological, geophysical and geochemical signatures, both directly and indirectly (e.g. remotely sensed) measured. This method, known as weights of evidence modelling, uses the locations of known mineral occurrences to determine coefficients for each individual binary map. Each map has two coefficients or weights— $W^+$  and  $W^-$ . These coefficients are indicative of how closely parts of the dataset relates to mineralization. Generally, the higher the  $W^+$  coefficient, the more closely related to mineralization the dataset is. And the converse applies to  $W^-$ , i.e. the coefficient relates to unprospectivity; with a high  $W^-$  rating indicating a poorer relationship to mineralization. As the maps produced are binary in nature, these coefficients refer to areas where the binary pattern is present (e.g. areas where the geology is conducive to mineralization, or areas close to faults if the mineralization is fault controlled), or not present respectively (areas where the geology is not mineralization related, or areas where no faults are present) (Bonham-Carter et al., 1989). Areas where data is missing or unknown are given a weighting of zero, to guarantee that areas with missing data are not given negative weightings, and therefore ensuring that the support of samples within the dataset used to create the binary map is consistent as far as possible.

The first step in any modelling is to define a set of training data set. These are points of known mineral occurrence, such as old workings or prospects. For Cyprus, the decision was taken to use only current or old workings, rather than prospects, as the data behind the actual workings was considered to be more reliable than data for prospects, which may just mark gossan outcrops, or areas that were once considered prospective, but are no longer. These former and current operations provide a solid backbone to the project—they are often well documented, and many are still visible today, and therefore can be visited for any analysis and re-examination.

Each binary map derived using these training points therefore has areas with one of three attributes: (i) a positive weighting,  $W^+$ , showing areas where the desired features are found, a negative weighting,  $W^-$ , showing areas where the desired features are missing, and possibly areas with no weighting, where data is missing or unknown (Agterberg et al., 1993). The map of Cyprus shown in Figure 118, based on the 1:250,000 geological map of Cyprus published by the GSD, gives such an example of a binary map, with yellow denoting negatively weighted areas (unprospective geology), brown denoting positively weighted areas (prospective geology), and blue denoting missing data (post-mineralization sedimentary cover, possibly with blind mineral deposits underlying the sediments).

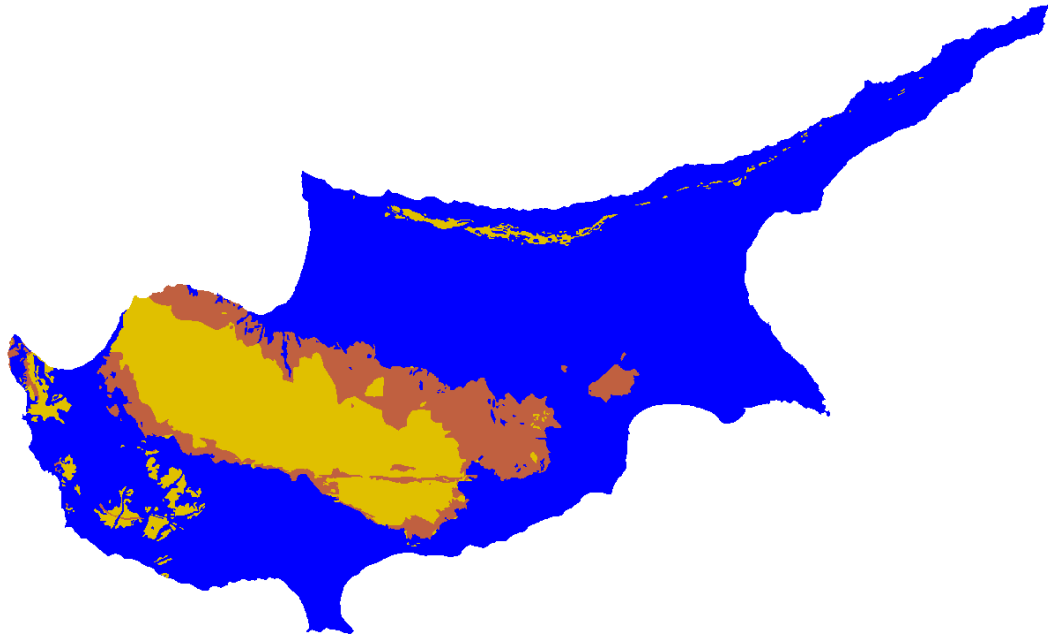


Figure 118 Binary map of the geology of Cyprus. Prospective geology is brown, unprospective geology is yellow, and missing data is Blue.

Binary maps can be created from a number of differing datasets. Data can be categorical, as in the case of the geological map in Figure 118, where single categories are defined as prospective or unprospective, or cumulative, as in the case of faults and geochemistry for example, where the prospectivity either increases or decreases away from the data point. For data such as faults, geochemistry, lineations, or other data where single points are used, buffers are used to increase the area that each individual point or line exerts a degree of control over. Figure 119 to Figure 121 show examples of this and illustrate how fault data are converted into a binary map.

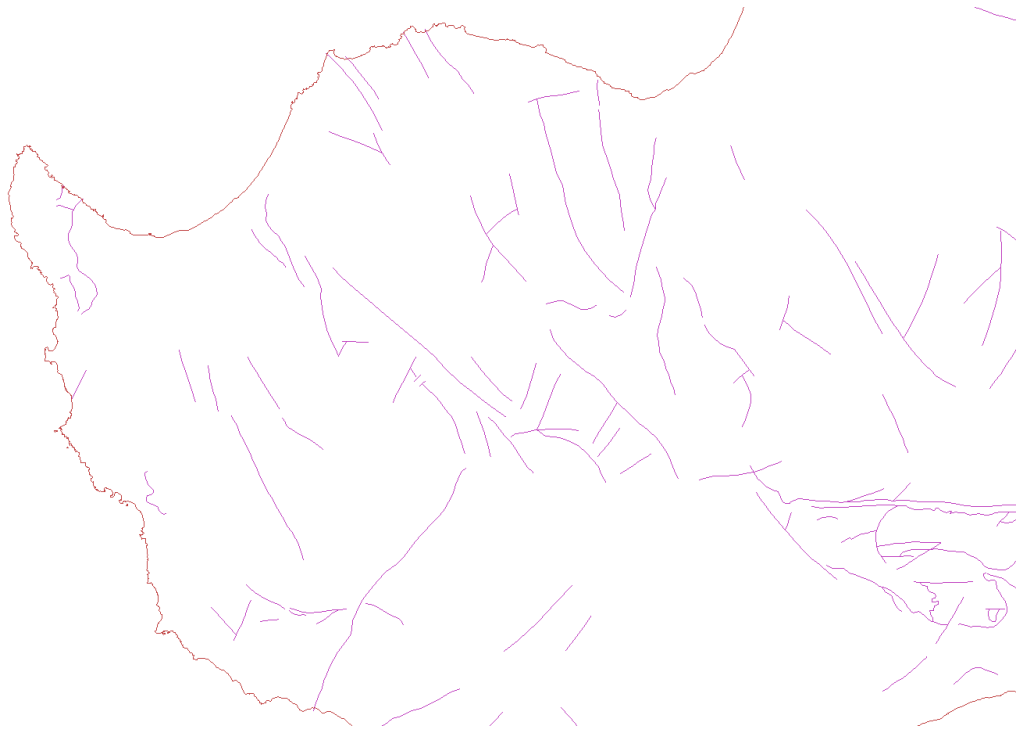


Figure 119 Map of part of Cyprus, showing faults digitised from 1:250 000 geological map of Cyprus, GSD.

The faults were buffered from 0–1500 m at 250 m intervals (Figure 120) and it was determined, using weights of evidence, that prospective areas were between 0–1500 m. At distances greater than 1500 m the difference (contrast) between prospective ( $W^+$ ) and unprospective ( $W^-$ ) is at a maximum and these cut-offs are aimed to maximise this difference, in order to obtain a clear difference between areas with positive weightings and negative weightings, or prospective and non-prospective areas (Bonham-Carter et al., 1990). Therefore, for the 1:250 000 fault dataset the binary map can be defined with the prospective areas being within 1500 m of a fault (Figure 121)



Figure 120 Buffered 1:250 000 faults, buffered at 250 m intervals from 0–1500 m.

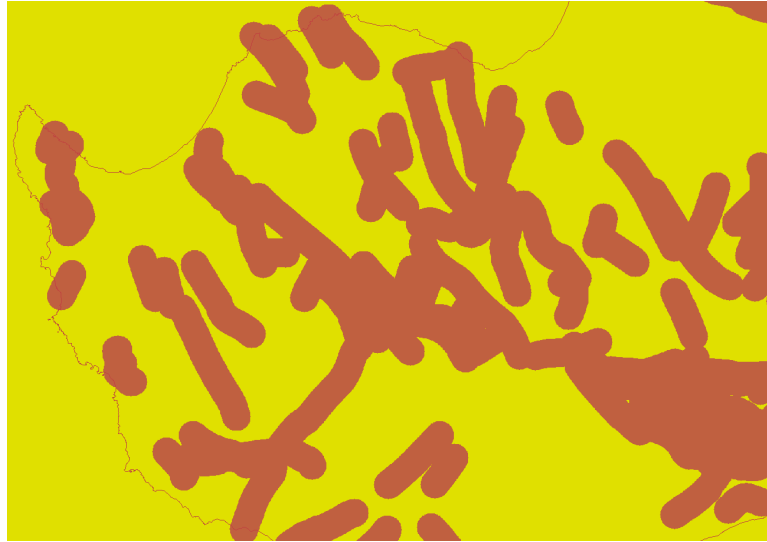


Figure 121 Binary map of 1:250,000 faults, showing prospective and non-prospective areas (brown—prospective; yellow—unprospective).

The modelling described above was undertaken using ARC-SDM. This is a software tool for ArcView and ArcGIS that derives mineralization potential maps from spatial data inputs. The statistical model is based on a log-linear form of Bayes' rule, with an inbuilt assumption that the evidential themes used are conditionally dependent with respect to the deposits. Put simply, Bayes' rule updates our belief about a hypothesis *A* in the light of new evidence *B*. More specifically, our posterior belief (belief after new evidence *B*,  $P(A|B)$ ) is calculated by multiplying our prior belief,  $P(A)$ , by the likelihood  $P(B|A)$  that *B* will occur if *A* is true (Agterberg et al., 1990).

There are five main steps in the calculation of weights of evidence for any given input, be it geochemical, geological, structural, geophysical.

1. Estimation of a Prior Probability—the probability of mineral occurrence in a unit area (usually 1 km<sup>2</sup>) given no further information.
2. The calculation of positive and negative weights for each individual binary predictor map using conditional probability ratios.
3. The application of a test for conditional independence of each pair of input maps possibly leading to the rejection or amalgamation of some input maps
4. The calculation of posterior probability and uncertainty for each unique overlap combination of the binary prediction maps.
5. The application of a goodness-of-fit test for testing the overall conditional independence assumption (Bonham-Carter et al., 1989).

Each step along this modelling path requires a number of sub-steps. Details of the required practical approach are given in Jowitt, 2003.

For completeness, below is a general description of the statistical concepts behind prospectivity mapping. For further information reader is also referred to papers by Agterberg et al., 1993; Asadi and Hale, 2001; Bonham-Carter et al., 1989; Bonham-Carter et al., 1990.

The study area (area of interest defined by a grid created by the user) is broken down into cells of a fixed area,  $ukm^2$ , with the total area being  $tkm^2$ . Therefore *T* (Total number of unit cells in the study area) is equal to  $t/u$ . If we also have *D* cells

containing an occurrence, then the probability that one unit cell, chosen at random, will contain an occurrence is as follows:

$$P(\text{Min Occ}) = D/T \quad (1)$$

*Equation 1* states that the probability of one cell chosen at random contains a mineral occurrence ( $P(\text{Min Occ})$ ) is given by the number of cells containing an occurrence ( $D$ ) divided by the total number of unit cells in the Study area ( $T$ ). *Equation 2* can express this in the form of odds.

$$O_{\text{prior}} = \frac{P(\text{MinOcc})}{1 - P(\text{MinOcc})} = \frac{\text{MinOcc}}{T - \text{MinOcc}} \quad (2)$$

*Equation 2* states that the Prior Probability odds of a random cell containing a mineral occurrence ( $O_{\text{prior}}$ ) is equal to the probability of a random cell containing a mineral occurrence ( $P(\text{MinOcc})$ ) divided by 1 minus the probability of a random cell containing a mineral occurrence. This is equal to the number of cells containing an occurrence ( $\text{MinOcc}$ ) divided by the total number of unit cells in the study area ( $T$ ) minus the number of cells containing an occurrence ( $\text{MinOcc}$ ). The prior probability is simply the probability of a random cell containing a mineral occurrence before we know anything about the cell. Posterior probability is defined as the probability of a random cell containing a mineral occurrence after we have learned something about the cell.

These equations therefore lead us to the conclusion that the posterior odds of a random cell containing a mineral occurrence can be calculated using Equations 3-6.

$$O_{\text{posterior}} = \exp \left\{ \ln(O_{\text{prior}} + \sum_{j=1}^n W_j^k) \right\} \quad (3)$$

$$\text{Where } W_j^k = W_j^+ \text{ if pattern } j \text{ is present} \quad (4)$$

$$\text{Or } W_j^k = W_j^- \text{ if pattern } j \text{ is not present} \quad (5)$$

$$\text{Or } W_j^k = 0 \text{ if pattern } j \text{ is unknown} \quad (6)$$

*Equation 3* states that the posterior odds ( $O_{\text{posterior}}$ ) are equal to the exponential of the natural log of the prior probability odds ( $O_{\text{prior}}$ ) added to the sum of the weights of evidence for this cell ( $\sum_{j=1}^n W_j^k$ ). These weights are defined by pattern  $j$ , the prospective areas defined by a binary map from a given dataset within the project, as shown by *Equations 4–6*. If the random cell is within a prospective area, therefore pattern  $j$  is present, and  $W_j^k = W_j^+$ , meaning that  $W_j^k$  is equal to the positive weighting attributed to prospective areas within the binary map, i.e.  $W^+$ . The opposite applies in *Equation 5*, where areas considered unprospective by the binary map are described as  $W_j^k = W_j^-$ , where the weightings for the cell concerned, and the overall posterior odds of a mineral deposit occurring are given by the negative or unprospective weightings given by  $W^-$ . If data is missing from the area, the area is not given a weighting, with  $W_j^k = 0$ , as shown in *Equation 6*. The Posterior probability ( $P_{\text{posterior}}$ ) of a mineral occurrence being found within a random cell is defined by *Equation 7*.

$$P_{\text{posterior}} = \frac{O_{\text{posterior}}}{(1 + O_{\text{posterior}})} \quad (7)$$

The estimates for the actual weights,  $W^+$  and  $W^-$  for the  $j^{\text{th}}$  pattern as defined from a binary map are determined from Equations 8 and 9.

$$W_j^+ = \ln \{P(j|d) / P(j|\bar{d})\} \text{ and} \quad (8)$$

$$W_j^- = \ln \{P(\bar{j}|d) / P(\bar{j}|\bar{d})\} \quad (9)$$

*Equation 8* defines the magnitude of the positive weighting  $W^+$  for pattern  $j$  as the natural log of the probability of  $j$  happening given that  $d$  – a deposit being located in the unit cell in question – has already occurred ( $j|d$ ) divided by the probability of  $j$  occurring given that  $d$  has not occurred  $j|\bar{d}$ . *Equation 9* defines the magnitude of the negative weighting  $W^-$  for pattern  $j$  as the natural log of the probability of  $j$  not occurring given that  $d$  has already happened divided by the probability of  $j$  not occurring given that  $d$  has not occurred.

True values for  $W^+$  and  $W^-$  could only be calculated if the unit area assumed for deposit points was infinitely small (Asadi and Hale, 2001). If we consider cell sizes of  $1 \text{ km}^2$ , this finally leads us to the conditional probability terms needed to calculate the above weightings used in binary map creation, calculated from

$$P(j|d) = A_{dj} / A_{dt}, \quad (10)$$

$$P(j|\bar{d}) = (A_j - A_{dj}) / (A_t - A_{dt}), \quad (11)$$

$$P(\bar{j}|d) = (A_{dt} - A_{dj}) / A_{dt}, \text{ and} \quad (12)$$

$$P(\bar{j}|\bar{d}) = (A_t - A_j - A_{dt} + A_{dj}) / (A_t - A_{dt}) \quad (13)$$

*Equation 10* defines the probability of  $j$  occurring given that  $d$  has already occurred. This is defined by the number of  $1 \text{ km}^2$  units containing a deposit in the total study area ( $A_{dt}$ ) divided by the number of  $1 \text{ km}^2$  units containing a deposit in pattern  $j$  ( $A_{dj}$ ). The probability that  $j$  occurs if  $d$  is not present is given by *Equation 11*, and is equal to the area of pattern  $j$  in  $\text{km}^2$  ( $A_t$ ) minus  $A_{dj}$ , divided by  $A_t$  minus  $A_{dt}$ . *Equation 12* gives the probability of  $j$  not occurring given that  $d$  has already occurred, whilst *Equation 13* gives the probability of  $j$  not occurring given that  $d$  has already not occurred and where  $A_j$  equals the total study area, in  $\text{km}^2$ .

In order to determine the optimum cut-offs for classifying patterns into the binary maps seen in Figure 118 and Figure 121 previously, the weights  $W^+$  and  $W^-$  can be calculated for a succession of cut-offs (e.g. as mentioned before differing buffer distances for fault traces), with the maximum contrast ( $W^+ - W^-$ ) giving the threshold value at which the predictive influence of the positive aspects of the dataset are maximised, representing the area of prospectivity defined in the binary mapping (Bonham-Carter et al., 1989; Bonham-Carter et al., 1990).

## 11.1 INFORMATION FOR SPATIAL DATA MODELLING

### 11.1.1 Geology

#### 11.1.1.1 1:31 680 MAP SERIES

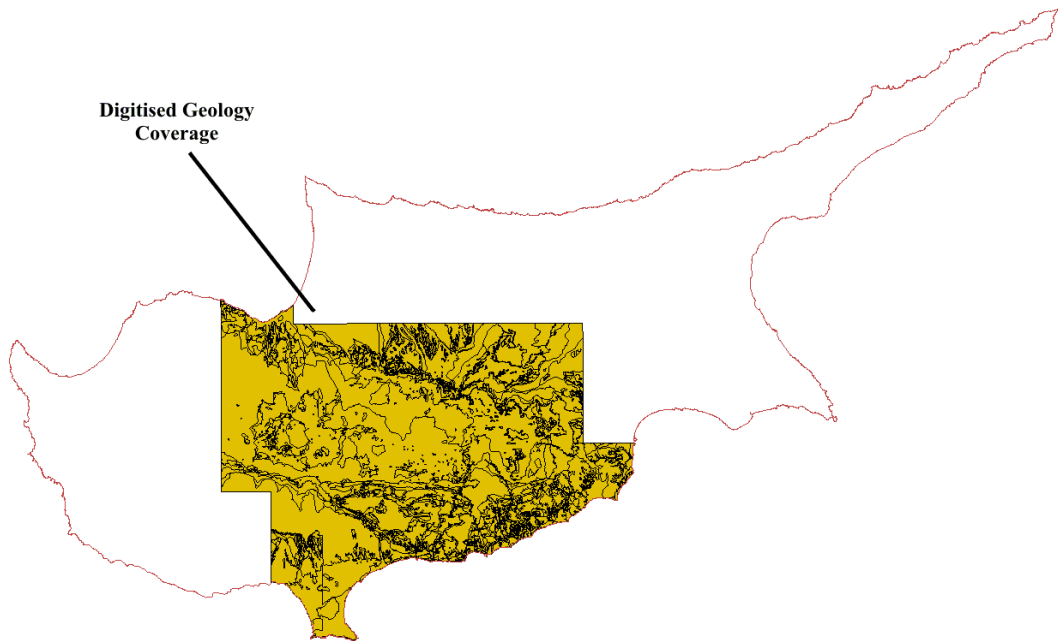


Figure 122 Digitised geology coverage at 1:31 680.

The 1:31 680 geological maps were scanned as greyscale TIFF images using an A0 scanner in the National Geoscience Data Centre, British Geological Survey. The Geological Survey Department of Cyprus digitised and georeferenced the geology as attributed polygons, also digitising towns and villages associated with the maps. The scanned greyscale images were georeferenced using co-ordinate points on the maps, and checked against topographic features from the 1:250 000 shape files—e.g. rivers and coastlines. These maps were based on the European Datum of 1950 (Zone 36) rather than the WGS84 projection that other files use. A simple change of projection using an ArcView 3.3 extension removed this. Mineral occurrences and faults on the maps were digitised as attributed point and line shape files. However, it should be noted that the digitised geology does not cover all of the memoir maps (Figure 122). Also, certain areas in the memoir geology—mapped as one unit—are recorded as two or more units in the later 1:250 000 geological maps (Figure 123). This reason for this difference is unclear. This meant that for completeness, and for better overall coverage, although at a lower resolution, the 1:250 000 geological map was used as the geological shape file, with the faults and mineral localities taken from the memoir geology. This is in keeping with the use of this GIS based system as a regional exploration tool.

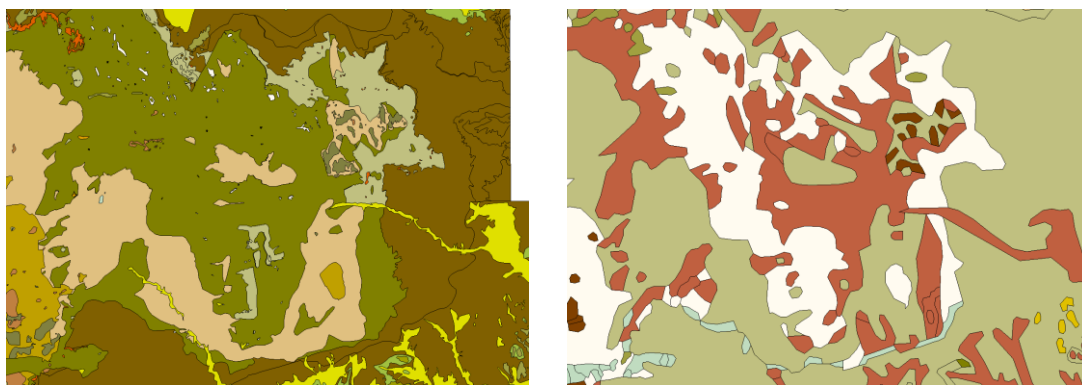


Figure 123 Comparison between 1:31 680 (left) and 1:250 000 (right) scale geological maps. Notice the central portion of the map changes from a single unit in the older 1:31 680 map to multiple units in the newer 1:250 000 map.

#### 11.1.1.2 1:250 000 MAP SERIES

The 1:250 000 maps series was published in revised form by the Geological Survey Department of Cyprus in 1995 and digitised by the Geological Survey Department, Cyprus. The geology (Figure 124) is as attributed polygons, with faults, rivers, coastline and contours being digitised as attributed lines.

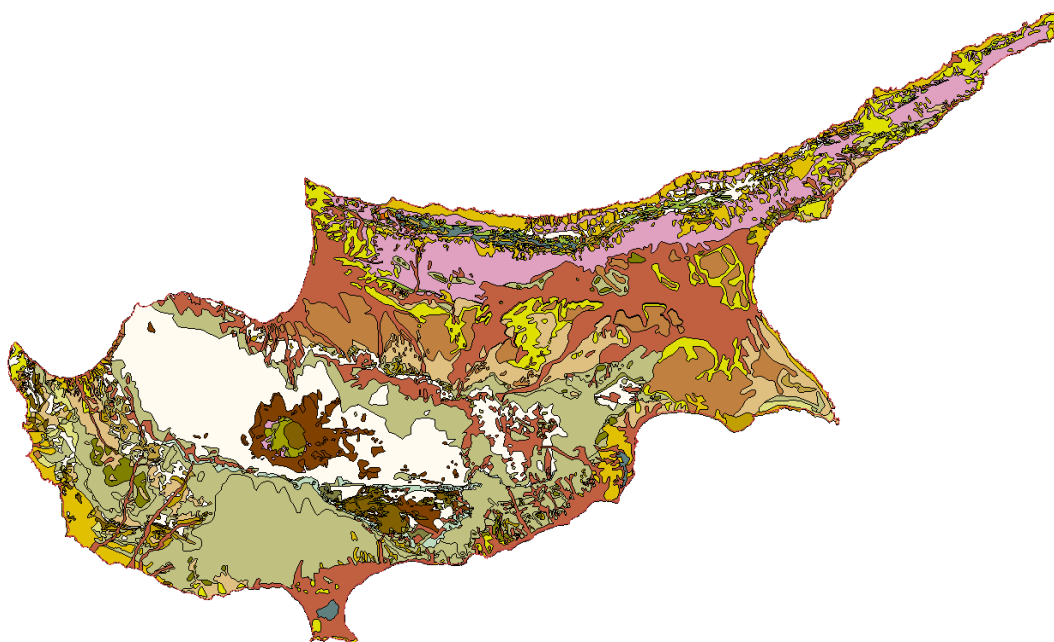


Figure 124. 1:250 000 geological map of Cyprus, digitised by the GSD

#### 11.1.1.3 METALLOGENIC MAP

This map, produced in 1982 by the Geological Survey Department of Cyprus, is based on an earlier version of the 1:250 000 map. The map was scanned and georeferenced by the Natural History Museum. It shows mineral occurrences throughout Cyprus: umber, ochre, bentonite, gypsum, crushed stone, building stone, lime, marble, brick clay, chalk and marl cement works, chromite, chrysotile asbestos, celestite, limestone, silica sand, Cu-Ni-Fe-Co sulphide, massive sulphide and stockwork sulphide mineralization. Current (for 1982) and former workings are shown, along with mineral prospects for certain commodities, as well as the

chemistry of the chromite deposits, the size of the deposits, and the copper and zinc grades, for the massive and stockwork sulphide deposits. Mineral occurrence data for massive sulphide and stockwork workings, former workings and copper mineralization prospects were digitised in point data form, using ArcView 3.3, although the prospect data was considered to be unreliable and was not used in the prospectivity mapping, as no indication or data was given about the size or grades of the mineralization at each locality.

#### 11.1.1.4 UNRFNRE MINERAL EXPLORATION IN WESTERN CYPRUS 1983 PROJECT

Much of the work carried out by the UN project was of limited use within the regional exploration concept of the GIS, as UNRFNRE work was done at a localised scale. Another additional problem is, as with another project carried out by the United Nations Development Programme, that maps and data have very few indications of where they were based—making georeferencing very difficult within the framework of the project GIS—this may need to be reconsidered for future development of the prospectivity mapping. However, some mineral working and occurrence data was taken from the project and used in the project GIS as training points for the mineralization potential mapping.

In addition, some satellite lineation analysis data from the project were digitised, but prospectivity analysis indicated that these lineations have little or no connection with mineralization. This may have been because these were interpreted large-scale features rather than the raw satellite data. The raw data for the UN satellite lineations along with UN geochemical survey data, were not available to the pilot GIS.

## 11.2 RESULTS—REGIONAL PROSPECTIVITY

### 11.2.1 Binary maps

#### 11.2.1.1 GEOLOGICAL DATA

Binary maps were produced for the 1:250 000 geology and buffered contacts between certain geological units. Figure 125 shows the map displaying prospective (brown—crustal sequence) and unprospective (yellow—mantle/plutonic sequence) geological units. In addition, it also shows areas with missing data (blue), where post mineralization sedimentary cover possibly overlies blind VHMS or stockwork deposits. Contacts between the Lower and Upper Pillow Lavas, the Lower Pillow Lavas–Basal Group and the Basal Group–Sheeted Dyke Complex were extracted and buffered (Table 24). These contacts were thought to have positive weightings, as each contact between units would represent either a hiatus in magmatism that would allow vigorous hydrothermal circulation to start, or a gap in the stratigraphy (time) allowing stratiform massive sulphides and the related stockwork mineralization to form. Binary maps generated from these three geological contacts are shown in Figure 126 to Figure 128.

<b>Dataset</b>	<b>Buffer Distances (number at X m)</b>	<b>Thresh old Value (m)</b>	<b>W<sup>+</sup></b>	<b>W<sup>-</sup></b>	<b>Contrast</b>
1:250 000 Geology	CD	CD			
1:31 680 Gossan occurrences	10 @ 250	1000	-1.1173	3.2137	-4.3310
Bouguer Gravity Anomaly Contours	CD	CD			
1:250 000 Geological contact between Lower and Upper Pillow Lavas	10 @ 250	750	-0.2347	2.2976	-2.5324
1:250 000 Geological contact between Basal Group and Lower Pillow Lavas	10 @ 250	1000	-0.4864	2.3534	-2.8398
1:250 000 Geological contact between Basal Group and Sheeted Dyke Complex	10 @ 250	1250	-0.1299	1.3212	-1.4511
1:250 000 fault data	20 @ 100	600	1.4153	-0.4433	1.8587
1:31 680 fault data	20 @ 100	100	1.7192	-0.3243	2.0435
ASTER Satellite Band Ratio Image, Ratio 1/3, > 10% of pixel values	20 @ 100	400	-0.0036	0.6391	-0.6427
ASTER Satellite Band Ratio Image, Ratio 1/5, > 10% of pixel values	20 @ 100	200	-0.0067	2.1163	-2.1230
ASTER Satellite Band Ratio Image, Ratio 2/3, > 10% of pixel values	20 @ 100	500	-0.0374	1.6113	-1.6487
ASTER Satellite Band Ratio Image, Ratio 2/5, > 10% of pixel values	20 @ 100	200	-0.0073	0.6473	-0.6546
ASTER Satellite Band Ratio Image, Ratio 4/5, > 10% of pixel values	20 @ 100	200	-0.0075	0.6768	-0.6843
ASTER Satellite Band Ratio Image, Ratio 6/1, > 10% of pixel values	20 @ 100	200	0.0014	-0.1671	0.1685
LandSat TM Band Ratio Image, Ratios 5/4, 5/7 and 3/1, > 10% of pixel values	20 @ 100	700	-0.0623	1.5350	-1.5974
ASTER Satellite derived lineations, E–W direction	10 @ 250	1000	0.9103	-0.3649	1.2752
ASTER Satellite derived lineations, NW–SE direction	10 @ 250	500	-0.1534	2.6378	-2.7912

CD: categorical data; gravity data—Gass and Masson-Smith, 1963

Table 24. Data used in prospectivity mapping, showing buffer distances and threshold distances as well W<sup>+</sup>, W<sup>-</sup> and contrast for each input theme.

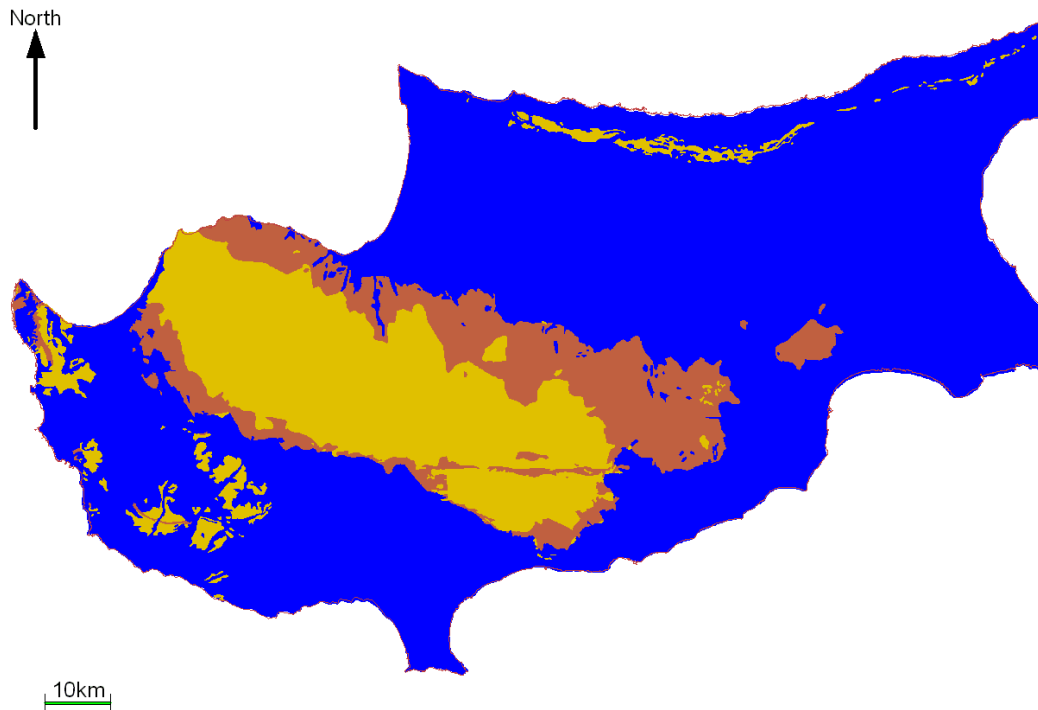


Figure 125. Binary prospectivity map of 1:250 000 geology of Cyprus. Red indicates prospective areas, green indicates unprospective areas, and blue indicates missing data

All three figures show that prospective areas are confined to the edge of the Troodos ophiolite complex. Contacts between the Upper and Lower Pillow Lavas, and the Lower Pillow Lavas–Basal Group appear to have a greater aerial extent than the Basal Group–Sheeted Dyke Complex contact, which is poorly prospective in the easternmost Troodos. Also, all three contacts also do not cover the entirety of the southern half of the Troodos ophiolite—each shows at least a 20 km gap between areas containing these prospective contacts. This gap is well illustrated by the Upper–Lower Pillow Lavas contact seen in Figure 126, with little or no evidence of a contact for around 60 km along the southern flank of the Troodos. This may be due to sedimentary cover on-lapping directly onto the Sheeted Dyke Complex, or due to lack of preservation of the Pillow Lava sequence.



Figure 126 Binary mineralization prospectivity map for the contact between the Upper and Lower Pillow Lavas, based on 1:250 000 geology. Red indicates prospective areas, green unprospective.



Figure 127 Binary mineralization prospectivity map for the contact between Lower Pillow Lavas and the underlying Basal Group, based on 1:250 000 geology. Red indicates prospective areas, green unprospective.



Figure 128 Binary mineralization prospectivity map for the contact between the Basal Group and the underlying Sheeted Dyke Complex, based on 1:250 000 geology. Red indicates prospective areas, green unprospective.

#### 11.2.1.2 FAULT DATA

Binary maps, based on fault data, were created from two separate datasets—1:250 000 and 1:31 680 geology—the 1:250 000 faults cover the entire island, whilst a smaller area is covered by the 1:31 680 memoir data. However, as most of the area of interest is covered by the memoir mapping, the higher resolution data were used—VHMS mineralization on Cyprus is commonly controlled by small faults and these are more likely to be recorded on the 1:31 680 maps than the regional 1:250 000 data. However, larger-scale faults may also be associated with mineralization, as they control the grabens and domains associated with the Troodos spreading ridge. The 1:250 000 faults (Figure 129) have good coverage, but information is restricted due to the limited number of faults displayed. The 1:31 680-fault data (Figure 130) are more useful. Areas of high fault density, and therefore high mineralization potential, are clearly picked out, and the range of sizes displayed by the faults indicates that many of the smaller faults controlling mineralization are mapped. It is worth noticing, in the 1:31 680 data, that the gaps in faulting to the

north and south (also visible in the 1:250 000 data) are not the result of missing data, or through lack of faulting. These are areas covered by sediments, and any faulting is probably located under the later sedimentary cover. Here, other techniques need to be used to try and detect these faults. The lack of faulting to the west in the 1:31 680 fault data is due to lack of coverage—these areas were not mapped in the 1:31 680 memoir series.

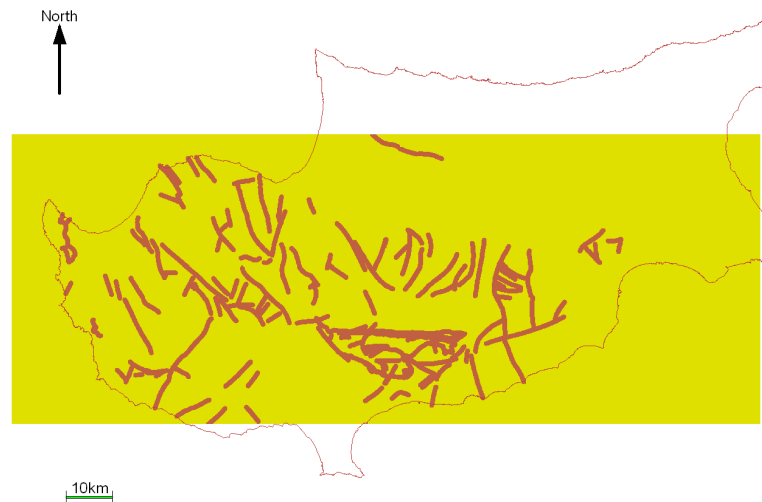


Figure 129 Binary mineralization prospectivity map based on 1:250 000 fault data. Areas shown as red are prospective and green unprospective.

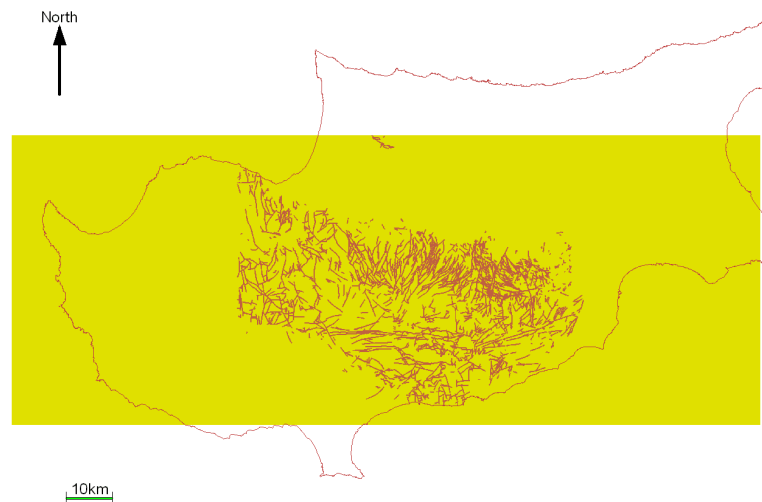


Figure 130 Binary mineralization prospectivity map based on 1:31 680 fault data. Red indicates prospective areas, green unprospective.

### 11.2.1.3 GOSSAN OCCURRENCES

Mineralization on Cyprus is often associated with gossans, presumed to have formed during exposure of the massive sulphides on the seafloor. Gossan occurrence data was obtained from 1:31 680 memoir geological maps, buffered and generalised (Table 24), creating the binary mineralization potential map seen in Figure 131. The distribution of gossans around the Troodos ophiolite is mainly based around the edges of the Troodos, with localised clusters of gossans possibly indicating high levels of mineralization. Again, the dataset is incomplete, with the lack of gossans in the west of the island due to no 1:31 680-memoir mapping in this area. The southern Troodos transform fault zone (STTFZ) also appears to act as a focus for

gossan occurrences, with significant clusters located around the edges of this structure. This is possibly due to the high density faulting in this area, and is also possibly a function of the additional presence of Limassol Forest-type mineralization.

<b>Dataset</b>	<b>Buffer Distances (number at X m)</b>	<b>Threshold Value (m)</b>	<b>W<sup>+</sup></b>	<b>W<sup>-</sup></b>	<b>Contrast</b>
1:250 000 Geology	CD	CD			
1:31 680 Gossan occurrences	10 @ 250	1000	-1.1173	3.2137	-4.3310
Bouguer Gravity Anomaly Contours	CD	CD			
1:250 000 Geological contact between Lower and Upper Pillow Lavas	10 @ 250	750	-0.2347	2.2976	-2.5324
1:250 000 Geological contact between Basal Group and Lower Pillow Lavas	10 @ 250	1000	-0.4864	2.3534	-2.8398
1:250 000 Geological contact between Basal Group and Sheeted Dyke Complex	10 @ 250	1250	-0.1299	1.3212	-1.4511
1:250 000 fault data	20 @ 100	600	1.4153	-0.4433	1.8587
1:31 680 fault data	20 @ 100	100	1.7192	-0.3243	2.0435
ASTER Satellite Band Ratio Image, Ratio 1/3, > 10% of pixel values	20 @ 100	400	-0.0036	0.6391	-0.6427
ASTER Satellite Band Ratio Image, Ratio 1/5, > 10% of pixel values	20 @ 100	200	-0.0067	2.1163	-2.1230
ASTER Satellite Band Ratio Image, Ratio 2/3, > 10% of pixel values	20 @ 100	500	-0.0374	1.6113	-1.6487
ASTER Satellite Band Ratio Image, Ratio 2/5, > 10% of pixel values	20 @ 100	200	-0.0073	0.6473	-0.6546
ASTER Satellite Band Ratio Image, Ratio 4/5, > 10% of pixel values	20 @ 100	200	-0.0075	0.6768	-0.6843
ASTER Satellite Band Ratio Image, Ratio 6/1, > 10% of pixel values	20 @ 100	200	0.0014	-0.1671	0.1685
LandSat TM Band Ratio Image, Ratios 5/4, 5/7 and 3/1, > 10% of pixel values	20 @ 100	700	-0.0623	1.5350	-1.5974
ASTER Satellite derived lineations, E–W direction	10 @ 250	1000	0.9103	-0.3649	1.2752
ASTER Satellite derived lineations, NW–SE direction	10 @ 250	500	-0.1534	2.6378	-2.7912

CD: categorical data; gravity data—Gass and Masson-Smith, 1963

Table 25. Data used in prospectivity mapping, showing buffer distances and threshold distances as well W<sup>+</sup>, W<sup>-</sup> and contrast for each input theme.

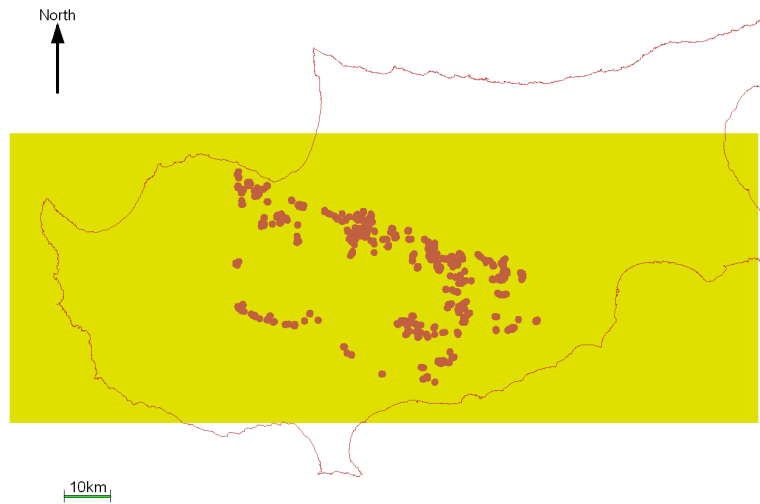


Figure 131 Binary mineralization potential map based on gossan occurrence data taken from 1:31 680 memoir based geological maps. Red indicates prospective areas, green unprospective.

#### 11.2.1.4 GRAVITY DATA

The resolution of the gravity data used in the pilot GIS is too coarse and covers too small an area to enable the definition of gravity lineaments or other crustal structures. However, a relationship was established between Bouguer gravity anomaly contours and mineralization. Figure 132 displays a band of gravity related prospectivity running across the Troodos. However, some unexpected areas are highlighted by the data. The large north-south running band to the extreme west may relate to the Mamonia complex and the Polis graben present in this area. It is also worth noticing the circle of unprospective representing the gravity low centred on the Mount Olympus serpentinite diapir, and the surrounding moderately prospective Sheeted Dyke Complex. The northern flank of the Troodos is also considered to be unprospective by this data, an unexpected result as the northern regions of the Troodos generally have been the areas where mining and mineral exploration has been concentrated.

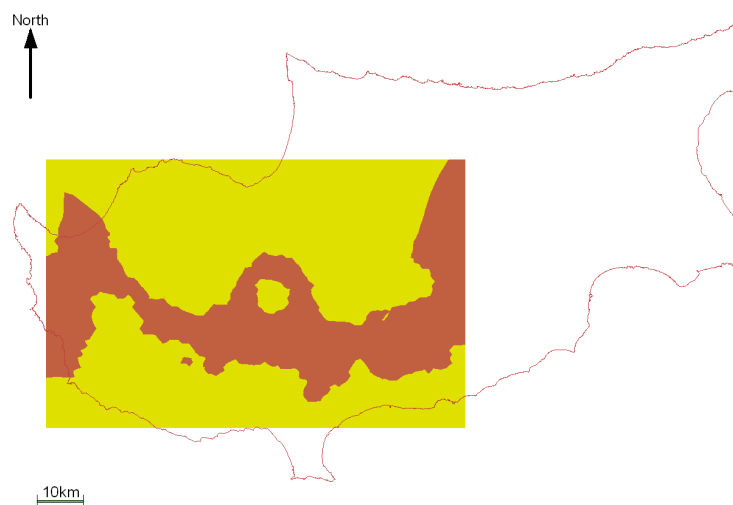


Figure 132 Binary mineralization potential map based on Bouguer gravity anomaly contour values. Red indicates prospective areas, green unprospective.

#### 11.2.1.5 ASTER BAND RATIO IMAGES

Binary band ratio images were created using ratios of ASTER SWIR Bands 1/3, 1/5, 2/3, 2/5, 4/5 and 6/1. These ratio images were thought to be the most indicative of prospectivity through PIMA ground-truthing and by comparison of the images to gossan and mineral occurrence data. Only the top 10% of pixel values of the greyscale images were used in creating the binary maps.

Figure 133 to Figure 138 show the binary prospectivity maps produced using this data. Five of these binary maps have linked distribution patterns, with Figure 138 appearing to highlight a more diffuse region seemingly unrelated to the other binary maps. The five closely related images all highlight one large region of the Troodos ophiolite, roughly in the centre of the binary map. However, these maps also seem to have slight differences, with Figure 133 and Figure 135 highlighting diffuse areas of alteration, whilst Figure 134, Figure 136 and Figure 137 stress more linear features running NW–SE. This suggests that these figures are emphasising assemblages closely related to each other, with one large region of alteration being highlighted in all five of the images. The more diffuse highlighting effect seen in Figure 138 also indicates the clustered area seen on all other band ratio images. However, the image also appears to highlight an area where the Sheeted Dyke Complex crops out. This suggests that the 6/1-band ratio may also be emphasising assemblages related to either weathering of the Sheeted Dykes, or the low-grade regional metamorphism that these units underwent after emplacement. The linear features picked out in Figure 134, Figure 136 and Figure 137 may be highlighting areas associated with epidosite zones as well as mineralization related alteration, as the features trend roughly parallel to dyke strike in the area, and are targeted towards known mineral deposits within the over lying Basal Group and Pillow Lava sequences. However if this is the case, then the rest of the epidosite zones within the Sheeted Dyke Complex should also be highlighted—why this is not seen is unclear.



Figure 133 Binary mineralization potential map created from an ASTER band ratio image, SWIR bands 1/3. Red indicates prospective areas, green unprospective.

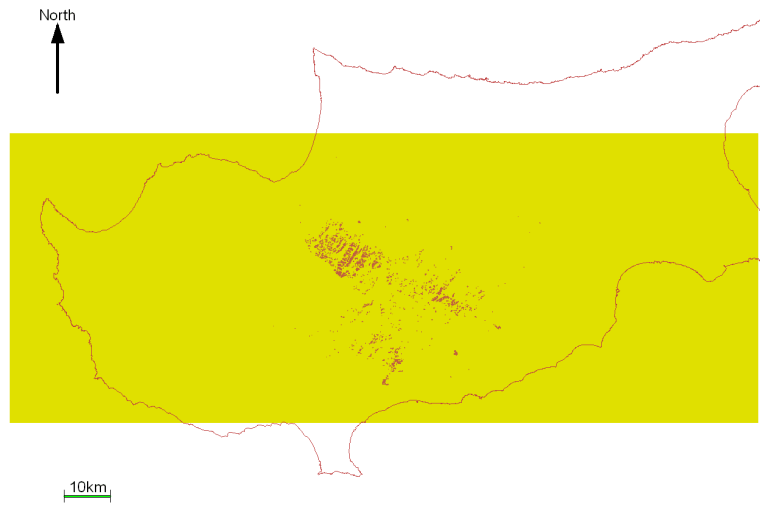


Figure 134 Binary mineralization potential map created from an ASTER band ratio image, SWIR bands 1/5. Red indicates prospective areas, green unprospective.



Figure 135 Binary mineralization potential map created from an ASTER band ratio image, SWIR bands 2/3. Red indicates prospective areas, green unprospective.



Figure 136 Binary mineralization potential map created from an ASTER band ratio image, SWIR bands 2/5. Red indicates prospective areas, green unprospective

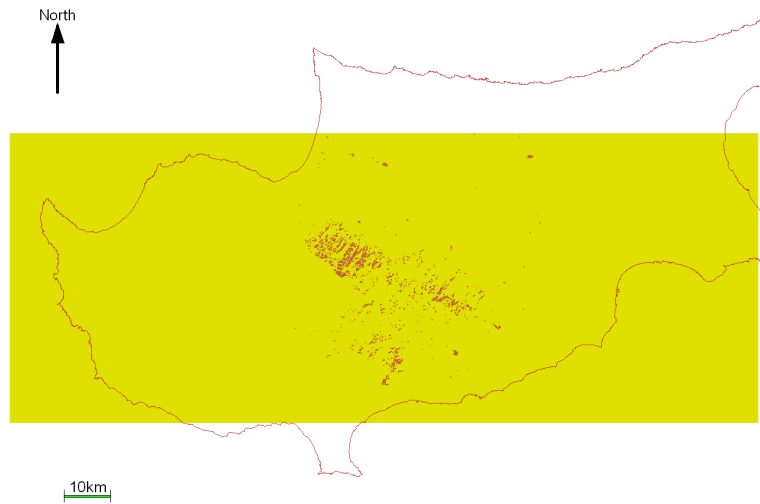


Figure 137 Binary mineralization potential map created from an ASTER band ratio image, SWIR bands 4/5. Red indicates prospective areas, green unprospective.



Figure 138 Binary mineralization potential map created from an ASTER band ratio image, SWIR bands 6/1. Red indicates prospective areas, green unprospective.

#### 11.2.1.6 LANDSAT TM BAND RATIO IMAGES

Three LandSat Thematic Mapper greyscale band ratio images (bands 5/4, 5/7 and 3/1, representing ferrous minerals, clay minerals and iron oxides respectively) were combined into one greyscale image, with the highest 10 % of pixel values being used to create the mineralization potential binary map. The LandSat TM binary map shown in Figure 139 highlights a wider and more diffuse range of occurrences when compared to ASTER binary maps. This, combined with the lower overall weighting calculated for the data (Table 24) suggests that the LandSat imaging is less selective in highlighting alteration mineral assemblages than the ASTER data. The binary map picks out areas of high mineralization prospectivity, but also highlights areas unrelated to mineralization. This is probably due to the wide bandwidths and, hence, less discriminatory band ratio images produced by the LandSat imagery.



Figure 139 Binary mineralization potential map created from 3 LandSat TM greyscale band ratio images. Red indicates prospective areas, green unprospective.

#### 11.2.1.7 ASTER SATELLITE DERIVED LINEATIONS

E–W and NW–SE running lineations derived from ASTER Digital Elevation Models were found to be prospective. These lineations form the binary mineralization potential maps seen in Figure 140 and Figure 141. These images are markedly different in several aspects. Figure 140 has fewer lineations than Figure 141, but these are clustered to the east of the image with a patchy distribution over the rest of the map. Figure 141 has a more evenly distributed set of lineations, however, gaps in the lineation data can be clearly seen on both Figures, possibly indicating areas covered by sediments, or areas that have no surface expression of faulting. In both datasets no lineations are present in the extreme west of the area, an area associated with a graben formation. Also, both maps do not highlight the STTFZ, an unexpected result considering the highly tectonised and faulted nature of the STTFZ.

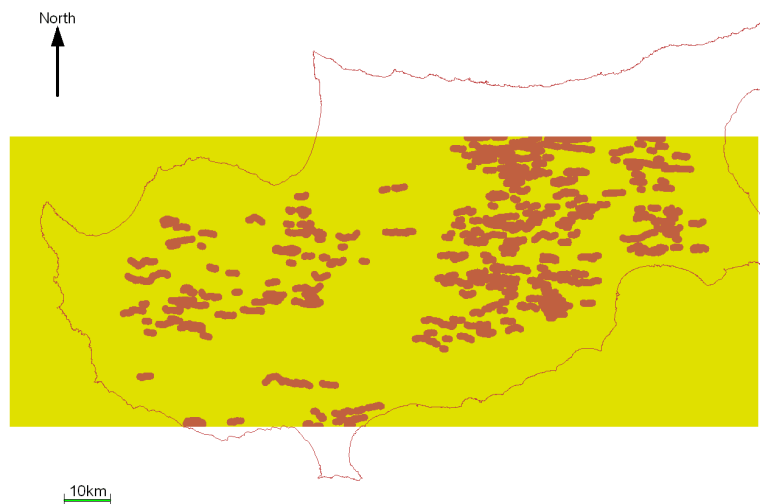


Figure 140 Binary mineralization potential map, created from East-West aligned satellite lineations; obtained from ASTER satellite DEM. Red areas are prospective, green unprospective.

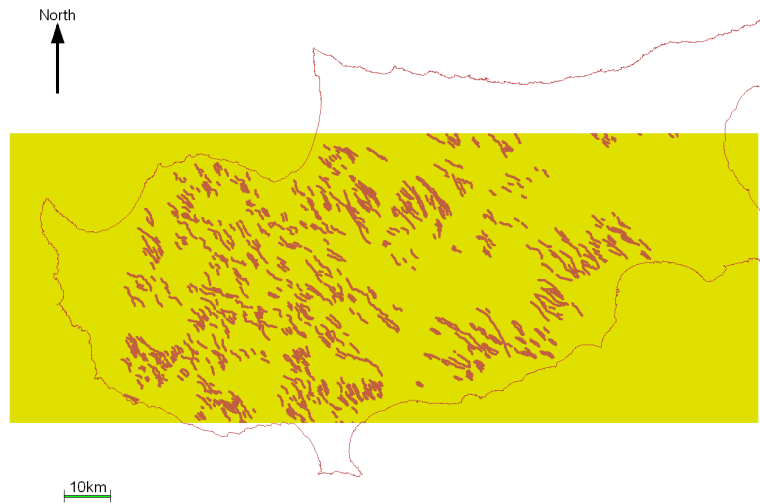


Figure 141 Binary mineralization potential map, created from Northeast-Southwest aligned satellite lineations, obtained from ASTER satellite DEM. Red indicates prospective areas, green unprospective.

### 11.2.2 Prospectivity maps

A weights of evidence analysis, using the mineral occurrence data (Figure 142) as training points, and the datasets described above was calculated using the Arc-SDM extension for ArcView GIS 3.3. Threshold values for each individual dataset were defined using the data shown in Table 24 to determine prospective and unprospective areas for each data set.

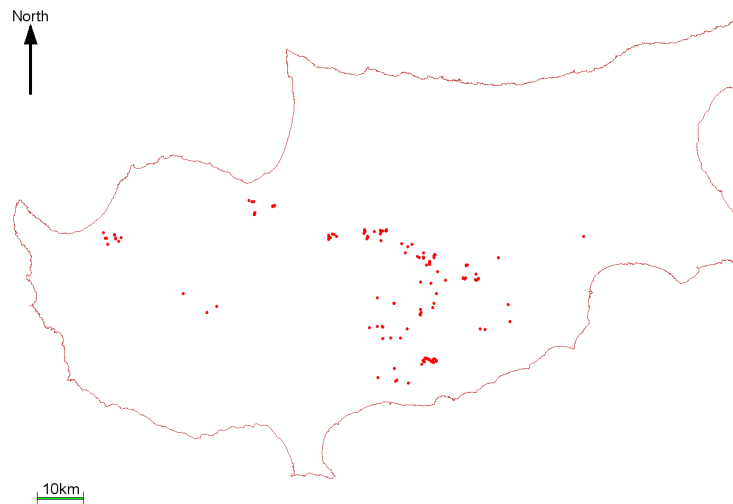


Figure 142 Copper-bearing massive sulphide and stockwork mineralization related mineral occurrences on Cyprus.

The regional mineralization potential map for copper on Cyprus is shown Figure 143. Areas of high potential are displayed as dark red with the background values in blue. The conditional dependence for this response theme is 0.38, indicating a high level of interdependence for datasets used in the GIS.

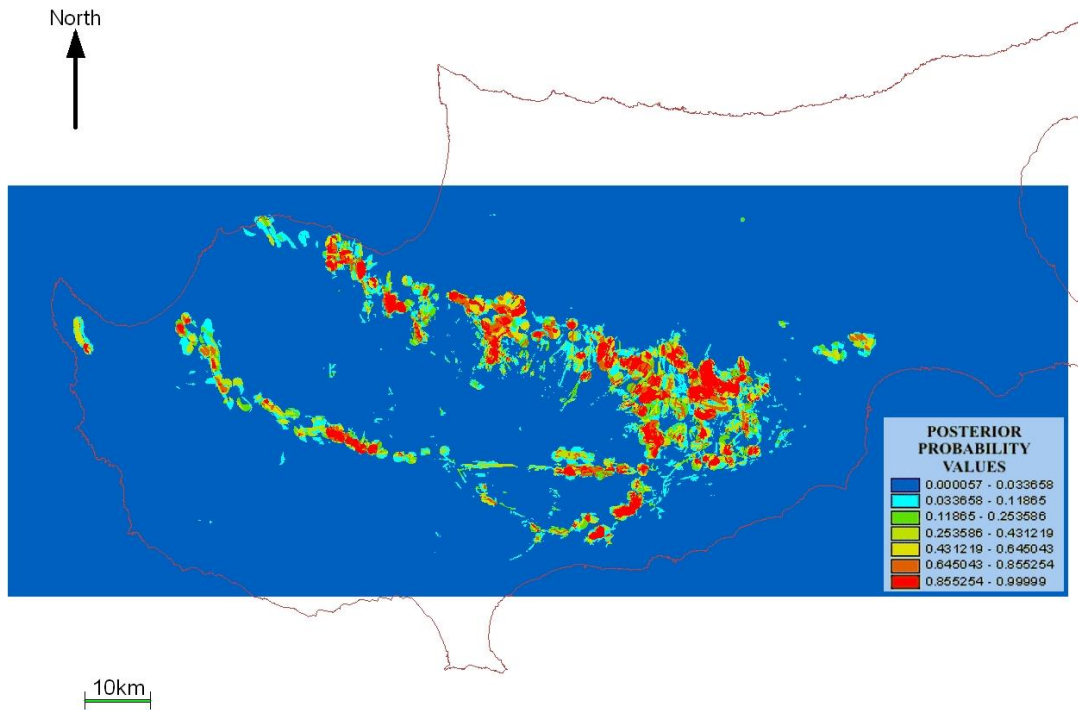


Figure 143 Mineralization potential map for copper mineralization on Cyprus.

The map shown in Figure 143 was adjusted to show areas of posterior probability higher than 0.93 and 0.98. This map, displayed in Figure 144, enabled the identification of eight areas (A–H) of very high mineralization potential described below and summarized in Table 26.

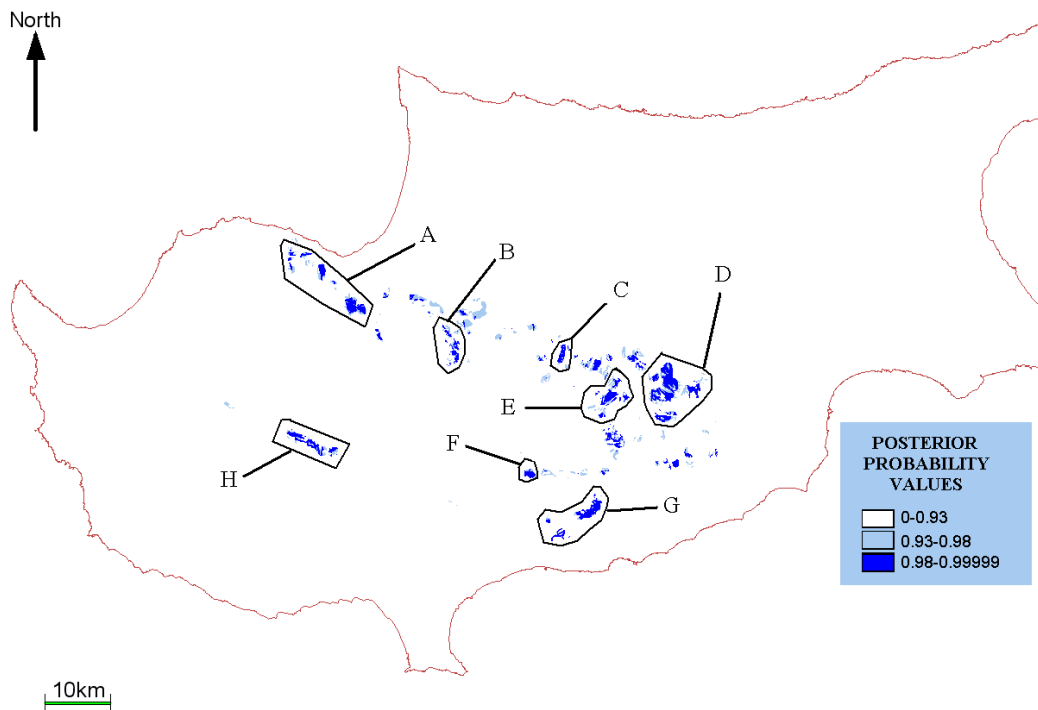


Figure 144 Areas of high mineralization potential (>93% and >98%) for copper-bearing massive sulphide and stockwork mineralization.

		Area A	Area B	Area C	Area D	Area E	Area F	Area G	Area H	
<b>Nearest Settlements</b>		Ampelikou, Apliki, Agios Epiphanos Soleas	Agios Georgios Kafkallou	Klirou, Malounta	Agia Varvara, Lefkosias, Sia, Mathiatis	Lythrodontas	Arakapas, Dierouna Eptagoneia	Asgata	Mandria Lemesou	
<b>Northing Easting Mineral Occurrences</b>		3884082 482665	3875145 500754	3873868 517565	3870037 534377	3867696 525013	3854928 512458	3849608 520757	3859823 479260	
<b>Geology</b>	Alluvium - Colluvium				■					
	Fanglomerate		■			■				
	Pakhna Formation								■	
	Lefkara Formation			■					■	
	Perapedhi Formation				■					
	Lava and Volcaniclastic Sediments						■	■		
	Lavas and Volcaniclastic Sediments			■			■	■	■	
	Upper Pillow Lavas	■	■		■	■				
	Lower Pillow Lavas	■	■	■	■	■	■	■	■	
	Basal Group	■	■	■	■	■	■	■	■	
	Sheeted Dyke Complex	■		■			■	■	■	
	Gabbro						■	■		
	Intrusive			■					■	
	Plutonic rocks									
	<b>1:250 000 Fault Data</b>		■	■	■	■	■	■	■	■
	<b>1:31 680 Fault Data</b>		■	■	■		■	■	■	■
	<b>Bouguer Anomaly</b>					M	■	■	■	■
	<b>Gossan Occurrence Data</b>		■	■	■	■	■	■	■	■
	<b>Lower and Upper Pillow Lava Contact</b>		■	■	■	■				
<b>Lower Pillow Lava Basal Group Contact</b>		■		■	■	■	■	■	■	
<b>Basal Group Sheeted Dyke Complex Contact</b>		■		■		■	■	■	■	
<b>Satellite E-W Lineations</b>		■			■	■	■			
<b>NW-SE Lineations</b>		■						■	■	
<b>LandSat TM Band Ratio Image</b>		■	■				■	■		
<b>ASTER Band Ratio Images</b>	1/3		■			■		■		
	1/5		■			■				
	2/3		■		■		■	■		
	2/5		■	■	■	■	■	■		
	4/5		■	■	■	■	■	■		
	6/1	■	■	■	■	■	■	■	■	

Table 26. Summary of areas with high copper mineralization potential (>98%) ■ = Area has this attribute, or is considered to be prospective according to this dataset, M = Missing data

#### 11.2.2.1 AREA A: AMPELIKOU, APLIKI, AGIOS EPIPHANOS SOLEAS

This area, the most northerly of the prospective areas (Figure 144), covers a narrow, arcuate zone around 20 km long and between 0 and 5 km wide (Figure 145). Rocks from the Upper and Lower Pillow Lavas, the Basal Group and the Sheeted Dyke Complex underlie the area, with faults from both the 1:250 000 and 1:31 680 data passing through the district. The area contains seven mineral occurrences: one old gold working, two massive sulphide deposits derived from the metallogenic map, two copper bearing pyrite mines from the 1:31 680 memoir series, and two sulphide mines from the 1983 UNRFNRE project. Gossan occurrences are seen in the area, along with all three geological contacts used in prospectivity mapping. The area also

contains E–W and NW–SE running satellite lineations and is highlighted by LandSat TM and ASTER 6/1 Band ratio images. The area is around 5 km west of the current Skouriotissa–Phoenix–Three Hills mine area, and contains the former Mavrovouni and Apliki mines. The extension of the high prospectivity zone to the north appears to be unexplored, with no known mineral occurrences.

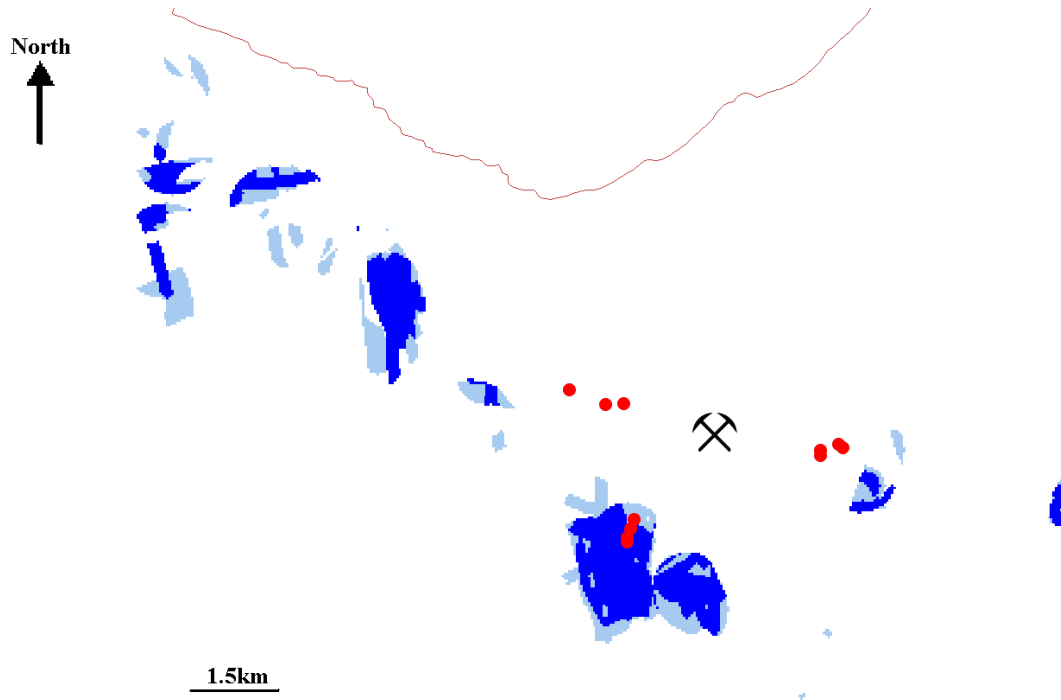


Figure 145 Area A, high prospectivity zone around Ampelikou, Apliki and Agios Epiphanos Soleas, • = mineral occurrence, ⚒ = mining district.

#### 11.2.2.2 AREA B: AGIOS GEORGIOS KAFKALLOU

This area, to the east of A and the Skouriotissa Mine (Figure 144), forms an irregularly shaped zone approximately 10 km from north to south and 12 to 2 km east to west and contains a large southern area of high mineralization potential, with several smaller high potential areas to the northwest and northeast (Figure 146). It hosts seven mineral occurrences: one old gold working, two mineralized stockworks, two sulphide mines, and two pyrite mines. Two major former mines are seen in the area—the Alestos and Memi mines, with the Kokkinoyia, Kokkinopezoula and Agrokipia mines located around 10 km further to the east. As with all other areas, it contains faults from both the 1:250 000 and 1:31 680 mapping. The geology of Area B comprises Upper and Lower Pillow Lavas, Basal Group and Fanglomerate units. However, only the Upper–Lower Pillow Lava contact is seen in the area. It contains gossans mapped from 1:31 680 memoir mapping, and is highlighted by all ASTER Band ratio images, but not the LandSat TM image. No satellite-derived lineations are seen in the area. The southern extension of the high prospectivity area with no known mineral occurrences appears to be the most prospective area within the zone covered by Area B, with no record of mining or working in this high prospectivity area close to former workings.

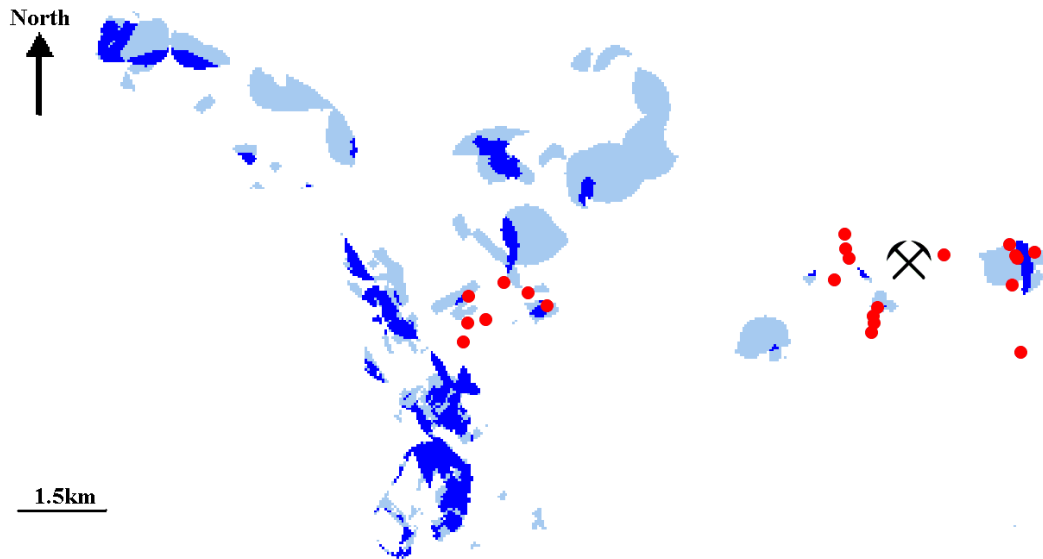


Figure 146. Area B high prospectivity zone around Agios Georgios Kafkallou, • = mineral occurrence, X = mining district.

#### 11.2.2.3 AREA C: KLIROU, MALOUNTA

Area C (Figure 144), located near the villages of Klirou and Malounta, is seen as a north–south trending rectangular shaped zone of high mineralization probability—around 600 m wide and 3 km long—with smaller areas of high potential spread erratically around the larger area (Figure 147). The area is located to the south of six mineral occurrence localities, comprising two pyrite mines, one old gold working, two stockwork mineralization localities and one UN sulphide mine. Lefkara chalks, lavas and volcanoclastic sediments, Lower Pillow Lavas, Basal Group lavas and dykes, Sheeted Dyke Complex rocks and intrusive plutonic rocks underlie the area. The area has 1:250 000 and 1:31 680 faults running through the prospective zones, and contains prospective areas for gossan and all geological contact datasets. It is also highlighted by ASTER band ratios 2/5 and 4/5. The area is sandwiched between two major mining districts to the east and west of the prospective area, with the nearest mines being the former workings at Memi (7 km to the east) and Alestos (6.5 km to the west), the locations around which the known mineral occurrences are located. The arcuate zone of high prospectivity appears to be relatively unexplored, with no known mineral occurrences, and no mining operations, either active or disused, present.

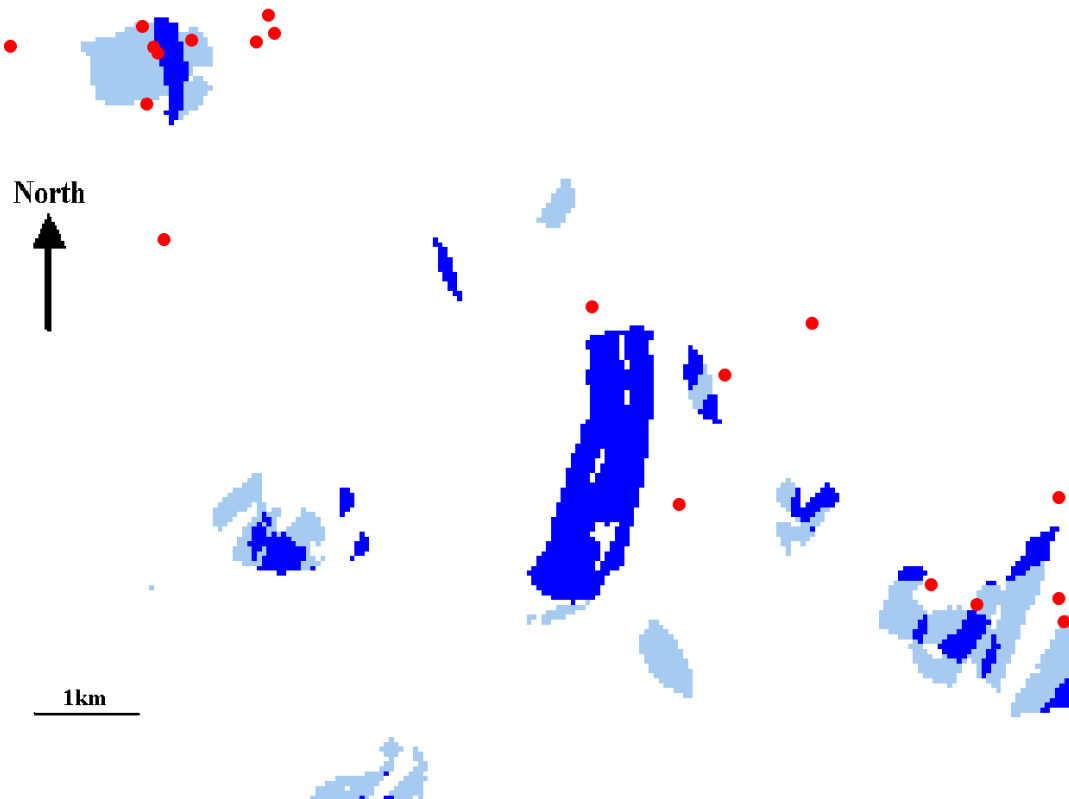


Figure 147 Area C high prospectivity zone around Klirou and Malounta, ● = mineral occurrence, ⚒ = mining district.

#### 11.2.2.4 AREA D: AGIA VARVARA LEFKOSIAS, SIA, MATHIATIS

This large zone of high prospectivity (Figure 144), an almost triangular area around 10km from north to south and thinning to the east, is located near to the villages of Agia Varvara Lefkosias, Sia and Mathiatis. The largest single area of high prospectivity, a reversed ‘L’ shape, 6 km from north–south and a maximum of 5 km east–west, is situated directly east of the Mathiatis–Sia mining district (Figure 148). Thirteen known mineral occurrences are seen within and adjacent to the zones of high prospectivity, comprising two ancient (Roman/Phoenician) slag dumps, four old gold workings, one pyrite mine, two massive sulphide deposits, three UN sulphide mines and one UN reported deposit. The area is underlain by geology from the Alluvium-Colluvium, Perapedhi, Upper and Lower Pillow Lava and Basal Group, and contains lithological contacts between the Lower–Upper Pillow Lavas and between the Lower Pillow Lavas–Basal Group. In addition, the zones of high prospectivity are outside the area of the Bouguer anomaly survey, and so Area D is considered to have a missing prospectivity attribute. Faults from both scales of mapping are present, along with gossan localities and east–west running satellite lineations. The area is further highlighted by 2/3, 2/5, 4/5 and 6/1 ASTER band ratio images. The area contains at least three former mines, the North and South Mathiatis mine and the Sia mine—all mined as open pits.

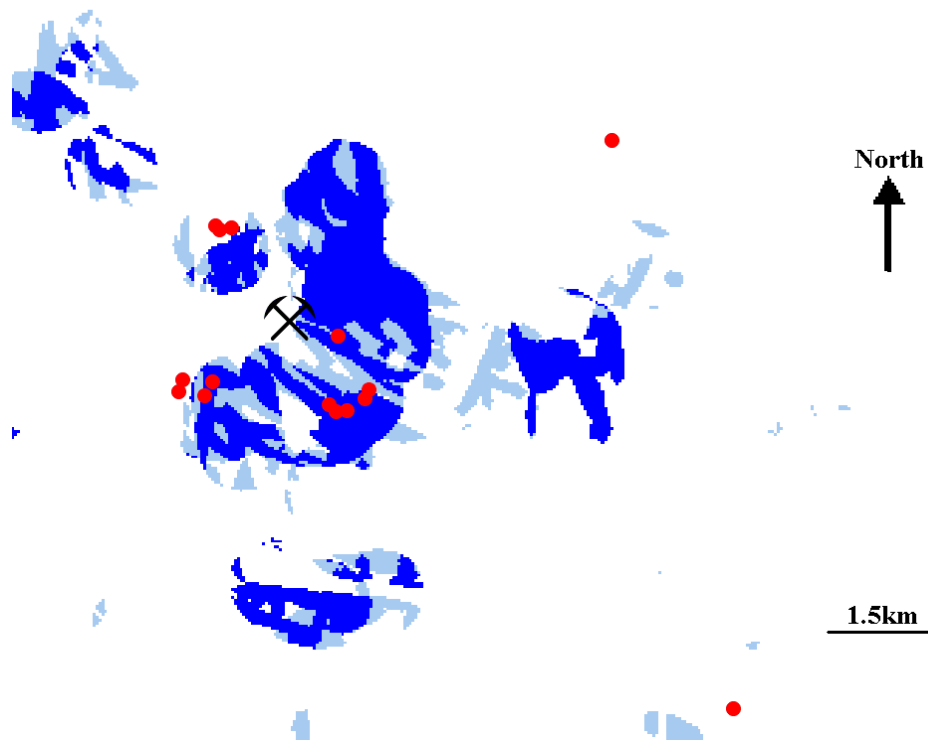


Figure 148 Area D, high prospectivity zone around Ampelikou, Apliki and Agios Epiphanos Soleas, ● = mineral occurrence, ⚒ = mining district.

#### 11.2.2.5 AREA E: LYTHRODONTAS

This area, to the south east of area C and to the west of area D (Figure 144), forms a small zone approximately 4 km wide by 6.5 km long, trending northeast–southwest, and elongate along this axis (Figure 149). Located near the village of Lythrodontas, the area is around 7 km south of the Kambia–Pitharokhoma–Peristerka–Kaphedes mining district, and around 10 km west of the Mathiatis–Sia district. The area is close to five mineral deposits, consisting of three ancient slag dumps, one old gold working and one stockwork mineralization locality. The geology of the area comprises Fanglomerates, Lavas and volcanoclastic sediments, Lower Pillow Lavas and Basal Group units, with 1:31 680 and 1:250 000 faults present. Bouguer gravity anomaly readings indicate the area is prospective, and the area has gossan occurrences and Lower Pillow Lavas–Basal group and Basal Group–Sheeted Dyke Complex contact are present. The area is also indicated to be prospective by E–W striking satellite lineations, and 1/3, 1/5, 2/5, and 4/5 ASTER Band ratios. The zone of high prospectivity appears to have had little former mining or exploration work carried out, and as such remains another relatively unknown area with the potential for undiscovered mineral deposits.

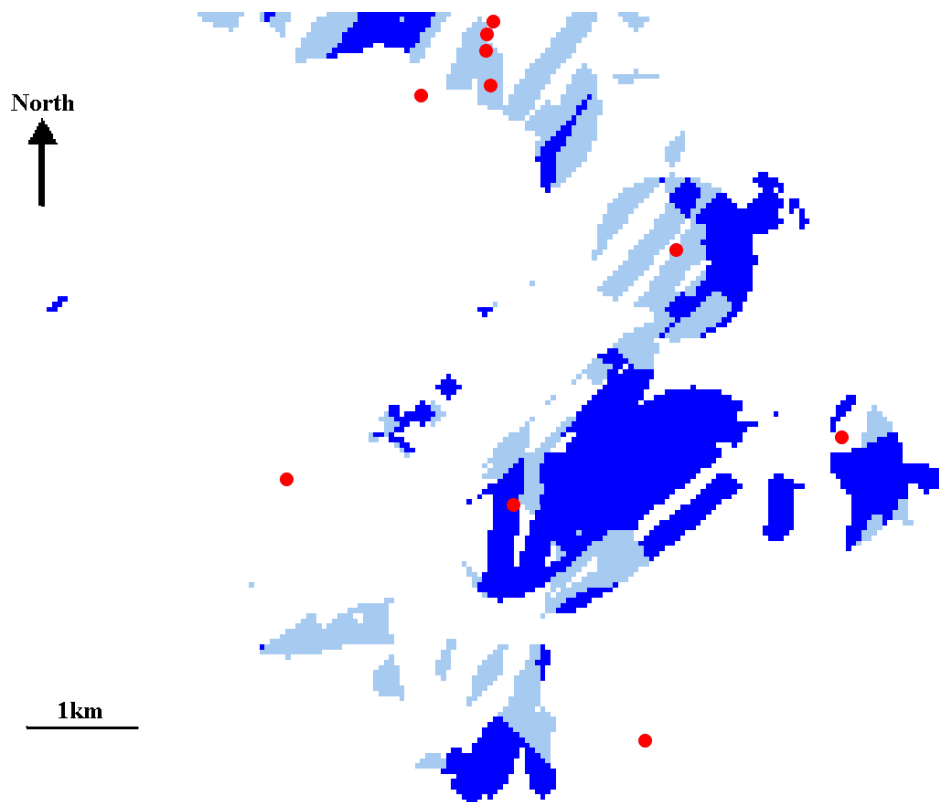


Figure 149 Area E, high prospectivity zone around Lythrodontas, • = mineral occurrence.

#### 11.2.2.6 AREA F: ARAKAPAS, DIEROUNA, EPTAGONEIA

Area F (Figure 144), an oval shaped high-prospectivity zone around 2 km in diameter and close to the settlements of Arakapas, Dierouna and Eptagoneia, is closely associated with the northern boundary of the Arakapas, or Southern Troodos, Transform Fault Zone (Figure 150). The area has no history of mining and no mining districts or former mines are located within 10 km of the prospective area. Seven mineral occurrences are known in the area, consisting of six former copper workings and one ancient slag dump. The area is underlain by Lavas and Volcaniclastic sediment, Lower Pillow Lava, Basal Group, Sheeted Dyke Complex and gabbro units, with 1:250 000 and 1:31 680 faults running through the area, and prospective Bouguer gravity anomaly. The area also hosts contacts between the Lower Pillow Lavas and the Basal Group, and the Basal Group–Sheeted Dyke Complex, along with gossan occurrences. East–west running satellite lineations are present in the area, and the prospective areas are also highlighted by LandSat TM and by 2/3, 2/5 and 4/5 ASTER band ratio images.

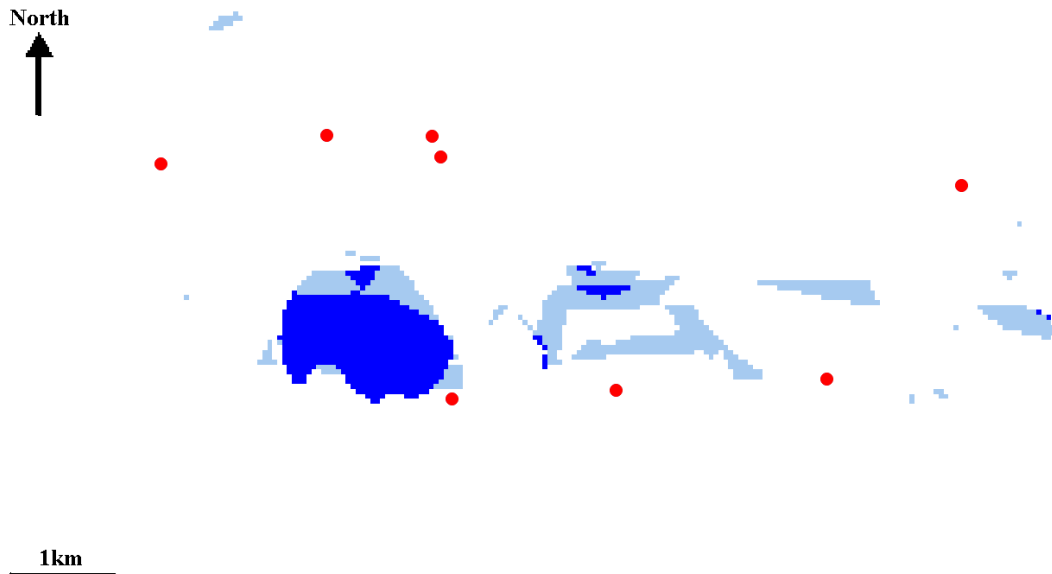


Figure 150 Area F, high prospectivity zone around Arakapas, Dierouna and Eptagoneia, • = mineral occurrence.

#### 11.2.2.7 AREA G: ASGATA

The prospective zone (Figure 144) close to the village of Asgata forms two distinct zones, a northern rectangular shaped zone around 6km long and 3 km wide, and a smaller and more irregular southern zone, split into two areas of high prospectivity, one oval with a 1km diameter, and an unevenly shaped zone around 1 km wide and 2 km long (Figure 151). The entire area runs along a northeast–southwest trend inside the ‘Anti-Troodos Plate’, following the eastern border of the STTFZ. The area is associated with thirteen mineral occurrences, consisting of two old gold workings, two old copper workings, five copper-bearing pyrite mines, two massive sulphide deposits, and two UN sulphide mines. The area is located between two mining districts, the Maghaleni–Parekklisha district, some 5 km to the west and the Kalavastos district, adjacent to eastern border of the northern section of the high-prospectivity zone. Several former mines are found in the area, including the Maghaleni, Kalavastos A, B, C, D and E mines, and the Parsata gold workings. The area is underlain by Lava and Volcaniclastic sediment, Lower Pillow Lava, Basal Group, Sheeted Dyke Complex, and Gabbro units, with contacts between Lower Pillow Lava and Basal group units, and Basal group and Sheeted Dyke Complex units. This high prospectivity area also contains gossan occurrences, as well as 1:250 000 and 1:31 680 faulting and NW–SE trending satellite lineations. The area is within the prospective zone defined by the Bouguer Gravity anomaly data, and is highlighted by LandSat TM and 1/3, 2/3, 2/5, 4/5 and 6/1 ASTER Band ratio images.

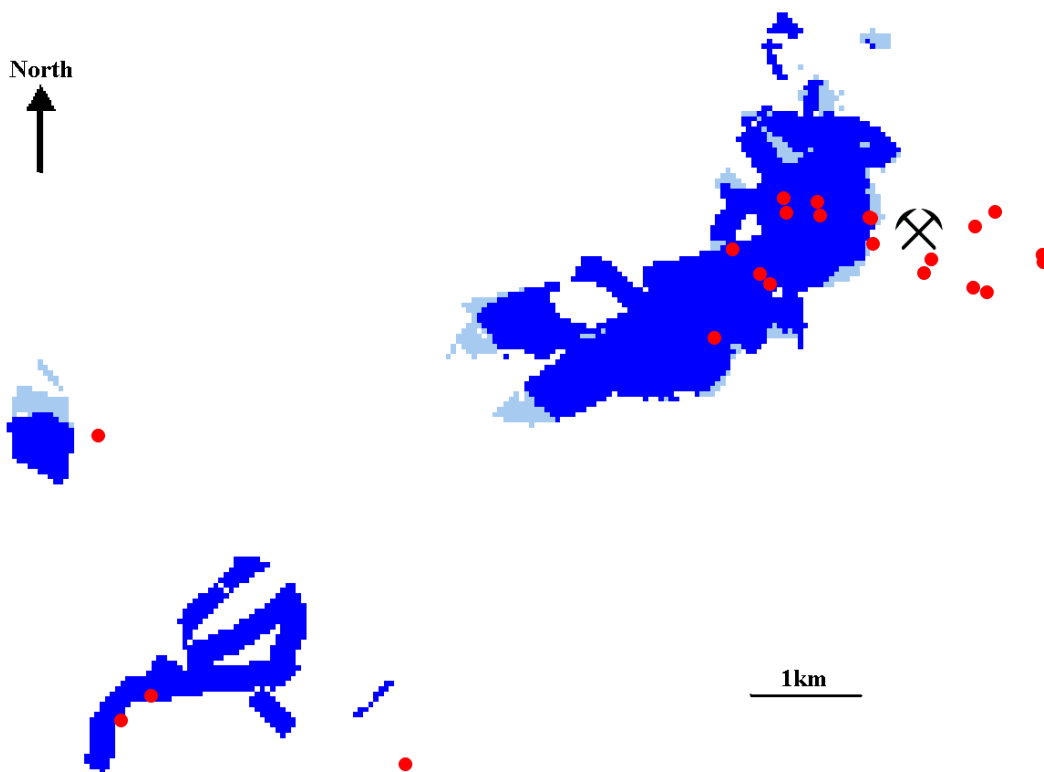


Figure 151. Area G, high prospectivity zone around Asgata, • = mineral occurrence, ⚒ = mining district.

#### 11.2.2.8 AREA H: MANDRIA LEMESOU

This area, in an isolated situation located to the south and west of other areas of high prospectivity, is located on the southern flank of the Troodos ophiolite (Figure 144). The zone is approximately 8km long, and a maximum of 2 km wide, and forms an irregularly shaped oblong, elongate along a northwest-southeast axis (Figure 152). The area is approximately 3 km away from the Pera Vesa–Vreccia mining district, and is associated with two mineral occurrences, an old copper working, and a massive sulphide deposit. The area is associated with Gossan occurrences, Pakhna, Lefkara, Lava and Volcaniclastic sediment, Lower Pillow Lavas, Basal Group, Sheeted Dyke Complex and Intrusive plutonic rock units, with faulting displayed at 1:250 000 and 1:31 680 scales. The high prospectivity zones are within an area defined by Bouguer gravity anomaly data, and are associated with Lower Pillow Lava–Basal Group and between Basal Group–Sheeted Dyke Complex contacts. NW–SE satellite lineations are associated with the high prospectivity areas, and the area is highlighted by the 6/1 ASTER band ratio image. The zone of high prospectivity hosts no known mineral occurrences, although the proximity to two known occurrences and a mining district suggests that this area could host undiscovered mineralization.

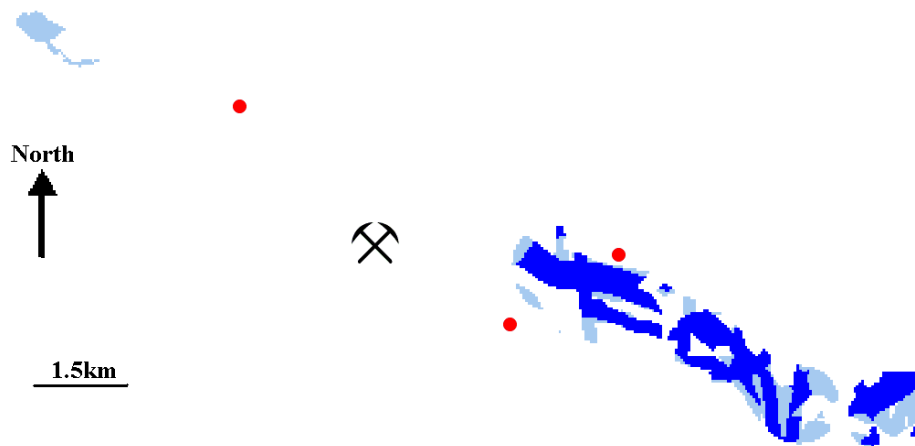


Figure 152. Area H, high prospectivity zone around Mandria Lemesou, ● = mineral occurrence, ⚒ = mining district.

## 11.3 DISCUSSION—REGIONAL PROSPECTIVITY

### 11.3.1 Binary maps

#### 11.3.1.1 GEOLOGICAL DATA

Geology is one of the major themes relating to copper mineralization on Cyprus. The most informative themes in the prospectivity GIS are the geological contact data maps. Here, it is worth noticing that the contact with the largest area of influence over mineralization, i.e. the highest threshold value, is in fact the stratigraphically lowest contact, between the Basal Group and the Sheeted Dyke Complex, having an area of influence of 1250 m compared to the threshold values of the contact between Lower and Upper Pillow Lavas (at 750m) and the Basal Group and the Lower Pillow Lavas (at 1000 m) (Table 24). This is moderated by the fact that the Basal Group–Sheeted Dyke Complex contact has the lowest prospectivity weighting of the three contacts, with a maximum contrast of 1.9220, compared to the maximum contrasts for the Basal Group–Lower Pillow Lavas contact of 4.2544 and the Lower and Upper Pillow Lavas contact of 2.8942. The large contrast (4.2544) and relatively large threshold value (1000 m) displayed by the contact between the Lower Pillow Lavas and the Basal Group indicates that this contact should be considered as the most prospective contact, rather than the other two contacts used in the GIS, although these contacts should also be considered prospective. This is at variance with current thinking that the Lower–Upper Pillow Lava boundary is the contact that acted as the main host for massive sulphide ore. In fact, the higher weighting given to the Lower Pillow Lava–Basal Group contact is suggestive that this contact, not the Lower–Upper Pillow Lava contact, should be considered as the most prospective. This feature from the pilot prospectivity mapping warrants further investigation and suggests that other geological contacts should also be considered for exploration, as they still retain a relatively high degree of prospectivity.

#### 11.3.1.2 FAULT DATA

Small-scale faults are considered to be a key factor in the formation of massive sulphide mineralization, with faults acting as preferential flow routes for hydrothermal fluids. This is clearly seen by the high prospectivity weightings for faults displayed on the 1:31 680 maps, even considering the small thresholds applied to these faults. The low threshold value applied to the small-scale faults (100 m) relates to the close relationship that these faults have with orebodies—in many cases, faults run through the orebodies, indicating a primary relationship between small faults and mineralization. Beyond this 100 m distance, these faults have little influence over mineralization, as their primary function as mineralizing fluid pathways does not extend further than a very localised zone close to the fault.

Larger scale faults, associated with the 1:250 000 geological map, have larger thresholds than the smaller scale faults. The threshold decided for this dataset was not just based on the weightings, but the fact that these faults rarely have a primary association with mineralization. Indeed, this threshold could, and probably should have been increased beyond the 500 m distance, as the weighting graph is more typical of a geochemical relationship. However, at threshold distances greater than this, buffer merging and convergence was a large factor in the weightings. This larger threshold value does not indicate a closer relationship with mineralization. Indeed, these faults most probably do not play much of a role in locating mineralization. Instead, they may represent large-scale extensional faults related to the Troodos spreading centre, indicating a relationship to the spreading ridge. Though they probably do not influence mineralization directly, they may indicate off-ridge locations that acted as the heat sources driving the hydrothermal systems.

One factor not used was fault directions, where each series of faults could be broken down according to azimuth. However, considering the fact that many of the mining districts on Cyprus can be related to grabens, each graben would have been considered independently, as the dominant direction of faulting related to mineralization in each separate graben would probably differ to adjacent grabens. The fact that the definition of individual grabens and their boundaries is unclear, and the time that these operations would require made this task unviable for the pilot prospectivity mapping. However, this may well be useful for any future work or prospectivity modelling, as long as individual grabens can be clearly and accurately delineated.

#### 11.3.1.3 GOSSAN OCCURRENCES

Gossans are necessarily linked directly to some kind of mineralization and the mapped gossans show a good correlation with metalliferous mineralization. Though, gossan outcrops provide a good guide to mineralization at surface they are, however, of limited use in locating deep blind deposits.

#### 11.3.1.4 GRAVITY DATA

The coarse nature and small coverage of the gravity data meant little data manipulation other than contouring could be carried out. However, certain Bouguer anomaly values do seem to be related to prospective areas and binary maps were produced. This, however, is probably a function of the underlying geology, although the correlation between the geology and gravity anomalies was better in some areas than others—e.g. the area around Mt. Olympus, and the south-western flank of the

Troodos. This may point to ophiolitic rocks underlying sedimentary sequences, and could also point to a buried extension of the ophiolite to the northeast. This gravity survey is also one of the few datasets used in this GIS that is able to see through the sedimentary cover to the underlying ophiolitic rocks, and possible mineral deposits. However, the poor coverage and low resolution of the data makes further conclusions difficult.

#### 11.3.1.5 ASTER BAND RATIO IMAGES

These images display areas with high concentrations of alteration mineral assemblages associated with mineralization, with the characteristic spectral attributes of the alteration assemblages being identified from PIMA analyses. Each band ratio image shows a distinct threshold value. This indicates a sharp transition from the high concentrations associated with mineralization-associated alteration and gossans to background levels, where alteration assemblages are found at lower concentrations. Ratios 1/3 and 2/3 have the largest threshold values of the band ratio images, although the 1/3 image has the lowest prospectivity weighting. Ratio 2/3 has the largest threshold, as well as the highest levels of prospectivity, and so should be considered representative of the dominant alteration mineral assemblage associated with sulphide mineralization.

One problem with using several different band ratio images is that they pick out similar alteration assemblages. For example, ASTER bands 1/5, 2/5, and 4/5 have very comparable binary maps (Figure 134, Figure 136 and Figure 137), although the actual weightings are different. This may be explained by the fact that each individual band ratio image is highlighting subtly different minerals or mineral mixtures within the same general alteration assemblage. This would explain the slight differences in the maps, and the differences in weightings (Table 24). This multiple selection of the same alteration assemblage may, however, cause a problem with conditional dependence, where the same area is being highlighted by more than one image. Using a combination of images to highlight all known prospective band ratios in one image would prevent this, but would also prevent the less prospective, but still important, assemblages from being identified, especially as not all alteration would be identical across the ophiolite. Another problem with the binary maps produced from the ASTER images is that these band ratio images occasionally highlight bodies of water. Selecting and removing known bodies of water can remedy this, but small lakes and rivers that escape detection due to the resolution of the image may have an effect on the image that cannot be removed.

#### 11.3.1.6 LANDSAT TM BAND RATIO IMAGES

The LandSat TM Band ratio image was aimed at highlighting ferrous minerals, clays and iron oxide minerals, and was a combination of three images designed to highlight these alteration styles. However, during the amalgamation of the three images, no weighting was used, which may have introduced errors, as the iron oxide image highlighted a large area, possibly associated with large amounts of iron oxides in soils, that the other two band ratio images did not. The images themselves show a relationship with mineralization over a greater distance than any of the ASTER images, with a threshold value of 700 m. This greater influence with mineralization is moderated by the lesser value placed on the prospectivity weighting of the LandSat image, lower than any of the ASTER images, showing a larger sphere of influence, but an overall lower impact on prospectivity. This again may be

highlighting minerals with a much greater freedom to move away and disperse from the orebody. The much greater bandwidths highlighted by the LandSat TM image also may have reduced the ability of the image to show selective assemblages, highlighting much broader ranges of alteration assemblages not necessarily related to mineralization.

#### 11.3.1.7 ASTER SATELLITE DERIVED LINEATIONS

ASTER satellite lineations were used to try and locate faults that are not located by the 1:31 680 and 1:250 000 scale mapping, and also lineations that may represent faults overlain by sedimentary cover sequences. A large number of lineations were visible from the satellite imagery; however, only lineations trending east–west and northwest–southeast had a clear relationship with mineralization. East–west trending lineations have a greater spatial relationship with mineralization, with a threshold value of 1000 m, although these lineation trends show a descending relationship, commonly associated with geochemical data, rather than the ascending relationship one would associate with faulting, as seen with the 1:250 000 fault mapping. However, a positive relationship with mineralization is present, and these lineations may represent a mixture of factors rather than just faulting. The NW–SE trending lineations show a more fault-based relationship with mineralization, although over shorter spatial distances than seen in the east–west lineation trend, and with a lower overall prospectivity. Again, the question of relating these lineations to grabens is possible. In addition, the lineations were digitised manually, and so the human error is a potential hazard that has to be considered when using this data, with the potential for lineations to be ignored or for certain areas to have more work done on them than others. This may well indicate that the overall support for the data may not be equal.

# 12 Pilot study

## 12.1 INTRODUCTION

The regional prospectivity analysis focussed on the whole of the Troodos ophiolite and did not include the airborne geophysical data. In addition, from the initial prospectivity analysis, a conditional dependence for the response theme of 0.38 (see section 11.2.2 above) indicated that there was significant correlation between various datasets. However, the analysis did indicate several areas worthy of further analysis (see section 11.2.2 above). Furthermore, as the companies had decided to allow use of their high-resolution digital geophysical data (see section 9.2 above) it was decided to undertake a further higher resolution and more complete prospectivity analysis using the proprietary geophysical data and a smaller study area with the aim of defining a number of drilling targets to test if a prospectivity analysis approach could be used to locate mineralization.

## 12.2 DETAILED PROSPECTIVITY ANALYSIS AND LOCATION OF BOREHOLES

Evidential Theme	W+	W-	Contrast	Confidence
Faults	1.1	-4.5	5.6	5.6
Gossan distribution	-1.1	3.2	4.3	22.0
Basal Group Lower Pillow Lava contact	-0.5	2.4	2.8	15.4
Magnetic lineaments	2.5	-0.3	2.8	13.9
Geology	-1.7	0.9	2.6	9.1
Pillow Lava contact	-0.2	2.3	2.5	11.6
Positive magnetic anomalies	2.3	-0.1	2.4	8.9
Aster Band 2 over Band 3	0.0	1.6	1.6	3.8
Basal Group Sheeted Dyke contact	-0.1	1.3	1.5	6.0
Landsat Fe-OH identification	-0.1	1.4	1.4	4.5
Aster EW Lineaments	-0.3	1.0	1.3	7.3
Aster NS lineaments	-0.1	1.2	1.3	4.8
Aster NE Lineaments	-0.5	0.5	1.0	5.7
Regional gravity data	-0.4	0.5	0.8	4.5
Aster NW lineaments	-0.1	0.7	0.8	3.7
Aster Band 4 over Band 5	0.0	0.7	0.7	0.9
Aster Band 2 over Band 5	0.0	0.6	0.7	0.9
Aster Band 1 over Band 3	0.0	0.6	0.6	0.6
Aster Band 6 over Band 1	0.0	-0.2	0.2	0.2
Aster Band 1 over Band 5	0.0	0.1	0.1	0.1
No. training points = 132				

Table 27 Contrast table for the geophysics prospectivity analysis

The focussed prospectivity analysis, delineated by the Huntings 1966 survey (), that includes the combined interpretation of the airborne magnetic surveys (see section 9.2) also included geological (lithology, contact and gossan distributions) and remote sensing data—individual data themes along with their relative prospectivity are given in Table 27. When combined in a weights of evidence model these themes produce a model with a conditional dependence of 0.98. This is significantly higher than the original value obtained for the whole of the regional Troodos prospectivity analysis and reflects a greater confidence that the geophysical model is a good representation of potential prospective areas.

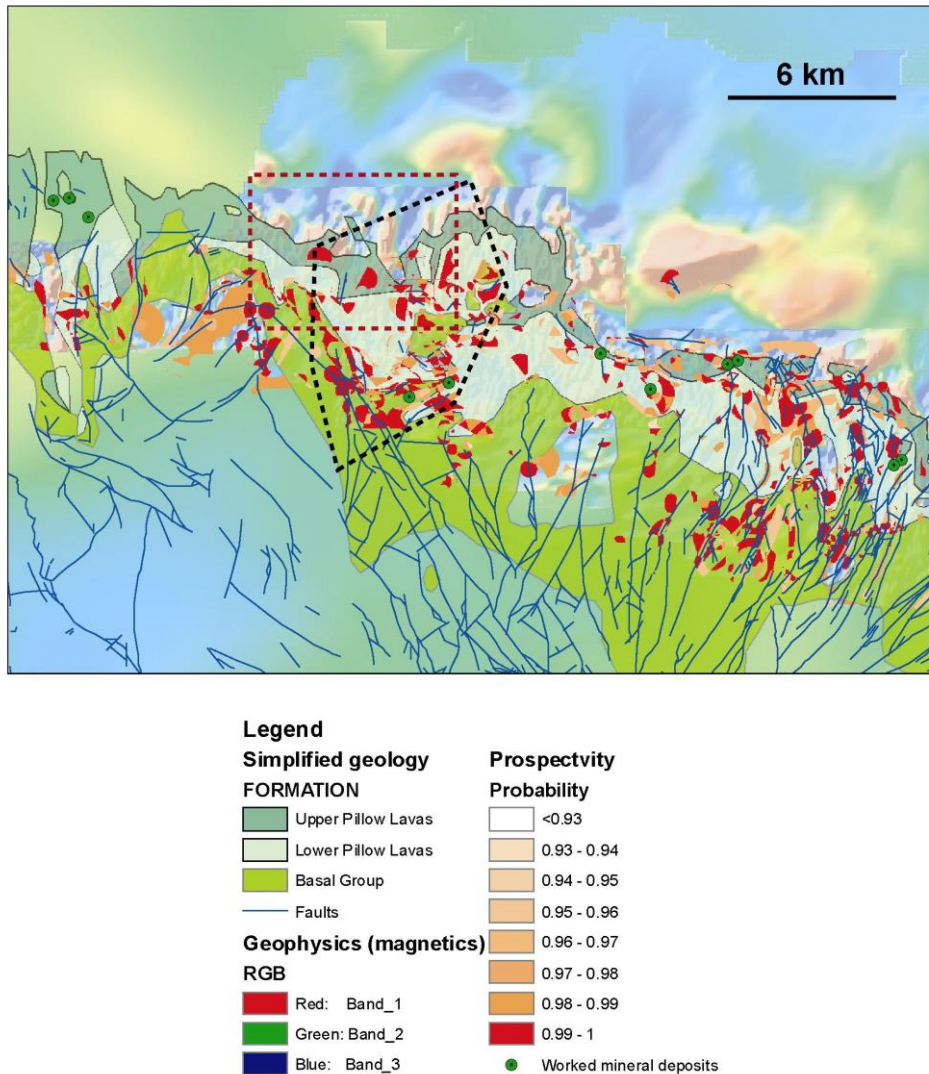


Figure 153 Results of the geophysical prospectivity analysis. Dashed lozenge shape indicates zone of high-prospectivity in the Alestos–Memi region and red dashed box shows location of Figure 154.

The response theme (map) for the detailed prospectivity analysis is given in **Error! Reference source not found.** There are three clear prospective areas: (i) Memi–Alestos (Zone A) (ii) Klirou–Kapedhes (Zone C) and (iii) Mathiati–Sia (Zone C). From these three areas Zone A—Memi–Alestos (Figure 153)—was selected as the best region to target a borehole. In this region there are a number of additional indications of a large-scale hydrothermal system. These include alteration picked out by satellite imagery in the basal group and zones of gossans that appear along the axis of the region. In addition Eastern Mediterranean Resources (EMR) had undertaken a ground geophysical IP survey.

The prospectivity analysis does not discriminate between economic mineral deposits and occurrences. Thus, from initial examination of Figure 153, it would appear that the Basal Group and Lower Pillow Lavas are more prospective. However, this relates to known to the abundance of known mineral occurrences, rather than the economic potential of a mineral deposit. Most of the worked mineral deposits occur in or close to the Upper Pillow Lavas. Therefore, any proposed drilling should concentrate on prospective areas in the vicinity of out- and subcrops of this formation.

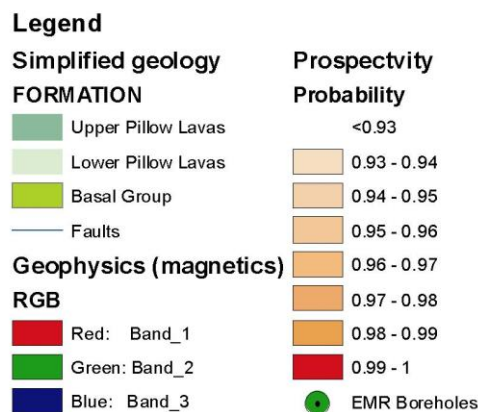
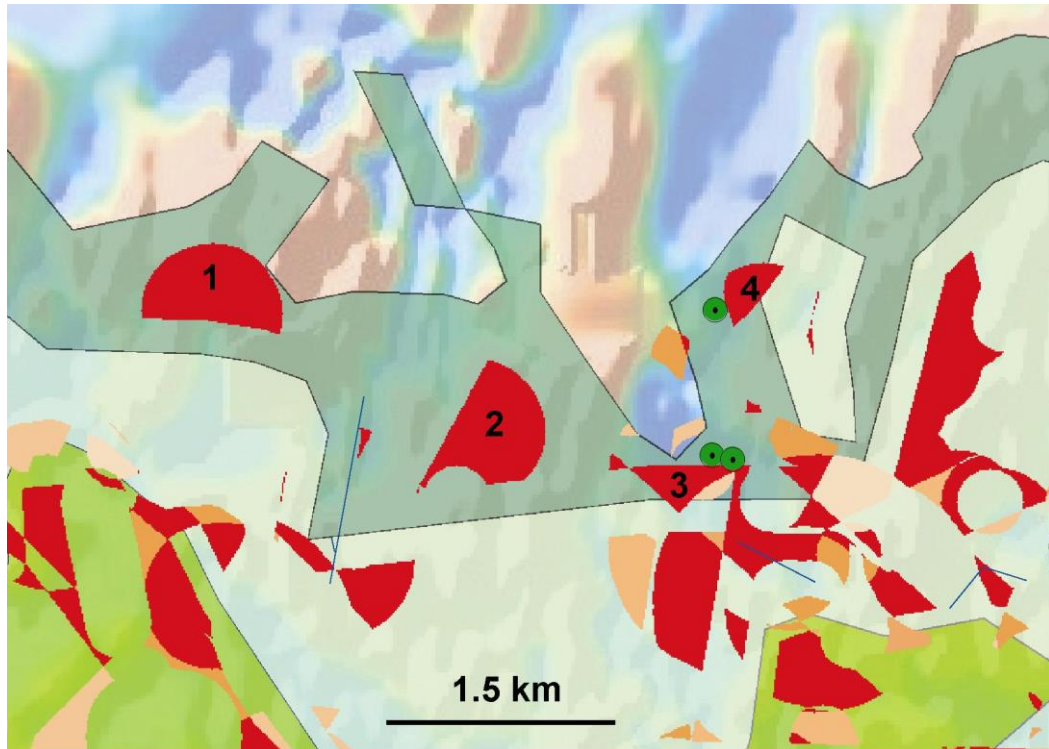


Figure 154 Prospective areas (red and labelled 1 to 4) hosted by the Upper Pillow (dark green) Lavas in the Alestos–Memi zone. Background shows results of airborne magnetic survey and green-filled circles the locations of EMR percussion boreholes.

Figure 154 shows the location of four prospective areas hosted by Upper Pillow Lavas in the Alestos–Memi trend. At this resolution prospectivity analysis alone is not able to rank the targets—additional local geological and geophysical information is required. Areas 1 and 2 (Figure 154) do not have any supporting geophysical information whereas Areas 3 and 4 are in the vicinity of an IP survey and there is



### 12.3 RESULTS OF DRILLING

Due to access difficulties two boreholes were drilled. The location of these is shown in Figure 156.

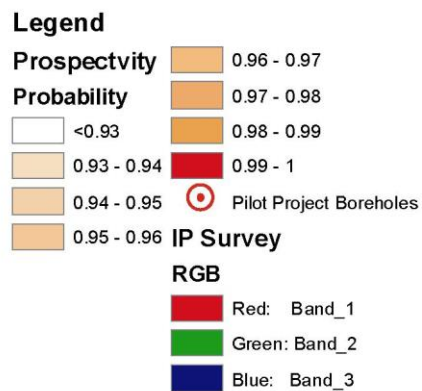
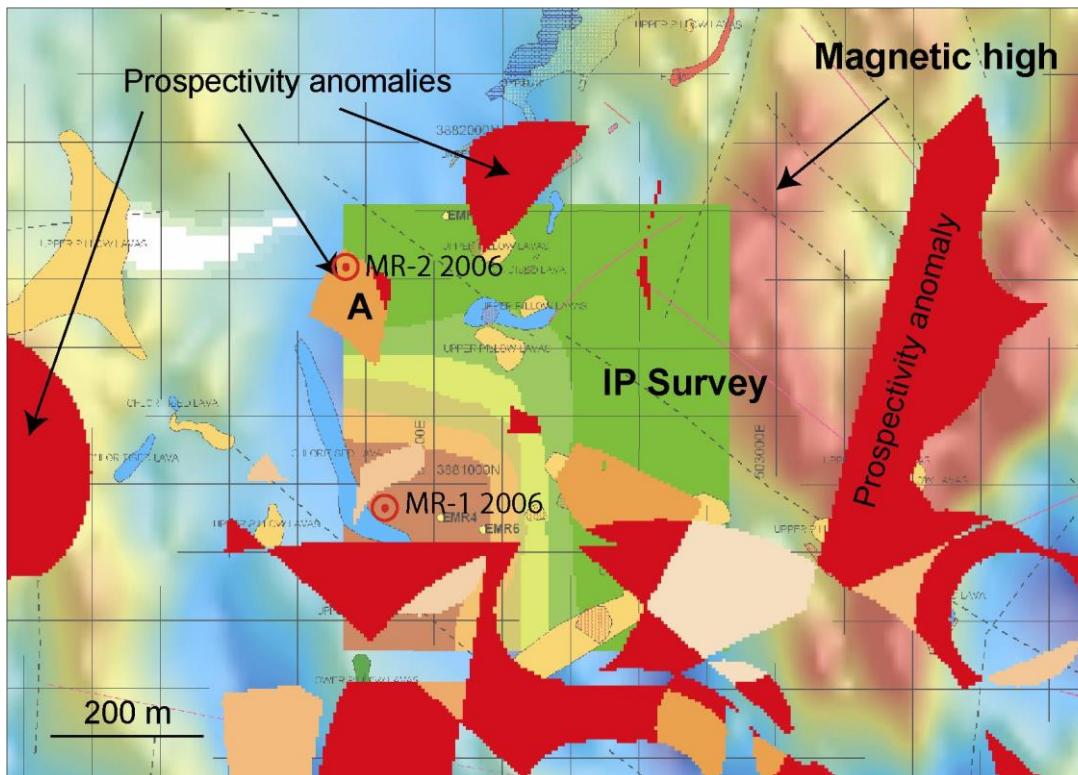


Figure 156 Location of pilot project boreholes.

Of the two boreholes only one—MR-2 2006—, which targeted prospectivity anomaly A (Figure 156) was mineralized. This comprised a 28 m zone of propylitically and argillically altered lava containing disseminated pyrite and rare chalcopyrite. The extent and intensity of the mineralization was difficult to determine, as core recovery was particularly low (~35%) in the mineralized zone.

Summary logs of the two boreholes are given Table 28 and Table 29. These are accompanied by photographs that record the general appearance of the drillcore (Figure 157 and Figure 158). In addition where appropriate detailed photographs of specific features (volcanic textures, mineralization)

### 12.3.1 Borehole MR1-06

From	To	Unit	Alteration	Mineralization	Notes
0.0	13.5	Massive basalt flow	Propylitic (seawater?), thin qtz veins	none	Shows signs of autobrecciation in places. 13.1 to 13.5 m spherulitic texture, basal contact of flow. Thin late qtz-carb veins
13.5	18.0	Pillowed basalt flow		none	Flow unit with distinct vesicular top, evidence of pillow breccia and peperitic textures. 13.5 to 14.0 m vesicular flow top
18.0	26.5	Massive basalt flow		none	Massive flow incorporating pillow breccia fragment between 23.0 to 23.5m
26.5	33.0	Thin basalt flows		none	Thin flow units with distinctive spherulitic and black glassy zones. Glassy spherulitic pillow? 26.5 to 27.0. Interflow sediments in places through this interval
33.0	43.5	Autobrecciated basalt flow	Propylitic (seawater?)	none	Distinct unit showing autobrecciation with clay alteration in the matrix. Larger chilled and non-chilled lava fragments incorporated in flow unit.
43.5	46.8	Massive basalt flow		none	Massive flow with distinctive flow top 43.5 to 44.0 which shows hyaloclastite texture with a lighter matrix. From 44.0m becomes massive, gery-green with lighter spherulites and occ vesicles visible.
46.8	49.8	Autobrecciated basalt flow		none	Series of flow breccia zones with evidence of spherulitic quenched material
49.8	119.5	Massive basalt flows	Carbonate, Gypsum veining (Oxidation 82.3m)	none	Sequence of more massive, less brecciated grey-green basalt flows. Autobrecciation apparent in places and thick sections showing black flecks up to 5mm long which appear to be glass. Glass-rich zones particularly apparent beyond 55m. Gypsum? carbonate vein @ 65m. Massive basalt often shows fine late jigsaw fractures cemented by quartz/calcite esp. @ 93m. 94.5m Flow top contact with thin breccia zone. 95m onwards, more abundant spherulite texture. 100.5 autobreccia texture. 110.8m Thin carbonate-hematite? veining Beyond 110.8m More massive grey-green unit with black glassy flecks very common.
119.5 EOH					

Table 28 Summary borehole log for MR-1 2006

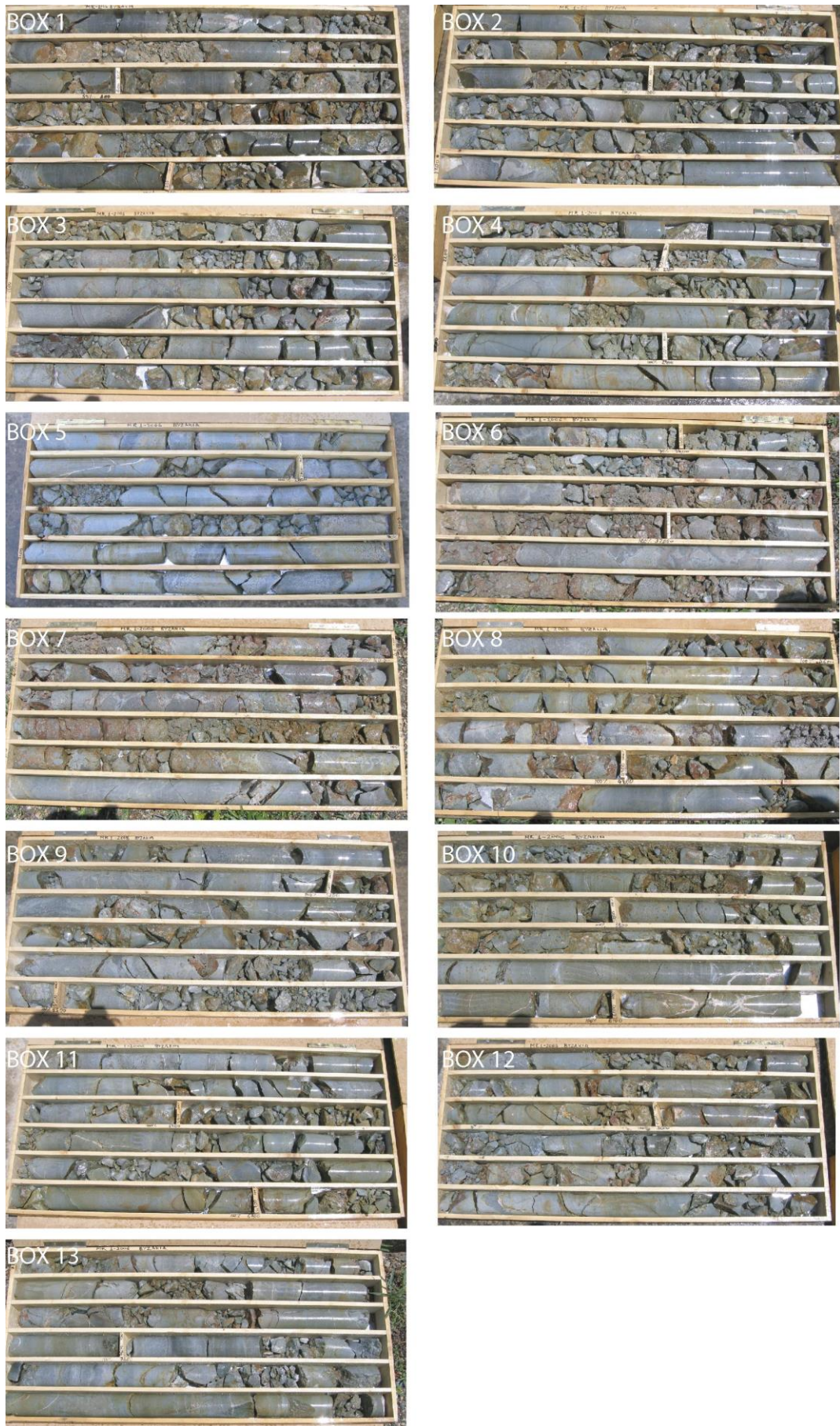


Figure 157 Sequence collage of core boxes from borehole MR1-2006. Top left is the first core box and bottom right the last—Total depth 119.5 m

Borehole MR-1 2006—Photographs of selected features



17 m—volcanic breccia



24 m—quartz veining along joints in lava



25.5 m—spherulitic textures in a possible pillow



25.5 m—spherulitic textures in possible pillow



37.5–38 m—banded sediments and breccias



37.5–38 m—banded sediments and breccias



37.5 m—hyaloclastite textures



44 m—spherules

Borehole MR-1 2006—Photographs of selected features



51 m—spherulites with chilled margins



61 m—vein textures in lava



65 m—Gypsum or carbonate veining in massive homogenous lava



82.3 m—possible glassy margins



93 m—stockwork style veining - possibly as part of localised seawater system



100.3 m—spherulitic textures and breccia



113 m—flow banded sediment

## 12.4 BOREHOLE MR2-06

From (m)	To Unit (m)	Alteration	Mineralization	Notes
0.0	26.0?			Core loss?
26.0	64.0 Vesicular pillowed basalt flows	Mg+ (seawater?)		Distinctive dark green pillowed and in part vesicular basalt sequence with intervals of intense chloritisation. Some minor zones of autobrecciated flows with interstitial vein infills (carbonate and gypsum?). Vesicles in part infilled with carbonat, chlorite or zeolite. Core more broken towards base of section with alteration of chlorite to clay minerals. Thin umber horizon 29.0m. Dark green (Mg-rich?) chlorite zones appear to mark margins to flows/pillows indicative of seawater reaction.
64.0	64.2 Sharp contact zone			Core loss?
64.2	64.4 Vesicular basalt flow	Oxidation		Thin iron-oxide altered vesicular basalt fragment flow or large fragemt. Marks top of breccia section
64.4	69.0 Clay cemented brecciated basalt	Argillic	disseminated pyrite	Zone of coherent clay-cemented polymictic breccia containing lithic fragments of mainly chl-ser-py altered basalt. Sulphide disseminations common through most clasts (ca 1-2% max in general although some fragments contain slightly more). Clay matrix also contains blastic pyrite crystals up to 0.5mm across. Other lithic fragments include jasper? oxidised lava and ochreous fragments. Some fragments show epidote impregnations. Core loss extensive beyond 69.0m
69.0	70.0 Altered vesicular basalt flows	Argillic-propylitic (chl-ser-epi-py)	disseminated pyrite + rare chalcopyrite	Highly broken core in altered vesicular lavas now intensely chlorite-sericite-epidote-pyrite altered. Pyrite disseminations throughout, rarely exceeds 2% overall but some thin (1-2 mm) replacement layers in basalt. Abundant vesicles up to 3mm infilled often with epidote.
70.0	73.0 Ochreous clay zone	Argillic-propylitic (chl-ser-epi-py) + Oxidation	disseminated pyrite	Red ochreous clay matrix containing fragments of chl-ser-epidote+py altered lavas
73.0	95.0 Altered vesicular basalt flows	Propylitic-argillic (chl-ser-epi-py)	disseminated pyrite	Similar to 69.0 to 70.0m - continues as broken chl-ser-epi-py altered basalt. Beyond 79.0m pyrite disseminations become less distinct with more epidote apparent. 82.0 to 85.0 better recovery in chl-ser-epi-py altered vesicular lava. 85.0 to 88.0m more brecciated unit with clay matrix apparent. Less epidote here with slight increase in py content. Beyond 88.0m epidote now apparent in cross-cutting veinlets with distinct white (feldspar?) vein selvages. Epidote veining in places clearly cut by sulphides. 94.0 to 95.0m contains coarser epidote clots in coarser vesicular facies.

From (m)	To Unit (m)	Alteration	Mineralization	Notes
95.0	97.0	Altered massive basalt flow	Propylitic-argillic disseminated (chl-ser-py) + epi pyrite veins	Finer grained chl-ser-py altered massive lava unit. Epidote only visible in cross-cutting veinlets. Py content decreases. 97m EOH
97m EOH				

Table 29 Summary borehole log for MR-2 2006

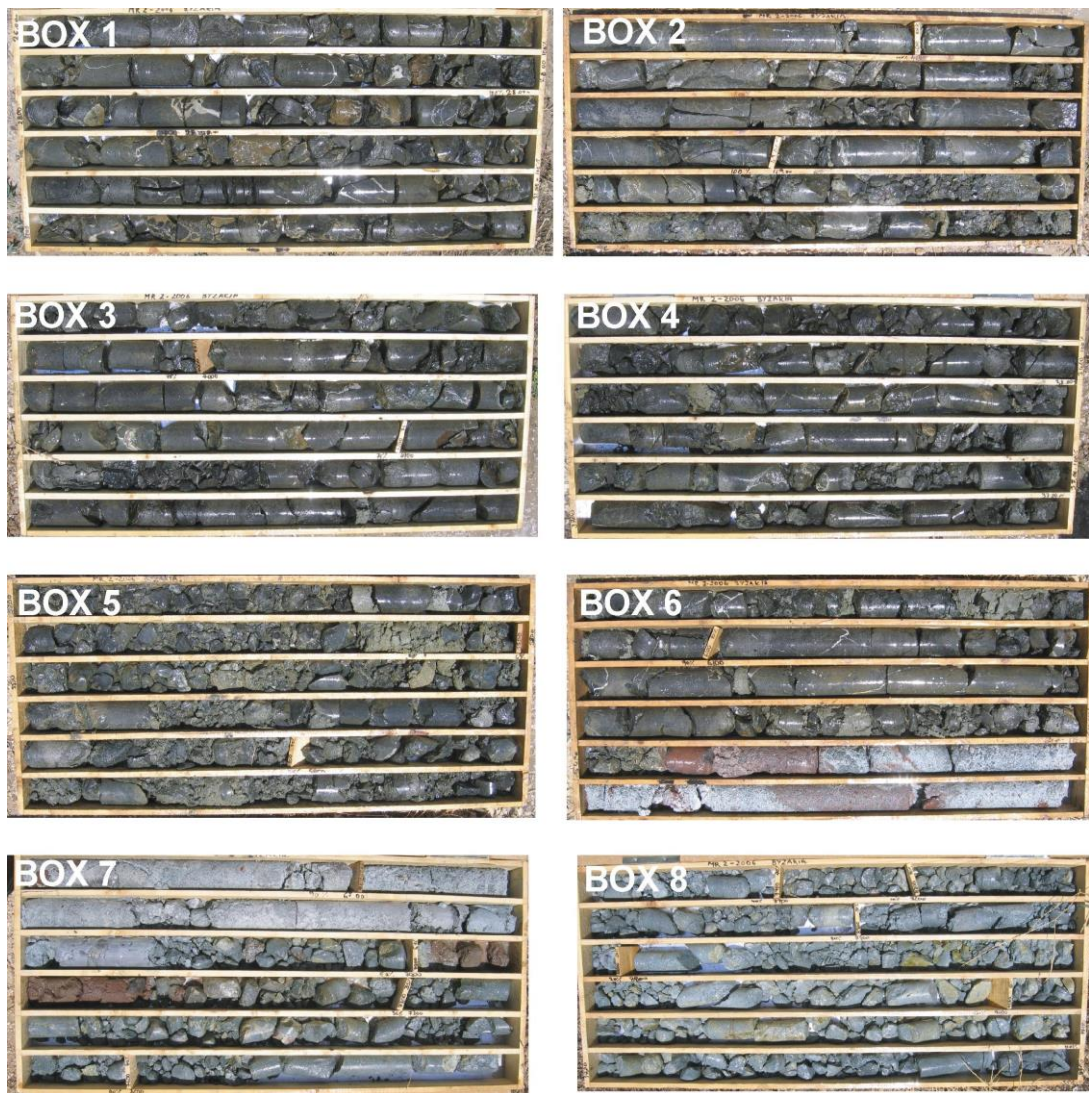


Figure 158 Sequence collage of core boxes from borehole MR2-2006. Top left is the first core box and bottom right the last. Note the distinct zone of alteration from the middle of Box 6 through to Box 8. Core recovery in the alteration zone was very poor—Total depth 97 m

Borehole MR-2 2006—Photographs of selected features



26.3 m—veined and vesicular chloritic alteration



28.3 m—chloritic altered lavas with ochre



28.5 m—gypsum veining



29.0 m—umber



39.0 m—vesicular chloritic alteration



46.0 m—chloritic alteration and veining



47.0 m—graded vesicular chloritic alteration



64.0 m—contact between sericite and chlorite zone JN

Borehole MR-2 2006—Photographs of selected features



66.0 m—possible fault rock - mineralized zone



68.5 m—sulphide bearing breccia



71 m—chalcopyrite and possible black sulphides



72.5 m—epidote vugs possibly similar to Apliki



73.2 m—possible late quartz vein linking epidote vugs



73 m—epidote-quartz filling vugs and veining



73 m—sulphide vein cross-cutting epidote vugs (1)



85 m—epidote on fracture surface

Borehole MR-2 2006—Photographs of selected features



85 m—sulphide bearing breccia



88 m—epidote-filled vugs



91 m—epidote veining

# 13 Results, conclusions and future work

## 13.1 PROJECT RESULTS AND CONCLUSIONS

To facilitate technology transfer and institutional strengthening the project delivered a number of office and field-based seminars and workshops. These included training in the use of GIS for prospectivity analysis, examination of potential epithermal style mineralization, lectures on: (i) epithermal mineralization in the Aegean, (ii) VHMS mineralization in the Urals and (iii) SX-EW hydrometallurgical techniques—These were given to the Cyprus society of geologists and engineers to ensure the widest dissemination. In addition, to give the project an international dimension, the results of the prospectivity analyses and examination of epithermal style mineralization were presented at two international conferences—*The 5<sup>th</sup> International Symposium on Eastern Mediterranean Geology* (Thessaloniki, Greece 2004) and *Mineral Deposit Research: Meeting The Global Challenge* (Beijing, China, 2005)

The project produced, using ArcSDM and a variety of geological, geophysical and remote sensing datasets, two prospectivity investigations: (i) a regional prospectivity map. This identified eight separate areas of high mineralization potential. The areas are generally located within 10 km of the boundary between the Troodos ophiolite and the autochthonous sedimentary cover sequences draping the ophiolite. (ii) A more detailed map focussed on an area of the northern Troodos defined by the Huntings 1966 airborne magnetic survey. This identified a drilling target in the Memi–Alestos area. In addition to construction of the GIS and the spatial data modelling with ArcSDM, key components to the prospectivity analysis included the (i) digitisation of minerals occurrences and gossan distribution. (ii) The analysis of remote sensing data using band ratio image processing techniques. This highlighted regional alteration trends—in particular one associated with the Memi–Alestos trend and this was used as supporting evidence to site the boreholes for the pilot project. (iii) The modelling and interpretation of airborne magnetic geophysical data. This comprised the amalgamation of three generations of data into a single data set and the identification of lineaments and regions positive and negative magnetic anomalies. Three primary domains in the data were recognised on the basis of the orientation of lineaments. The predominant trends are NNE, WNW and ENE. These data formed key themes for the detailed prospectivity analysis.

Further to the development of the ophiolite-hosted prospectivity GIS for the Troodos, the project addressed two new metallogenetic concepts for Cyprus—namely:

1. The investigation of potential epithermal-style VHMS mineralization using infrared spectroscopic and X-ray diffraction techniques. This study identified high temperature advanced argillic alteration phases and concluded that sub-seafloor boiling was a possible mechanism, perhaps induced by rejuvenated magmatism, for explaining the gold enrichment at the Tourounjia deposit
2. The development of low-grade supergene Cu mineralization associated with massive sulphide mineralization. This showed that in the specific case of the Phoenix deposit, the favourable interplay between the mineralization and topography played an important role in the development of the large secondary orebody where weathering of the topographically higher massive sulphide

deposit provided large quantities of Cu-charged acidic groundwater to a lower pyritic feeder zone that reprecipitated the copper from solution. The exploration strategy for this would be to look for zones where a cupriferous massive sulphide may have oxidised at surface producing copper-bearing acid groundwaters that may have migrated to a suitable deposition site (such as a propylitic alteration zone). A substantial body of oxidising pyrite is needed to ensure the generation of acidic groundwaters for a significant period of time. A strategy for exploring for such a supergene copper target would be to assess all surface gossans developed in topographic highs and seek potential downslope areas where reducing conditions may have developed to reprecipitate the copper—use of high resolution digital elevation models provided by techniques such as LiDAR (see below) could be a way forward in this respect

Professor John Monhemius, Imperial College London, undertook a review of the use of SX-EW hydrometallurgical techniques as applied to Cyprus. This study concluded that the decline in copper recoveries in the heap leach process used at Skouriotissa is due to increasing amounts of primary chalcopyrite, a refractory mineral that is very resistant to dissolution by oxidation, in the run-of-mine ore as mining gets deeper. Recent processes developed for the hydrometallurgical treatment of chalcopyrite all involve the use of extreme conditions, such as high temperature pressure leaching, ultra-fine grinding, or intensified bacterial leaching—these may not be appropriate for Skouriotissa and the best option for extending the life of the plant may be the discovery and exploitation of further reserves of supergene altered copper ores containing leachable copper oxide and secondary sulphide minerals. This will allow production to continue using the heap leaching technology currently in use. If necessary, the effectiveness of this leaching method towards secondary copper sulphide minerals could be improved by introducing tanks for bacterially pre-oxidising the leach solutions under optimum conditions, prior to being sprayed on to the ore heaps.

One key component of the assignment was to formulate and implement a pilot project based on the results of the regional GIS. The goal of the pilot project was to site a borehole to test if prospectivity analysis had the capability to predict the location of unknown mineralization. The application of a detailed prospectivity GIS using public domain and proprietary geophysical data focussed on the northern Troodos identified a high prospectivity zone in the Memi-Alestos region. Two boreholes were sited to test for the presence of mineralization beneath approximately 70 m of Upper Pillow Lava cover. One borehole (MR-2 2006) encountered over 20 m of argillically and propylitically altered lavas containing minor amounts of pyrite and chalcopyrite. This shows that prospectivity analysis approach used in this project could be a useful tool for locating buried VHMS mineralization on Cyprus. This is especially so when high-resolution geophysical data are available.

Thus to conclude, the project has provided:

- A very useful combination in a GIS format of previous exploration data
- The analysis of lithochemical data showed that the chlorite and Ishihara alteration indexes are a useful tool for identifying alteration associated with mineralization.
- The PIMA and XRD studies at Tourounjia identified submarine epithermal-style mineralization with features similar to active sea-floor systems.

- Band ratio processing of ASTER satellite imagery has enabled the identification of regional alteration features
- Prospectivity analysis, using Weights of Evidence modelling, has been attempted on Cyprus for the first time. Though it has revealed difficulties in combining certain legacy data sets. It has, however, been very successful in delineating prospective zones, one of which was tested in by follow-up drilling and found to have significant but low-grade mineralization—a technical success

## **13.2 FUTURE WORK**

### **13.2.1 New surveys**

Within the framework of this project it is important to note at its start in 2002, copper was priced at \$1 400 US, but now (July 2006) it is well over five times this amount and it is currently close to \$8 000 US. This historically high price has significantly stimulated exploration for copper on Cyprus, and sustainable mining and mineral exploration could become a significant component of the Cyprus economy in the future. With this in mind, it is important that a geological survey organisation is equipped to provide modern pre-competitive geoscientific information for a mining and minerals exploration industry that includes both minerals exploration and baseline environmental data. This project, in terms of GIS-based approach to regional prospectivity provides a starting point for this information delivery. However, further work on improving the dataset behind the prospectivity GIS should be undertaken. Though there is a significant amount of legacy data, its current format and focussed geographical coverage mean that it would probably not be a good investment to digitise this to provide new data for future prospectivity analyses, though it is important that paper records are archived and there are metadata to describe its existence. To progress the prospectivity GIS, it is important that good quality geochemical and geophysical data are incorporated into the prospectivity model to help predict possible blind deposit occurrences. To this, it may be better to undertake fresh regional geochemical and geophysical surveys rather than try and utilize legacy data, which was not really conceived for this purpose. It understood that a new environmental geochemical soil survey is currently being undertaken, though not ideal for mineral exploration, its results would be useful in a new prospectivity GIS. Perhaps of more importance for metallic mineral exploration, where the location of new deposits is highly probably going to be under the autochthonous sedimentary or Upper Pillow Lava cover, would be a high-resolution geophysical survey. Moreover new modern surveys of this type have multiple applications particularly in the field of environmental hazard identification.

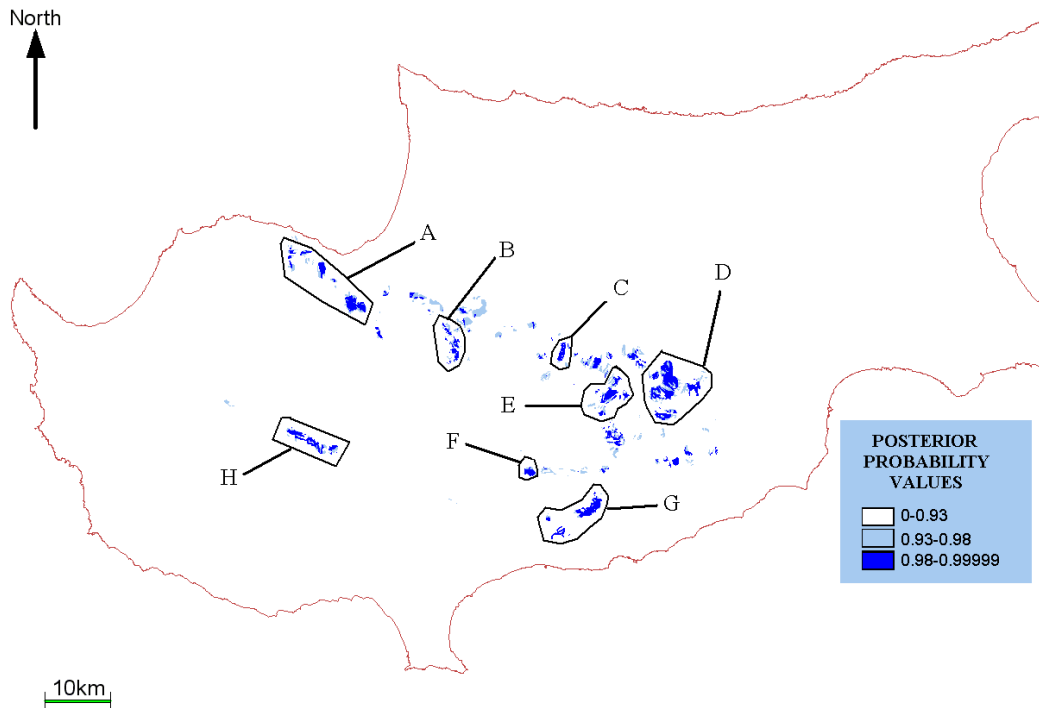


Figure 159 Selected areas of interest for further investigation

It is recognized that island wide or even ophiolite-focussed regional high-resolution airborne geophysical could be logistically difficult and have high mobilisation costs. Therefore, there may be a need to prioritize exploration areas. The first prospectivity analysis identified eight prospective areas (Figure 159). Each of these would be suitable for further investigation as long as the zone of interest can extend into the Upper Pillow Lavas and autochthonous sedimentary cover.

*Area A.* The largest known mineral deposits (e.g. Skouriotissa and Mavrovouni) are located on the northern limb and at the western end of the ophiolite (Area A—Figure 159). This would be the most obvious area for further investigation and would be the highest priority. However, the proximity of this area to the Green Line could make field-based logistics difficult.

*Area B* contains the significant mineral deposits of Memi and Alestos. In addition, this area was selected for the pilot project and the existence of mineralisation and alteration has been proved by drilling. However, this area is currently the focus of an exploration campaign by Eastern Mediterranean Mining and it may not be appropriate to undertake operations in parallel with this activity

*Area C* is located near the villages of Klirou and Malounta. Currently the Klirou prospect is subject to preliminary feasibility study by Eastern Mediterranean Mining and is, therefore, probably not appropriate for further geophysical investigations if the goal of these surveys is to attract inward investment from other mining companies.

*Area D and E.* These two areas are close to each other and are located towards the eastern end of the ophiolite in a region where there is considerable outcrop of pillow lavas. It also includes the Mathiatis–Sia mining district. Preliminary reconnaissance of a prospectivity anomaly located close to the village of Strongyli (Figure 160) showed hydrothermal alteration associated with a gossan at outcrop. It was suggested that this would be a suitable location for another test borehole if finances permitted. In terms of the wider district, these two prospective areas are relatively close to the Troulli inlier. Therefore, district scale geophysical surveys that linked

these two areas with the Troulli inlier, which also has recorded mineral deposits, would be an extremely valuable pre-competitive data resource as it would potentially contain information enabling the identification of buried mineral deposits. In addition, this region is only partially covered by the EMM helicopter survey and would therefore represent new data.

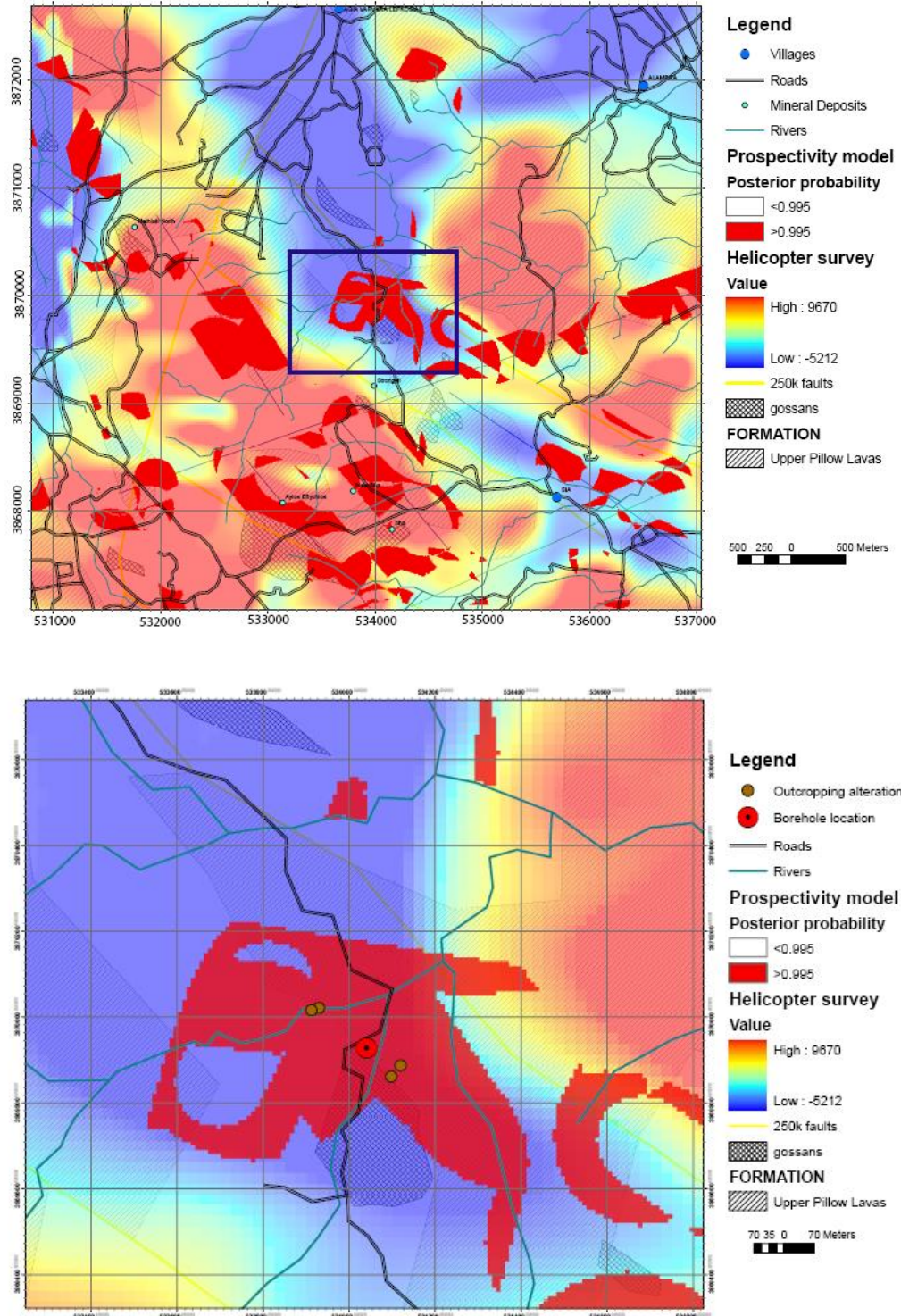


Figure 160 Location of prospectivity anomaly close to village of Strongyli with indicated site for a possible borehole

*Area F* is closely associated with the northern limits of the Arakapas Transform Fault. In the prospectivity analysis, all types of sulphide mineralisation were included in the investigation. Therefore, considering its proximity to the Arakapas Transform Zone, the zones of high prospectivity may represent Limassol Forest-style Cu-Co-Ni mineralisation rather than Cyprus-type VHMS. Unless the focus of exploration activity changes from copper to Ni and/or Co, this area is probably not a high priority.

*Areas G and H* are located on the southern limb of the ophiolite. Generally, speaking the majority of discovered mineralisation is located to the north. Though mineralisation is known on the southern limb, it is not as widespread. In addition the Limni area has produced metal. It is also important to note that in the southern portion of the ophiolite data coverage in a number of important themes is incomplete (gossans, small scale geology–structure) or absent (and high-resolution geophysics). Therefore, the general low prospectivity compared with the northern limb areas may be due to poor data support rather than because of geological reasons. In the context of additional geographically focussed geophysical surveys, with the lack of background information it would be difficult to prioritize regions on the southern limb of ophiolite. However, this should not negate the importance of this area—indeed an airborne geophysical survey, similar in scope and scale to the EMM helicopter survey could reveal significant information regarding mineralisation potential.

Thus, if a low risk priority area to compliment existing information is required then this should be a region that links at least Area D, and preferably Areas D and E, with the Troulli inlier. Second priority should be to gain high resolution geophysical information on the southern limb of the ophiolite. However, this would require careful examination of existing data linked to an analysis of current and future exploration market conditions to decide an appropriate area for a focussed study.

### **13.2.2 Additional GIS techniques**

In terms of additional GIS techniques, a fuzzy logic approach—also possible through Arc SDM—may well be useful as both a stand-alone project, and as a comparison to the Weights of Evidence model produced in this project. Unlike Weights of Evidence modelling, no known occurrences are needed for use as training points as the model is expert driven—therefore this methodology could be used to target mineralization under cover. Also, instead of using binary maps, where areas have either true or false membership of the class (i.e. they are considered as either prospective or non-prospective), fuzzy logic uses a continuous form of classification, where areas can be defined from prospective to non-prospective, and anywhere in between the two end-member values. The key to a successful fuzzy logic prospectivity analysis is the a comprehensive explanation of the steps required to undertake full-scale and detailed fuzzy logic analyses is beyond the scope of this report. However, the methodology behind fuzzy logic approach is given in Chapter 9 of the following publication:

G.F. Bonham-Carter (2002) *Geographic Information Systems for Geoscientists: Modelling with GIS (Computer Methods in the Geosciences Vol 13)* Elsevier Science Inc. New York, 398 p.

At the start of the project Arc SDM was only available for ArcGIS 3.2. It is now available for the most recent version of ERSI GIS software ArcGIS 9.1, the main GIS platform used at the Geological Survey Department, and can be downloaded, with

full documentation (including the above reference), without charge from the following website located at the Instituto de Geociências - Universidade Estadual de Campinas – UNICAMP R. João Pandiá Calógeras, 51, CEP: 13083-870 Brazil

<http://www.ige.unicamp.br/sdm>

Assuming the Geological Survey Department has access to ArcVIEW 3.x or ArcGIS 9.x produced by ESRI, the above website contains all the necessary software, and instructions to undertake a fuzzy logic prospectivity analysis. Use of the software in publications requires reference to the following:

Sawatzky, D.L., Raines, G.L., Bonham-Carter, G.F., and Looney, C.G., 2004, *ARCSDM3.1: ArcMAP extension for spatial data modelling using weights of evidence, logistic regression, fuzzy logic and neural network analysis*. <http://www.ige.unicamp.br/sdm/ARCSDM31/>.

As a guide to undertaking prospectivity analysis,

Lastly, it is important to stress that the same problems regarding geochemical and geophysical support for the weights of evidence models described in Chapters 11 and 12 would still be present in the data used for the fuzzy logic approach, a possibly fundamental problem that, as already stated, is probably best addressed through new data acquisitions.

### **13.2.3 New remote sensing data**

The ASTER data and imagery also proved to be a highly valuable resource, especially when compared to the older Landsat TM data, which was also used in the regional GIS. The precision given by the ASTER platforms higher spatial resolution, narrower bandwidths and larger array of wavelength coverage meant that any band ratio images created using this data was of far higher value than any Landsat imagery. To progress this further successful applications were made to fly an airborne remote sensing surveys over the northern margin of the Troodos and around the Paphos area—this was additional to the original project specifications and free of charge—the surveys were equivalent to a grant in kind worth approximately UK£30,000. This produced, for Cyprus, a nationally important high-resolution (1.5 m) spectral surveys and digital elevation models. Unfortunately, data delivery was not until close to the end of the Cu metallogeny project. The data will be extremely useful as pre-competitive mineral exploration information. In particular the high resolution digital elevation model (the LiDAR data) could be used to help target supergene copper deposits suitable for SX-EW hydrometallurgical treatment. In addition, the ability of the LiDAR and high-resolution spectral data to map mine waste means they are an enormously important resource for mine waste assessment and remediation. If possible, perhaps through the Cyprus Research Foundation, resources should be made available to process and interpret this information in a geo-environmental context.

# References

Most of the references listed below are held in the Library of the British Geological Survey at Keyworth, Nottingham. Copies of the references may be purchased from the Library subject to the current copyright legislation.

- Abrams M, Hook S, Ramachandran B (2002) *ASTER User Handbook Version 2*. Jet Propulsion Laboratory, California Institute of Technology.
- Adamides N (1990) Hydrothermal circulation and ore deposition in the Troodos Ophiolite, Cyprus In: Malpas J, Moores EM, Panayiotou A, Xenophontos C (eds) *Ophiolites; oceanic crustal analogues; proceedings of the symposium "Troodos 1987"*. Minist. Agric. and Nat. Resour., Nicosia, Cyprus, pp 685-704.
- Adamides N (2004) Notes on the geology of the Mavrovouni deposits Unpublished Report to Hellenic Copper Mines Ltd. pp 12.
- Adamides NG (1980) The form and environment of formation of the Kalavassos ore deposits, Cyprus In: Panayiotou A (ed) *Ophiolites; Proceedings, International ophiolite symposium*. Cyprus, Minist. Agric. Nat. Resour., Geol. Surv. Dep., Nicosia, Cyprus, pp 117-127.
- Agterberg FP, Bonham CGF, Cheng Q, Wright DF (1993) Weights of evidence modeling and weighted logistic regression for mineral potential mapping In: Davis John C, Herzfeld Ute C (eds) *Computers in geology; 25 years of progress*. Oxford University Press, New York-Oxford, United States, pp 13-32.
- Agterberg FP, Bonham CGF, Wright DF (1990) Statistical pattern integration for mineral exploration In: Gaal G, Merriam Daniel F (eds) *Computer applications in resource estimation; prediction and assessment for metals and petroleum*. Pergamon, Oxford-New York, International, pp 1-21.
- Asadi HH, Hale M (2001) A predictive GIS model for mapping potential gold and base metal mineralization in Takab area, Iran. *Comput. Geosci.* 27: 901-912.
- Bagnall BS (1960) The geology and mineral resources of the Pano Lefkara-Larnaca area Geological Survey Department, Cyprus, Nicosia, pp 122.
- Bailey S (1980) Crystal structures of clay minerals and their X-ray identification In: Brindley G, G B (eds) *Structures of layer silicates*. pp 1-124.
- Barrie CT, Cathles LM, Erendi A, Schwaiger H, Murray C (1999a) Heat and fluid flow in volcanic-associated massive sulfide-forming hydrothermal systems In: Barrie CT, Hannington Mark D (eds) *Volcanic-associated massive sulfide deposits; processes and examples in modern and ancient settings*. Society of Economic Geologists, Socorro, NM, United States, pp 201-219.
- Barrie CT, Hannington MD (1999) Classification of volcanic-associated massive sulfide deposits based on host-rock composition In: Barrie CT, Hannington Mark D (eds) *Volcanic-associated massive sulfide deposits; processes and examples in modern and ancient settings*. Society of Economic Geologists, Socorro, NM, United States, pp 1-11.
- Barrie CT, Hannington MD, Bleeker W (1999b) The giant Kidd Creek volcanic-associated massive sulfide deposit, Abitibi Subprovince, Canada In: Barrie CT, Hannington Mark D (eds) *Volcanic-associated massive sulfide deposits; processes and examples in modern and ancient settings*. Society of Economic Geologists, Socorro, NM, United States, pp 247-269.
- Bear LM (1960) The geology and mineral resources of the Akaki-Lythrodondha area Geological Survey Department, Cyprus, Nicosia, pp 122.
- Bear LM (1963) The mineral resources and mining industry of Cyprus. Geological Survey Department, Nicosia, Cyprus.
- Bear LM (1995) Geological map of Cyprus, 1:250 000 Geological Survey Department, Cyprus, Nicosia.
- Bear LM, Morel SW (1960) The geology and mineral resources of the Agro-Akrotiri area Geological Survey Department, Cyprus, Nicosia, pp 88.
- Bebien J, Dautaj N, Shallo M, Turku I, Barbarin B (1997) Diversite des plagiogranites ophiolitiques; l'exemple albanais. *Comptes Rendus de l'Academie des Sciences, Serie II. Sciences de la Terre et des Planetes* 324: 875-882.
- Bednarz U, Brace T, Cann JR, Herzig PM, Jamieson HE, Lydon JW, Malpas J (1987) Major element and trace element analytical Data: Cyprus crustal study project hole CY2-2a In: Robinson PT, Gibson IL, Panayiotou A (eds) *Cyprus crustal study project: Initial report, holes CY-2 and 2a*. Geological survey of Canada, Ottawa, pp 353-381.
- Bickle MJ, Teagle DAH, Beynon J, Chapman HJ (1998) The structure and controls on fluid-rock interactions in ocean ridge hydrothermal systems; constraints from the Troodos Ophiolite In: Mills RA, Harrison K (eds) *Modern ocean floor processes and the geological record*. Geological Society of London, London, United Kingdom, pp 127-152.

- Bodnar R (1993) Revised equation and table for determining the freezing point depression of H<sub>2</sub>O-NaCl solutions. *Geochemica et Cosmochemica Acta* 57: 683-684.
- Bonham-Carter GF, Agterberg FP, Wright DF (1989) Weights of Evidence Modelling :a new approach to mapping mineral potential In: Agterberg FP, Bonham Carter GF (eds) *Statistical Applications in the Earth Sciences*. Geological Survey of Canada, pp 171-183.
- Bonham-Carter GF, Agterberg FP, Wright DF (1990) Integration of geological datasets for gold exploration in Nova Scotia In: Pequet Donna J, Marble Duane F (eds) *Introductory readings in geographic information systems*. Taylor & Francis, London, United Kingdom, pp 170-182.
- Booij E, Bettison-Varga L, Farthing D, Staudigel H (2000) Pb-isotope systematics of a fossil hydrothermal system from the Troodos ophiolite, Cyprus: Evidence for a polyphased alteration history. *Geochim. Cosmochim. Acta* 64: 3559-3569.
- Boyle JF (1990) The composition and origin of oxide metalliferous sediments from the Troodos Ophiolite, Cyprus In: Malpas J, Moores EM, Panayiotou A, Xenophontos C (eds) *Ophiolites; oceanic crustal analogues; proceedings of the symposium "Troodos 1987"*. Minist. Agric. and Nat. Resour., Nicosia, Cyprus, pp 705-717.
- Carr JM, Bear LM (1960) The geology and mineral resources of the Peristerona-Lagoudhera area Geological Survey Department, Cyprus, Nicosia, pp 78.
- Collins M, Kofluk D (1998) Hydrometallurgical process for the extraction of copper from sulphide concentrates, US Patent, 5,730,776, March 24, 1998.
- Constantinides CC, Kingston GA, Fisher PC (1980) The occurrence of platinum group minerals in the chromitites of the Kokkinorotsos chrome mine, Cyprus In: Panayiotou A (ed) *Ophiolites; Proceedings, International ophiolite symposium*. Cyprus, Minist. Agric. Nat. Resour., Geol. Surv. Dep., Nicosia, Cyprus, pp 93-101.
- Constantinou G (1980) Metallogensis associated with the Troodos Ophiolite In: Panayiotou A (ed) *Ophiolites; Proceedings, International ophiolite symposium*. Cyprus, Minist. Agric. Nat. Resour., Geol. Surv. Dep., Nicosia, Cyprus, pp 663-674.
- Constantinou G, Govett G (1973) Geology, Geochemistry, and Genesis of Cyprus Sulfide Deposits. *Economic Geology* 68: 843-858.
- Cooke DR, Simmons SF (2000) Characteristics and genesis of epithermal gold deposits In: Hagemann SG, Brown PE (eds) *Gold in 2000*. Society of Economic Geologists, INC., Boulder, USA, pp 221-244.
- Corrans I, Angove J (1993) Activation of a mineral species, Australian Patent 663525, April 29, 1993.
- Cowan J, Cann JR (1988) Supercritical two-phase separation of hydrothermal fluids in the Troodos ophiolite. *Nature* 333: 259-261.
- Cox DP, Singer DA (1986) Mineral deposit models. U. S. Geological Survey, Reston, VA, United States.
- Date J, Watanabe Y, Saeki Y (1983) Zone alteration around the Fukazawa Kuroko deposits, Akita Prefecture, northern Japan. *Economic Geology Monograph* 5.
- Dilek Y, Moores EM (1990) Regional tectonics of the eastern Mediterranean ophiolites In: Malpas J, Moores EM, Panayiotou A, Xenophontos C (eds) *Ophiolites; oceanic crustal analogues; proceedings of the symposium "Troodos 1987"*. Minist. Agric. and Nat. Resour., Nicosia, Cyprus, pp 295-309.
- Evans AM (1980) An introduction to ore geology. Blackwell Sci., Oxford, United Kingdom.
- Flower MFJ, Russo RM, Tamaki K, Hoang N (2001) Mantle contamination and the Izu-Bonin-Mariana (IBM) "high-tide mark"; evidence for mantle extrusion caused by Tethyan closure In: Lallemand S, Liu Char S, Angelier J, Tsai YB (eds) *Active subduction and collision in Southeast Asia (SEASIA)*. Elsevier. Amsterdam, Netherlands. 2001.
- Franklin J, Gibson H, Jonasson I, Galley A (2005) Volcanogenic massive sulfide deposits. *Economic Geology* 100th Anniversary Volume: 523-560.
- Fraser SJ, Camuti K, Huntingto JF, Cuff C (1990) A study of superficial clay distribution at Mount Leyshon: a comparison between XRD and spectral reflectance methods Proceedings of the Fifth Australian Remote Sensing Conference. pp 906-914.
- Galley AG, Koski RA (1999) Setting and characteristics of ophiolite-hosted volcanogenic massive sulfide deposits In: Barrie CT, Hannington Mark D (eds) *Volcanic-associated massive sulfide deposits; processes and examples in modern and ancient settings*. Society of Economic Geologists, Socorro, NM, United States, pp 221-246.
- Garfunkel Z (1998) Constrains on the origin and history of the Eastern Mediterranean basin. *Tectonophysics* 298: 5-35.
- Gass IG (1960) The geology and mineral resources of the Dhali area Geological Survey Department, Cyprus, Nicosia, pp 116.
- Gass IG (1980) The Troodos Massif; its role in the unravelling of the ophiolite problem and its significance in the understanding of constructive plate margin processes In: Panayiotou A (ed) *Ophiolites; Proceedings, International ophiolite symposium*. Cyprus, Minist. Agric. Nat. Resour., Geol. Surv. Dep., Nicosia, Cyprus, pp 23-35.

- Gass IG (1990) Ophiolites and oceanic lithosphere In: Malpas J, Moores EM, Panayiotou A, Xenophontos C (eds) Ophiolites; oceanic crustal analogues; proceedings of the symposium "Troodos 1987". Minist. Agric. and Nat. Resour., Nicosia, Cyprus, pp 1-10.
- Gass IG, MacLeod CJ, Murton BJ, Panayiotou A, Simonian KO, Xenophontos C (1994) The geology of the southern Troodos transform fault zone. Ministry of Agriculture and Natural Resources, Geological Survey Department, Nicosia, Cyprus.
- Gass IG, Masson-Smith D (1963) The geology and gravity anomalies of the Troodos massif, Cyprus. Philosophical Transactions of the Royal Society of London, Series A: Mathematical and Physical Sciences 255: 417-467.
- Gass IG, Masson-Smith DJ (1951) The geology and gravity anomalies of the Troodos Massif, Cyprus Overseas Geological Surveys, London.
- Gibson HL, Morton RL, Hudak GJ (1999) Submarine volcanic processes, deposits, and environments favorable for the location of volcanic-associated massive sulfide deposits In: Barrie CT, Hannington Mark D (eds) Volcanic-associated massive sulfide deposits; processes and examples in modern and ancient settings. Society of Economic Geologists, Socorro, NM, United States, pp 13-51.
- Gillis KM, Robinson PT (1990a) Multistage alteration in the extrusive sequence of the Troodos Ophiolite, Cyprus In: Malpas J, Moores EM, Panayiotou A, Xenophontos C (eds) Ophiolites; oceanic crustal analogues; proceedings of the symposium "Troodos 1987". Minist. Agric. and Nat. Resour., Nicosia, Cyprus, pp 655-664.
- Gillis KM, Robinson PT (1990b) Patterns and processes of alteration in lavas and dykes of the Troodos ophiolite, Cyprus. Journal of Geophysical Research 95: 21.523-521.548.
- Gunn AG, Rollin KE (2000) Exploration methods and new targets for epithermal gold mineralisation in the Devonian rocks of Northern Britain BGS Research Report RR/00/08. British Geological Survey, Nottingham, pp 1-95.
- Hannington M, Poulsen K, Thompson J, Sillitoe R (1999) Volcanogenic gold in the massive sulphide environment. In: Barrie C, Hannington M (eds) Volcanic-associated Massive Sulfide Deposits; Processes and Examples in Modern and Ancient Settings. Society of Economic Geologists, pp 325-356.
- Hannington MD, Galley AG, Herzig PM, Petersen S, Ocean Drilling Program L, Shipboard Scientific Party, College Station, Tx, United States, (1998) Comparison of the TAG mound and stockwork complex with cyprus-type massive sulfide deposits In: Herzig Peter M, Humphris Susan E, Miller DJ, Alt Jeffrey C, Becker K, Brown D, Bruegmann Gerhard E, Chiba H, Fouquet Y, Gemmel JB, Guerin G, Hannington Mark D, Holm Nils G, Honnorez Jose J, Iturrino Gerardo J, Knott R, Ludwig Rainer J, Nakamura Ko i, Petersen S, Reysenbach Anna L, Rona Peter A, Smith Susan E, Sturz Anne A, Tivey Margaret K, Zhao X, Riegel Ruth N (eds) Proceedings of the Ocean Drilling Program, scientific results, TAG, drilling an active hydrothermal system on a sediment-free slow-spreading ridge; covering Leg 158 of the cruises of the drilling vessel JOIDES Resolution, Las Palmas, Gran Canaria, to Las Palmas, Gran Canaria, Site 957, 23 September-22 November 1994. Texas A & M University, Ocean Drilling Program, College Station, TX, United States, pp 389-415.
- Hannington MD, Tivey MK, Larocque ACL, Petersen S, Rona P (1995) The occurrence of gold in sulphide deposits of the TAG hydrothermal field, Mid-Atlantic Ridge. Canadian Mineralogist 33: 1285-1310.
- Harper GD (1999) Structural styles of hydrothermal discharge in ophiolite/ sea-floor systems In: Barrie CT, Hannington Mark D (eds) Volcanic-associated massive sulfide deposits; processes and examples in modern and ancient settings. Society of Economic Geologists, Socorro, NM, United States, pp 53-73.
- Hedenquist J, Izawa E, Arribas J, A, White N (1996) Epithermal gold deposits; styles, characteristics and exploration Society of Resource Geology; Resource Geology Special publication.
- Hedenquist JW (2000) Gold exploration in the Troodos ophiolite, Cyprus Hedenquist Consulting Inc. for Eastern Mediterranean Minerals (Cyprus) Ltd., pp 11.
- Herrington R, Maslennikov V, Zaykov V, Seravkin I, Kosarev A, Buschmann B, Orgeval J-J, Holland N, Tesalina S, Nimis P, Armstrong R (2005) 6: Classification of VMS deposits: Lessons from the South Uralides. Ore Geology Reviews 27: 203-237.
- Herzig PM, Hannington MD, Fouquet Y, Stackelberg UV, Petersen S (1993) Gold-rich polymetallic sulphides from the Lau back arc and implications for the geochemistry of gold in sea-floor hydrothermal systems of the southwest Pacific. Economic Geology 88: 2182-2209.
- Horan M (1996) Atmospheric mineral leaching process, Australian Patent, 9649331, September, 26, 1996
- Hoy T (1995a) Cyprus massive sulphide Cu (Zn) In: Lefebure David V, Ray Gerald E (eds) Selected British Columbia mineral deposit profiles. British Columbia Ministry of Energy, Mines and Petroleum Resources, Vancouver, BC, Canada, pp 49-50.
- Hoy T (1995b) Noranda/ Kuroko massive sulphide Cu-Pb-Zn In: Lefebure David V, Ray Gerald E (eds) Selected British Columbia mineral deposit profiles. British Columbia Ministry of Energy, Mines and Petroleum Resources, Vancouver, BC, Canada, pp 51-52.

- Huston DL (2000) Gold in volcanic-hosted massive sulfide deposits: Distribution, genesis, and exploration In: Hagemann SG, Brown PE (eds) Gold in 2000. Society of Economic Geology, Boulder, USA, pp 401-426.
- Ishikawa Y, Sawaguchi T, Iwaya S, Horiuchi M (1976) Delineation of prospecting targets for Kuroko deposits based on modes of volcanism of underlying dacite and alteration haols. *Mining Geology* 26: 105-117.
- Janissen K (1988) Investigation of decrepitation activity, fluid inclusions and alteration minerals in the Alestos sulphide deposit, Cyprus. (in German) Aachen University of Technology, Germany, pp 256.
- Jowitt S (2003) The Potential for Copper Mineralisation on Cyprus: A GIS based Methodology Cambourne School of Mines, Exeter University, pp 209.
- King J (1997) US Patent No. 5,698,170.
- Loukola-Ruskeeniemi K (1999) Origin of black shales and serpentinite-associated Cu-Zn-Co ores at Outukumpu, Finland. *Economic Geology* 94: 1007-1103.
- Luders V, Banks D, Halbach P (2002) Extreme Cl/Br and del37Cl isotope fractionation in fluids of modern submarine hydrothermal systems. *Mineralium Deposita* 37: 765-771.
- Maliotis G, Herzig PM (2000) Potential for epithermal-style gold mineralization in the Troodos ophiolite, Cyprus Confidential company report, Eastern Mediterranean Minerals (Cyprus) Ltd., pp 8.
- Malpas J (1987) The geology and geophysics of the area surrounding the CY-2 and CY-2a drill holes of the Cyprus crustal study project In: Robinson PT, Gibson IL, Panayiotou A (eds) Cyprus crustal study project: Initial report, holes CY-2 and CY-2a. Geological Survey of Canada, Ottawa, pp 19-28.
- Marumo K (1989) Genesis of kaolin minerals and pyrophyllite in Kuroko deposits of Japan: Implications for the origins of the hydrothermal fluids from mineralogical and stable isotope data. *Geochim. Cosmochim. Acta* 53: 2915-2924.
- Michalski B (1998) The Mineral Industry of Cyprus In: Anonymous (ed) United States Geological Survey: Minerals Yearbook. United States Geological Survey, Reston, Virginia.
- Milsom J (1989) Field Geophysics. Open University Press, Milton Kenes.
- Mobbs PM (2000) The Mineral Industry of Cyprus In: Anonymous (ed) United States Geological Survey: Minerals Yearbook. United States Geological Survey, Reston, Virginia.
- Mobbs PM (2001) The Mineral Industry of Cyprus In: Anonymous (ed) United States Geological Survey: Minerals Yearbook. United States Geological Survey, Reston, Virginia.
- Moore TA (1960) The geology and mineral resources of the Astromeritis-Kormakiti area Geological Survey Department, Nicosia, pp 96.
- Moores EM, Vine FJ (1971) Troodos Massif, Cyprus and other ophiolites as oceanic crust - evaluation and implications. *Philosophical Transactions of the Royal Society of London Series a-Mathematical and Physical Sciences* 268: 443-&.
- Murphy P, Meyer G (1998) A gold-copper association in ultramafic hosted hydrothermal sulfides from the Mid-Atlantic Ridge. *Economic Geology* 93.
- Naldrett A (1981) Nickel sulphide deposits: classification, composition and genesis. *Economic Geology* 75th Anniversary Volume: 628-685.
- NASA (2003) National Aeronautics and Space Administration: Advanced Spaceborne Thermal Emission and Reflection Radiometer Homepage <http://asterweb.jpl.nasa.gov/>.
- Nillos TEP, Elipane BR (1998) Redhills (Kokkinovounaros) prospect. Preliminary report on the two week grid rock chip sampling and mapping and data review Confidential Company Report, Eastern Mediterranean Minerals (Cyprus) Ltd., pp 18.
- Nillos TEP, Elipane BR, Gough J (1998a) Alestos prospect. Preliminary report on the two-week grid rock chip sampling and mapping Confidential Company Report, Eastern Mediterranean Minerals (Cyprus) Ltd, pp 7.
- Nillos TEP, Elipane BR, Gough J (1998b) Papoutsi Prospect. Preliminary report on the one-week grid rock chip sampling and mapping Confidential Company Report, Eastern Mediterranean Mining (Cyprus) Ltd., pp 6.
- Nillos TEP, Elipane BR, Gough J (1998c) Tounounja prospect. Preliminary report on the one-week grid rock chip sampling and mapping. Confidential Company Report, Eastern Mediterranean Minerals (Cyprus) Ltd., pp 7.
- Nillos TEP, Elipane BR, Gough J (1998d) Tourounja prospect. Preliminary report on the one-week grid rock chip sampling and mapping. Confidential Company Report, Eastern Mediterranean Minerals (Cyprus) Ltd., pp 7.
- Nimis P, Tesalina S, Omenetto P, Tartarotti P, Lerouge C (2004) Phyllosilicate minerals in the hydrothermal mafic-ultramafic-hosted massive-sulfide deposit of Ivanovka (Southern Urals); comparison with modern ocean seafloor analogues. *Contributions to Mineralogy and Petrology* 147: 363-383.
- Osborn R (2004) The application of short wavelength infrared spectroscopy to characterise typical and atypical alteration in Cyprus-type VHMS deposits. University of Exeter, pp 122.

- Panayiotou A (1980) Cu-Ni-Co-Fe sulphide mineralization, Limassol Forest, Cyprus In: Panayiotou A (ed) Ophiolites; Proceedings, International ophiolite symposium. Cyprus, Minist. Agric. Nat. Resour., Geol. Surv. Dep., Nicosia, Cyprus, pp 102-116.
- Pantazis TM (1967) The geology and mineral resources of the Pharmakas-Kalavassos area Geological Survey Department, Cyprus, pp 190.
- Peacey J, Guo X, Robles E (2003) Copper hydrometallurgy – current status, preliminary economics, future direction and positioning versus smelting Copper 2003. Santiago, Chile.
- Peter JM, Scott SD (1999) Windy Craggy, northwestern British Columbia; the world's largest beshi-type deposit In: Barrie CT, Hannington Mark D (eds) Volcanic-associated massive sulfide deposits; processes and examples in modern and ancient settings. Society of Economic Geologists, Socorro, NM, United States, pp 261-295.
- Peterson S, Herzig P, Hannington M (2000) Third dimension of a presently forming VMS deposit, TAG hydrothermal mound, Mid-Atlantic Ridge, 26N. Miner. Depos. 35: 233-259.
- Pontual S, Merry N, Cocks T (1995) Feild-based alteration mapping using the PIMA In: Mauk JL, St George JD (eds) Proceedings of the 1995 PACRIM congress; Exploring the rim. Australasian Institute of Mining and Metallurgy, Victoria, pp 479-484.
- Pontual S, Merry N, Gamson P (1997a) G-MEX Version 1.0: Spectral Interpretation Field Manual. AusSpec International Pty. Ltd.
- Pontual S, Merry N, Gamson P (1997b) Spectral interpretation field manual: Spectral analysis guides for mineral exploration. AusSpec International Pty. Ltd.
- Poulsen KH, Hannington MD (1995) Volcanic-associated massive sulfide gold. Geology of Canada.
- Prichard HM, Maliotis G (1998) Gold mineralization associated with low-temperature, off-axis, fluid activity in the Troodos ophiolite, Cyprus. J. Geol. Soc. 155: 223-231.
- Richards HG, Cann JR, Jensenius J (1989) Mineralogical zonation and metasomatism of the alteration pipes of Cyprus sulfide deposits. Economic Geology 84: 91-115.
- Richardson CJ, Cann JR, Richards HG, Cowan JG (1987) Metal-depleted root zones of the Troodos ore-forming hydrothermal systems, Cyprus. Earth and Planetary Science Letters 84: 243-253.
- Robertson AFH, Rigby S, Dixon J (2003a) Honours Geology and GPG excursion to Cyprus: Feild guide Edinburgh University School of Geosciences, pp 1-60.
- Robertson AHF (1978) Metallogenesis along a fossil oceanic fracture zone; Arakapas fault belt, Troodos Massif, Cyprus. Earth and Planetary Science Letters 41: 317-329.
- Robertson AHF (1990) Tectonic evolution of Cyprus In: Malpas J, Moores EM, Panayiotou A, Xenophontos C (eds) Ophiolites; oceanic crustal analogues; proceedings of the symposium "Troodos 1987". Minist. Agric. and Nat. Resour., Nicosia, Cyprus, pp 235-250.
- Robertson AHF (1998) Tectonic significance of the Eratosthenes Seamount; a continental fragment in the process of collision with a subduction zone in the eastern Mediterranean (Ocean Drilling Program Leg 160) In: Robertson Alastair HF, Comas Menchu C (eds) Collision-related processes in the Mediterranean region. Elsevier, Amsterdam, Netherlands, pp 63-82.
- Robertson AHF (2000) Tectonic evolution of Cyprus in its easternmost Mediterranean setting In: Panayides I, Xenophontos C, Malpas J (eds) Proceedings of the Third international conference on the Geology of the eastern Mediterranean. Ministry of Agriculture, Natural Resources and Environment, Geological Survey Department. Nicosia, Cyprus. 2000.
- Robertson AHF (2002) Overview of the genesis and emplacement of Mesozoic ophiolites in the Eastern Mediterranean Tethyan region. Lithos 65: 1-67.
- Robertson AHF, Degnan P (1998) Significance of modern and ancient oceanic Mn-rich hydrothermal sediments, exemplified by Jurassic Mn-cherts from southern Greece In: Mills RA, Harrison K (eds) Modern ocean floor processes and the geological record. Geological Society of London, London, United Kingdom, pp 217-240.
- Robertson AHF, Dixon JE, Rigby S, Boulton S, Rice S (2003b) Edinburgh University School of Geosciences Honours Geology and GPG excursion to Cyprus Field Guide. Edinburgh University School of Geosciences, Edinburgh.
- Robertson AHF, Woodcock NH (1980) Tectonic setting of the Troodos Massif in the East Mediterranean In: Panayiotou A (ed) Ophiolites; Proceedings, International ophiolite symposium. Cyprus, Minist. Agric. Nat. Resour., Geol. Surv. Dep., Nicosia, Cyprus, pp 36-49.
- Robertson AHF, Xenophontos C (1997) Cyprus In: Moores Eldridge M, Fairbridge Rhodes W (eds) Encyclopedia of European and Asian regional geology. Chapman & Hall, London, United Kingdom, pp 160-171.
- Robinson PT, Gibson IL (1987) Cyprus crustal study project. Hole CY-2a lithologic unit summaries In: Robinson PT, Gibson IL, Panayiotou A (eds) Cyprus Crustal Study Project: Initial report, holes CY-2 and 2a. Geological survey of Canada, Ottawa, pp 45-56.
- Robinson PT, Hall JM (1983) Hydrothermal circulation and base metal sulfide deposition in oceanic crust; results of research drilling in the Agrokipia ore deposits, Cyprus Geological Association of Canada;

- Mineralogical Association of Canada; Canadian Geophysical Union; joint annual meeting. Geological Association of Canada, Waterloo, ON, Canada, pp A58.
- Robinson PT, Malpas J (1990) The Troodos Ophiolite of Cyprus; new perspectives on its origin and emplacement In: Malpas J, Moores EM, Panayiotou A, Xenophontos C (eds) Ophiolites; oceanic crustal analogues; proceedings of the symposium "Troodos 1987". Minist. Agric. and Nat. Resour., Nicosia, Cyprus, pp 13-26.
- Sabins FF (1999) Remote sensing for mineral exploration. *Ore Geology Reviews* 14: 157-183.
- Sillitoe R (1993) Epithermal models: genetic types, geometrical controls and shallow features In: Kirkham R, Sinclair W, Thorpe R, Duke J (eds) *Mineral Deposit Modeling*. pp 403-417.
- Sillitoe RH, Hannington MD, Thompson JFH (1996) High sulfidation deposits in the volcanogenic massive sulfide environment. *Economic Geology and the Bulletin of the Society of Economic Geologists* 91: 204-212.
- Singer DA, Mosier DL (1986) Grade and tonnage model of Cyprus massive sulfide In: Cox Dennis P, Singer Donald A (eds) *Mineral deposit models*. U. S. Geological Survey, Reston, VA, United States, pp 131-135.
- Spooner ETC, Bray CJ, Chapman HJ (1977) A sea water source for the hydrothermal fluid which formed the ophiolitic cupriferous pyrite ore deposits of the Troodos Massif, Cyprus. *Journal of the Geological Society of London* 134 Part 3: 395.
- Swarbrick RE (1980) The Mamonnia Complex of S.W. Cyprus; a Mesozoic continental margin and its relationship to the Troodos Complex In: Panayiotou A (ed) *Ophiolites; Proceedings, International ophiolite symposium*. Cyprus, Minist. Agric. Nat. Resour., Geol. Surv. Dep., Nicosia, Cyprus, pp 86-92.
- Tangestani MH, Moore F (2001) Porphyry copper potential mapping using the weights-of-evidence model in a GIS, northern Shahr-e-Babak, Iran. *Aust. J. Earth Sci.* 48: 695-701.
- Tesalina SG, Nimis P, Auge T, Zaykov VV (2003) Origin of chromite in mafic-ultramafic hosted hydrothermal massive sulfides from the Main Uralian Fault, South Urals, Russia., *Lithos* 70: 39-59.
- Thalhammer O, Stumpfl EF, Panayiotou A (1986) Postmagmatic, Hydrothermal Origin of Sulfide and Arsenide Mineralizations at Limassol Forest, Cyprus. *Miner. Depos.* 21: 95-105.
- Thomas R (2005) Evidence for low sulphidation epithermal mineralization in the Troodos ophiolite, Cyprus Imperial College of Science and Technology, pp 88.
- Tivey M, Mills R, Teagle D (1998) Temperature and salinity of fluid inclusions in anhydrite as indicators of seawater entrainment and heating in the TAG active mound In: Herzig P, Humphries S, Miller J (eds), pp 179-190.
- UnitedNationsDevelopmentFund (1970) *Survey of Groundwater and Mineral Resources, Cyprus*. United Nations, New York.
- Van Staden P (1998) The Mintek/Bactech copper bioleach process *Alta 1998 Copper Sulphide Symposium*, October, 1998. Brisbane, Australia
- Varga RJ, Moores EM (1990) Intermittent magmatic spreading and tectonic extension in the Troodos Ophiolite; implications for exploration for black smoker-type ore deposits In: Malpas J, Moores EM, Panayiotou A, Xenophontos C (eds) *Ophiolites; oceanic crustal analogues; proceedings of the symposium "Troodos 1987"*. Minist. Agric. and Nat. Resour., Nicosia, Cyprus, pp 53-64.
- Wessel P, Smith W (1991) Free software helps map and display data. *EOS Transactions of the American Geophysical Union* 72: 441.
- Wilson RAM (1959) *The geology of the Xeros-Troodos area*.
- Wilson RAM, Ingham FT (1959) *The geology of the Xeros-Troodos area* Geological Survey Department, Nicosia, pp 184.

## Appendix 1 Copper mineralization associated mineral occurrences in Cyprus

ID	Name	Easting	Northing	Type of Mineralization	Source of Data
1	Umber Old Working	538686	3872369	Umber Pigment, Old Working associated with sulphides	1:31,680 scale Memoirs and Map, 1950's
2	Umber Old Working	522394	3873445	Umber Pigment, Old Working associated with sulphides	1:31,680 scale Memoirs and Map, 1950's
3	Gold Old Working	489718	3883440	Formed Gold Working (Sulphide or Umber related)	1:31,680 scale Memoirs and Map, 1950's
4	Gold Old Working	485765	3881661	Formed Gold Working (Sulphide or Umber related)	1:31,680 scale Memoirs and Map, 1950's
5	Gold Old Working	527165	3867593	Formed Gold Working (Sulphide or Umber related)	1:31,680 scale Memoirs and Map, 1950's
6	Gold Old Working	531501	3867852	Formed Gold Working (Sulphide or Umber related)	1:31,680 scale Memoirs and Map, 1950's
7	Gold Old Working	531681	3870857	Formed Gold Working (Sulphide or Umber related)	1:31,680 scale Memoirs and Map, 1950's
8	Gold Old Working	533706	3867697	Formed Gold Working (Sulphide or Umber related)	1:31,680 scale Memoirs and Map, 1950's
9	Gold Old Working	534409	3867968	Formed Gold Working (Sulphide or Umber related)	1:31,680 scale Memoirs and Map, 1950's
10	Gold Old Working	523096	3850573	Formed Gold Working (Sulphide or Umber related)	1:31,680 scale Memoirs and Map, 1950's
11	Gold Old Working	522766	3850602	Formed Gold Working (Sulphide or Umber related)	1:31,680 scale Memoirs and Map, 1950's
12	Gold Old Working	509458	3877566	Formed Gold Working (Sulphide or Umber related)	1:31,680 scale Memoirs and Map, 1950's
13	Gold Old Working	501876	3876298	Formed Gold Working (Sulphide or Umber related)	1:31,680 scale Memoirs and Map, 1950's
14	Gold Old Working	510210	3876480	Formed Gold Working (Sulphide or Umber related)	1:31,680 scale Memoirs and Map, 1950's
15	Gold Old Working	513081	3877460	Formed Gold Working (Sulphide or Umber related)	1:31,680 scale Memoirs and Map, 1950's
16	Gold Old Working	524747	3872385	Formed Gold Working (Sulphide or Umber related)	1:31,680 scale Memoirs and Map, 1950's
17	Gold Old Working	523781	3870980	Formed Gold Working (Sulphide or Umber related)	1:31,680 scale Memoirs and Map, 1950's
18	Gold Old Working	535818	3856907	Formed Gold Working (Sulphide or Umber related)	1:31,680 scale Memoirs and Map, 1950's
19	Slag Dump	531106	3868141	Ancient Slag Dump	1:31,680 scale Memoirs and Map, 1950's
20	Slag Dump	531033	3867936	Ancient Slag Dump	1:31,680 scale Memoirs and Map, 1950's
21	Slag Dump	515905	3862540	Ancient Slag Dump	1:31,680 scale Memoirs and Map, 1950's
22	Slag Dump	524759	3862472	Ancient Slag Dump	1:31,680 scale Memoirs and Map, 1950's
23	Slag Dump	513527	3857311	Ancient Slag Dump	1:31,680 scale Memoirs and Map, 1950's
24	Slag Dump	524814	3850474	Ancient Slag Dump	1:31,680 scale Memoirs and Map, 1950's
25	Slag Dump	517629	3875386	Ancient Slag Dump	1:31,680 scale Memoirs and Map, 1950's
26	Slag Dump	511687	3878053	Ancient Slag Dump	1:31,680 scale Memoirs and Map, 1950's
27	Slag Dump	514198	3878100	Ancient Slag Dump	1:31,680 scale Memoirs and Map, 1950's
28	Slag Dump	521816	3867191	Ancient Slag Dump	1:31,680 scale Memoirs and Map, 1950's
29	Slag Dump	525270	3864669	Ancient Slag Dump	1:31,680 scale Memoirs and Map, 1950's
30	Slag Dump	525563	3869393	Ancient Slag Dump	1:31,680 scale Memoirs and Map, 1950's
31	Slag Dump	523113	3870887	Ancient Slag Dump	1:31,680 scale Memoirs and Map, 1950's
32	Slag Dump	518518	3873376	Ancient Slag Dump	1:31,680 scale Memoirs and Map, 1950's
33	Slag Dump	518984	3874696	Ancient Slag Dump	1:31,680 scale Memoirs and Map, 1950's

<b>ID</b>	<b>Name</b>	<b>Easting</b>	<b>Northing</b>	<b>Type of Mineralization</b>	<b>Source of Data</b>
34	Slag Dump	540841	3862299	Ancient Slag Dump	1:31,680 scale Memoirs and Map, 1950's
35	Slag Dump	534827	3856959	Ancient Slag Dump	1:31,680 scale Memoirs and Map, 1950's
36	Cu Old Workings	477569	3861860	Copper Sulphides	1:31,680 scale Memoirs and Map, 1950's
37	Cu Old Workings	516054	3862564	Copper Sulphides	1:31,680 scale Memoirs and Map, 1950's
38	Cu Old Workings	521732	3861275	Copper Sulphides	1:31,680 scale Memoirs and Map, 1950's
39	Cu Old Workings	521943	3860509	Copper Sulphides	1:31,680 scale Memoirs and Map, 1950's
40	Cu Old Workings	521666	3860165	Copper Sulphides	1:31,680 scale Memoirs and Map, 1950's
41	Cu Old Workings	521760	3860031	Copper Sulphides	1:31,680 scale Memoirs and Map, 1950's
42	Cu Old Workings	524436	3861575	Copper Sulphides	1:31,680 scale Memoirs and Map, 1950's
43	Cu Old Workings	513638	3854846	Copper Sulphides	1:31,680 scale Memoirs and Map, 1950's
44	Cu Old Workings	515309	3854935	Copper Sulphides	1:31,680 scale Memoirs and Map, 1950's
45	Cu Old Workings	517463	3855052	Copper Sulphides	1:31,680 scale Memoirs and Map, 1950's
46	Cu Old Workings	510668	3857239	Copper Sulphides	1:31,680 scale Memoirs and Map, 1950's
47	Cu Old Workings	512362	3857528	Copper Sulphides	1:31,680 scale Memoirs and Map, 1950's
48	Cu Old Workings	513438	3857522	Copper Sulphides	1:31,680 scale Memoirs and Map, 1950's
49	Cu Old Workings	512362	3863723	Copper Sulphides	1:31,680 scale Memoirs and Map, 1950's
50	Cu Old Workings	518834	3857017	Copper Sulphides	1:31,680 scale Memoirs and Map, 1950's
51	Cu Old Workings	516649	3845802	Copper Sulphides	1:31,680 scale Memoirs and Map, 1950's
52	Cu Old Workings	516364	3845570	Copper Sulphides	1:31,680 scale Memoirs and Map, 1950's
53	Cu Old Workings	519111	3845142	Copper Sulphides	1:31,680 scale Memoirs and Map, 1950's
54	Cu Old Workings	516138	3848322	Copper Sulphides	1:31,680 scale Memoirs and Map, 1950's
55	Pyrite Mine	534340	3867797	Pyrite, current working	1:31,680 scale Memoirs and Map, 1950's
56	Pyrite Mine	503194	3877299	Pyrite, current working	1:31,680 scale Memoirs and Map, 1950's
57	Pyrite Mine	501970	3876683	Pyrite, current working	1:31,680 scale Memoirs and Map, 1950's
58	Pyrite Mine	509671	3878471	Pyrite, current working	1:31,680 scale Memoirs and Map, 1950's
59	Pyrite Mine	513540	3878116	Pyrite, current working	1:31,680 scale Memoirs and Map, 1950's
60	Pyrite Mine	513199	3877978	Pyrite, current working	1:31,680 scale Memoirs and Map, 1950's
61	Pyrite Mine	510328	3876999	Pyrite, current working	1:31,680 scale Memoirs and Map, 1950's
62	Pyrite Mine	524709	3872719	Pyrite, current working	1:31,680 scale Memoirs and Map, 1950's
63	Pyrite Mine	523742	3871314	Pyrite, current working	1:31,680 scale Memoirs and Map, 1950's
64	Cu-Bearing Pyrite Mine	489718	3883537	Copper Sulphide, current working	1:31,680 scale Memoirs and Map, 1950's
65	Cu-Bearing Pyrite Mine	485703	3884496	Copper Sulphide	1:31,680 scale Memoirs and Map, 1950's
66	Cu-Bearing Pyrite Mine	485765	3881758	Copper Sulphide	1:31,680 scale Memoirs and Map, 1950's
67	Cu-Bearing Pyrite Mine	522097	3849253	Copper Sulphide	1:31,680 scale Memoirs and Map, 1950's
68	Cu-Bearing Pyrite Mine	522794	3850467	Copper Sulphide	1:31,680 scale Memoirs and Map, 1950's
69	Cu-Bearing Pyrite Mine	522277	3850113	Copper Sulphide	1:31,680 scale Memoirs and Map, 1950's
70	Cu-Bearing Pyrite Mine	523124	3850439	Copper Sulphide	1:31,680 scale Memoirs and Map, 1950's

<b>ID</b>	<b>Name</b>	<b>Easting</b>	<b>Northing</b>	<b>Type of Mineralization</b>	<b>Source of Data</b>
71	Cu-Bearing Pyrite Mine	523634	3850166	Copper Sulphide	1:31,680 scale Memoirs and Map, 1950's
72	Cu-Bearing Pyrite Mine	524624	3850329	Copper Sulphide	1:31,680 scale Memoirs and Map, 1950's
73	UN Sulphide Mine	453878	3875182	Sulphide, unclassified	UNRFNER Project, 1983
74	UN Sulphide Mine	453609	3876615	Sulphide, unclassified	UNRFNER Project, 1983
75	UN Sulphide Mine	455625	3876480	Sulphide, unclassified	UNRFNER Project, 1983
76	UN Sulphide Mine	455356	3877242	Sulphide, unclassified	UNRFNER Project, 1983
77	UN Sulphide Mine	522541	3849875	Sulphide, unclassified	UNRFNER Project, 1983
78	UN Sulphide Mine	523616	3850413	Sulphide, unclassified	UNRFNER Project, 1983
79	UN Sulphide Mine	524198	3850009	Sulphide, unclassified	UNRFNER Project, 1983
80	UN Sulphide Mine	524736	3849696	Sulphide, unclassified	UNRFNER Project, 1983
81	UN Sulphide Mine	525273	3850054	Sulphide, unclassified	UNRFNER Project, 1983
82	UN Sulphide Mine	533828	3867567	Sulphide, unclassified	UNRFNER Project, 1983
83	UN Sulphide Mine	531633	3868105	Sulphide, unclassified	UNRFNER Project, 1983
84	UN Sulphide Mine	531768	3870792	Sulphide, unclassified	UNRFNER Project, 1983
85	UN Sulphide Mine	524801	3872963	Sulphide, unclassified	UNRFNER Project, 1983
86	UN Sulphide Mine	523746	3871478	Sulphide, unclassified	UNRFNER Project, 1983
87	UN Sulphide Mine	522397	3872415	Sulphide, unclassified	UNRFNER Project, 1983
88	UN Sulphide Mine	521088	3872552	Sulphide, unclassified	UNRFNER Project, 1983
89	UN Sulphide Mine	513155	3878043	Sulphide, unclassified	UNRFNER Project, 1983
90	UN Sulphide Mine	514386	3878180	Sulphide, unclassified	UNRFNER Project, 1983
91	UN Sulphide Mine	502329	3876754	Sulphide, unclassified	UNRFNER Project, 1983
92	UN Sulphide Mine	503580	3877027	Sulphide, unclassified	UNRFNER Project, 1983
93	UN Sulphide Mine	510263	3876675	Sulphide, unclassified	UNRFNER Project, 1983
94	UN Sulphide Mine	509755	3877985	Sulphide, unclassified	UNRFNER Project, 1983
95	UN Sulphide Mine	485329	3884472	Sulphide, unclassified	UNRFNER Project, 1983
96	UN Sulphide Mine	485837	3881932	Sulphide, unclassified	UNRFNER Project, 1983
97	UN Sulphide Mine	490175	3883593	Sulphide, unclassified	UNRFNER Project, 1983
98	UN Reported Mineral Deposit	456824	3876638	Reported Sulphide Deposit, Unclassified	UNRFNER Project, 1983
99	UN Reported Mineral Deposit	456341	3875936	Reported Sulphide Deposit, Unclassified	UNRFNER Project, 1983
100	UN Reported Mineral Deposit	533852	3868917	Reported Sulphide Deposit, Unclassified	UNRFNER Project, 1983
101	Stockwork	512550	3846330	Sulphide Stockwork Mineralization, Worked	Metallogenic Map, GSD, 1983
102	Stockwork	557272	3876969	Sulphide Stockwork Mineralization, Worked	Metallogenic Map, GSD, 1983
103	Stockwork	541204	3858539	Sulphide Stockwork Mineralization, Worked	Metallogenic Map, GSD, 1983
104	Stockwork	452953	3877793	Sulphide Stockwork Mineralization, Worked	Metallogenic Map, GSD, 1983
105	Stockwork	453383	3876576	Sulphide Stockwork Mineralization, Worked	Metallogenic Map, GSD, 1983
106	Stockwork	501981	3877220	Sulphide Stockwork Mineralization, Worked	Metallogenic Map, GSD, 1983
107	Stockwork	502697	3877506	Sulphide Stockwork Mineralization, Worked	Metallogenic Map, GSD, 1983
108	Stockwork	510248	3876826	Sulphide Stockwork Mineralization, Worked	Metallogenic Map, GSD, 1983
109	Stockwork	513254	3876075	Sulphide Stockwork Mineralization, Worked	Metallogenic Map, GSD, 1983
110	Stockwork	521557	3872353	Sulphide Stockwork Mineralization, Worked	Metallogenic Map, GSD, 1983
111	Stockwork	524006	3866941	Sulphide Stockwork Mineralization, Worked	Metallogenic Map, GSD, 1983
112	Massive Sulphide	475499	3860507	Massive Sulphide Mineralization, Worked	Metallogenic Map, GSD, 1983
113	Massive Sulphide	470274	3864695	Massive Sulphide Mineralization, Worked	Metallogenic Map, GSD, 1983
114	Massive Sulphide	455673	3876540	Massive Sulphide Mineralization, Worked	Metallogenic Map, GSD, 1983
115	Massive Sulphide	455387	3877399	Massive Sulphide Mineralization, Worked	Metallogenic Map, GSD, 1983
116	Massive Sulphide	485913	3882123	Massive Sulphide Mineralization, Worked	Metallogenic Map, GSD, 1983
117	Massive Sulphide	490100	3883662	Massive Sulphide Mineralization, Worked	Metallogenic Map, GSD, 1983
118	Massive Sulphide	484589	3884771	Massive Sulphide Mineralization, Worked	Metallogenic Map, GSD, 1983
119	Massive Sulphide	509676	3878186	Massive Sulphide Mineralization, Worked	Metallogenic Map, GSD, 1983
120	Massive Sulphide	513039	3878258	Massive Sulphide Mineralization, Worked	Metallogenic Map, GSD, 1983

<b>ID</b>	<b>Name</b>	<b>Easting</b>	<b>Northing</b>	<b>Type of Mineralization</b>	<b>Source of Data</b>
121	Massive Sulphide	514328	3878365	Mineralization, Worked Massive Sulphide	Metallogenic Map, GSD, 1983
122	Massive Sulphide	519875	3875216	Mineralization, Worked Massive Sulphide	Metallogenic Map, GSD, 1983
123	Massive Sulphide	524921	3873033	Mineralization, Worked Massive Sulphide	Metallogenic Map, GSD, 1983
124	Massive Sulphide	522451	3872174	Mineralization, Worked Massive Sulphide	Metallogenic Map, GSD, 1983
125	Massive Sulphide	523811	3871601	Mineralization, Worked Massive Sulphide	Metallogenic Map, GSD, 1983
126	Massive Sulphide	531971	3870814	Mineralization, Worked Massive Sulphide	Metallogenic Map, GSD, 1983
127	Massive Sulphide	534011	3867593	Mineralization, Worked Massive Sulphide	Metallogenic Map, GSD, 1983
128	Massive Sulphide	522630	3849771	Mineralization, Worked Massive Sulphide	Metallogenic Map, GSD, 1983
129	Massive Sulphide	523597	3850416	Mineralization, Worked Massive Sulphide	Metallogenic Map, GSD, 1983
130	Massive Sulphide	525279	3849986	Mineralization, Worked Massive Sulphide	Metallogenic Map, GSD, 1983
131	Massive Sulphide	524599	3849736	Mineralization, Worked Massive Sulphide	Metallogenic Map, GSD, 1983
132	Massive Sulphide	524127	3849880	Mineralization, Worked Massive Sulphide	Metallogenic Map, GSD, 1983

## Appendix 2 Gossan occurrence data

ID	Easting	Northing	Area (m <sup>2</sup> )
1	528469	3872796	15829
2	528699	3872561	19782
3	529013	3872261	6961
4	529947	3871618	7012
5	530088	3871259	12246
6	530566	3871468	7460
7	530953	3871426	25003
8	531685	3870550	55163
9	533965	3871491	24658
10	534325	3871841	6807
11	533615	3870817	60205
12	534058	3869719	66321
13	533869	3868993	15918
14	534545	3868857	94101
15	534650	3869407	8932
16	533157	3867654	478349
17	534054	3867729	73308
18	531640	3867512	40166
19	526971	3867267	10697
20	537937	3868557	330787
21	538028	3867619	4581
22	537938	3867530	11248
23	477405	3862001	50212
24	476271	3861625	11085
25	476471	3861247	8980
26	477033	3860736	3313
27	477670	3860498	2972
28	479259	3859978	10013
29	479459	3859831	4644
30	479562	3859687	5031
31	479687	3859702	6220
32	480049	3859635	18442
33	479917	3859578	2124
34	480129	3859379	6278
35	481053	3858978	5922
36	483006	3858820	75422
37	482733	3858791	5481
38	482615	3858665	3736
39	483980	3858184	9835
40	484239	3858328	7008
41	487396	3857802	7360
42	488649	3857555	108628
43	475835	3870916	9207
44	475926	3870926	9479
45	476085	3871076	3517
46	476191	3870724	9181
47	476512	3871263	8540
48	477162	3883742	22297
49	477387	3883825	14706
50	477137	3884568	13571
51	477129	3886304	35245
52	477537	3886970	28571
53	476336	3887588	102372
54	476493	3889623	41278
55	476155	3890308	9239
56	476419	3890844	16420
57	478434	3888459	27119
58	478660	3888029	119625
59	478977	3888320	70614
60	480533	3887298	18259
61	480814	3887139	13197
62	479902	3886662	18486
63	480418	3886404	281833
64	480479	3885570	13824
65	479958	3885542	11318
66	480874	3886065	53446
67	482770	3884295	29590
68	484746	3880979	10432

ID	Easting	Northing	Area (m <sup>2</sup> )
69	484815	3881197	30173
70	484999	3881382	12996
71	485184	3881273	14003
72	485293	3880910	3602
73	485736	3881494	70601
74	486360	3880901	5922
75	486384	3880690	16745
76	486256	3880475	9083
77	486889	3880549	57542
78	487053	3880285	8126
79	489341	3879278	10138
80	489165	3876848	3642
81	489205	3876383	5450
82	489142	3875472	18749
83	489535	3875721	15436
84	490596	3883501	23811
85	490479	3883049	13308
86	489711	3883505	267278
87	488008	3884614	41184
88	482018	3880801	52583
89	481513	3879579	47454
90	481991	3879258	69873
91	481613	3879068	25680
92	481397	3878971	14827
93	483817	3879474	18462
94	485491	3879716	52651
95	481942	3887109	12160
96	482707	3887799	41316
97	486625	3857686	16829
98	493791	3858655	13922
99	490815	3858494	11653
100	491970	3860083	22507
101	507610	3846931	13900
102	499387	3852854	41375
103	500049	3851503	16901
104	500978	3851118	56120
105	512782	3855512	36186
106	513329	3856265	51019
107	515415	3855029	46280
108	515117	3855965	14857
109	515837	3855966	28576
110	515218	3856138	92673
111	517200	3855548	29571
112	517501	3855013	31367
113	519013	3855558	10576
114	518975	3857183	21088
115	518833	3857003	15427
116	520736	3855939	13478
117	521181	3856036	5829
118	523898	3856049	14657
119	524090	3855822	9237
120	524084	3855541	5236
121	515991	3857616	9790
122	515257	3857519	33644
123	514681	3857898	31952
124	513661	3858168	45663
125	513332	3858341	49568
126	513046	3857377	9926
127	512178	3858349	427901
128	511041	3857742	12059
129	510789	3857915	10704
130	514051	3859536	20454
131	514275	3859538	43610
132	522223	3862066	47772
133	521820	3861390	23036
134	522679	3862264	6791
135	524066	3861000	24327
136	524284	3861614	38278
137	524249	3861422	11658
138	525526	3861046	12821
139	525237	3862143	135538
140	525874	3862697	13719
141	524240	3860302	10367
142	526605	3860200	7729
143	526020	3859661	14866

ID	Easting	Northing	Area (m <sup>2</sup> )
144	525380	3859202	79211
145	525069	3858240	10432
146	525477	3858219	12252
147	525664	3858442	6519
148	522315	3851724	9878
149	516480	3845794	15430
150	517431	3846050	14941
151	517313	3846343	26231
152	516074	3848394	15499
153	516467	3848279	32581
154	519832	3849808	28192
155	519751	3849519	11933
156	520152	3849275	9181
157	520312	3849223	7353
158	520517	3849279	10361
159	520823	3849889	16715
160	521173	3849675	18639
161	521410	3849462	8103
162	521882	3849406	36013
163	522844	3850553	34818
164	523159	3850582	25498
165	519038	3845168	5471
166	500488	3876174	3698
167	500942	3876033	3994
168	501066	3875563	3763
169	501654	3874951	5323
170	501783	3876140	9577
171	501938	3876130	1871
172	502218	3876824	146611
173	505224	3875857	3431
174	505738	3875817	4962
175	505959	3875132	3792
176	505697	3875093	1517
177	507849	3876114	11311
178	508426	3876210	6638
179	508548	3876098	3734
180	508661	3876081	2860
181	501276	3873491	6081
182	501200	3873024	8877
183	500974	3872917	2752
184	500792	3872556	3669
185	508979	3874898	3858
186	508893	3874492	3720
187	508727	3874517	5439
188	505963	3873230	7244
189	497352	3881220	2838
190	497442	3881056	7381
191	497710	3880722	4286
192	498090	3880750	3674
193	497993	3880493	4171
194	498968	3881756	2850
195	499028	3880035	12274
196	499810	3880622	4359
197	499775	3880227	3548
198	500088	3878238	3625
199	500202	3877921	3731
200	500170	3877833	2451
201	500489	3877645	7238
202	501015	3877528	2708
203	501803	3877498	5268
204	502125	3877336	9725
205	503515	3877267	58788
206	503791	3877454	29559
207	503362	3877072	2822
208	503333	3876843	14455
209	503967	3876888	4310
210	503909	3877113	3862
211	504038	3876669	25494
212	504249	3876948	14329
213	504521	3877675	5346
214	506010	3877957	12066
215	506077	3877771	3633
216	504112	3879436	5077
217	504351	3879252	5574
218	503878	3878953	9599

ID	Easting	Northing	Area (m <sup>2</sup> )
219	504191	3878796	2222
220	504475	3878842	2084
221	504699	3878839	2610
222	504807	3878803	2704
223	503163	3878445	2239
224	503290	3878283	8563
225	501756	3878731	3743
226	501834	3880780	5762
227	502396	3880293	8115
228	502237	3880608	4363
229	502325	3880641	3943
230	502057	3881387	4277
231	502095	3881204	1798
232	502944	3881118	2410
233	502930	3881001	2916
234	503082	3880710	3389
235	502266	3881585	9725
236	503485	3881821	4090
237	503619	3882299	3181
238	503592	3882113	2597
239	503703	3882162	2544
240	503632	3882004	2337
241	505221	3881660	2928
242	505357	3881371	3715
243	505356	3881178	2887
244	505117	3880869	2385
245	504922	3880740	2973
246	504772	3880605	5811
247	503360	3880416	2595
248	503716	3880390	3910
249	503512	3880487	3079
250	503392	3880271	11075
251	503017	3881241	4123
252	502768	3878549	4310
253	509644	3878180	3140
254	509372	3877645	5574
255	505590	3879954	7601
256	504977	3879616	5277
257	495216	3882460	8508
258	495488	3881975	1464
259	495975	3881820	11076
260	496301	3881627	3927
261	496432	3881607	4195
262	495130	3882179	2117
263	500552	3881037	6482
264	503237	3881523	4149
265	510329	3877053	90883
266	510620	3876684	19911
267	510342	3876445	19888
268	513256	3878015	66101
269	513354	3876178	27397
270	513833	3876195	13975
271	516775	3876120	14857
272	517553	3875402	9764
273	517660	3875613	10830
274	509751	3878437	74001
275	514479	3872933	36041
276	514214	3872575	22455
277	514149	3871455	30061
278	515277	3870123	62725
279	517754	3875122	40128
280	517624	3874197	50448
281	517662	3873912	28845
282	517952	3873715	14170
283	517817	3872739	23622
284	517704	3872489	17594
285	518120	3872472	8710
286	518441	3872711	17295
287	518266	3873158	12308
288	518199	3873401	14565
289	518194	3873713	37335
290	518487	3874472	21524
291	518318	3874166	91838
292	518051	3874036	10572
293	519020	3875261	5981

ID	Easting	Northing	Area (m <sup>2</sup> )
294	518941	3874501	20971
295	518980	3874234	20719
296	518662	3873629	27851
297	518525	3873189	35426
298	518711	3873183	9862
299	518905	3873338	18541
300	518923	3873126	12719
301	519155	3872728	21571
302	519342	3872611	12135
303	519500	3872948	19251
304	518923	3872566	4829
305	518288	3871743	62125
306	518639	3872110	13697
307	518646	3871758	37303
308	519100	3871941	34589
309	519615	3871021	13713
310	519424	3870323	11172
311	520701	3871957	25863
312	520029	3869838	163400
313	520096	3869563	35378
314	522525	3870959	12987
315	522778	3870905	19346
316	523062	3871115	27836
317	523730	3871321	105677
318	522944	3872325	34826
319	522553	3872387	11219
320	523028	3870377	35883
321	523989	3870714	39386
322	524927	3872133	35820
323	525070	3871849	36656
324	525546	3869313	11109
325	524579	3868441	10383
326	523496	3868069	13113
327	523836	3868099	13650
328	522385	3868284	7085
329	525222	3867055	16080
330	524794	3866653	16553
331	524289	3866683	18352
332	525660	3867268	12135
333	522791	3865214	14028
334	521424	3865361	25074
335	523286	3864952	7574
336	524015	3864677	5491
337	523992	3864866	9847
338	524395	3873013	17421
339	524698	3872705	53904
340	521334	3871859	30581
341	533596	3864274	283504
342	534931	3856468	27206
343	535807	3856832	361873
344	537221	3858756	12524
345	532341	3856508	46572
346	532285	3859440	33546
347	541164	3858499	124116
348	483282	3859598	12924

## Appendix 3 Publications and presentations at international conferences

1. Naden J, Nicolaides S, Jowitt SM., Bateson, L, McEvoy, FM Gunn, AG and Rollin KE (2004) Mineral potential mapping and exploration for cupriferous sulphide mineralisation, Cyprus. In Chaztipetros, A. & Pavlides, S. (Eds.) *5<sup>th</sup> International Symposium on Eastern Mediterranean Geology, Proceedings Volume III*, p. 1439–1142
2. Jowitt, SM, Naden, Nicolaides S, Bateson, L, Rollin KE and Gunn AG. (2004) Preliminary results of GIS-based mineralisation potential mapping for ophiolite-hosted volcanic massive sulphide (VHMS) deposits, Cyprus. *Transactions of the Institution of Mining and Metallurgy Section B Applied Earth Science*, 113, p. 147–148
3. Jowitt, SM, Jenkin GRT, Naden, J and Coogan LA (2005) Geochemical variation in epidiosites of the Troodos Ophiolite, Cyprus: the source of metals in volcanic hosted massive sulphide (VHMS) deposits. *Mineral Deposits Studies Group AGM*, Imperial College, London, January 2005 [abs].
4. Jowitt, SM, McEvoy, FM, Williamson, JP, Bateson, L, Naden, J, Gunn, AG and Nicolaides, S (2005) Mineralisation potential mapping for ophiolite-hosted volcanic massive sulphide (VHMS) deposits, Troodos Ophiolite, Cyprus. In: Mao, J., and Bierlein, F. P. (Eds.) *Mineral Deposit Research: Meeting the Global Challenge* Rotterdam, Millpress, p. 1469–1473.
5. Jowitt, SM, Osborn, RGM, Thomas, R, Naden, J, Gunn, AG, Herrington, RJ and Nicolaides, S (2005) 'T'-type mineralisation - a pseudo-epithermal style of VHMS associated gold mineralisation, Cyprus. In: Mao, J., and Bierlein, F. P. (Eds.) *Mineral Deposit Research: Meeting the Global Challenge*, Rotterdam, Millpress, p. 635–638.

## Appendix 4 Outline prospectivity guide

Below is a generalised and schematic illustration of the steps with a commentary involved in a prospectivity analysis. It is not intended to be a comprehensive flow sheet, but act as shorthand guide to the processes required to produce a prospectivity map

PROCESSES INVOLVED IN A WEIGHTS OF EVIDENCE PROSPECTIVITY ANALYSIS	COMMENTS AND EXAMPLES
<p><b>1. Determine the data model</b></p> <p><i>Paper records–legacy data</i></p> <p><b>Metadata for future use</b></p> <ul style="list-style-type: none"> <li>Spatial location and scale of map</li> <li>Map theme</li> <li>Field/laboratory notebooks</li> <li>Scientific literature</li> </ul> <p><i>Requirements for digitisation</i></p> <p><b>Direct from paper records with geo-registration</b></p> <p><b>Fieldwork/surveying required to correctly position map</b></p> <p><i>Existing digital data</i></p> <p><b>Geological survey data</b></p> <ul style="list-style-type: none"> <li>Geology</li> <li>Geochemistry</li> <li>Geophysics</li> </ul> <p><b>External sources</b></p> <ul style="list-style-type: none"> <li>Satellite imagery</li> <li>Digital elevation models</li> <li>Commercial surveys</li> </ul> <p><i>New data</i></p>	<p>The purpose of this exercise is to determine what data exists, its configuration (digital, paper maps, written records) and the resources required to get it into a digital format</p> <p>It is highly unlikely that all the spatial geoscientific data will be in digital format. Therefore there is a need to document and assess the type and quality of the paper and other analogue records</p> <p>When assessing paper records even though it may not be feasible to utilise the information in a prospectivity analysis it is important to document the information the map contains in a consistent manner</p> <p>If the contents of the map are not to be digitised then at least its spatial extent along with appropriate metadata should be in a digital form so it can be displayed within a GIS</p> <p>Eg. geochemical sampling points, ground based magnetics hand contoured, geology at 1:2500 scale etc.</p> <p>Field and laboratory notebooks often contain important spatial information and should not be neglected as a source of information</p> <p>The published scientific literature can contain useful information such as maps and geochemical data that can be used in a prospectivity analysis. Therefore a literature review should be an integral part of assessing available data</p> <p>This is an important step as converting analogue maps and other paper record into a digital format can be a labour intensive and time consuming process</p> <p>Where maps are accurate and have a recognisable coordinate system it is possible to digitise directly from the map. It is important to note that for a prospectivity analysis data should be digitised as attributed points, lines and polygons – not simply scanned</p> <p>Some maps have local or unknown coordinate systems and it may be necessary to re-survey particular locations so the map can be framed within a known coordinate system (eg. UTM 36N)</p> <p>For an initial prospectivity analysis existing digital data is going to be the most important source of information, as, in terms of time and effort, this is the most cost effective data to obtain.</p> <p>Corporate digital databases are a valuable source of exploration spatial geoscientific information and should always be one of the primary sources of information</p> <p>When considering information for a prospectivity analysis external or commercial data source should not be neglected some of the are extremely useful and free or relatively inexpensive to purchase</p> <p>ASTER and LANDSAT imagery can be valuable data for mapping alteration and structure at the regional (1:250 000) to district scales (1:50 000)</p> <p>DEM's can provide valuable structural information. These can be at a range of scales from SRTM 90 m resolution to LiDAR with 1 m resolution</p> <p>Commonly mineral exploration companies have proprietary data, such as high resolution geophysical and geochemical data that could be very useful in a prospectivity analysis for</p> <p>Whilst making an inventory of existing data it is also appropriate to consider if acquiring new data would assist in the prospectivity analysis</p>
<p><b>2. Develop and refine the mineral deposit model</b></p> <p><i>Target mineralisation</i></p> <p><i>Literature review</i></p> <p><b>Determine key mineral deposit factors</b></p> <ul style="list-style-type: none"> <li>Hydrothermal alteration</li> <li>Geochemical signature</li> <li>Structural associations</li> <li>Surface expressions</li> <li>Form of mineralisation</li> </ul>	<p>The mineral deposit model acts as a guide to identify the type(s) of data that will be needed in the prospectivity analysis</p> <p>The first step is to select the target style of mineralisation so that the correct foundation mineral deposit model can be determined and developed. In addition to Fe-Cu VMS deposits, on Cyprus this could be supergene copper, Au-rich VMS and Limassol/Forest style Co-Ni mineralisation</p> <p>Most of the required information concerning the mineral deposit can be located in the literature, but may need to be modified for local variations</p> <p>Alteration is commonly distinctive for a given mineral deposit type and can be recognised in remote sensing imagery</p> <p>Determining of elements associated with mineralisation is important for identifying which pathfinder elements to utilise from regional geochemical surveys</p> <p>Structural situation is key factor in locating many mineral deposits</p> <p>Eg. Mapped gossans</p> <p>Eg. Veins, stockwork, stratabound, ancient sea-floor mounds</p>

### 3. Establish a practical exploration model

#### Determine most appropriate themes for analysis

How complete is data coverage for the area of interest?

Are the data at an appropriate scale?

What map themes best reflect features in the mineral deposit model?

Faults  
Distribution of gossans  
Satellite imagery

Defining the exploration model is based on the result of the data modelling and mineral deposit modelling exercises. It aims identify the most appropriate map themes to use in the prospectivity analysis

Not all the data contained in the data model will be suitable for the prospectivity analysis

It is important that missing data in an individual theme are minimised as missing data. For example sporadic but high resolution geochemical surveys will not be suitable for a regional analysis as it is not possible to correlate between surveys

It is essential that the selected data themes are at an appropriate scale for the analysis. Eg. A low resolution regional gravity survey would not be an appropriate for a district scale prospectivity analysis

For example, the distribution of faults will be important for vein hosted mineral deposits and will be an important loci for a series of exhalative deposits. Satellite imagery may be important for identifying hydrothermal alteration and surface feature such as gossan may help locate zones of mineralisation

### 4. Construct a project GIS (ArcGIS 9.1)

#### Digitise mineral occurrence data

#### Select appropriate digital data themes

#### Select appropriate legacy data themes and digitise paper records

#### Generate, refine and combine data themes

Contour point data

Calculate distribution of fault intersections

Generate lineament maps from remote sensing imagery

To undertake a prospectivity analysis the data must be in a digital and spatial format. A GIS gives this platform

To undertake a weights of evidence analysis, there is a requirement to have a training point theme that comprises the location of known mineral deposits

These will be determined by the exploration model

Using the GIS it is possible to create new data themes. In addition to those shown on the left, examples include contacts between geological units

### 5. Undertake the prospectivity analysis (ArcSDM3 weights of evidence)

#### Determine area of interest

#### Select training point theme

#### Select analysis themes

#### Calculate theme weights

#### Generalise themes

#### Generate prospectivity map

Select themes for weights of evidence model

Test and refine model

The last step is the production of a prospectivity map using the GIS developed using ArcGIS. This is done with an extension to the software called ArcSDM3. This is available at

Prior to undertaking a weights of evidence analysis the area to be investigated must be selected along with the training point theme (the location of known mineral deposits) and the response themes identified from the exploration model

This process identifies the most prospective evidential themes by examining the spatial relationship between the GIS data and the location of mineral deposits

For the prospectivity analysis to work the input data must be in a raster format and be binary (prospective or unprospective). Generalisation converts a range of continuous (eg. geochemistry) and categorical (e.g. geological) into binary maps

This is achieved through adding and removing themes to obtain optimal statistical combination of data